INFERRING THE ORIENTED ELASTIC TENSOR FROM SURFACE WAVE OBSERVATIONS

by

JIAYI XIE

B.S., University of Science and Technology of China, 2010

A thesis submitted to the

Faculty of the Graduate School of the

University of Colorado in partial fulfillment

of the requirement for the degree of

Doctor of Philosophy

Geophysics in the Department of Physics

2016

This thesis entitled:

Inferring the oriented elastic tensor from surface wave observations

written by Jiayi Xie
has been approved for the Geophysics Program in the Department of Physics

Michael H. Ritzwoller

Shijie Zhong

Michael A. Calkins

Craig H. Jones

Vera Schulte-Pelkum

Date_____

The final copy of this thesis has been examined by the signatories, and we find that both the content and the form meet acceptable presentation standards of scholarly work in the above mentioned discipline.

Xie, Jiayi (Ph.D., Geophysics)

Inferring the oriented elastic tensor from surface wave observations

Thesis directed by Professor Michael H. Ritzwoller

Abstract

Seismic anisotropy yields important constraints on the character of past and present deformation of the Earth's interior. It is therefore of great interest to seismologists. In this thesis, I develop and apply a new method to estimate the tilted elastic tensor for a hexagonally symmetric medium based on seismic surface wave (i.e. Rayleigh and Love waves) data. I apply the method to infer crustal anisotropy in the western US and eastern Tibet. The goal is to obtain more accurate and reliable information about the anisotropic properties of the Earth's crust to help improve the understanding of crustal composition and past deformation.

In terms of method development, my inversion technique simultaneously reconciles observations of surface wave azimuthal and radial anisotropy to provide novel information about the inherent anisotropy and the orientation of the foliated anisotropic material that composes Earth's crust. My inferences occur within the framework of a Bayesian Monte Carlo inversion, which yields posterior distributions for the components of the elastic tensor and its orientation and naturally propagates data uncertainties into model uncertainties.

In terms of application of the methodology, I process seismic data from several arrays in the US and China (USArray, PASSCAL, CEArray, ChinaArray) recorded between the years 2000 and 2012 to obtain high resolution measurements of Rayleigh and Love wave phase speeds and the azimuthal variation of Rayleigh wave phase speeds. Data in both regions can be fit well simultaneously by a tilted hexagonally symmetric medium. The resulting models of the tilted

elastic tensor are geologically correlated. An example result is that in the interior of eastern Tibet, where the crust is thicker than elsewhere in the world, I infer a shallowly dipping middle-to-lower crust that I believe is caused by ductile deformation underlying a steeply dipping upper crust that I believe reflects brittle deformation. In contrast, near the periphery of the Tibetan Plateau the foliation is moderately-to-steeply dipping throughout the entire crust, which may reflect the redirection and shearing of crustal flows imposed by less deformable media surrounding Tibet. The spatial and vertical variations of the estimated elastic tensor and its orientation may provide new insights into the composition and deformation history of Tibetan Plateau in the future.

CONTENTS

TABLES

Table

FIGURES

Figure

CHAPTER I

INTRODUCTION

Seismic anisotropy refer to the phenomena that the seismic wave speeds depend on propagation and polarization directions. The concept of seismic anisotropy was first introduced to geophysics in the last years of the 19th century, and was initially thought of as an unwanted complication [*Helbig and Thomsen*, 2005]. Professor Maurice Rudzki is probably among the first persons that bring anisotropy to seismology *[*Aki, *1964;* Kanamori and Anderson, *1977;* Anderson and Dziewonski, *1982;* Leary et al., *1990;* Babuška, *1991;* Barruol and Mainprice, *1993;* Karato, *1993;* Levshin et al., *1994*, *2005*, *2010;* Christensen and Mooney, *1995;* Kennett et al., *1995;* Chen and Wilson, *1996;* Christensen, *1996;* Levin and Park, *1997b;* Babuška et al., *1998;* Ekstrom and Dziewonski, *1998;* Cotte et al., *1999;* James and Ritzwoller, *1999;* Frederiksen and Bostock, *2000;* Godfrey et al., *2000;* Barmin et al., *2001;* Levshin and Ritzwoller, *2001;* Crampin and Chastin, *2003;* Gung et al., *2003;* Brocher, *2005;* Cholach et al., *2005;* Maceira et al., *2005;* Cholach and Schmitt, *2006*, *2006;* Jiang et al., *2006*, *2011;* Kitamura, *2006;* Mahan, *2006;* Barberini et al., *2007;* Bensen et al., *2007*, *2009;* Harmon et al., *2007*, *2007;* Becker et al., *2008;* Hall et al., *2008;* Lin et al., *2008*, *2009*, *2011;* Caldwell et al., *2009;* Guo et al., *2009;* Kawakatsu et al., *2009;* Li et al., *2009;* Lloyd et al., *2009;* Acton et al., *2010;* Bai et al., *2010;* Chen et al., *2010*, *2010;* Duret et al., *2010;* Huang et al., *2010;* Erdman et al., *2013;* Figueiredo et al., *2013]*. Decades after his death in 1916, the importance of anisotropy for seismology have increased significantly, because the increasing quality and quantity of data forced the recognition that anisotropy is important for accurate inversion for the Earth's structure.

Because deformation induced fabric in the Earth's interior likely causes seismic anisotropy, the characterization of seismic anisotropy has been used to infer global plate motions [*Park and*

Levin, 2002; *Fouch and Rondenay*, 2006], and is therefore of great interest to seismologists. Anisotropy is widely observed in the Earth's upper mantle [e.g., *Anderson*, 1961; *Hess*, 1964; *Raitt et al*., 1969; *Forsyth*, 1975; *Crampin and King*, 1977]. However, the crustal anisotropy was harder to measure on a large scale using passive source seismic data, mainly because of the limited data and observational methods we had. The deployment of large arrays (e.g., USArray, CEArrya) has produced enormous high quality seismic data, and has stimulated many innovations in the seismology discipline. With the new data and innovative observational methods, tracing information related to crustal anisotropy becomes easier.

In this thesis, I will concentrate on measuring crustal anisotropy using surface waves (i.e., Rayleigh and Love waves) that travel along the Earth's surface. Because surface wave provide a homogeneous sampling of the Earth's crust and uppermost mantle over large areas, robust inference about anisotropy from surface waves are typically not restricted to small regions, allowing conclusions to be drawn broadly over a variety of geologic and tectonic settings. As our ability to make seismic observations improves, different components of surface wave anisotropy can be obtained at the same time with high quality. Instead of explaining different components of the data separately, we would want to have one single model that is simple enough to be easily understood, and also complicated enough to explain/reconcile different components of the data simultaneously.

I will present you the crustal anisotropy observations I made in eastern Tibet and western US using surface waves, and will describe an inversion method I developed, which explains/reconcile different surface wave anisotropy components (i.e., azimuthal anisotropy and radial anisotropy) simultaneously in terms of a tilted hexagonally symmetric medium.

In this Chapter, I start by introducing the elastic tensor in section 1.1, which is the essence of seismic velocity models. In section 1.2, I describe the traditional anisotropy observations made with

surface waves, and the limitations of those approaches. In section 1.3, I propose a method to explain the observed surface waves in a more comprehensive way. And finally in section 1.4, I present the arrangement of this thesis.

1.1 Background of the study (elastic tensor and anisotropy)

Seismic imaging uses travel time, phase or amplitude of the observed seismic waves to infer the elastic properties of the deep earth, that directly constrains complex structures in the subsurface, providing information about density, composition and temperature of the earth's interior. The process of inferring elastic properties from observed seismic waves is called "inversion". The mathematical description of the elastic properties is called a "model", which is the elastic tensor that constitutes the earth medium. In a linearly elastic material, the stress and strain are related by a constitutive equation called Hookes' law, $\sigma = \boldsymbol{C}e$ where the **C** is the elastic tensor that describes the elastic property of the material, and thus determines the properties (such as travel time, phase, or amplitude) of seismic waves propagating through it.

The elastic tensor is a forth-order tensor with 81 components, and it can be reduced to 21 independent components when the symmetry of stress and strain, and the idea of strain energy are considered.

The simplest form of elastic tensor is the isotropic elastic tensor:

$$C_{isotropic} = \begin{bmatrix} \lambda+2\mu & \lambda & \lambda & 0 & 0 & 0 \\ \lambda & \lambda+2\mu & \lambda & 0 & 0 & 0 \\ \lambda & \lambda & \lambda+2\mu & 0 & 0 & 0 \\ 0 & 0 & 0 & \mu & 0 & 0 \\ 0 & 0 & 0 & 0 & \mu & 0 \\ 0 & 0 & 0 & 0 & 0 & \mu \end{bmatrix} \tag{1.1}$$

which is described by two parameters λ and μ that are related to the velocities of compressional and shear waves (Vp, Vs). In such a medium, the properties are identical in all directions; therefore seismic speeds are not directional dependent, which means that this medium is isotropic. In many cases, isotropy is a reasonable first-order approximation for much of the Earth's interior. However, isotropy is probably an oversimplified assumption for the real earth, because individual crystals and most rocks are observed to be anisotropic (i.e., elastic properties vary with directions). In fact, seismic observations directly prove the existence of anisotropy in the Earth's interior.

The cause of anisotropy is primarily related to shape preferred orientation (SPO) and lattice-preferred orientation (LPO) of the Earth's materials. In the crust, SPO can be caused by fluid-filled cracks and layering of materials with different compositions [e.g., *Crampin*, 1984]. In the mantle, SPO can result from melt-filled layers or compositional lamellae [e.g., *Kawakatsu et al*., 2009]. Other than SPO, another possible key cause of seismic anisotropy is LPO of crystallographic axes of elastically anisotropic minerals. Mica and amphibole are primary candidates for crustal anisotropy [e.g., *Mainprice and Nicolas*, 1989], and olivine is assumed to be important for upper mantle anisotropy [e.g., *Mainprice and Silver*, 1993].

Observations of anisotropy can be made using various methods, including shear wave splitting [e.g., *Kind et al*., 1985; *Silver and Chan*, 1988; *Vinnik et al*., 1989, 1992; *Levin et al*., 1999; *Savage*, 1999; *Fouch et al*., 2000; *Park and Levin*, 2002], receiver function [e.g., *Levin and Park*, 1997; *Frederiksen et al*., 2003; *Schulte-Pelkum et al*., 2005], relative delay time [e.g., *Babuška*, 1991, and references therein; *Bokelmann*, 2002], Pn anisotropy [e.g., *Hess*, 1964; *Smith and Ekström*, 1999], and surface waves [e.g., *Anderson*, 1961; *Forsyth*, 1975; *Dziewonski and Anderson*, 1981; *Kawasaki and Kon'no*, 1984; *Tanimoto and Anderson*, 1985; *Montagner and*

Nataf, 1986; *Gee and Jordan*, 1992; *Gaherty and Jordan*, 1995; *Laske and Masters*, 1998; *Trampert and Woodhouse*, 2001; *Shapiro and Ritzwoller*, 2002; *Gung et al*., 2003; *Beghein and Trampert*, 2004; *Smith et al*., 2004; *Forsyth and Li*, 2005]. In this thesis, I will only concentrate on anisotropy inferred from surface waves (i.e., Rayleigh and Love waves), and the focus is in the crust instead of the mantle.

Before introducing the surface wave observations, I will briefly describe the anisotropic elastic tensor. There are various forms of anisotropic elastic tensors, here I introduce the study by *Montagner and Nataf* [1986], which relates a general weakly anisotropic elastic tensor to the surface wave observations that will be described in the next session. Based on the study of *Montagner and Nataf* [1986], the elastic tensor **C** of a weakly anisotropic medium can be decomposed into two parts:

$$C_{weakly\ ani.} = \begin{bmatrix} C_{11} & C_{12} & C_{13} & C_{14} & C_{15} & C_{16} \\ C_{12} & C_{22} & C_{23} & C_{24} & C_{25} & C_{26} \\ C_{13} & C_{23} & C_{33} & C_{34} & C_{35} & C_{36} \\ C_{14} & C_{24} & C_{34} & C_{44} & C_{45} & C_{46} \\ C_{15} & C_{25} & C_{35} & C_{45} & C_{55} & C_{56} \\ C_{16} & C_{26} & C_{36} & C_{46} & C_{56} & C_{66} \end{bmatrix} = C_{VTI} + C_{azi.ani.}$$

$$= \begin{bmatrix} \hat{A} & \hat{A}-2\hat{N} & \hat{F} & 0 & 0 & 0 \\ \hat{A}-2\hat{N} & \hat{A} & \hat{F} & 0 & 0 & 0 \\ \hat{F} & \hat{F} & \hat{C} & 0 & 0 & 0 \\ 0 & 0 & 0 & \hat{L} & 0 & 0 \\ 0 & 0 & 0 & 0 & \hat{L} & 0 \\ 0 & 0 & 0 & 0 & 0 & \hat{N} \end{bmatrix} + \begin{bmatrix} \delta C_{11} & \delta C_{12} & \delta C_{13} & \delta C_{14} & \delta C_{15} & \delta C_{16} \\ \delta C_{12} & \delta C_{22} & \delta C_{23} & \delta C_{24} & \delta C_{25} & \delta C_{26} \\ \delta C_{13} & \delta C_{23} & \delta C_{33} & \delta C_{34} & \delta C_{35} & \delta C_{36} \\ \delta C_{14} & \delta C_{24} & \delta C_{34} & \delta C_{44} & \delta C_{45} & \delta C_{46} \\ \delta C_{15} & \delta C_{25} & \delta C_{35} & \delta C_{45} & \delta C_{55} & \delta C_{56} \\ \delta C_{16} & \delta C_{26} & \delta C_{36} & \delta C_{46} & \delta C_{56} & \delta C_{66} \end{bmatrix} \quad (1.2)$$

The first part is hexagonally symmetric with a vertical symmetry axis (Figure 1.1a), and it is referred to as a *vertical hexagonally symmetric medium or VHS medium*. Such a medium is defined by five depth-dependent elastic moduli, $\hat{A}, \hat{C}, \hat{F}, \hat{L}, \hat{N}$ where $\hat{A}$ and $\hat{C}$ are the compressional moduli and $\hat{N}$ and $\hat{L}$ are the shear moduli.

With this VHS tensor, one can directly solve the Christoffel equation to get the velocities of P and S waves with given propagation and polarization directions. In this VHS medium, horizontally propagating SV wave has the same speed in all azimuths, indicating it is azimuthally isotropic. In other words, this part represents the azimuthally averaged component of the original weakly anisotropic elastic tensor. However, horizontally propagating SV and SH waves could have different speeds (Figure 1.1a), and the strength of the difference is characterized by the difference between

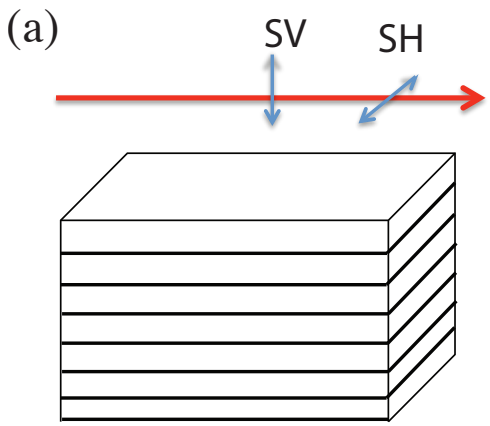

Vertical Hexagonally Symmetric medium (VHS)

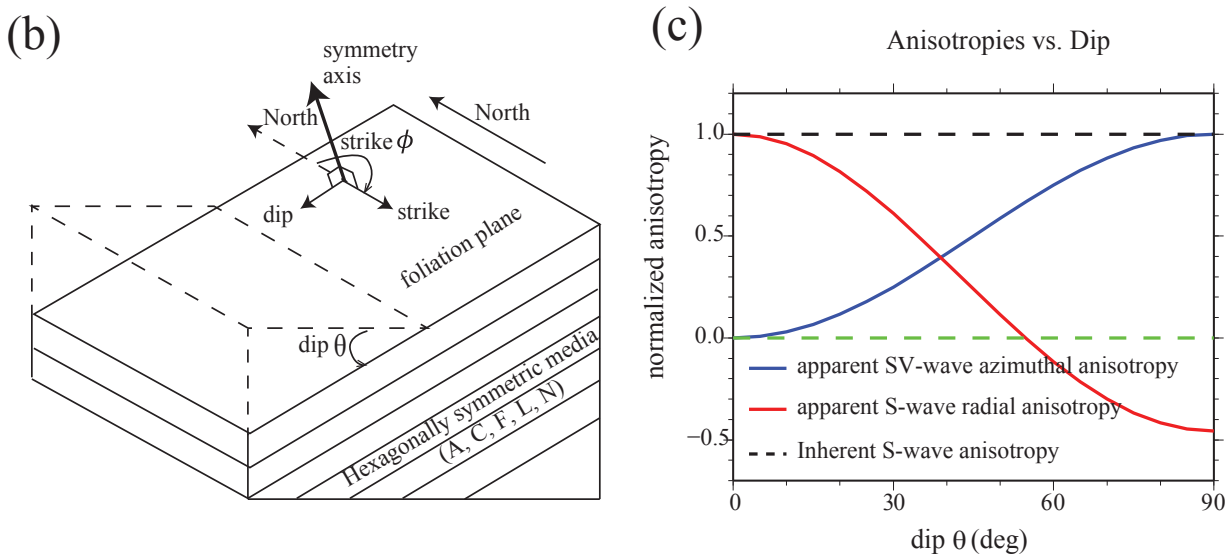

Tilted Hexagonally Symmetric medium (THS)

Figure 1.1 Depiction of (a) a vertical hexagonally symmetric medium (VHS), and (b) a tilted hexagonally symmetric medium (THS). (c) Illustrative computation of the variation of apparent S-wave radial anisotropy and apparent SV-wave azimuthal anisotropy as a function of dip angle θ**.** All amplitudes are normalized by the amplitude of maximum inherent S-wave anisotropy.

elastic moduli $\hat{L}$ and $\hat{N}$. The speed difference between the horizontally and vertically propagating P waves (PH, PV) is characterized by the difference between elastic moduli $\hat{A}$ and $\hat{C}$. Typically, the difference between moduli $\hat{L}$ and $\hat{N}$, or between horizontally propagating SV and SH waves is referred to as *radial anisotropy*.

The second part describes an azimuthally anisotropic component; it represents the azimuthally dependent perturbation relative to the VHS medium described above. This part does not affect the azimuthally averaged part of the surface wave speeds, but only the azimuthally dependent variations. It makes the speed of horizontally propagating SV wave different between north and east directions. The 21 elastic moduli in this tensor can be reformatted into 8 parameters (B_c, B_s, E_c, E_s, G_c, G_s, H_c, and H_s; *Montagner and Nataf*, 1986; *Xie et al*., 2015) that are more directly related to the azimuthally dependent part of surface waves. Among those 8 parameters, $G_c = (\delta C_{55} - \delta C_{44})/2$, $G_s = \delta C_{54}$ are most commonly used due to their strong sensitivity in Rayleigh waves. And $|G| = \sqrt{G_c^2 + G_s^2}$ describes the strength of *azimuthal anisotropy*.

1.2 Traditional surface wave approaches and their limitations

In this section, I discuss the early anisotropy studies using surface waves (i.e. Rayleigh and Love waves), and how their results relate to the elastic tensors described above.

In a weakly anisotropic medium, Rayleigh and Love waves would have the following form [*Smith and Dahlen*, 1973]:

$$c(T,\psi) = c_0(T)[1 + a_2\cos(2(\psi - \varphi_{FA2})) + a_4\cos(4(\psi - \varphi_{FA4}))] \quad (1.3)$$

where T is period, ψ is the azimuth of propagation of the wave measured clockwise from north, c0 is isotropic phase speed, φ_{FA2} is what we call the 2ψ fast axis direction, φ_{FA4} is an analogous phase angle for 4ψ variations in phase speed, and a2 and a4 are the relative amplitudes of the 2ψ and 4ψ anisotropy.

As will be described in the next few paragraphs, different components of the surface waves are generally used separately to infer different aspects of the elastic property of the earth, e.g., the isotropic part, the radially anisotropic part, and the azimuthally anisotropic part.

(isotropic model)

In practice, the last two components of Equation 1.3 (azimuthally varying components) are not easy to measure, because good azimuthal coverage is required to measure them precisely. In addition, the anisotropy of the target region is so weak that anisotropy is buried in the data noise. Therefore, azimuthally averaged term $C_0(T)$ is most commonly used. (However, in the case of strong anisotropy and biased azimuthal coverage, the measurement of $C_0(T)$ could be strongly biased.) In many studies [e.g., *Yang et al*., 2012; *Shen et al*., 2013], when performing inversions, researchers use azimuthally averaged Rayleigh wave alone, which provides no information on the directional dependence of the wave speeds. Therefore, the inverted elastic tensor (or the "model") is assumed to be isotropic with the form shown in Equation 1.1.

(radially anisotropic model)

When azimuthally averaged Rayleigh and Love waves ($C_0(T)$ for Rayleigh and Love waves) are both obtained, we can move beyond isotropic model, and radial anisotropy (if exists) of the medium can be inferred. Because Rayleigh and Love waves have different motions, they provide

information on the direction/polarization dependence of waves traveling through the medium, i.e., the anisotropic property of the medium.

In many places, Rayleigh and Love waves cannot be explained simultaneously using an isotropic model. And this phenomenon is referred to as Rayleigh-Love discrepancy [e.g., *Forsyth*, 1975; *Dziewonski and Anderson*, 1981; *Shapiro et al*., 2004; *Moschetti et al*., 2010; *Xie et al*., 2013]. In this case, an anisotropic VHS model as shown in Equation 1.2 is introduced to solve the discrepancy. As described in Section 1.1, in a VHS medium, horizontally propagating SV and SH waves could have different speeds, and this difference quantifies (S-wave) radial anisotropy. VHS medium is hexagonally symmetric which is described by 5 independent elastic moduli, and this is the simplest plausible model that explains anisotropy. This VHS model is azimuthally isotropic, which is expected because only the azimuthally averaged measurements ($C_0(T)$) are used in generating this model.

Despite its simplicity, the VHS medium is sometimes misused. For example, some studies only invert for the two most data sensitive parameter ($\hat{L}, \widehat{N}$ or Vsv, Vsh) while scaling other three parameters ($\hat{A}, \hat{C}, \hat{F}$ or Vph, Vpv, eta) without specifically showing or noticing them. Please note that in no physically realizable material can anisotropy be approximated with only two parameters, such as Vsv and Vsh. Besides, sometimes P-wave anisotropy is ignored while observed S-wave anisotropy implies that it must be important.

(azimuthally anisotropic model)

When information on the directional dependence of surface wave is introduced, azimuthal anisotropy can be inferred. As number of seismic stations increases and new techniques are innovated, azimuthally varying surface waves can be more easily/accurately measured. The 2ψ

component of azimuthally varying Rayleigh wave is most commonly used (C_0 and a_2 of Rayleigh wave, Equation 1.3). The strength of Rayleigh wave azimuthal anisotropy is correlated with 8 azimuthal parameters (B_c, B_s, E_c, E_s, G_c, G_s, H_c, and H_s) derived from the azimuthally dependent part of the weakly anisotropic tensor described in Section 1.1, with the strongest sensitivity to G_c, G_s. Therefore, with the azimuthally varying Rayleigh wave, one can invert for the azimuthal parameters (typically G_c, G_s) that are related to the azimuthally dependent part of the weakly anisotropic tensor shown in Equation 1.2 [e.g., *Yao et al*., 2010; *Lin et al*., 2011].

At this point, we understand how different aspects of surface wave observations are used to invert for different parts of the elastic tensors. Azimuthally averaged Rayleigh alone is used to invert for an isotropic model. Azimuthally averaged Rayleigh and Love waves combined are used to invert for the VHS part of the anisotropic elastic tensor, and azimuthally varying Rayleigh wave is used to invert for the azimuthally dependent parameters. Moreover, with a few exceptions [e.g., *Montagner and Jobert*, 1988; *Montagner and Nataf*, 1988; *Yuan et al*., 2011], different aspects of the observation are commonly used separately to infer different aspects of the elastic tensor, and are interpreted separately.

However, this kind of 'separate' inversion approach has potential problems. Because different inversions typically have different model parameterization and assumptions, it is challenging to integrate those different inversion results (i.e., the models) together, and the results may not be compatible with each other. Moreover, the form of the original (before decomposition; Equation 1.2) elastic tensor is unclear. All the inferences above are obtained without knowing the property or orientation of the original elastic tensor. It's like measuring the length of a tree's shadow, without knowing the real height of the tree or its orientation relative to the sunlight. The former is the apparent property, while the latters are the inherent properties. In the following sessions, I will

refer the radial and azimuthal anisotropies related to the decomposed elastic tensors (Equation 1.2) as *apparent radial and apparent azimuthal anisotropies*, and refer the anisotropy associated with the original elastic tensor as *inherent anisotropy*.

The goal of this thesis is to show you the crustal anisotropies measured by surface waves in eastern Tibet and western US, and present an inversion approach that explains different aspects of surface wave measurements (azimuthally averaged and azimuthally varying part of the Rayleigh and Love waves) simultaneously, which infers the form of the original elastic tensor and its orientation. The original elastic tensor is assumed to be hexagonally symmetric with a tilted symmetry axis (Figure 1.1b) as will be described in the next few sessions. And I name this inversion approach the *oriented elastic tensor inversion*.

1.3 Challenges and our approaches

There are a few challenges related to this oriented elastic tensor inversion:

(1) Azimuthally dependent surface wave measurements are hard to make. In order to observe the azimuthally varying surface waves, I need data with good azimuthal coverage. Besides, surface waves propagate over long paths will tend to average out the azimuthal anisotropy that may present locally, therefore, dense seismic stations are preferred to help resolve anisotropy at much finer scales. Both of the problems are solved with the deployment of large and dense arrays (~70km spacing; e.g. USArray, CEArray), and array-based innovations, such as the ambient noise technique [*Shapiro et al.,* 2005] and eikonal tomography [*Lin et al.,* 2009]. More specifically, in ambient noise technique, each seismic station is both a source and receiver; therefore, we are not constrained by the location of the earthquakes (the traditional sources), and could make good observation as long as we have

good station coverage, which is achieved by the deployment of large arrays. The typical station spacing of the large array is about 70km, which helps obtain surface wave anisotropy at relatively fine scale. Because ambient noise signal is mainly constrained to periods below about 60 sec, our focus is in the upper ~100km of the earth.

(2) The elastic tensor is too complex. The most general form of elastic tensor has 21 free parameters (elastic moduli), which is too complicated to study, considering the limited observations I have. The number of independent elastic moduli can be reduced if additional symmetries are presented in the elastic tensor. A useful starting point on which to base estimate of the elastic tensor is the simplifying assumption that the medium possess hexagonal symmetry. Such a medium has one symmetry axis, and the elastic property is described by 5 elastic moduli, A, C, F, L, N (please note that these are inherent elastic moduli which are independent of medium's orientation, they are different from the apparent moduli $\hat{A}, \hat{C}, \hat{F}, \hat{L}, \hat{N}$ shown in in Equation 1.2). The orientation of its symmetry axis is described by 2 angles, strike and dip, as shown in Figure 1.1b. In total, 7 depth-dependent parameters describe this tilted hexagonally symmetric (THS) elastic medium, which is also called tilted transversely isotropic medium (TTI). Figure 1.1c illustrates the variation of apparent radial and apparent azimuthal anisotropy as the dip of (simplified) THS varies. For this simplified THS model, the amplitude of apparent azimuthal anisotropy increases with increasing dip, and the apparent radial anisotropy decreases with increasing dip angle. When the dip is 0°, there is strong positive apparent S-wave apparent radial anisotropy but no apparent azimuthal anisotropy. When the dip is 90°, the apparent radial anisotropy becomes negative, and apparent azimuthal anisotropy attains its maximum value. Therefore, values of apparent radial anisotropy and apparent azimuthal anisotropy provide information on the inherent property and orientation of the original (un-tilted) elastic tensor.

(3) How to perform the inversion? Rayleigh and Love waves are strongly sensitive to part of the seven unknowns that define a rotated hexagonally symmetric elastic medium. Therefore, a straightforward inversion of the elastic tensor is impractical using surface waves alone. For this reason, I cast the inverse problem in terms of a Bayesian Monte Carlo approach in which I estimate a range of elastic tensors that agree with the data. Therefore, for each model parameter, I obtain a distribution instead of one single value. From the distribution I can compute the most likely value and its standard deviation. In addition, this method works well even in the situation of multiple solutions.

1.4 Organization of the thesis

The major parts of the thesis are divided into 3 parts. First, Chapter II presents the apparent radial anisotropy I observed in eastern Tibet. This is the observation on the VHS component of the elastic tensor (Equation 1.2), which is azimuthally isotropic. The results there show some interesting features. For example, on average the upper crust has negative or zero apparent radial anisotropy while the middle crust has strong positive apparent radial anisotropy. Besides, in the middle crust, positive radial anisotropy is observed over most E. Tibet, but it turns negative or zero near the boundary of Tibet, where the high plateau meets the rigid lithosphere underlying the Sichuan Basin. One potential explanation on this variation (changes between positive and negative apparent radial anisotropy) is the change of the orientation of the foliation planes of anisotropic material (Figures 1.1b, c). But in order to test this hypothesis, I need to combine the azimuthally independent and azimuthally varying components of surface wave measurements, and develop a new inversion method that uses both components simultaneously. And this motivates the second study presented in the next chapter.

Chapter III describes an inversion method I developed, it interprets observations of surface wave apparent radial and apparent azimuthal anisotropies simultaneously under the assumption of a hexagonally symmetric elastic tensor with a tilted symmetry axis (i.e., THS medium). The inversion is performed in terms of a Bayesian Monte Carlo approach, and this method is referred to as oriented elastic tensor method. I apply this method to W. US where over 800 USArray stations are deployed. I find that measurements of Rayleigh and Love wave phase speeds and the azimuthal variation of Rayleigh wave phase speeds in W. US can be fit well by this tilted hexagonally symmetric medium. Besides, two groups of models with distinct strike fit the data equally well.

With the successful application in W. US, in Chapter IV, I then focus back to Tibet, and apply the oriented elastic tensor method to E. Tibet and its surroundings where ~800 stations from PASSCAL, CEArray, and China Array were deployed. The crust of Tibet is almost twice as thick as that of W. US, and many studies have observed significant complications in crustal structure, such as double Moho and the crustal low velocity zones. What effect would these complications have on the inverted oriented elastic tensor is the main question I try to answer in Chapter IV.

CHAPTER II

CRUSTAL RADIAL ANISOTROPY ACROSS EASTERN TIBET AND THE WESTERN YANGTZE CRATON

Jiayi Xie[1], Michael H. Ritzwoller[1], Weisen Shen[1], Yingjie Yang[2], Yong Zheng[3], and Longquan Zhou[4]

1 – Center for Imaging the Earth's Interior, Department of Physics, University of Colorado at Boulder, Boulder, CO, 80309, USA (jiayi.xie@colorado.edu)

2 – Department of Earth and Planetary Sciences, Macquarie University, 2109, Sydney Australia

3 – State Key Laboratory of Geodesy and Earth's Dynamics, Institute of Geodesy and Geophysics, CAS, Wuhan, 430077, China

4 - China Earthquake Network Center, Beijing, 100045, China

Abstract

Phase velocities across eastern Tibet and surrounding regions are mapped using Rayleigh (8-65 sec) and Love (8-44 sec) wave ambient noise tomography based on data from more than 400 PASSCAL and CEArray stations. A Bayesian Monte-Carlo inversion method is applied to generate 3-D distributions of Vsh and Vsv in the crust and uppermost mantle from which radial anisotropy and isotropic Vs are estimated. Each distribution is summarized with a mean and standard deviation, but is also used to identify "highly probable" structural attributes, which include (1) positive mid-crustal radial anisotropy (Vsh > Vsv) across eastern Tibet (spatial average = 4.8% ± 1.4%) that terminates abruptly near the border of the high plateau, (2) weaker (-1.0% ± 1.4%) negative radial anisotropy (Vsh < Vsv) in the shallow crust mostly in the Songpan-Ganzi terrane, (3) negative mid-crustal anisotropy (-2.8% ± 0.9%) in the Longmenshan

region, (4) positive mid-crustal radial anisotropy (5.4% ± 1.4%) beneath the Sichuan Basin, and (5) low Vs in the middle crust (3.427 ± 0.050 km/s) of eastern Tibet. Mid-crustal Vs < 3.4 km/s (perhaps consistent with partial melt) is highly probable only for three distinct regions: the northern Songpan-Ganzi, the northern Chuandian, and part of the Qiangtang terranes. Mid-crustal anisotropy provides evidence for sheet silicates (micas) aligned by deformation with a shallowly dipping foliation plane beneath Tibet and the Sichuan Basin and a steeply dipping or subvertical foliation plane in the Longmenshan region. Near vertical cracks or faults are believed to cause the negative anisotropy in the shallow crust underlying Tibet.

2.1 Introduction

The amplitude and distribution of elastic anisotropy in earth's crust and mantle provide valuable information about the deformation history of the solid earth. Mantle anisotropy has been particularly well studied in the laboratory and in the field and is believed principally to reflect the lattice preferred orientation of olivine produced by mantle kinematics [e.g., *Schlue and Knopoff, 1977; Montagner and Anderson, 1989; Montager and Tanimoto*, 1991; *Ekström and Dziewonski*, 1998; *Mainprice*, 2007; *Becker et al.,* 2008]. Crustal anisotropy has probably been explored less fully although seismological studies that relate observed anisotropy to crustal deformation and metamorphism have been developing rapidly [e.g., *Okaya et al*., 1995; *Levin and Park*, 1997; *Godfrey et al*., 2000; *Vergne et al*., 2003; *Ozacar and Zandt*, 2004; *Shapiro et al*., 2004; *Sherrington et al*., 2004; *Champion et al*., 2006; *Xu et al*., 2007; *Readman et al*., 2009]. In parallel, petrophysical understanding of the causes of crustal anisotropy has also been growing quickly [e.g., *Barruol and Mainprice,* 1993; *Nishizawa and Yoshino*, 2001; *Okaya and McEvilly*, 2003; *Cholach et al*., 2005; *Cholach and Schmitt*, 2006; *Kitamura*, 2006; *Mahan*, 2006; *Barberini et al*., 2007; *Tatham et al*., 2008; *Lloyd et al*., 2009; *Ward et al*., 2012*; Erdman et al*., 2013]. With the development of ambient noise tomography, surface waves now can be observed at periods short enough to allow shear wave speed models to be constructed at crustal depths including models both of azimuthal [e.g., *Lin et al*., 2011; *Xie et al*., 2012] and polarization or radial [e.g., *Bensen et al*., 2009; *Huang et al*., 2010; *Moschetti et al*., 2010a, 2010b; *Takeo et al*., 2013] anisotropy. The current paper reports on the application of ambient noise tomography to infer radial anisotropy in eastern Tibet and surrounding regions.

Radial anisotropy is a property of a medium in which the speed of the wave depends on its polarization and direction of propagation. For a transversely isotropic medium, such as a

medium with hexagonal symmetry with a vertical symmetry axis, there are two shear wave speeds: Vsv and Vsh. In such a medium, a shear wave that is propagating horizontally and polarized vertically or a shear wave that is propagating vertically and polarized horizontally will propagate with speed Vsv. In contrast, a wave that is propagating in a horizontal direction and polarized horizontally will propagate with speed Vsh. We refer to this difference in wave speed as Vs radial anisotropy or in some places merely as radial anisotropy, which is represented here as the percentage difference between Vsh and Vsv in the medium: γ = (Vsh-Vsv)/Vs. In this case, Vs is the isotropic or effective shear wave speed, and is computed from Vsh and Vsv via a Voigt-average, $Vs = \sqrt{(2Vsv^2 + Vsh^2)/3}$ [*Babuška and Cara*, 1991].

The direct observation of radial anisotropy with regionally propagating shear waves, which are confined to the crust and uppermost mantle, is extremely difficult. Thus, the existence of radial anisotropy is typically inferred from observations of a period-dependent discrepancy between the phase or group speeds of Rayleigh and Love waves. As discussed later in the paper and in many other papers [e.g., *Anderson and Dziewonski*, 1982; *Montagner and Nataf*, 1986], Rayleigh waves are strongly sensitive to Vsv and Love waves to Vsh. The Rayleigh-Love discrepancy is identified by the inability of a simply parameterized isotropic shear velocity model to fit the dispersion characteristics of both types of waves simultaneously. Observations of this discrepancy attributed to radial anisotropy in the mantle in which Vsh > Vsv date back about half a century [*Aki*, 1964; *Aki and Kaminuma*, 1963; *McEvilly*, 1964; *Takeuchi et al*., 1968]. Much more recently, radial anisotropy in the uppermost mantle has been mapped worldwide [*Montagner and Tanimoto*, 1991; *Trampert and Woodhouse*, 1995; *Babuška et al*., 1998; *Ekström and Dziewonski*, 1998; *Shapiro and Ritzwoller*, 2002; *Nettles and Dziewoński*, 2008], and there have also been inroads made into mapping radial anisotropy in the crust beneath the

US [*Bensen et al*., 2009; *Moschetti and Yang*, 2010; *Moschetti et al*., 2010] and Tibet [*Shapiro et al*., 2004; *Chen et al*., 2010; *Duret et al*., 2010; *Huang et al*., 2010]. The observations in Tibet are part of a steady improvement in the reliability and the lateral and radial resolutions of surface wave dispersion studies that cover all [*Ritzwoller et al*., 1998; *Villaseñor et al*., 2001; *Levshin et al*., 2005; *Maceira et al*., 2005; *Zheng et al., 2010; Caldwell et al*., 2009; *Acton et al*., 2010; *Yang et al*., 2010, 2012] or parts of the high plateau [*Levshin et al*., 1994; *Cotte et al*., 1999; *Rapine et al*., 2003; *Yao et al*., 2008, 2010; *Guo et al*., 2009; *Li et al*., 2009; *Jiang et al*., 2011; *Zhou et al*., 2012].

The observation of crustal radial anisotropy has been taken as evidence for the existence of strong elastically anisotropic crustal minerals aligned by strains associated with processes of deformation [*Shapiro et al*., 2004; *Moschetti et al*., 2010]. Many continental crustal minerals are strongly anisotropic as single crystals [*Barruol and Mainprice*, 1993; *Mahan*, 2006], but some of the most common minerals (e.g., feldspars, quartz) have geometrically complicated anisotropic patterns that destructively interfere with polycrystalline aggregates [*Lloyd et al*., 2009; *Ward et al*., 2012]. Micas and amphiboles are exceptions that exhibit more robust alignment in both crystallographic direction and shape that produce simple patterns of seismic anisotropy [*Tatham et al*., 2008; *Lloyd et al*., 2009]. For this reason, recent observations of strong anisotropy in the middle crust have been attributed to the crystallographic preferred orientation (CPO) of mica [*Nishizawa and Yoshino*, 2001; *Shapiro et al*., 2004; *Moschetti et al*., 2010]. In the lower crust, amphibole may also be an important contributor to seismic anisotropy [*Kitamura*, 2006; *Barberini et al*., 2007; *Tatham et al*., 2008].

Shapiro et al. [2004] showed that crustal radial anisotropy is strong in western Tibet and may extend into eastern Tibet where the resolution of their study was weaker. Subsequently,

Duret et al. [2010] presented evidence from individual seismograms using aftershocks of the Wenchuan earthquake of 12 May 2008 that the Rayleigh-Love discrepancy is so significant for paths crossing Tibet that crustal radial anisotropy probably also extends into eastern Tibet. *Huang et al*. [2010] confirmed this expectation by mapping crustal radial anisotropy in far southeastern Tibet. Example cross-correlations of ambient noise for a path in the Qiangtang terrane (Figure 2.1) contain Rayleigh and Love waves as shown in Figure 2.2a. Figure 2.2b illustrates that a Rayleigh-Love discrepancy exists for this path, revealing that crustal radial anisotropy, indeed, is present between stations located within eastern Tibet.

The objective of this paper is to map crustal radial anisotropy across all of eastern Tibet (Figure 2.1), extending the results into adjacent areas north and east of the high plateau for comparison. Rayleigh and Love wave phase velocity curves are measured from ambient noise cross-correlations between each pair of simultaneously operating stations between 8 and 44 sec period for Love waves and 8 and 65 sec for Rayleigh waves. As shown later, the inability to observe Love waves at longer periods implies that radial anisotropy cannot be reliably mapped deeper than about 50 km, which means that we cannot place tight constraints on the strength of radial anisotropy in the lowermost crust beneath Tibet. For this reason, we focus discussion on mid-crustal radial anisotropy.

The inversion of surface wave data for a 3-D radially anisotropic shear wave speed model consists of two stages: first, a tomographic inversion is performed using measured Rayleigh and Love wave dispersion curves for period-dependent phase speed maps on a 0.5°×0.5° grid using the tomographic method of *Barmin et al*. [2001] with uncertainties estimated using eikonal tomography [*Lin et al*., 2009] (Section 2.2), and second, a Bayesian Monte Carlo inversion [*Shen et al*., 2013b] is carried out for a 3-D radially anisotropic shear velocity (Vsv, Vsh) model of the

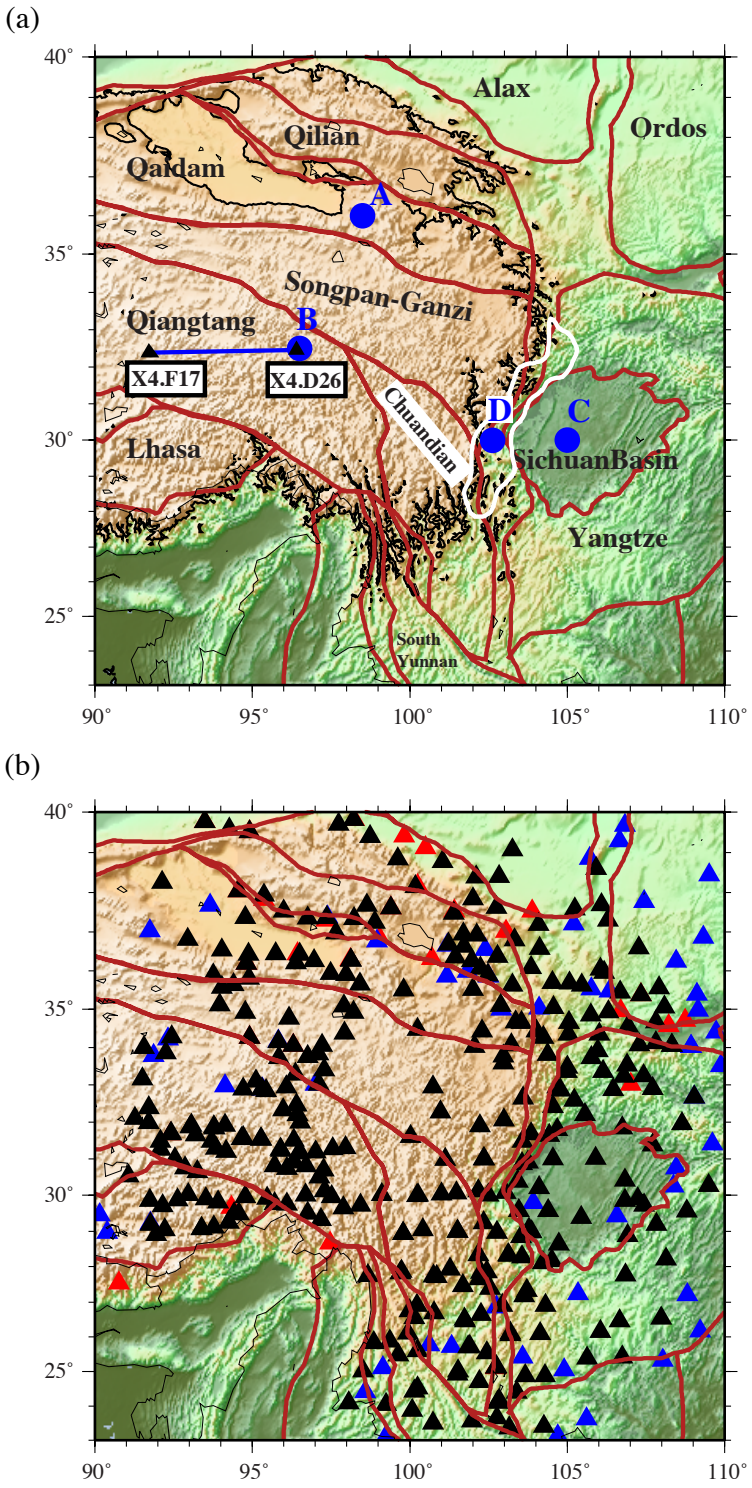

Figure 2.1. (a) Reference map of the study region in which red lines indicate the boundaries of major geological units and basins [*Zhang et al.*, 1984, 2003]. The white contour outlines what we refer to as the Longmenshan region. The blue line is the path between stations X4.F17 and X4.D26 referenced in Fig. 2. Points A, B, C, and D indicate sample points referenced in Figs. 6, 7, 13, 16, 17, and 19. (b) Locations of seismic stations used in this study. Red and black triangles are stations used to measure Love wave dispersion, while blue and black triangles indicate stations used for Rayleigh wave measurements.

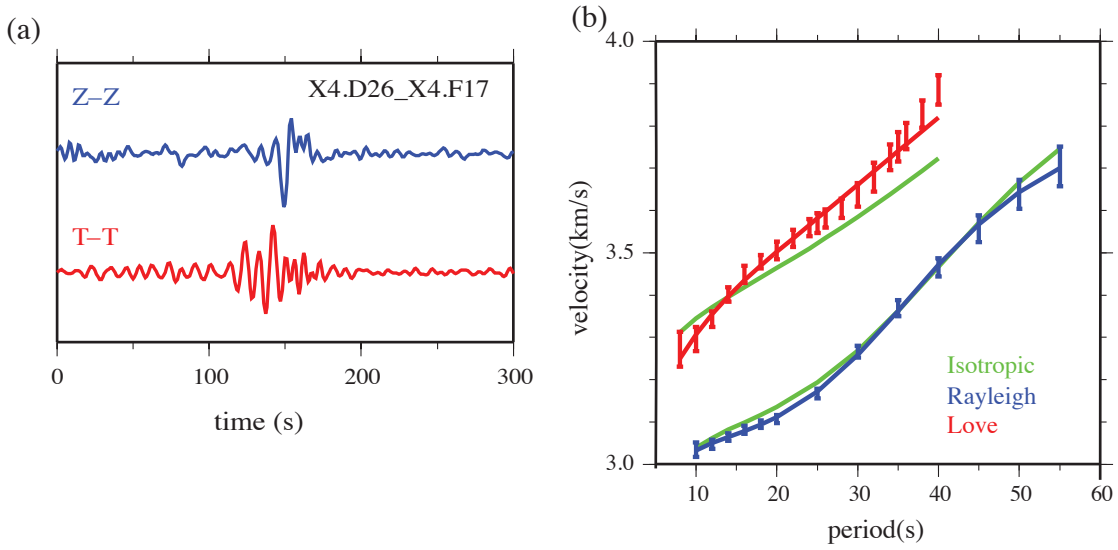

Figure 2.2. (a) Example of Rayleigh wave (blue, vertical-vertical, Z-Z) and Love wave (red, transverse-transverse, T-T) cross-correlations for a pair of stations (X4.F17, X4.D26) located in the Qiangtang terrane (Fig. 1a), band pass filtered between 5 and 100 sec period. (b) Observed Rayleigh and Love wave phase speed curves measured from the cross-correlations are presented as 1 standard deviation (1σ) error bars (red-Love, blue-Rayleigh). Inverting these data for an isotropic model (Vs = Vsh = Vsv) produces the best fitting green curves, which demonstrates a systematic misfit to the data (predominantly the Love waves) and a Rayleigh-Love discrepancy. Allowing crustal anisotropy (Vsh ≠ Vsv), produces the blue and red dispersion curves that fit the data.

crust (Section 2.3). The inversion estimates the posterior distribution of accepted models at each location, which is used in two ways. First, at each grid node we summarize the distribution at each depth with its mean and standard deviation. Using the mean of the distribution, we show that strong mid-crustal positive (Vsh > Vsv) radial anisotropy is observed across all of eastern Tibet and terminates abruptly as the border of the high plateau is reached. It is also observed in the middle crust beneath the Sichuan Basin. Negative radial anisotropy (Vsv > Vsh) is observed in the shallow crust beneath eastern Tibet and in the middle crust of the Longmenshan region. Second, we also query the entire posterior distribution of models in order to determine which structural attributes are highly probable, which are only likely, and which are prohibited. Throughout, we attempt to address how uncertainties in prior knowledge (e.g., Vp/Vs in the crust) affect the key inferences. In particular, we investigate if prior constraints and assumptions are likely to bias the posterior distribution significantly. Finally, we ask how the observations reflect on the presence or absence of pervasive partial melt in the middle crust across Tibet and speculate on the physical causes of several observed radial anisotropy features.

2.2 Data processing and tomography

2.2.1 Love wave and Rayleigh wave tomography

For Love wave data processing, we apply the procedure described by *Bensen et al*. [2007] and *Lin et al*. [2008] to recordings at 362 stations (Figure 2.1), consisting of 180 PASSCAL and GSN stations and 182 Chinese Earthquake Array (CEArray) stations [*Zheng et al*., 2010]. We downloaded all available horizontal component data for PASSCAL and GSN stations between years 2000 and 2011 from the IRIS DMC. Horizontal component data for the CEArray stations were acquired for the years 2007 through 2009. We cut horizontal component ambient noise

records into 1-day long time series and then cross-correlate the transverse components (T-T) between all possible station pairs, after the performance of the time domain and frequency domain normalization procedures described by *Bensen et al*. [2007]. As *Lin et al*. [2008] demonstrated, Love wave energy dominates transverse-transverse (T-T) cross-correlations. *Yang et al*. [2008] showed that Rayleigh wave cross-correlations between stations in Tibet are typically not symmetric, but there is significant energy from most directions with the primary directions of propagation of the waves being dependent on both period and season. This is also true for Love waves, but the strongest waves (highest SNR) typically come from the southeast. After the cross-correlations, we applied automated frequency-time analysis (FTAN) [e.g., *Levshin and Ritzwoller*, 2001; *Bensen et al*., 2007]) to produce Love wave phase speed curves for periods between 8 and 30 to 50 sec (depending on the signal-to-noise ratio) for each station pair.

Rayleigh wave phase speed measurements are obtained from cross-correlations of vertical-component ambient noise, the vertical-vertical (Z-Z) cross-correlations, which are rich in Rayleigh waves. *Yang et al*. [2010] generated Rayleigh wave phase velocity maps from ambient noise across the Tibetan Plateau. Instead of using their dispersion maps directly, we re-selected the measurements for stations within our study region and re-performed the tomography as described below. Example T-T and Z-Z cross-correlations and measured phase speeds between the station-pair X4.D26 and X4.F17 are shown in Figure 2.2**.**

For dispersion measurements at different periods, we exploited three criteria to identify reliable measurements: (1) the distance between two stations must be greater than two wavelengths to ensure sufficient separation of the surface wave packet from precursory arrivals and noise and to satisfy the far-field approximation (the use of a three-wavelength criterion

changes results negligibly); (2) measurements must have a signal-to-noise ratio (SNR) > 10 for Love wave and SNR > 15 for Rayleigh wave to ensure the reliability of the signal; and (3) the observed travel times and those predicted from the associated phase velocity map between each accepted station-pair must agree within a specified tolerance [*Zhou et al*., 2012]. We found that horizontal components are problematic (mainly relative to criterion (3) above) for 61 stations. Their removal left us with the 362 stations shown in Figure 2.1. The vertical components of 26 stations are similarly identified as problematic and are rejected from further analysis leaving 406 stations from which we obtain Rayleigh wave measurements. This procedure produces about 30,000 Love wave phase velocity curves and 40,000 Rayleigh wave curves.

Because eikonal tomography [*Lin et al*., 2009] models off-great circle propagation, it would be preferable to straight ray tomography [*Barmin et al*., 2001]. Eikonal tomography works best, however, where there are no spatial gaps in the array of stations. There are gaps in our station coverage near 33°N, 100°E in eastern Tibet (Figure 2.1b). Thus, we apply straight-ray tomography [*Barmin et al*., 2001] to generate phase velocity maps, but use eikonal tomography to estimate uncertainties in these maps, as described in Section 2.2.2. To reduce the effect of non-ideal azimuthal coverage at some locations, we simultaneously estimate azimuthal anisotropy, but these estimates are not used here. What results are Love wave phase velocity maps ranging from 8 to 44 sec and Rayleigh wave phase velocity maps from 8 to 65 sec period. Above 44 sec period, the SNR of Love waves decreases dramatically, which degrades the ability to produce reliable high-resolution maps. Examples of Rayleigh and Love wave phase speed maps at periods of 10 and 40 sec are shown in Figure 2.3. At 10 sec period, the maps are quite sensitive to shallow crustal structures to about 20 km depth including the existence of sediments, and at 40

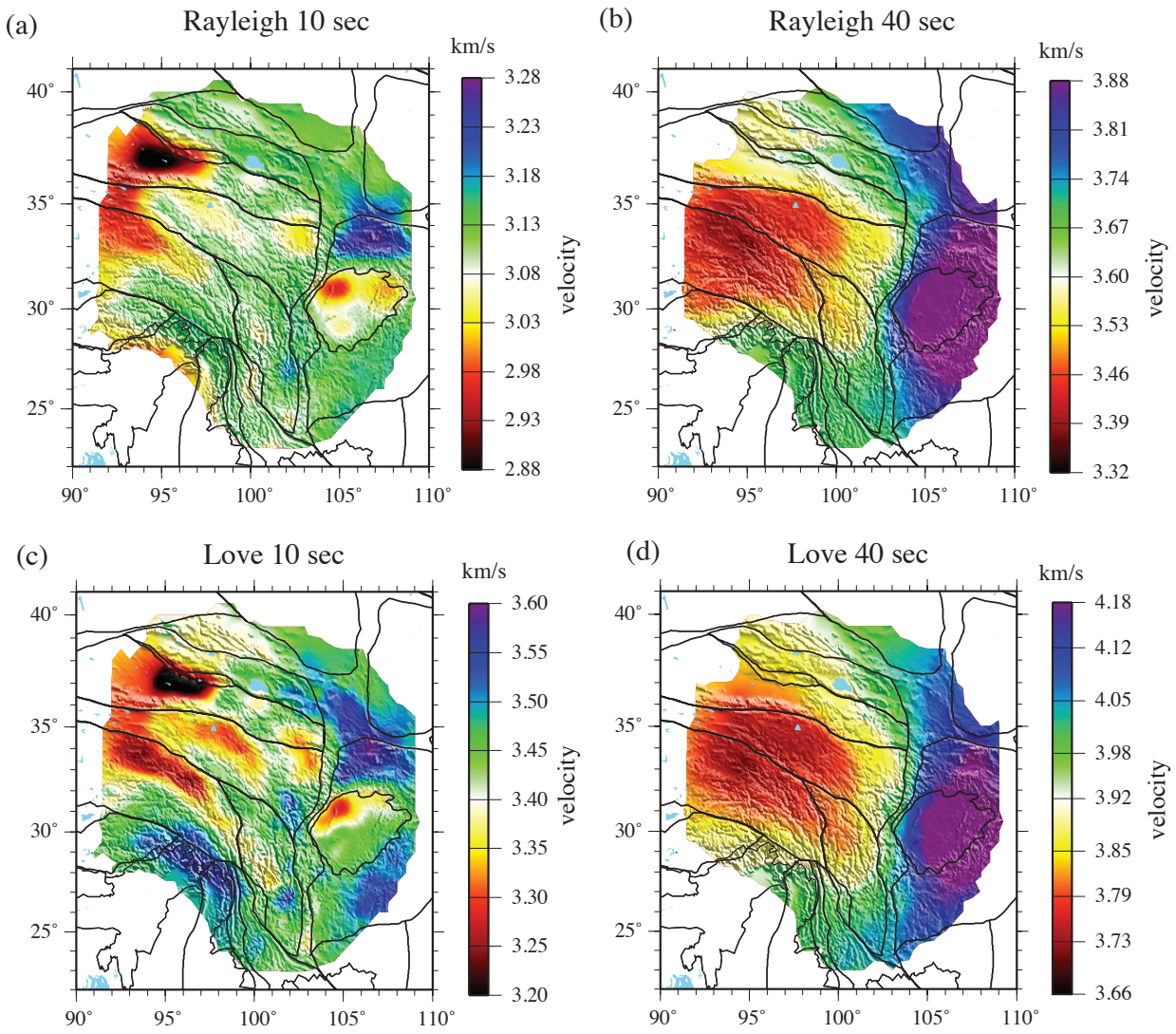

Figure 2.3. Example estimated Rayleigh (a,b) and Love (c,d) wave phase speed maps at 10 (a,c) and 40 sec (b,d) period determined from ambient noise cross-correlations.

sec period the maps are predominantly sensitive to structures near the Moho such as crustal thickness.

2.2.2 Uncertainties and local dispersion curves

Local uncertainty estimates for each of the phase speed maps provide the uncertainties used in the inversion for 3-D structure. Estimates of uncertainties in the Rayleigh and Love wave phase speed maps are determined by eikonal tomography [*Lin et al*., 2009], which, as discussed above, does not produce uniformly unbiased phase speed estimates where there are gaps in station coverage. We find, however, that it does produce reliable uncertainty estimates, even in the presence of spatial gaps. Averaging the one-standard deviation uncertainty maps across the study region, average uncertainties are found to range between 0.012 to 0.057 km/s for Rayleigh waves and 0.016 to 0.060 km/s for Love waves (Figure 2.4), minimize between about 12 and 25 sec period, and increase at both shorter and longer periods. Because of the lower SNR and the smaller number of Love wave measurements, uncertainties for Love waves tend to be larger than for Rayleigh waves. In addition, the SNR decreases faster at long periods for Love waves than Rayleigh waves, so the uncertainty for Love waves at long periods is higher still than for Rayleigh waves. Uncertainties for both wave types increase toward the borders of the maps at all periods.

Having estimated maps of period-dependent dispersion and uncertainty, local Rayleigh and Love wave dispersion curves with associated uncertainties are generated on a 0.5°×0.5° grid across the study region. These data are the input for the 3-D model inversion that follows.

2.3 Bayesian Monte Carlo inversion of local dispersion curves

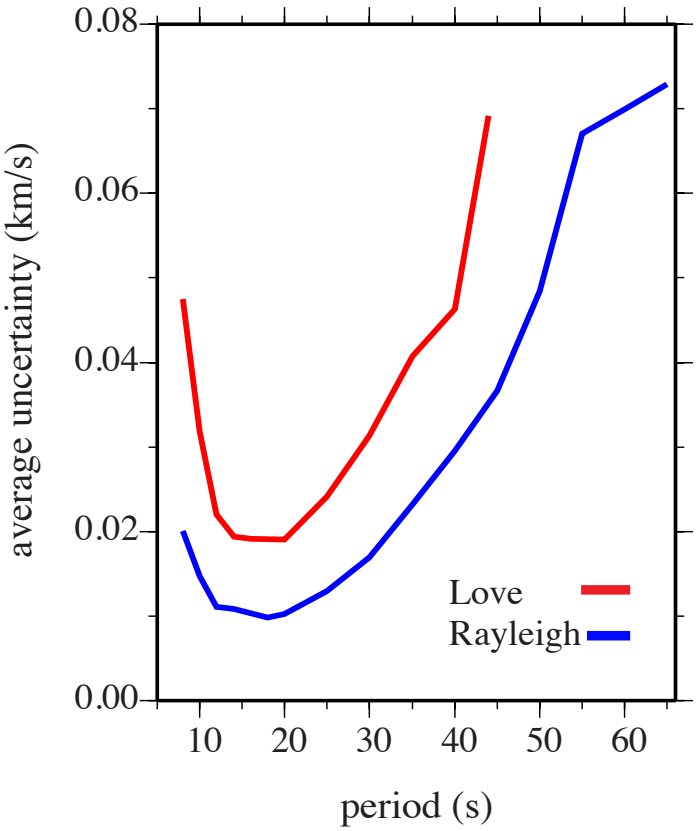

Figure 2.4. Uncertainties (1σ) in the Rayleigh and Love wave phase speed maps averaged across the study region estimated using the eikonal tomography method of *Lin et al.*[2009].

2.3.1 Model parameterization and prior constraints

The 3-D model comprises a set of 1-D models situated on a 0.5°×0.5° grid. Following *Shen et al*. [2013a, 2013b], each of the 1-D models is parameterized with three principal layers: a sedimentary layer, a crystalline crustal layer, and a mantle layer to a depth of 200 km. The sedimentary layer is isotropic and is described by two parameters: layer thickness and constant shear wave speed Vs. Anisotropy in the sedimentary layer is physically possible, but with the data used here cannot be resolved from anisotropy in the crystalline crust. In addition, it has little affect in the period range of the observed Rayleigh-Love discrepancy as discussed further in Section 2.4. For these reasons, we include anisotropy only below the sediments.

We represent anisotropy through the elastic moduli of a transversely anisotropic medium (also referred to as radial anisotropy). In such a medium the elastic tensor is specified by five moduli: A, C, L, N, and F. The moduli A and C are related to the P-wave speeds (Vph, Vpv) and L and N are related to the S-wave speeds (Vsv, Vsh) as follows: $A = \rho V^2_{ph}$, $C = \rho V^2_{pv}$, $L = \rho V^2_{sv}$, and $N = \rho V^2_{sh}$, where ρ is density. Some authors summarize radial anisotropy with three derived parameters: $\xi = N/L = (Vsh/Vsv)^2$, $\phi = C/A = (Vpv/Vph)^2$, and $\eta = F/(A-2L)$. We prefer to summarize Vs and Vp anisotropy with two different parameters in addition to η, defined as follows: $\gamma = (Vsh - Vsv)/Vs$ and $\varepsilon = (Vph - Vpv)/Vp$, where Vs is the Voigt average of Vsh and Vsv and Vp similarly is the Voigt average of Vph and Vpv. We refer to γ as Vs radial anisotropy and ε as Vp radial anisotropy. These parameters are simply related to those used by some other authors: $\gamma + 1 \approx \xi^{1/2}$ and $\varepsilon + 1 \approx \phi^{-1/2}$. In an isotropic medium, Vsh = Vsv, Vph = Vpv, and F = A – 2L, thus $\xi = \phi = \eta = 1$ and $\gamma = \varepsilon = 0$.

We make the simplifying (but nonphysical) assumption that only Vs anisotropy is present in the elastic tensor in the crust and mantle. Thus, we allow Vsh to differ from Vsv, but restrict Vph = Vpv ($\varepsilon = 0$) and $\eta = 1$. Strictly speaking this is physically unrealistic because in real mineral assemblages Vs anisotropy would be accompanied by Vp anisotropy with η differing from unity [e.g., *Babuška and Cara*, 1991; *Erdman et al*., 2013]. In Section 2.5.4.4 we show, however, that the effect of this assumption on our estimate of crustal Vs anisotropy is negligible. Therefore, although we represent radial anisotropy in terms of Vs anisotropy alone, our results are consistent with the inclusion of Vp anisotropy in the elastic tensor along with η that differs from unity.

The crystalline crustal layer is described by nine parameters: layer thickness, five B-splines (1-5) for Vsv (Figure 2.5), and three more independent B-splines for Vsh (2-4). We set Vsh = Vsv for B-splines 1 and 5. Because B-splines 2 and 4 extend into the uppermost and lowermost crust, respectively, radial anisotropy can extend into these regions but its amplitude will be reduced relative to models in which Vsh and Vsv for B-splines 1 and 5 are free. The effect of this constraint is discussed in Section 2.5.4.1.

Mantle structure is modeled from the Moho to 200 km depth with five B-splines for Vsv. Vsh in the mantle differs from Vsv by the depth-dependent strength of radial anisotropy taken from the 3-D model of *Shapiro and Ritzwoller* [2002]. Thus, in the mantle we estimate Vsv, but set Vsh = Vsv $+\delta V$ where δV is the difference between Vsh and Vsv in the model of *Shapiro and Ritzwoller* [2002]. Below 200 km the model reverts to the 1D model ak135 [*Kennett et al*., 1995]. The effect on estimates of crustal anisotropy caused by fixing the amplitude of mantle anisotropy is considered in Section 2.5.4.2. Overall, there are 16 free parameters at each point and the model parameterization is uniform across the study region.

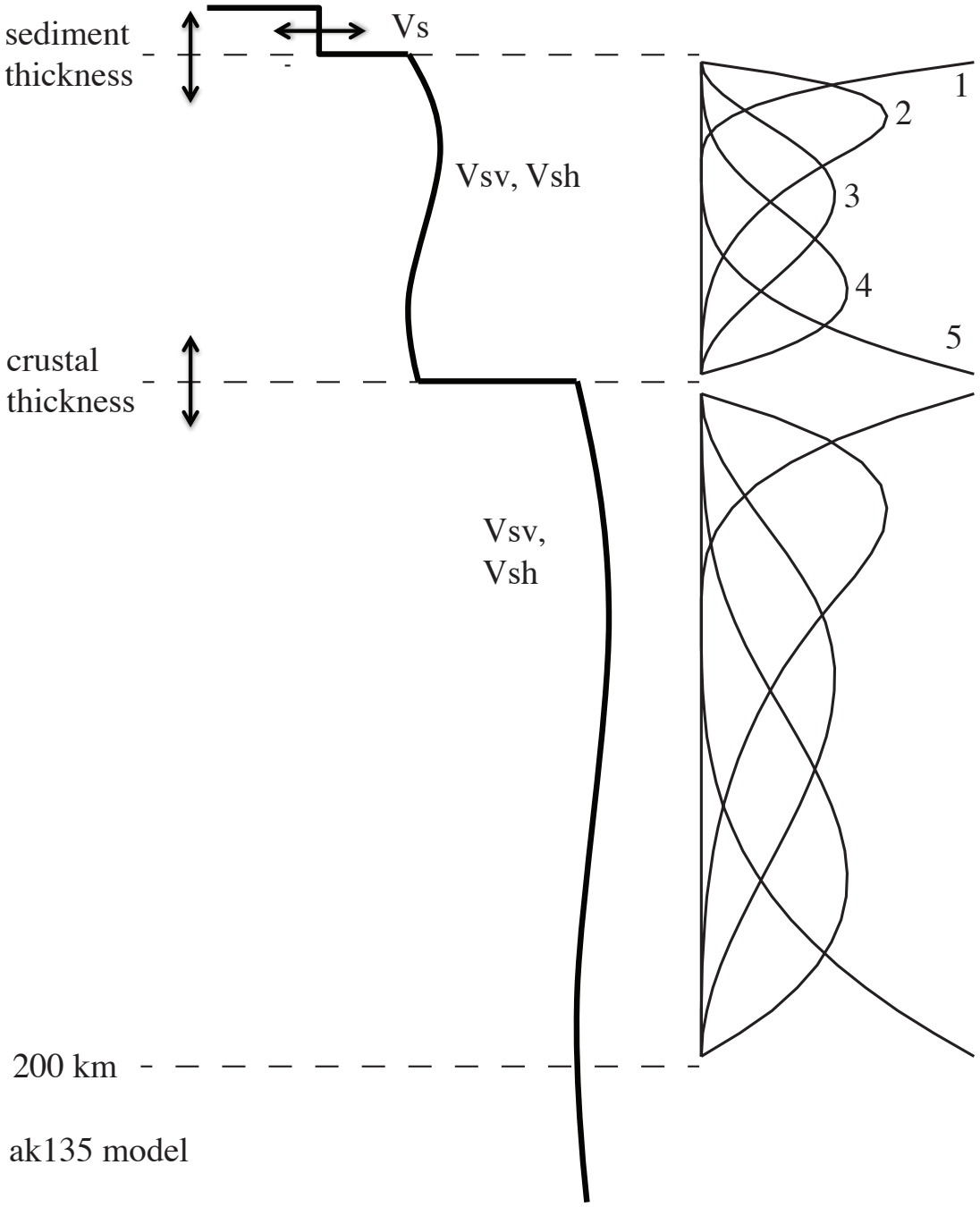

Figure 2.5. Representation of the parameterization used across the study region. In the crust, five B-splines (1-5) are used to represent Vsv, but three B-splines (2-4) are used to represent Vsh. In the mantle, five B-splines are estimated for Vsv but Vsh is derived from the strength of radial anisotropy in the model of *Shapiro and Ritzwoller* [2002]. A total of 16 parameters represent the model at each spatial location.

Because Rayleigh and Love wave velocities are mainly sensitive to shear wave speeds, other variables in the model such as compressional wave speed, Vp, and density, ρ, are scaled to the isotropic shear wave speed model, Vs. Vp is converted from Vs using a Vp to Vs ratio such that Vp/Vs is 2.0 in the sediments and 1.75 in the crystalline crust and mantle, consistent with a Poisson solid. For density, we use a scaling relation that has been influenced by the studies of *Christensen and Mooney* [1995] and *Brocher* [2005] in the crust, and by *Karato* [1993] in the mantle where sensitivity to density structure is much weaker than in the crust. The Q model comes from ak135 [*Kennett et al*., 1995] with some modifications: shear Q is 600 in the upper 20 km and 400 between 20 and 80 km depth outside the Tibetan Plateau, while we set it to 250 within the Tibetan Plateau [*Levshin et al*., 2010]. Vs, Vsv, and Vsh are converted to a reference period of 1 sec. To test the effect of uncertainties in the physical dispersion correction [*Kanamori and Anderson*, 1977] on estimates of Vsv and Vsv caused by ignorance of the Q of the crust, we lowered values of Q from 250 to 100 between 20 and 80 km depth. We found that the amplitude of the resulting depth averaged crustal radial anisotropy decreased only slightly for the smaller Q beneath point B shown in Figure 2.1a. As a constant Q of 100 between these depths is almost certainly too low and we are concerned with anisotropy amplitudes greater than 1%, uncertainties in the Q model can be ignored here.

To avoid consideration of physically unreasonable models, we imposed prior constraints on the parameter space explored in the inversion. (1) Although velocity is not constrained to increase monotonically with depth, it cannot decrease with depth at a rate ($-\Delta v/\Delta h$) larger than 1/70 s^{-1}. This constraint reduces (but does not entirely eliminate) the tendency of the shear-wave speeds to oscillate with depth. (2) Shear-wave speeds increase with depth across the sediment-

basement interface and across Moho. (3) Both Vsv and Vsh are constrained to be less than 4.9 km/s at all depths. (4) The amplitude of radial anisotropy in the uppermost and lowermost crust is constrained by setting Vsh=Vsv for splines 1 and 5 (Figure 2.5). The last constraint is imposed to mitigate against radial anisotropy oscillating with depth, and its effect is discussed further in Section 2.5.4.1.

The model space is then explored starting with perturbations (Table 2.1) to a reference model consisting of sedimentary structure from *Laske and Masters* [1997] and crystalline crustal and uppermost mantle structure from *Shapiro and Ritzwoller* [2002]. Imposing the prior constraints in model space defines the prior distribution of models, which aims to quantify the state of knowledge before data are introduced. In particular, a new model m_i is generated by perturbing the initial model m_0 following the procedure described by *Shen et al*. [2013b]. The set of all models that can be produced in this way is called the prior distribution and example plots for various model variables are shown in Figure 2.6.

2.3.2 Inversion procedure

With the parameterization and constraints described above, we perform a Bayesian Monte Carlo inversion based on the method described by *Shen et al*. [2013b]. This method is modified to produce a radially anisotropic model using both Love and Rayleigh wave data without receiver functions. The main modifications lie in the forward calculation of surface wave dispersion for a transversely isotropic (radially anisotropic) medium, which we base on the code MINEOS [*Masters et al*., 2007]. Unlike most seismic dispersion codes, the MINEOS code consistently models a transversely isotropic medium. In order to accelerate the forward calculation, we compute numerical first-order partial derivatives relative to each model parameter. Given the range of model space explored, the use of first-derivatives is sufficiently

Table 2.1. Model parameter constraints

	Model parameter	Perturbation	Reference model
Sedimentary layer	Sediment thickness Vsv in sediment Vsh in sediment	+/- 100% +/- 1.0 km/s equals to Vsv	*Laske & Masters* [1997]
Crystalline crustal layer	Crustal thickness 5 Vsv B-splines* 5 Vsh B-splines*	+/- 10% +/- 20% +/- 20%	*Shapiro & Ritzwoller* [2002]
Mantle layer to 150 km	5 Vsv B-splines Anisotropy	+/- 20% 0	*Shapiro & Ritzwoller* [2002]

* $\Delta v/\Delta h \geq 0$ or -1/70 $s^{-1} \leq \Delta v/\Delta h < 0$

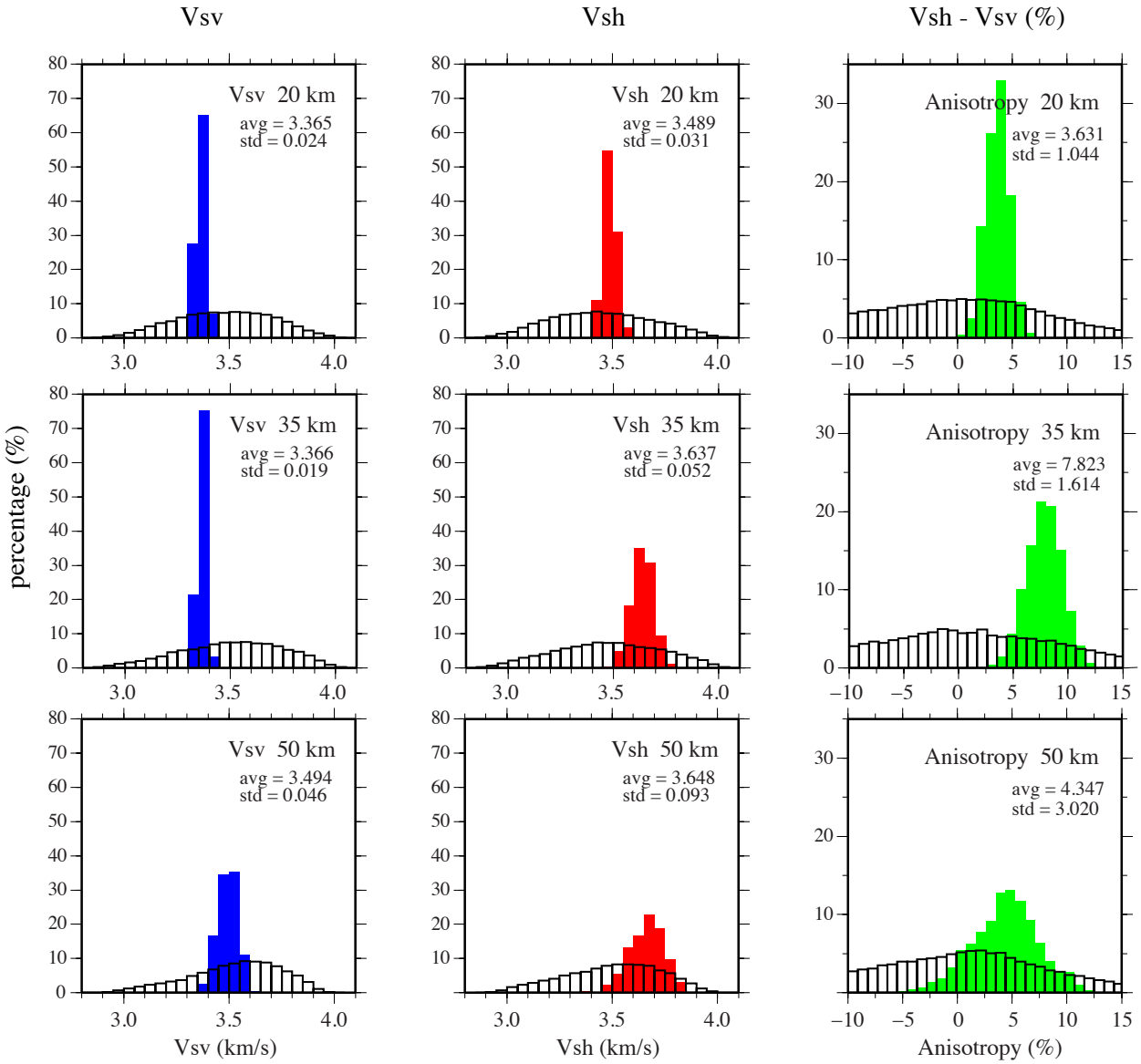

Figure 2.6. Prior (white histograms) and posterior distributions for Vsv (blue), Vsh (red) and Vs radial anisotropy (green, γ in percent) at 20, 35, and 50 km depth for point B in the Qiangtang terrane (Fig. 1a). The mean and standard deviation for each posterior distribution are shown in each panel.

accurate [*James and Ritzwoller*, 1999; *Shapiro and Ritzwoller*, 2002]. For every spatial location, we start from the reference model described above, $\boldsymbol{p}_{ref}$, and the corresponding Rayleigh or Love wave dispersion curves, $\boldsymbol{D}_{ref}$, and the partial derivatives $(\partial \mathrm{D}/(\partial \mathrm{p_i})$ are computed numerically for all 16 free parameters using the MINEOS code. With these partial derivatives, dispersion curves $\boldsymbol{D}$ for any model $\boldsymbol{p}$ may be approximated as:

$$\boldsymbol{D} = \boldsymbol{D}_{ref} + \sum_{\boldsymbol{i}} \left(\frac{\partial \boldsymbol{D}_{\boldsymbol{ref}}}{\partial p_i}\right) \delta p_i \tag{2.1}$$

where $\delta p_i = p_i - p_{ref\,i}$, is the perturbation to model parameter i.

The model space sampling process is guided by the Metropolis law, and goes as follows. Within the model space defined by the prior information, an initial model m_0 is chosen randomly from the prior distribution, and its likelihood function $L(m_0)$ is computed:

$$L(m) = exp\left(-\frac{1}{2} S(m)\right) \tag{2.2}$$

where

$$S(m) = S_{Rayleigh} + S_{Love} = \sum_i \frac{(D(m)_i^{pred} - D_i^{obs})^2}{\sigma_i^2} + \sum_i \frac{(D'(m)_i^{pred} - D'^{obs}_i)^2}{\sigma'^2_i} \tag{2.3}$$

where $D(m)_i^{pred}$ is the predicted phase velocity for model m at period i (computed from (1)), and D_i^{obs} is the observed phase velocity. Here, D represents Rayleigh wave phase velocities and D' indicates Love wave phase velocities. Standard deviations of the Rayleigh and Love wave phase velocity measurements are given by σ and σ', respectively.

A new model m_i is generated by perturbing the initial model m_0 following the procedure described by *Shen et al*. [2013b]. The likelihood function $L(m_i)$ is obtained through a similar computation as described above. The model m_i is accepted or rejected according to a probability function P defined as follows:

$$P_{accept} = min\,(1, L(m_i)/L(m_0)) \quad (2.4)$$

If m_i is not accepted, a new m_i is generated by perturbing the initial model m_0; this perturbation continues until a m_i is accepted. If m_i is accepted, the next model sampled in model space will be based on it rather than m_0. This sampling process repeats until the likelihood function levels off, after which a new initial model is chosen randomly from the prior distribution. The process is continued until at least 5000 models have been accepted from at least 5 initial starting points. We then calculate average values of each parameter in the >5000 accepted models and take that average as a new reference model, and then recalculate dispersion curves and partial derivatives. With this new reference model and a similar sampling procedure, we repeat the process until we find an additional 5000 models accepted from at least 10 initial starting points. The use of various initial models minimizes the dependence on the initial parameters, but we find that initial model dependence is weak. That is, convergence tends to be to similar models irrespective of the initial model starting point.

The use of partial derivatives aims to accelerate computations during the process of identifying acceptable models in the Monte-Carlo search. In order to eliminate possible bias caused by the use of the partial derivatives, the Rayleigh and Love wave phase velocity curves are recomputed for each accepted model using MINEOS when the algorithm terminates at each location. This recomputation of the dispersion curves actually takes longer than the entire Monte-Carlo search, but there is little difference between the dispersion curves computed with MINEOS and the partial derivatives. This justifies reliance on the partial derivatives to save computation time without sacrificing accuracy.

The Monte Carlo sampling will generate an ensemble of anisotropic models that fit the data better than the reference model. The ensemble is reduced further in size by an additional acceptance criterion defined as follows:

$$\chi \leq \begin{cases} \chi_{min} + 0.5 & if\ \chi_{min} < 0.5 \\ 2\,\chi_{min} & if\ \chi_{min} \geq 0.5 \end{cases}$$

where misfit $\chi = \sqrt{S/N}\ is\ the$ square root of reduced chi-squared value, S is misfit defined by equation (2.3), and N is the number of observed data (number of discrete points along the Rayleigh and Love wave phase velocity curves). Thus, on average, this posterior distribution includes models whose misfit is less than about twice that of the best-fitting model, which has a square root of reduced chi-squared value of χ_{min}.

Finally, the mean and standard deviation of Vsv and Vsh are used to summarize the posterior distribution for each depth and location. As an example, consider point B (Figure 2.1a), where mid-crustal anisotropy is needed to fit the data (Figure 2.6). The widths of the posterior distributions reflect how well Vsv, Vsh, and their differences are constrained at each depth. Uncertainties in shear wave speeds at depths of 20 and 35 km are less than about 50 m/s, but are about twice as large at 50 km. Moreover, radial anisotropy is inescapable at 20 and 35 km depth, but not required, if still likely, at 50 km. The poorer resolution at 50 km results from the lack of long-period Love wave data, increasing data uncertainties with period, and the tradeoff between lower crustal and uppermost mantle structures. Therefore, as mentioned earlier, we mainly focus discussion on structures no deeper than about 50 km.

We performed the Bayesian Monte Carlo inversion at every grid point in the study region to produce posterior distributions. In Section 2.4, we present the spatial variations in the means

and standard deviations of the distribution. Then in Section 2.5, we query the entire distribution to address particular scientific questions.

2.4 Inversion Results

2.4.1 Example results at various locations

As examples of local dispersion curves and the results of their inversion to produce a radially anisotropic model, we consider results at four locations in different parts of eastern Tibet and its surroundings (Figure 2.1a, points A-D). For point A, which is north of the Kunlun fault near the eastern edge of the Qaidam Basin, the gray-shaded areas of the inverted model representing the 1σ uncertainty of the posterior distribution of accepted models in Vsh and Vsv (Figure 2.7b) give no indication of crustal radial anistropy. Vsh and Vsv are approximately equal in the crust, and no Rayleigh-Love discrepancy is observed (Figure 2.7a). In contrast, for point B in in the middle of eastern Tibet, a strong Rayleigh-Love discrepancy is seen for all isotropic models (Figure 2.7c), and large differences are required in Vsh and Vsv between ~20 and 50 km depth, as large as about 7.8%±1.6% (Figure 2.7d). The model uncertainty increases near the base of the sedimentary layer (not shown) and near the Moho, which reflects the velocity-depth tradeoff near interfaces characteristic of surface wave inversions. This prevents precise imaging of the discontinuities using surface waves alone. Although the inversion is performed to a depth of 200 km, we concentrate discussion on the crust where radial anisotropy is well resolved.

For point C in the Sichuan Basin, the Rayleigh and Love wave dispersion curves (Figure 2.7e) call for anisotropy only in the upper 20 km of crust (Figure 2.7f). As discussed in Section 2.4.3, the anisotropy could be confined to the sediments but would need to be about four times

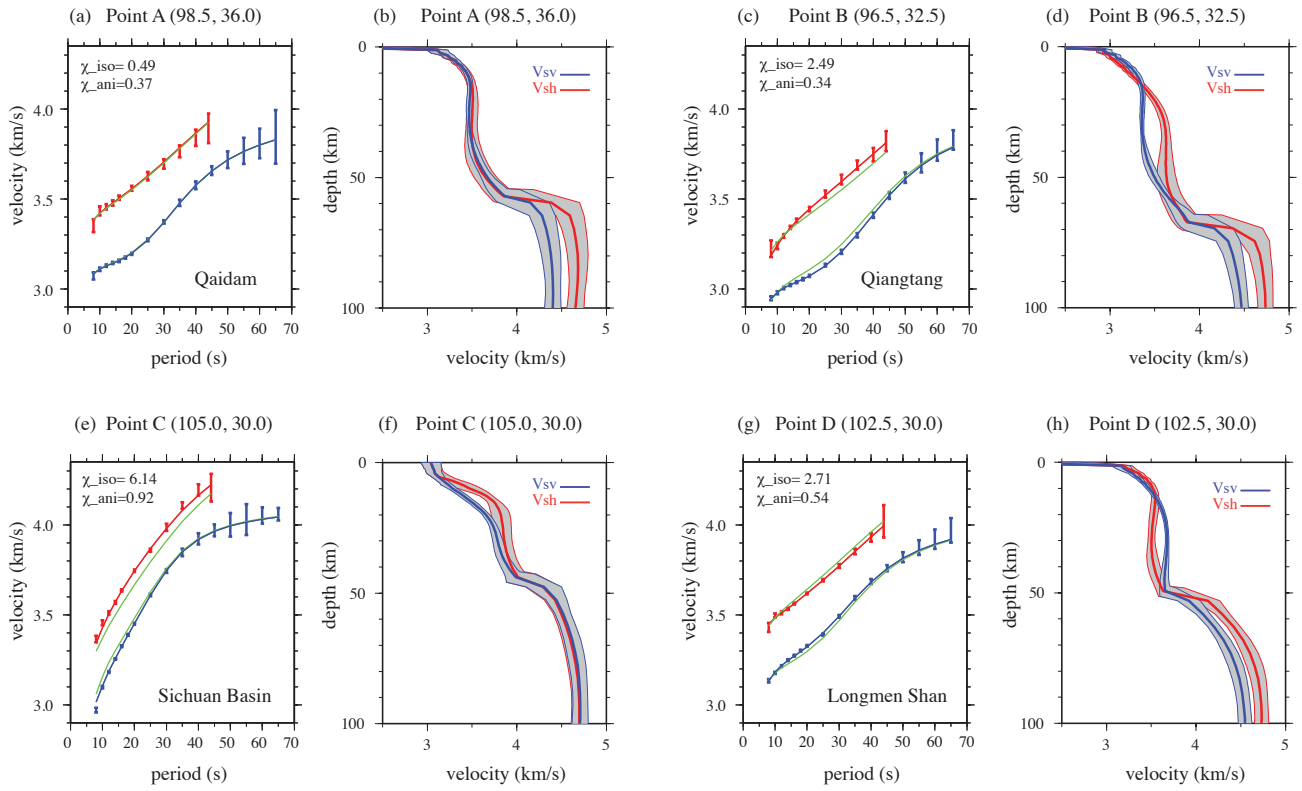

Figure 2.7. Examples of dispersion curves and estimated radially anisotropy for four spatial locations (A, B, C, D) identified in Fig. 2.1a. (a) Point A (98.5, 36.0) near the eastern edge of the Qaidam Basin. Local Rayleigh and Love wave phase speed curves presented as one standard deviation (1σ) error bars. Predictions from the average of the anisotropic model distribution in (b) are shown as solid lines and green lines are predictions from the Voigt-averaged isotropic Vs model. Misfits (defined as $\chi = \sqrt{S/N}$ where S is defined in eq. (3)) correlated with anisotropic and isotropic models are shown at the upper left corner. (b) Point A (cont.). Inversion result in which the one standard deviation (1σ) model distributions are shown with the grey corridors for Vsh and Vsv, with the average of each ensemble plotted with bold blue (Vsv) and red (Vsh) lines. The model ensembles are nearly coincident in the crust, consistent with an isotropic crust. (c) & (d) Point B (96.5, 32.5) in the Qiangtang terrane where the central crust has strong positive radial anisotropy between 20 and 50 km depth and weak negative anisotropy above about 15 km depth. (e) & (f) Point C (105.0, 30.0) in the Sichuan Basin where the central crust has strong positive radial anisotropy between depths of 10 and 25 km. (g) & (h) Point D (102.5, 30.0) between Tibet and the Sichuan Basin where the central crust has strong negative radial anisotropy between 20 and 50 km depth.

stronger. For point D in the Longmenshan region between Tibet and the Sichuan Basin, mid-crustal radial anisotropy is required, but in this case Vsv > Vsh and radial anisotropy is negative.

In Figure 2.7, green lines on the dispersion curves represent the predicted curves for the best-fitting isotropic Vs model in the crust, although the mantle contains radial anisotropy. They show the observed Rayleigh-Love discrepancy, how the best-fitting isotropic model misfits the data at points B, C, and D where radial anisotropy is required in the middle crust.

2.4.2 Maps of Vsv, Vsh, and Voigt-averaged Vs

Maps of the mean of the resulting posterior distributions for Vsv, Vsh, and the Voigt averaged isotropic Vs in the middle crust of Tibet (~35 km) are shown in Figure 2.8, in addition to the mean of crustal thickness. The most prominent feature is the low mid-crustal shear wave speed across all of eastern Tibet compared with much higher speeds outside of Tibet. In the mid-crustal Vsv map (Figure 2.8a), anomalies are similar to those presented in an earlier study using a similar data set [*Yang et al*., 2012]. The Vsh model is faster than Vsv across the high plateau, indicating strong positive radial anisotropy. Combining Vsv and Vsh, an isotropic Vs estimate is computed from the Voigt averaging method mentioned in Section 2.1. In these maps, white contours outline regions with shear wave speeds lower than 3.4 km/s, below which partial melting may be expected to exist [e.g., *Yang et al*., 2012]. Although Vsv < 3.4 km/s exists across much of eastern Tibet, Vsh > 3.4 km/s is present across the majority of the region. The difference between Vsv and Vsh causes the white contour in the Vsv map to contract toward the interior of eastern Tibet in the Vs map, predominantly within the Songpan-Ganzi and the northern Chuandian terrane. This feature of the Vs model is discussed further in Section 2.5.

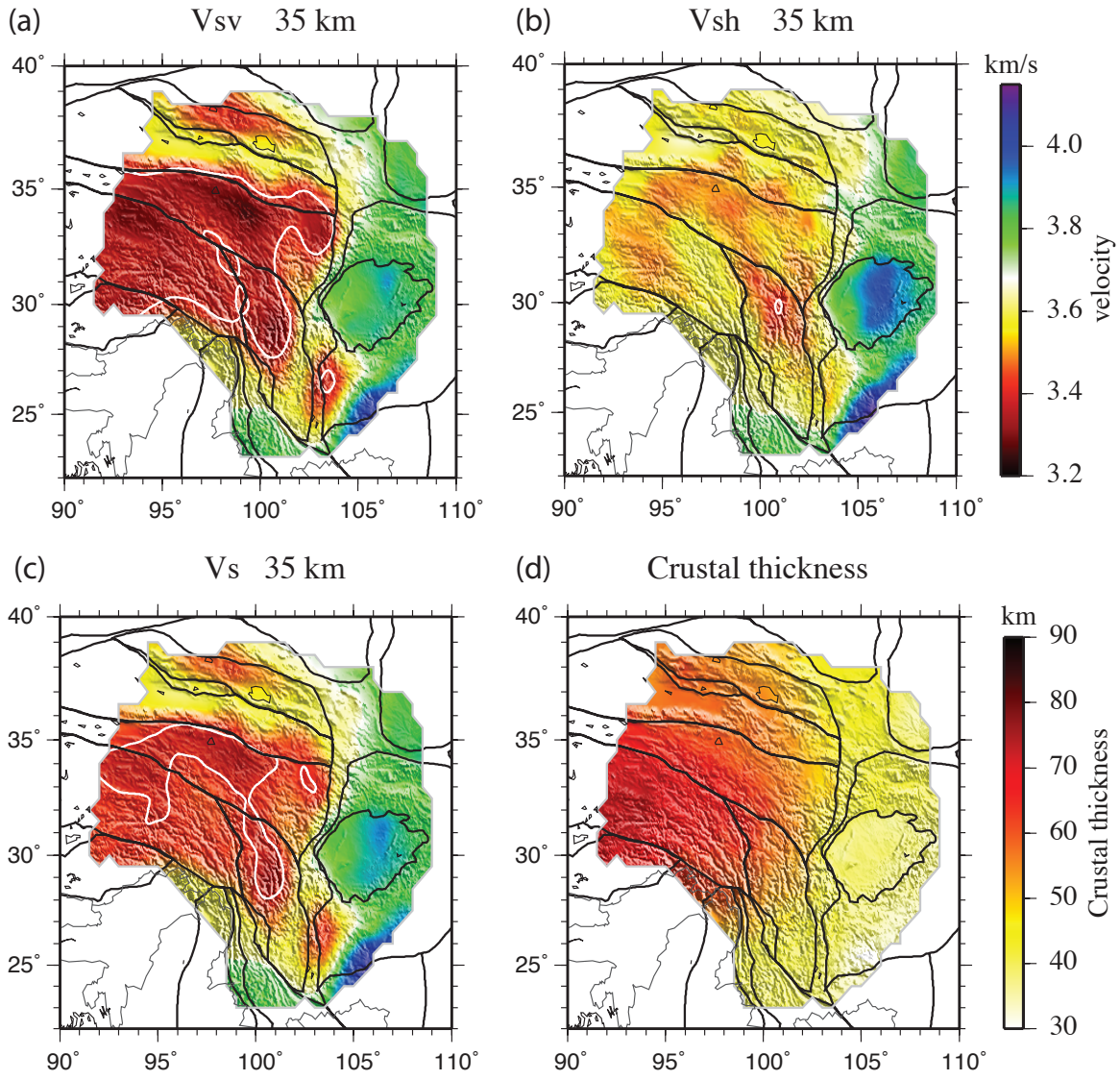

Figure 2.8. The average of the posterior distributions of (a) Vsv, (b) Vsh, and (c) Vs at 35 km depth in km/s, which is in the middle crust beneath the Tibetan Plateau. Regions with very low velocities (<3.4 km/s) are encircled by white contours. (d) The average of the posterior distribution of crustal thickness in km.

2.4.3 Radial anisotropy

From the posterior distributions of Vsv and Vsh at each location we obtain the radial anisotropy model. Radial anisotropy at different depths and along different vertical profiles is shown in Figures 2.9 and 2.10. In this section we first discuss the distribution of radial anisotropy qualitatively, and then the estimated uncertainties are presented and discussed in Section 2.4.4.

In the upper crust (Figure 2.9a), radial anisotropy beneath the Tibetan Plateau is negative, on average. Beneath the Sichuan Basin, in contrast, it is positive with amplitudes in excess of 6%. Actually, the depth extent of the strong upper crustal radial anisotropy beneath the Sichuan Basin is not well constrained by the data. For example, it could also have been confined to the sediments, but in this case radial anisotropy of about 25% would be needed to fit the data. Because of this exceptionally large amplitude, we prefer a model with radial anisotropy confined to the upper crystalline crust.

In the middle crust (Figure 2.9b), relatively strong positive radial anisotropy with amplitudes ranging from 4% to 8% is observed across most of eastern Tibet, where the strongest anisotropy is concentrated near the northern margin of the Qiangtang terrane. Near the northern and eastern margins of the Tibetan Plateau, radial anisotropy decreases in amplitude. To the north, radial anisotropy decreases abruptly across the Kunlun fault, and to the east radial anisotropy decreases and becomes negative near the Longmenshan west of the Sichuan Basin. The northern margin of radial anisotropy closely follows the Kunlun fault. In contrast, the termination of radial anisotropy near the southeastern margin of Tibet does not follow the topography or geological boundaries. Strong radial anisotropy covers only the northern half of

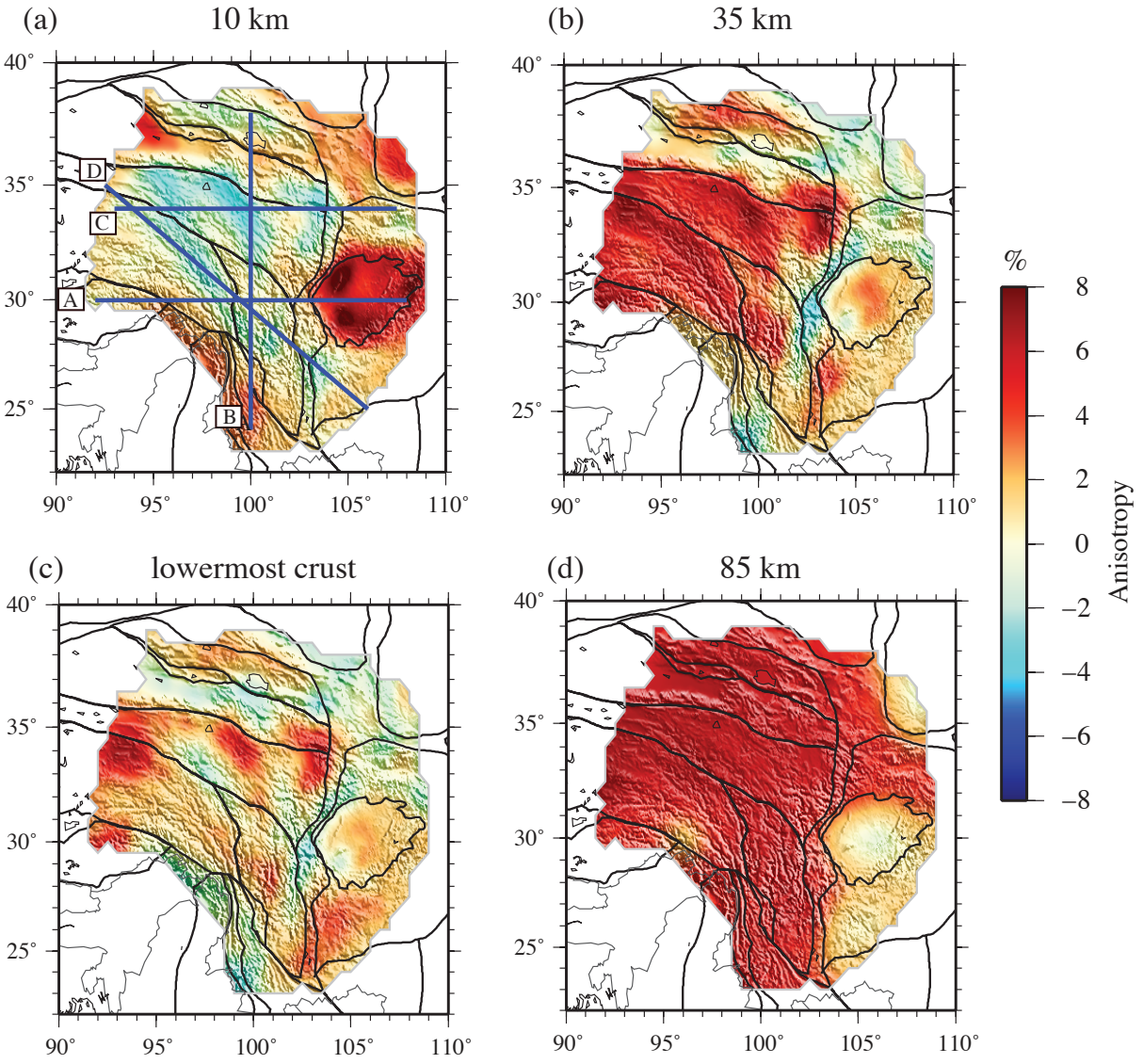

Figure 2.9. Maps of the mean of the posterior distribution for estimates of radial anisotropy at (a) 10 km depth, (b) 35 km depth, and (c) 90% of the depth to Moho in the lowermost crust. Radial anisotropy is the percent difference between Vsh and Vsv at each location and depth (γ) and Vs is the Voigt-averaged shear wave speed. Blue lines in (a) identify the locations of the vertical cross-sections in Fig. 2.10**.**

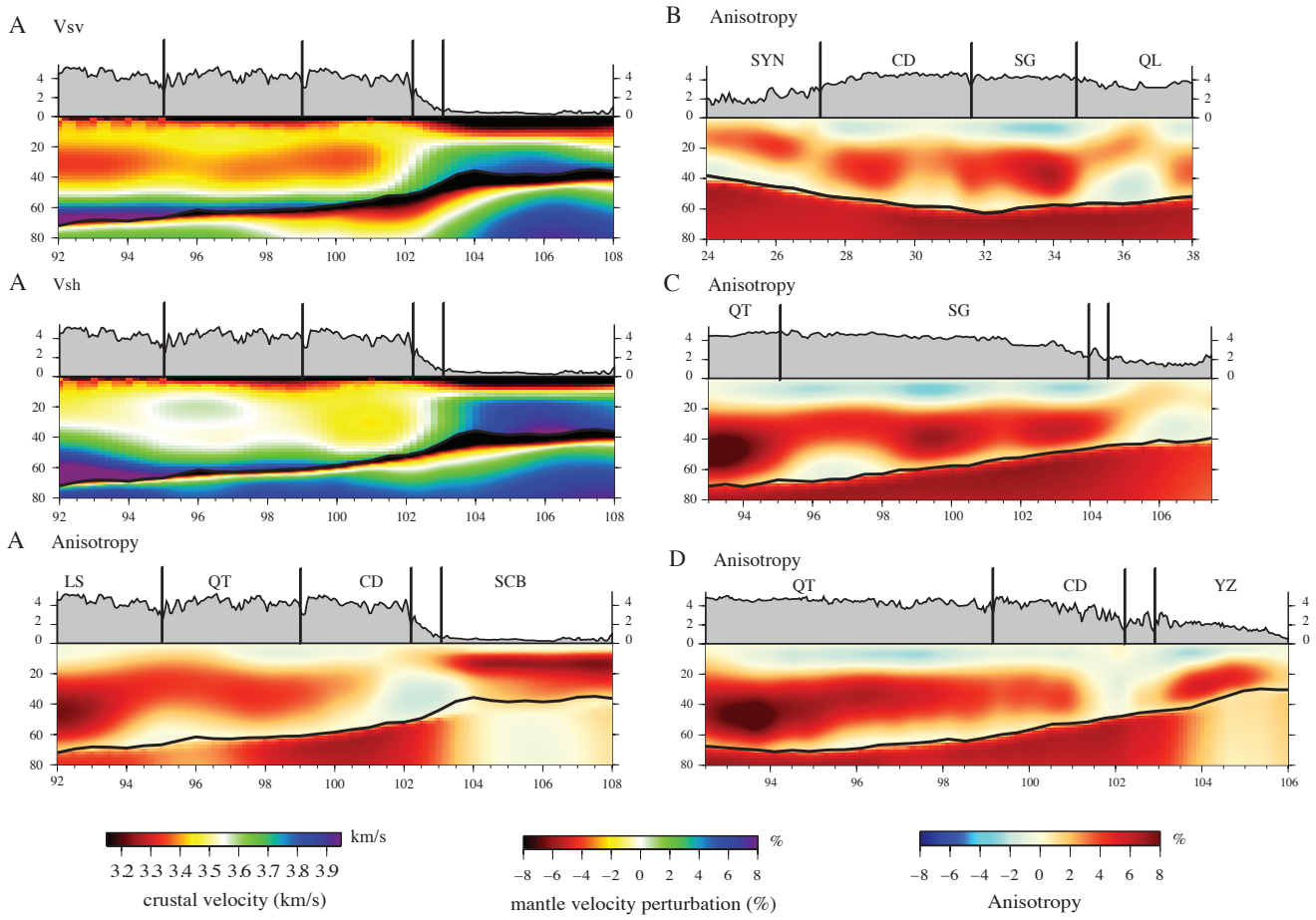

Figure 2.10. Vertical cross-sections of (upper left) Vsv, (middle left) Vsh, and (lower left) Vs radial anisotropy γ along profile A (Fig. 9a), taken from the mean of the posterior distribution at each location and depth**.** Topography is shown at the top of each panel as are locations of geological-block boundaries (SG: Songpan-Ganzi terrane, CD: Chuandian terrane, LS: Lhasa terrane, QL: Qilian terrane, SCB: Sichuan Basin, SYN: South Yunnan region, YZ: Yangtze craton). Crustal shear velocities are presented in absolute units (km/s), Vs radial anisotropy is presented as the percent difference between Vsh and Vsv (γ), and mantle velocities are percentage perturbations relative to 4.4 km/s. (Right) Vs radial anisotropy is presented beneath profiles B, C, and D (Fig. 9a).

the Chuandian terrane and it ends before the plateau drops off and topography decreases. To the east of the Tibetan Plateau, negative radial anisotropy shows up near the Longmenshan, in a narrow strip between the Chuandian terrane and the Sichuan Basin. Outside the Tibetan Plateau, mid-crustal radial anisotropy is weak except within and south of the Sichuan Basin and in the Qilian terrane.

In the lower crust (Figure 2.9c), radial anisotropy is weak across most of the region of study, with notable isolated anomalies in the northern Songpan-Ganzi and Qiangtang terranes. In fact, radial anisotropy at this depth is not determined reliably because anisotropy trades off with both Moho depth and radial anisotropy in the uppermost mantle. This phenomenon is reflected in the large uncertainties shown in Figure 2.11c.

In Figure 2.9d, uppermost mantle anisotropy at 85 km depth is shown, which is taken from the model of *Shapiro and Ritzwoller* [2002], as mentioned in Section 2.3.1. Shapiro's model of anisotropy is fairly uniform across the study region with an average positive anisotropy of ~6%, but much weaker mantle anisotropy exists within and south of the Sichuan Basin. In fact, weak negative anisotropy exists beneath parts of the Sichuan Basin in their model.

The locations of the four vertical transects are shown in Figure 2.9a and the vertical transects themselves are presented in Figure 2.10. For profile A, Vsv, Vsh, and radial anisotropy are presented. For profiles B, C, and D, only radial anisotropy is presented.

For profile A, Vsv is similar to the result presented by *Yang et al*. [2012] using a similar data set. Within the high plateau, a Vsv minimum in the middle crust is seen clearly from about 20 to 40 km depth. In the Sichuan Basin, a very slow sedimentary layer is present along with faster lower crust. Compared to Vsv, Vsh is faster from the surface to the base of the crust except in the uppermost crust of the high plateau and the mid-crustal velocity minimum seen for Vsv is

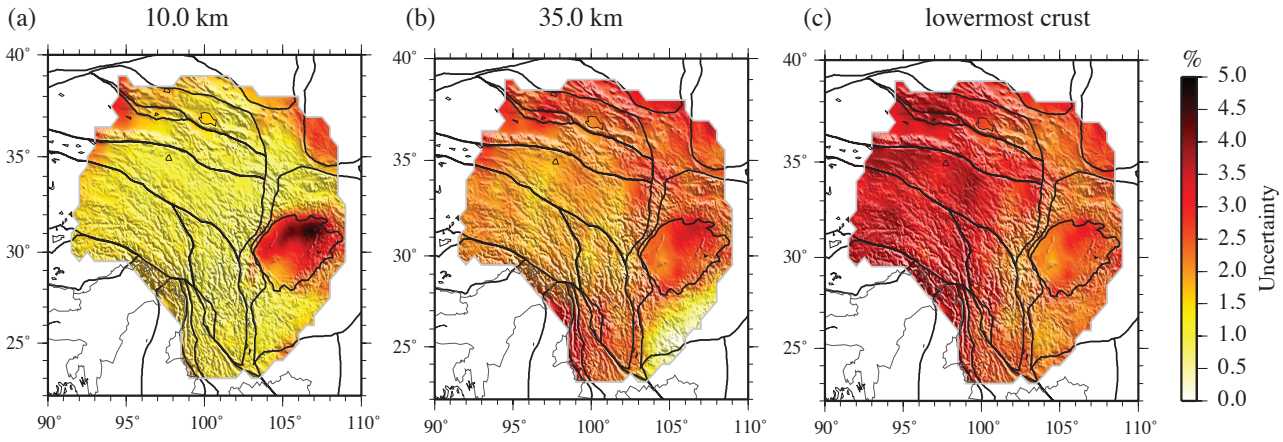

Figure 2.11. Maps of the one standard deviation (i.e., error) of the posterior distribution for estimates of Vs radial anisotropy at (a) 10 km depth, (b) 35 km depth, and (c) 90% of the depth to Moho. Results are in the same units as radial anisotropy, not in the percentage of radial anisotropy at each point.

much more subtle. There are differences in upper crustal Vsv and Vsh in the Sichuan Basin as well. Radial anisotropy beneath the high plateau along profile A increases from an average of about -1% in the uppermost crust to values of 4% to 6% between 20 and 50 km depth. Radial anisotropy then decreases with depth in the lower crust. Near the eastern edge of the plateau, radial anisotropy vanishes as surface elevation falls off, perhaps changing sign before elevation plummets at the Longmenshan.

The three other vertical profiles shown in Figure 2.10 are similar to profile A in the vertical distribution of radial anisotropy in the crust across the Tibetan Plateau: radial anisotropy is negative, on average, in the uppermost crust, positive and peaks in amplitude in the middle crust, decreases in the lower crust, and terminates near the border of the high plateau except within and south of the Sichuan Basin. The nature of the termination of radial anisotropy near the border of the plateau varies from place to place. For example, in profile C, which runs across the northeastern part of the plateau, radial anisotropy decreases gradually as topography decreases. In contrast, in profile D, which goes through the southeastern part of the plateau, radial anisotropy ends abruptly before topography decreases.

In summary, within the Tibetan Plateau, strong positive radial anisotropy begins at about 20 km depth and peaks between 30 and 50 km depth. It is almost continuous between different terranes, but there is some diminishment in amplitude near terrane boundaries as profile B illustrates. Radial anisotropy has a somewhat broader depth range in the Qiangtang terrane compared with other terranes. Outside of the Tibetan plateau, strong upper-to-middle crustal radial anisotropy shows up in and south of the Sichuan Basin. Negative anisotropy is mostly confined to the uppermost crust beneath Tibet and in the middle crust in the Longmenshan region, near the border between Tibet and the Sichuan Basin.

2.4.4 Uncertainty in radial anisotropy

Figure 2.11 presents uncertainties in the estimated radial anisotropy in the region of study at depths of 10 and 35 km, as well in the lower crust at a depth of 90% of crustal thickness. The uncertainty is defined as one standard deviation of the posterior distribution at each depth. Except beneath the Sichuan Basin, uncertainties grow with depth in the crust because a smaller percentage of the observed dispersion curves are sensitive to the greater depths. Beneath the Sichuan Basin, the higher shallow uncertainties result from the trade-off of shear velocities in the crystalline crust and sediments. At 10 km depth, the average uncertainty in eastern Tibet is about 1%, whereas in the mid-crust it is about 2%, and in the lower crust it is about 3.5%. As discussed in Section 2.5.4.1, if we had not constrained Vsh=Vsv for crustal B-splines 1 and 5 (Figure 2.5) in the uppermost and lowermost crust, uncertainties in radial anisotropy in the uppermost and lowermost crust would have been larger. The higher uncertainties in the lower crust result from the fact that Love waves do not constrain Vsh well at these depths and there are trade-offs with crustal thickness and uppermost mantle structure and is why we concentrate discussion on shallower depths.

2.4.5 Computation of regional averages

Several of the attributes of the model observed here appear to be fairly homogeneous over extended areas. These attributes include positive mid-crustal radial anisotropy beneath eastern Tibet and the Sichuan Basin, negative mid-crustal radial anisotropy near the Longmenshan adjacent to the eastern border of Tibet, negative radial anisotropy in the shallow crust beneath parts of eastern Tibet (notably the Songpan-Ganzi terrane), and Vs in the mid-crust beneath eastern Tibet. We present here averages of the means and the standard deviations of the mean of these variables defined over the four regions. These standard deviations, in contrast with

those presented in Figure 2.11 and discussed in Section 2.4.4, principally reflect spatial variations rather than uncertainties.

There are four regions over which we compute the averages. First, we consider "eastern Tibet" to be defined by the interior of the 84.2% probability contour (orange, red colors) of positive mid-crustal radial anisotropy near Tibet, which is presented later in the paper (Figure 2.13a). This contour approximately follows the outline of the high plateau. Second, we consider the Longmenshan region near the border between Tibet and the Sichuan Basin to be contained within the 15.8% probability contour (blue colors) of positive mid-crustal radial anisotropy (Figure 2.13a). Finally, we use the geological outlines of the Sichuan Basin and the Songpan-Ganzi terrane as the third and fourth regions.

In the Songpan-Ganzi terrane, the distribution of the means of shallow crustal (~10 km) radial anisotropy is presented in Figure 2.12a. The average of the means in this region is -1.03% ± 1.38%. This is the structural attribute with the relatively largest variability. The distribution of the means of mid-crustal radial anisotropy across eastern Tibet (~35 km) and the Sichuan Basin (~15 km) are presented in Figures 2.12b,c. Mid-crustal radial anisotropy averages 4.81% ± 1.41% in eastern Tibet. Across the Sichuan Basin the average is somewhat larger, 5.35% ± 1.43%. Also in the middle crust, but averaged over the Longmenshan region (~30 km), the distribution of the means of mid-crustal radial anisotropy is presented in Figure 2.12d. The average is -2.80% ± 0.94%. Finally, mid-crustal Vs averaged over eastern Tibet is 3.427 km/s ± 0.050 km/s, as seen in Figure 2.12e.

2.5 Identifying highly probable model attributes

The means of the posterior distributions of the models that result from the Bayesian Monte Carlo inversion of Rayleigh and Love wave dispersion curves have been used to infer that

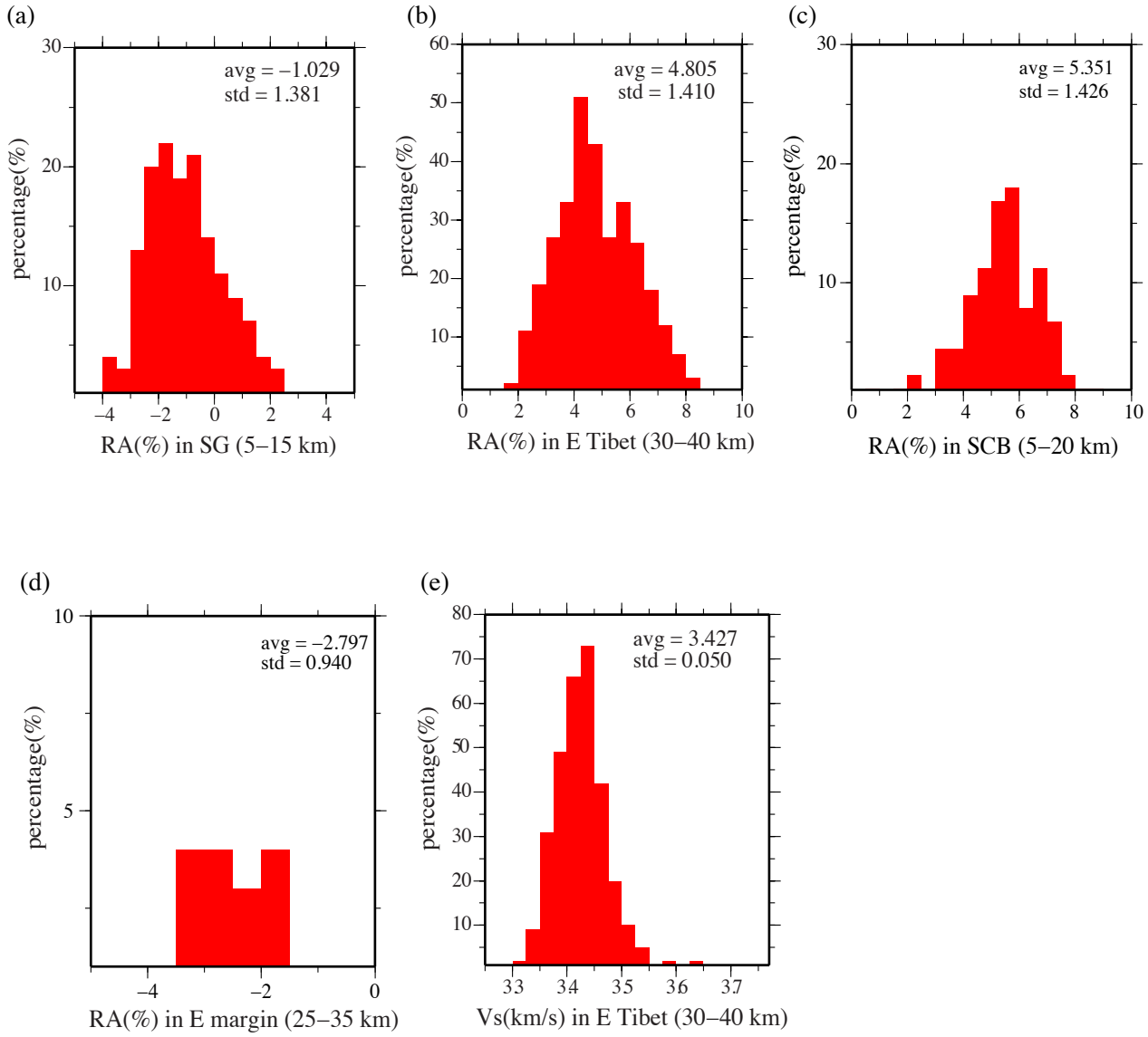

Figure 2.12. Plots of the spatial distribution of the mean of the posterior distributions of Vs radial anisotropy across (a) the Songpan-Ganzi terrane between depths of 5 and 15 km, (b) eastern Tibet at depths between 30 and 40 km, (c) the Sichuan Basin at depths between 5 and 20 km, and (d) the Longmenshan region between eastern Tibet and the Sichuan Basin between 25 and 35 km. (e) The distribution of the mean of the posterior distribution for Voigt-averaged shear wave speed Vs across eastern Tibet between depths of 30 and 40 km.

(1) positive (Vsh>Vsv) mid-crustal radial anisotropy exists across the entirety of eastern Tibet with an average amplitude (γ) of about 4.8% (~35 km) and at much shallower depths (~15 km) beneath the Sichuan Basin with an average amplitude of about 5.4%, (2) weaker negative radial anisotropy (Vsh<Vsv) appears in the middle crust (~30 km) along the Longmenshan region (-2.8%) and in the shallow crust (~10 km) across the Songpan-Ganzi terrane (-1.03%) , and (3) the Voigt averaged shear wave speed in the middle crust (~35 km) averages about 3.427 km/s across eastern Tibet. From the geographical spread of the local means of the posterior distributions of these attributes we have inferred that these observations are characteristic of each region. Radial anisotropy in the lowermost crust is more poorly constrained than at shallower depths because of a trade-off with crustal thickness and radial anisotropy in the mantle.

Although the mean of the posterior distribution is interpreted as its maximum likelihood, the Bayesian Monte Carlo inversion delivers a distribution of models at each depth. For this reason, within a Bayesian framework, the probability that the model achieves a particular attribute can be computed. Here we address the following questions across the region of study: (1) What is the probability that positive (Vsh>Vsv) radial anisotropy exists in the shallow crust or in the middle crust? (2) Similarly, what is the probability for negative radial anisotropy? (3) What is the probability that the Voigt averaged shear wave speed lies below or above 3.4 km/s in the middle crust?

In computing these probabilities, we acknowledge that the posterior distribution represents a conditional probability in which the likelihood is conditioned on prior information that appears in the range of the model variables allowed, the constraints imposed, the parameterization chosen, the details of the search algorithm, and the assumptions made (e.g., ρ/Vs, Vp/Vs, Q). From a Bayesian perspective, the distribution represents the authors' degree of

belief in the results, but if the prior information is wrong then the resulting distribution of models may be biased. In Section 2.5.4, we identify several potential sources for bias and discuss how these choices may affect the mean of the estimated posterior distribution of the selected model attributes.

2.5.1 Computing the probability of a model attribute from the posterior distribution

Figure 2.13a,b illustrates the computation of the probability for the existence of positive radial anisotropy in the middle crust. The probability that Vsh > Vsv (positive radial anisotropy) at 35 km depth is mapped in Figure 2.13a. It is computed at each point from the local posterior distribution, examples of which are shown for locations A, B, and D from Figure 2.1a in Figure 2.13b. For point A, a location that we interpret as isotropic in the crust, approximately half (54%) of the posterior distribution shows positive anisotropy and half negative. For point B, which we interpret as possessing strong positive mid-crustal anisotropy, 100% of the posterior distribution has Vsh>Vsv at 35 km depth. For point D, where we observe negative anisotropy on average, only ~0.12% of the models in the posterior distribution have Vsh>Vsv. Thus, at this point, more than 99.8% of the models in the posterior distribution display negative anisotropy in the middle crust.

The values mapped in Figure 2.13a are simply the percentage of models in the posterior distribution at each point with positive mid-crustal radial anisotropy. Examples of the probability of positive radial anisotropy at depths of 10 and 15 km are also shown in Figure 2.13c,d. Similarly, from the local posterior distributions of the isotropic Vs, the probabilities that Vs is greater than 3.4 km/s or less than 3.4 km/s are mapped in Figure 2.14.

In general, we consider a model attribute (e.g., Vsh > Vsv, Vs < 3.4 km/s) to be “highly probable” if it appears in more than 97.8% of the models in the posterior distribution. In this case,

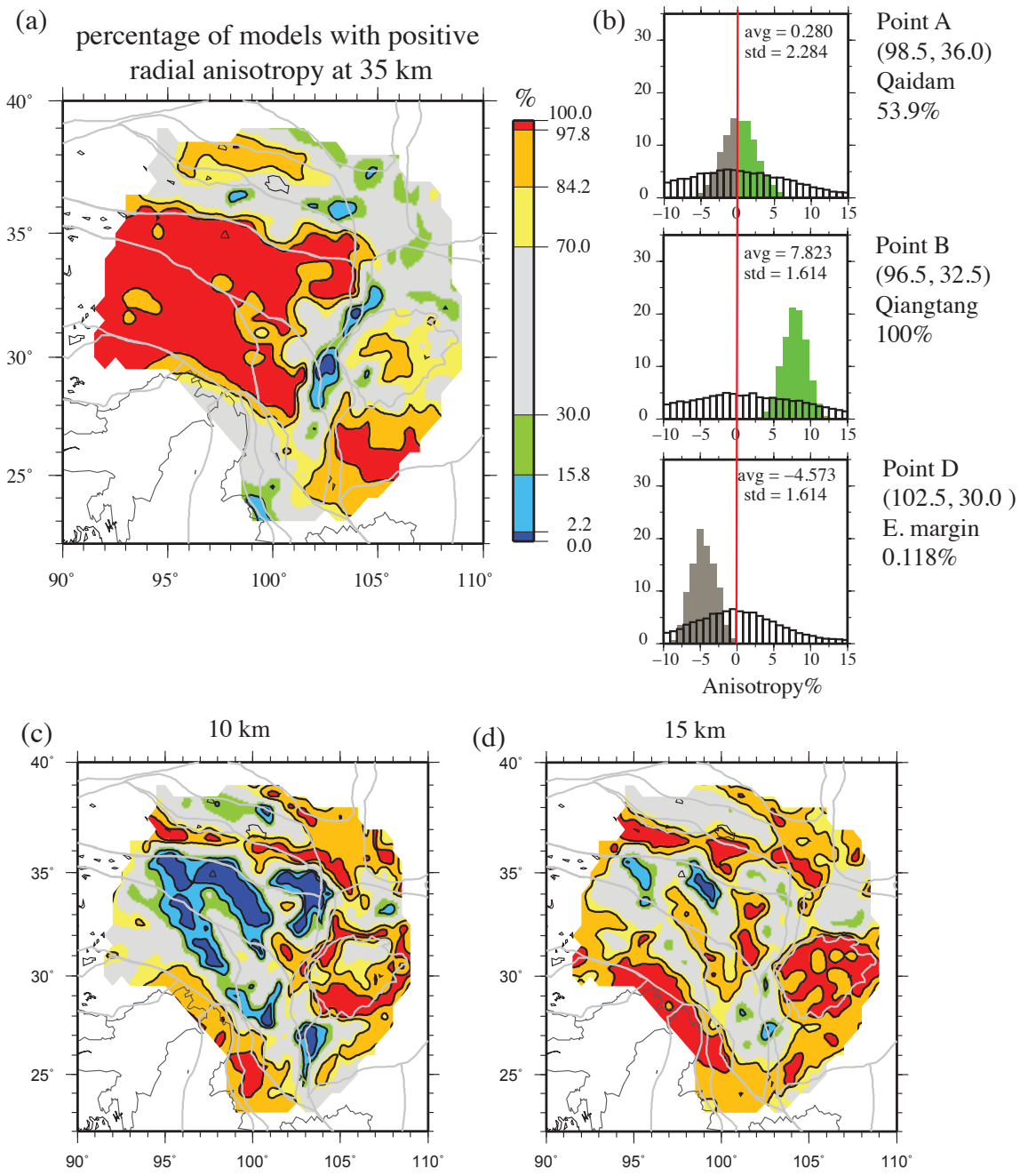

Figure 2.13. (a) Percent of accepted models at each location with positive Vs radial anisotropy γ (Vsh > Vsv) at 35 km depth. Values of 2.2%, 15.8%, 84.2%, and 97.8% are contoured by black lines, which are correlated with the position of $\pm 1\ \sigma$ and $\pm 2\ \sigma$ for a Gaussian distribution. (b) Prior (white histogram in the background) and posterior (colored histogram) distributions of Vs radial anisotropy in percent at 35 km depth for locations A, B, and D of Fig. 1a. The red line indicates the position of zero radial anisotropy. The percent of models with positive radial anisotropy is indicated to the right of each panel. (c) Same as (a), but for positive Vs radial anisotropy at 10 km depth. (d) Same as (a), but for positive Vs radial anisotropy at 15 km depth.

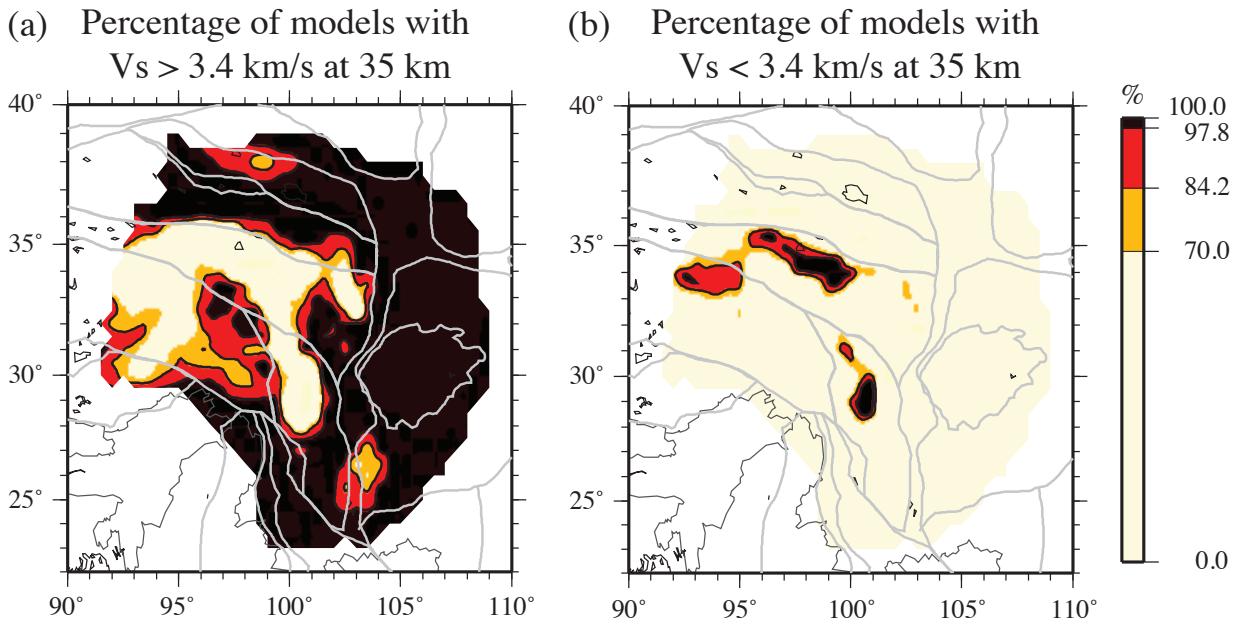

Figure 2.14. (a) Similar to Fig. 13a, but this figure is the percentage of accepted models at each location with Voigt-averaged Vs > 3.4 km/s at 35 km depth. (b) Same as (a), but for Vs < 3.4 km/s at 35 km depth.

all or nearly all of the models in the posterior distribution possess the specified attribute. If the attribute appears in less than 2.2% of the accepted models, then the converse of the attribute (e.g., Vsh < Vsv, Vs > 3.4 km/s) would be deemed "highly probable". One could introduce other grades of probability (e.g., probable, improbable, the converse is probable, etc.), but we do not do so here.

2.5.2 Regions with high probability of positive or negative radial anisotropy

High probability regions for positive radial anisotropy in the middle crust appear as red colors in Figure 2.13a and for negative mid-crustal anisotropy as dark blue regions. Red colors cover most of eastern Tibet, including the Qiangtang terrane, most of the Songpan-Ganzi terrane, and the northern Chuandian terrane. Another region strongly favoring positive mid-crustal radial anisotropy lies south of the Sichuan Basin, largely in Yunnan province. Mid-crustal radial anisotropy has a lower average probability there (orange colors, Figure 2.13a) than beneath Tibet, because the crust is thinner (~40 km) and at 35 km depth crustal radial anisotropy trades-off with crustal thickness and uppermost mantle radial anisotropy. Blue colors appear in the Longmenshan region near the border of Tibet and the Sichuan Basin, indicating the high probability of negative mid-crustal radial anisotropy there.

At shallower depths, the high probability zones of positive or negative radial anisotropy are smaller and more variable than in the middle crust. At 10 km depth (Figure 2.13c), highly probable negative radial anisotropy is mainly confined to the Songpan-Ganzi terrane but also extends into parts of the Qiangtang and Chuandian terranes. By 15 km (Figure 2.13d), neither positive nor negative radial anisotropy attains high probabilities pervasively across Tibet, but positive radial anisotropy is highly probable across most of the Sichuan Basin.

2.5.3 Probability of low shear wave speeds in the middle crust

Middle-to-lower crustal low velocity zones (LVZ) have been reported in several studies [e.g., *Yao et al*., 2008; *Yang et al*., 2012], but most of these considered Vsv alone. The existence of crustal radial anisotropy with Vsh>Vsv across most of eastern Tibet increases the Voigt-averaged shear wave speed relative to Vsv, and reduces the strength of a crustal LVZ. *Yang et al*. [2012] argued that 3.4 km/s is a reasonable speed below which partial melt may plausibly begin to occur at a depth of about 35 km depth, although this threshold is poorly known and is probably spatially variable. Other values could also be used. At this depth, the mean value of the Voigt average shear wave speed in the posterior distribution is shown in Figure 2.8c and the distribution of the mean values across eastern Tibet is presented in Figure 2.12e. Although shear wave speeds across eastern Tibet average 3.427 km/s, there is substantial spatial variability and the likelihood that Vs dips below 3.4 km/s in some locations is high.

In the attempt to quantify the likelihood of shear wave speeds less than 3.4 km/s in the middle crust, Figure 2.14 presents the percentage of models in the posterior distribution at each point with Vs > 3.4 km/s and Vs < 3.4 km/s at 35 km depth. As Figure 2.14a shows, Vs > 3.4 km/s is highly probable across most of the study region, but does not rise to the level of high probability across much of Tibet. Conversely, Figure 2.14b shows that Vs < 3.4 km/s at this depth is also not highly probable across most of the high plateau. Unfortunately, this means that we cannot infer with high confidence either that mid-crustal Vs is greater than or less than 3.4 km/s across much of Tibet. However, there are two disconnected regions where more than 97.8% of the accepted model have Vs < 3.4 km/s, such that we would infer the high probability of Vs < 3.4 km/s. These regions are in the northern Songpan-Ganzi terrane near the Kunlun fault and in the northern Chuandian terrane. A third region of low Vs that nearly rises to the level of high probability lies in the northern Qiangtang terrane.

2.5.4 Caveats: Quantifying the potential for bias in the posterior distribution

Measurements of mid-crustal radial anisotropy, particularly its amplitude, and of shear wave speed Vs, particularly the minimum value it attains in the middle crust, are affected by a variety of information introduced in the inversion, including the parameterization of crustal radial anisotropy, crustal thickness in the reference model, the fixed amplitude of radial anisotropy in the mantle, the fixed value of the Vp/Vs ratio in the crust, and the fixed zero amplitude of Vp radial anisotropy and $\eta = 1$ in the crust. Errors in these assumptions could bias the posterior distribution and introduce a systematic error that may bias the probability estimates presented in Sections 2.5.1 to 2.5.3. We discuss here the effects of these assumptions and also discuss and then dismiss the possibility of overtones, particularly from Love waves, interfering with the estimation of radial anisotropy using fundamental modes.

2.5.4.1 Relaxing constraints on radial anisotropy in the uppermost and lowermost crust

All results presented above include the constraint that Vsh=Vsv for the crustal B-splines 1 and 5 (Figure 2.5). Figure 2.15 shows the range of the means of the posterior distributions for radial anisotropy averaged across the high plateau with this constraint applied (blue bars). This is compared with a similar spatial average computed without the constraint (red bars), so that the number of unknowns increases from 16 to 18. The less constrained inversion approximately encompasses the more tightly constrained result. The relaxation of the constraint on radial anisotropy increases the variability of the model, particularly in the uppermost and lowermost crust and shifts the mean of the distribution in the lowermost crust to larger values. Between depths of 25 and 45 km, however, the means of the distributions are nearly indistinguishable, implying that this constraint does not bias estimates of mid-crustal radial anisotropy.

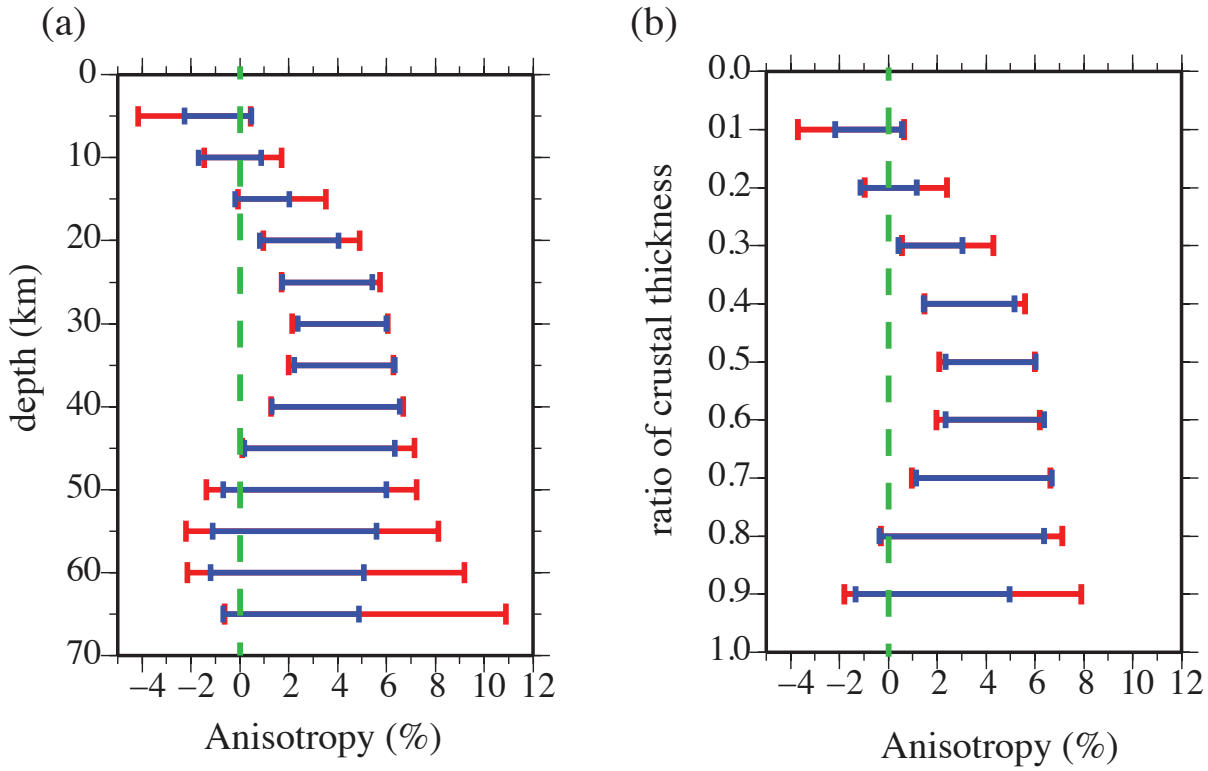

Figure 2.15. The spatially averaged effect of crustal parameterization of radial anisotropy on the mean and standard deviation of Vs radial anisotropy averaged across the Tibetan crust. Crustal radial anisotropy and uncertainty are presented as error bars as a function of (a) absolute depth and (b) depth measured as a ratio of crustal thickness, averaged over the study region where surface elevation is more than 3 km (black contour in Fig. 2.1a). The middle of each error bar is the average amplitude of Vs radial anisotropy in percent and the half-width of the error bar is the average one-standard deviation uncertainty. Blue bars result from the more tightly constrained inversion (uppermost and lowermost crust are approximately isotropic, Vsh=Vsv for crustal B-splines 1 and 5 in Fig. 2.5, but Vsh and Vsv can differ for splines 2 to 4). Red bars are results from the less constrained inversion (radial anisotropy is allowed across the entire crust, Vsv may differ from Vsh for all five crustal B-splines).

2.5.4.2 Crustal thickness and mantle radial anisotropy

The crustal thickness in the reference model (around which the Monte Carlo search occurs) and the fixed amplitude of radial anisotropy in the mantle do affect aspects of the posterior distribution in the middle crust, including the amplitude of radial anisotropy and the isotropic shear wave speed. The effects of these properties of the deeper parts of the model will be stronger, however, where the crust is thinner. This is reflected in the uncertainties in mid-crustal radial anisotropy shown in Figure 2.11b. Uncertainties are smaller across eastern Tibet (~1.75%) where the crust is thicker than in adjacent regions outside Tibet (2.0-3.0%). Indeed, we find that changes in crustal thickness in the reference model and in the fixed amplitude of radial anisotropy in the mantle do not strongly and systematically affect either the amplitude of radial anisotropy or isotropic Vs in the middle crust beneath eastern Tibet. However, these changes do have a systematic impact on these model attributes where the crust is thinner, for example in the Longmenshan region near the border of Tibet and the Sichuan Basin. For this reason, we present results here of the impact of changing crustal thickness in the reference model and the amplitude of mantle radial anisotropy at location D (Figure 2.1a) in the Longmenshan region.

Figure 2.16a,b present the estimates of depth averaged (±5 km around the middle crust) mid-crustal radial anisotropy as well as depth averaged mid-crustal Vs, which result by changing the fixed amplitude of mantle radial anisotropy averaged from Moho to 150 km depth. Error bars reflect the one standard deviation variation in the posterior distribution in each of the inversions, which are performed identically to the inversions used to produce the model described earlier in the paper (which is the middle error bar with a triangle in the center in Figure 2.16a,b). The effect of mantle radial anisotropy on Vs is very weak but increasing mantle radial anisotropy

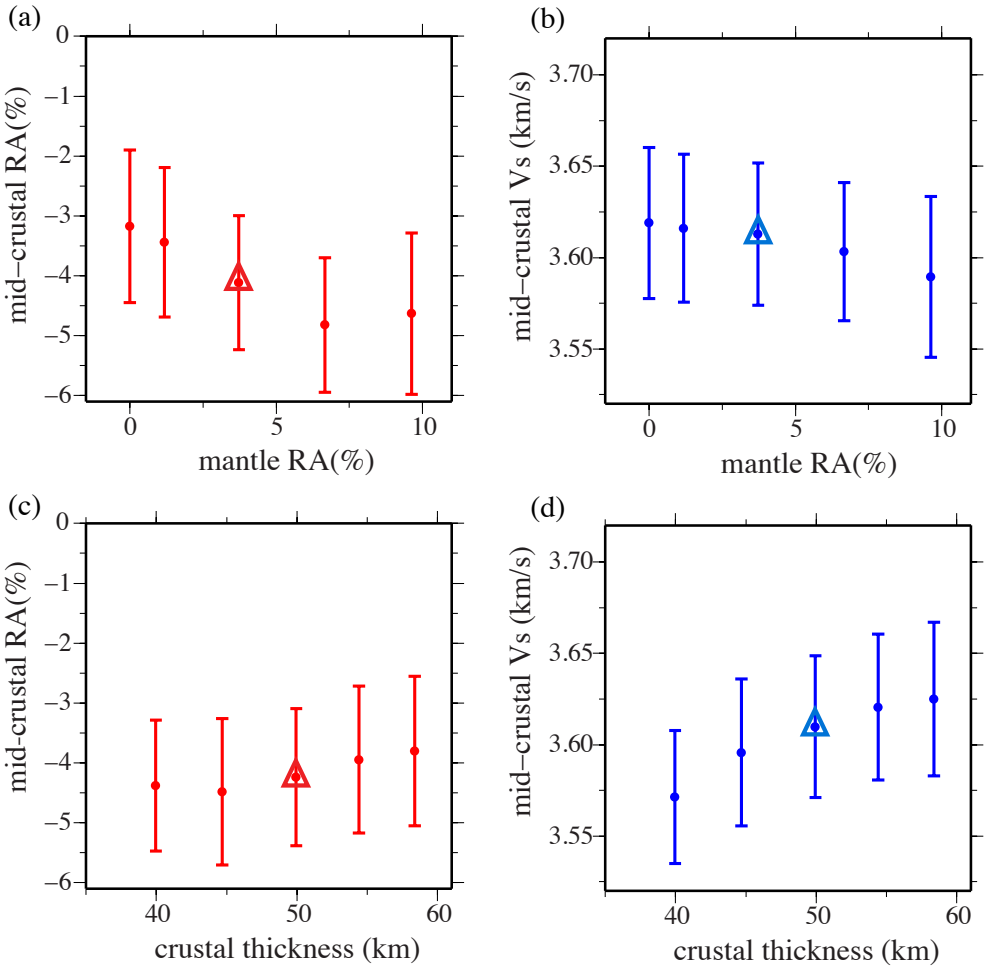

Figure 2.16. Trade-off between the depth-averaged (from Moho to 150 km) mantle Vs radial anisotropy used in the inversion and (a) the depth-averaged (±5 km around the middle crust) mid-crustal Vs radial anisotropy and (b) the depth-averaged (±5 km around the middle crust) mid-crustal Voigt-averaged Vs. Each dot is the depth-averaged value and half-widths of the error bars are the depth-averaged one-standard deviation uncertainty. Both come from the inversion with the given mantle radial anisotropy at location D identified in Fig. 2.1a. The triangles are the values in our final model. (c)&(d) Similar to (a)&(b), but showing the trade-off between the crustal thickness and (c) the depth-averaged mid-crustal Vs radial anisotropy and (d) the depth-averaged mid-crustal Voigt-averaged Vs.

does systematically reduce crustal radial anisotropy. Changing the depth-averaged mantle radial anisotropy from about 4% to 0% or 10% changes the estimated depth-averaged crustal radial anisotropy by less than ±1%, however. Because we believe that mantle radial anisotropy is probably known better than this range, this possible systematic shift in crustal radial anisotropy is probably an overestimate. Still, it lies within the stated errors of crustal radial anisotropy in the Longmenshan region. If potential systematic errors lie within stated uncertainties, we consider them not to be the cause for concern.

Similarly, Figure 2.16c,d present estimates of depth averaged (±5 km around the middle crust) mid-crustal radial anisotropy and depth averaged mid-crustal Vs caused by changing crustal thickness in the reference model. Again, the middle error bar is the result of the inversion for the model presented earlier in this paper, so that in the Longmenshan region the crustal thickness of the reference model was about 50 km. Changing the crustal thickness in the reference model (around which the Monte Carlo inversion searches) from 40 to 60 km has a systematic affect both on crustal radial anisotropy and mid-crustal isotropic Vs. But, again, the effect is relatively small (±0.5% in mid-crustal radial anisotropy, ±25 m/s in mid-crustal Vs). Although the range of crustal thickness considered is considerably larger than what we consider physically plausible for this location, the effect on model characteristics is below the stated model uncertainty.

Therefore, both mid-crustal Vs and the mid-crustal radial anisotropy are affected by the fixed amplitude of mantle radial anisotropy and the crustal thickness in the reference model, but the effects are below estimated model uncertainties and could only become significant if the effects were correlated and would add constructively. Although this is possible, in principle, it is unlikely to occur systematically across the region. Tighter constraints on crustal thickness and

mantle radial anisotropy would result from the joint interpretation of receiver functions and longer period dispersion measurements from earthquakes. Uncertainties in these quantities, therefore, are expected to reduce over time, but we believe that these improvements will not change the results presented here appreciably.

2.5.4.3 Vp/Vs in the crust

The strongest and also the most troubling parameter that may produce a systematic error in estimates of radial anisotropy is crustal Vp/Vs, which has been fixed in the crust at Vp/Vs = 1.75, the value for a Poisson solid which is generally considered to be typical of continental crust [*Zandt and Ammon*, 1995; *Christensen*, 1996]. Although normal Vp/Vs (~1.75) has been widely observed across much of eastern Tibet [*Vergne et al*., 2002; *Xu et al*., 2007; *Wang et al*., 2010; *Mechie et al*., 2011, 2012; *Yue et al*., 2012], very low crustal Vp/Vs values also have been observed in the northern Songpan-Ganzi terrane [*Jiang et al*., 2006], and very high crustal Vp/Vs has been observed near the Kunlun fault [*Vergne et al*., 2002], the eastern margin of the plateau [*Xu et al*., 2007; *Wang et al*., 2010], as well as parts of the Qiangtang terrane [*Yue et al*., 2012]. Thus, the assumption of a uniform Vp/Vs across all of Tibet may be inappropriate.

To test the effect of the assumption that crustal Vp/Vs=1.75 on the amplitude of mid-crustal radial anisotropy, we have inverted with different crustal Vp/Vs ratios and have plotted the resulting depth-averaged mid-crustal radial anisotropies for point B (Figure 2.1a) in Figure 2.17a. We apply these tests at a point in eastern Tibet, in contrast with the tests presented in Section 2.5.4.2, which were for the Longmenshan region. Positive correlation is observed between the applied crustal Vp/Vs and depth-averaged radial anisotropy, and mid-crustal radial anisotropy may become zero when Vp/Vs drops below 1.60. This extremely low Vp/Vs could exist at depths where the Alpha-Beta quartz transition (ABQT) occurs, namely in a thin layer that

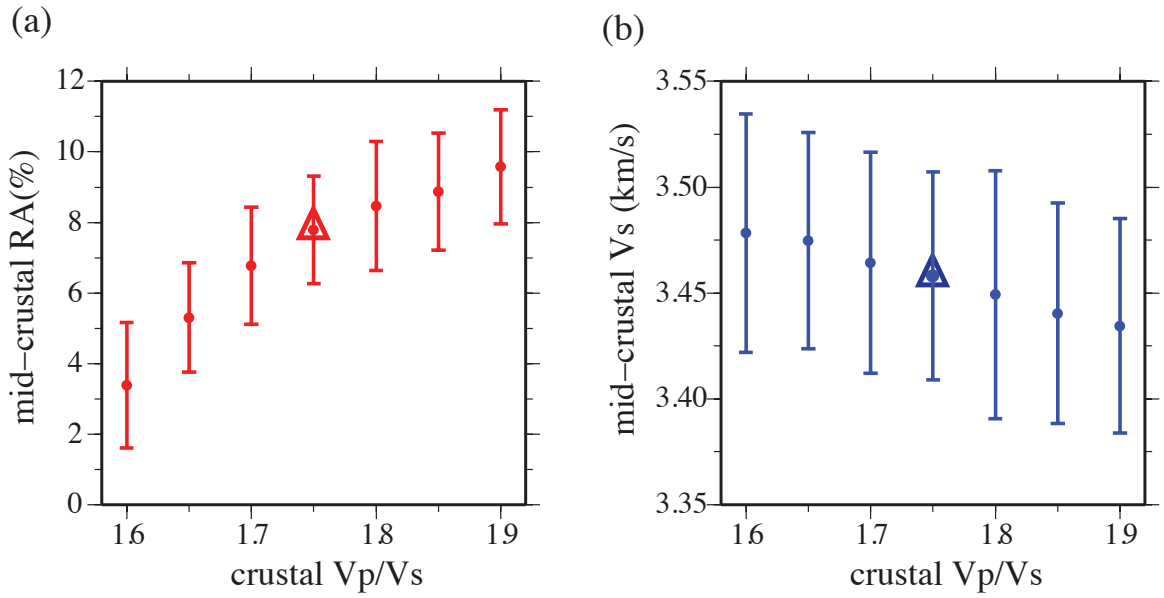

Figure 2.17. Similar to Fig. 2.16, but shows the trade-off between the fixed value of the crustal Vp/Vs used in the inversion and (a) the depth-averaged (from 30 to 40 km) crustal Vs radial anisotropy and (b) the depth-averaged (from 30 to 40 km) mid-crustal Voigt-averaged Vs. Values are from inversion with the given crustal Vp/Vs at location B identified in Fig. 2.1a.

occurs somewhere between 20 to 30 km depth [*Mechie et al*., 2011]. Also, a relatively low crustal Vp/Vs may be caused by crust with a felsic composition [*Mechie et al*., 2011]. However, both alternatives are for a thin low Vp/Vs layer, not the whole crust, and it is physically unlikely to have an average crustal Vp/Vs of 1.60. With values of Vp/Vs ranging from 1.70 to 1.80, the effect is to change the amplitude of radial anisotropy only by about ±1%. Although radial anisotropy is required across eastern Tibet, the reliability of estimates of its amplitude would be improved with better information about Vp/Vs across Tibet.

The value of crustal Vp/Vs not only affects the amplitude of crustal radial anisotropy, but also the shear wave speed (Vs). Figure 17b shows that crustal Vp/Vs and depth averaged mid-crustal Vs are anti-correlated, with Vs decreasing as crustal Vp/Vs increases. This result may seem counterintuitive. With a fixed Vp/Vs, increasing radial anisotropy will increase Vs. In addition, increasing Vp/Vs tends to increase radial anisotropy. Nevertheless, increasing Vp/Vs in the inversion reduces the inferred Vs because increasing Vp at a constant Vs increases the Rayleigh wave speed but not the Love wave speed. In this case, Vsv must be lowered to reduce the Rayleigh wave speed in order to fit the Rayleigh-Love discrepancy. The lowering of Vsv (caused by increasing Vp/Vs) thus lowers Vs. For Vp/Vs running between the physically more plausible range of 1.7 to 1.8, the effect on mid-crustal Vs is well within stated uncertainties, about ±9 m/s.

2.5.4.4 Vp radial anisotropy and η in the crust

As discussed in Section 2.3.1, our inversions are performed with the simplifying but nonphysical assumption that the elastic tensor possesses only Vs anisotropy with $\gamma = (Vsh - Vsv)/Vs \neq 0$, but $Vph = Vpv$ so that Vp radial anisotropy $\varepsilon = (Vph - Vpv)/Vp = 0$ and $\eta = 1$. More realistically, however, Vp anisotropy is expected to accompany Vs anisotropy so that $\varepsilon \neq 0$

and $\eta \neq 1$. We discuss the effect of the imposition of this simplification on the posterior distribution of Vs anisotropy.

Figure 2.18 presents the sensitivity of Rayleigh and Love wave phase speeds at 30 sec period to perturbations in Vsv, Vsh, Vpv, Vph, and η at different depths. Love waves are sensitive almost exclusively to Vsh, being only weakly sensitive to Vsv and completely insensitive to Vph, Vpv, or η. In contrast, Rayleigh waves are sensitive to all of the parameters except Vsh. In order to determine the effect of Vp anisotropy (ε) and η on our estimate of Vs anisotropy (γ) we concentrate on the Rayleigh wave.

Vph and Vpv have opposite effects on Rayleigh wave phase speeds. Thus, increasing Vph or decreasing Vpv (i.e., increasing ε) will have a similar effect to decreasing Vsv (Figure 2.18a). For an isotropic medium, the opposite signs of the Vph and Vpv kernels cause them to cancel approximately in the deeper parts of the kernel and restrict isotropic Vp sensitivity to a zone much shallower than primary Vs sensitivity. But for an anisotropic medium this is not true. Anisotropic Vp sensitivity extends as deeply as anisotropic Vs sensitivity. An increase in Vp radial anisotropy will decrease the Rayleigh wave phase speed just like an increase in Vs radial anisotropy. Therefore, as *Anderson and Dziewonski* [1982] point out, the existence of Vp radial anisotropy will tend to decrease the Vs radial anisotropy needed to resolve the Rayleigh-Love discrepancy. However, the fifth modulus η must also be taken into account. As shown in Figure 2.18a, the sensitivity of Rayleigh wave phase speeds to η is similar to that of Vph so that a decrease in η will increase the Rayleigh wave phase speed, increasing the Vs radial anisotropy needed to resolve the Rayleigh-Love discrepancy. Thus, an increase (decrease) in Vp radial anisotropy and a decrease (increase) in η may compensate each other. Whether an increase in Vp

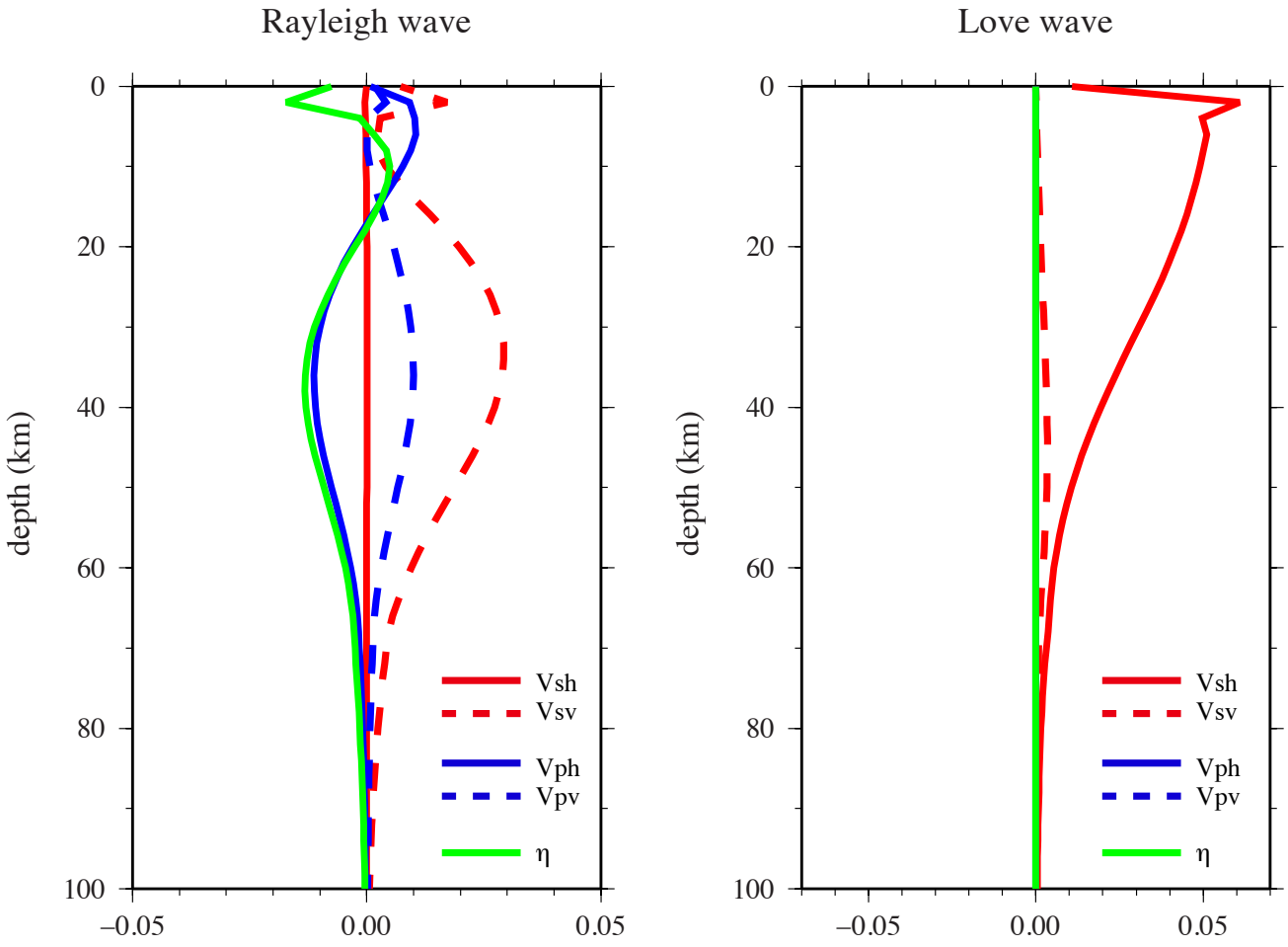

Figure 2.18. Example sensitivity kernels for Rayleigh and Love wave phase speeds at 30 sec period to perturbations in Vsv, Vsh, Vpv, Vph, and η at different depths.

radial anisotropy is expected to correlate with a reduction in η needs to be explored by investigating the elastic tensor of real crustal rock samples.

For many different crustal and mantle rocks, Vp radial anisotropy and η can be scaled approximately to Vs radial anisotropy [*Gung et al*., 2003; *Becker et al*., 2008; *Takeo et al*., 2013]. To obtain approximate scaling relationships, we use the elastic tensors of three crustal rock samples measured by *Erdman et al*. [2013] and provided to us by B. Hacker. Following the procedure described by *Montagner and Anderson* [1989], we rotate the elastic tensors to all possible orientations and compute the five corresponding Love coefficients (A, C, F, L, and N) for every elastic tensor at each orientation. We then analyze the variation of Vp radial anisotropy (ε) and η as a function of Vs radial anisotropy (γ) over all orientations. This analysis shows that the relationship between Vp and Vs radial anisotropy is nonlinear, particularly for negative Vs radial anisotropy ($\gamma < 0$), and ε may be non-zero when γ goes to zero. However, ignoring the possible offset between ε and γ, for weak anisotropy a linear relationship between γ and ε fits the data adequately and we find: $\varepsilon \approx 0.5\ \gamma$. The relationship between η and Vs radial anisotropy is much more linear with an average slope of about -4.2, and the offset between η and γ is negligible. As a result, based on the elastic tensor data of *Erdman et al*. [2013] we obtain the following approximate linear scaling relationships between Vs anisotropy (γ) with Vp anisotropy (ε) and η:

$$\varepsilon \approx 0.5\ \gamma \qquad\qquad \eta \approx 1.0 - 4.2\ \gamma \qquad\qquad (5)$$

Thus, an increase in Vs radial anisotropy is correlated with a smaller increase in Vp radial anisotropy but a larger decrease in η.

With the scaling relationships summarized by equation (2.5), we re-perform the inversions at four geographical points (A-D of Figure 2.1a) and present the results in Figure 2.19. On the vertical axis of Figure 2.19a are the estimates of Vs radial anisotropy (γ) with the realistic elastic tensor in which Vp anisotropy and η are scaled to Vs anisotropy via equation (2.5). The horizontal axis presents the estimates of Vs radial anisotropy with the simplified elastic tensor in which all anisotropy is in Vs so that $\varepsilon=0$ and $\eta=1$. In each case the results represent a depth average of Vs anisotropy, which is performed over the upper crust for location C and over the middle crust at the other locations. As expected, the scaling of Vp anisotropy and η to Vs anisotropy has almost no effect at location A where the crust is nearly isotropic, but does have an effect at the locations where there is significant crustal Vs anisotropy. Both the positive (location B) and negative (location D) mid-crustal Vs anisotropy tend to increase in amplitude in the inversion based on the more realistic elastic tensor, which means that the amplitude of mid-crustal Vs anisotropy presented in Section 2.4 may be slightly underestimated. However, for all four locations, differences between estimates of Vs anisotropy with the simplified or realistic models of radial anisotropy are small, generally lying within the 1σ uncertainty because the effects of Vp radial anisotropy and η compensate on another.

2.5.4.5 Possibility of overtone interference?

Levshin et al. [2005] discussed how higher modes observed across Central Asia can be used to improve crustal models in this region. The potential existence of higher modes, however, could complicate observations of fundamental mode Rayleigh and Love waves. In the Sichuan Basin, based on our 3D model the fundamental and first overtone modes for Love wave should be well separated with a difference between them of at least 350 m/s for periods above 8 sec, which is much larger than the observed Rayleigh-Love discrepancy (Figure 2.7c). Therefore,

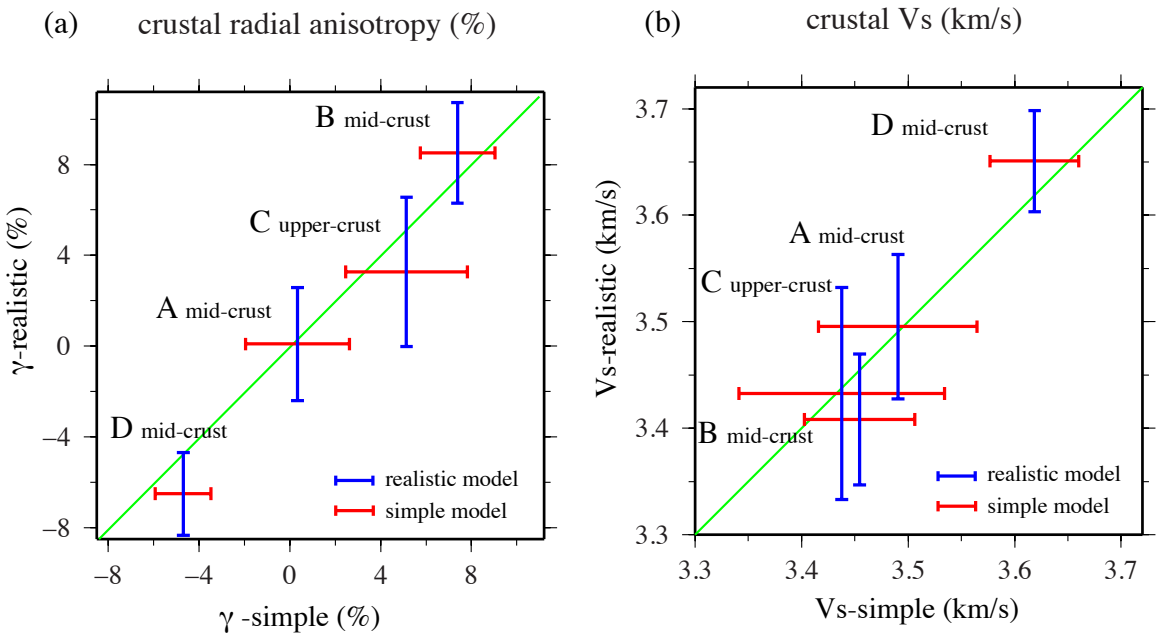

Figure 2.19. Comparison of the inversion results between the simple model of Vs radial anisotropy (γ-simple, red error-bars; ε =0, η =1) and the realistic model (γ-realistic, blue error-bars; ε = 0.5γ, η = 1-4.2γ) for (a) crustal Vs radial anisotropy and (b) crustal Voigt-averaged Vs. Both plots are for the four locations (A-D) identified in Fig. 1a. The results at locations A, B, and D are depth-averaged over the middle crust, while results at location C is depth-averaged over the upper crust. The half-widths of the error bars are the depth-averaged uncertainty (1σ). Green lines are the locus of points for identical results from the simple and realistic models of Vs radial anisotropy and all error bars overlap this line.

overtones cannot interfere with fundamental mode Love wave measurements in the Sichuan Basin. However, in Tibet where the crust is much thicker, the fundamental mode and overtone Love waves are closer. Figure 2.20a presents Love wave group and phase speeds for the fundamental and first overtone modes computed based on our 3D model at a point in eastern Tibet (point B of Figure 2.1a). The group speed of the first Love overtone closely approaches (and can overlap at some locations) the fundamental group speed at about 15 sec period. Higher overtones will approach the fundamental mode group speed curves at successive shorter periods. It is, therefore, important to consider if Love wave overtones could be mistaken for the fundamental mode and potentially bias the Love wave phase speed measurements in the period band of our study (≥ 8 sec). The relevance of this consideration is amplified by recent observation of *Poli et al*. [2013] of Love wave overtones at periods below about 8 sec using ambient noise in the Baltic shield.

In contrast with the observations obtained by *Levshin et al*. [2005] based on intermediate and deep earthquakes in Central Asia, we do not see obvious overtones on FTAN diagrams of ambient noise cross-correlations in the region at periods above 6 sec. This does not mean that the overtones do not exist because they could be obscured by the fundamental modes. But, the determination of the likelihood of overtone interference reduces to a consideration of the relative excitation of the fundamental and overtone modes. Figure 2.20b presents theoretical source spectra computed from a horizontal force for the fundamental and first Love overtone modes for source depths of 0 and 20 km (computed at the same location as in Figure 2.20a). For the surface source, the fundamental mode has much higher amplitude than the first overtone at all periods. However, for a mid-crustal source depth, the fundamental and overtone mode have similar amplitudes only below about 8 sec period. Figure 2.20c-d illustrate these amplitudes by

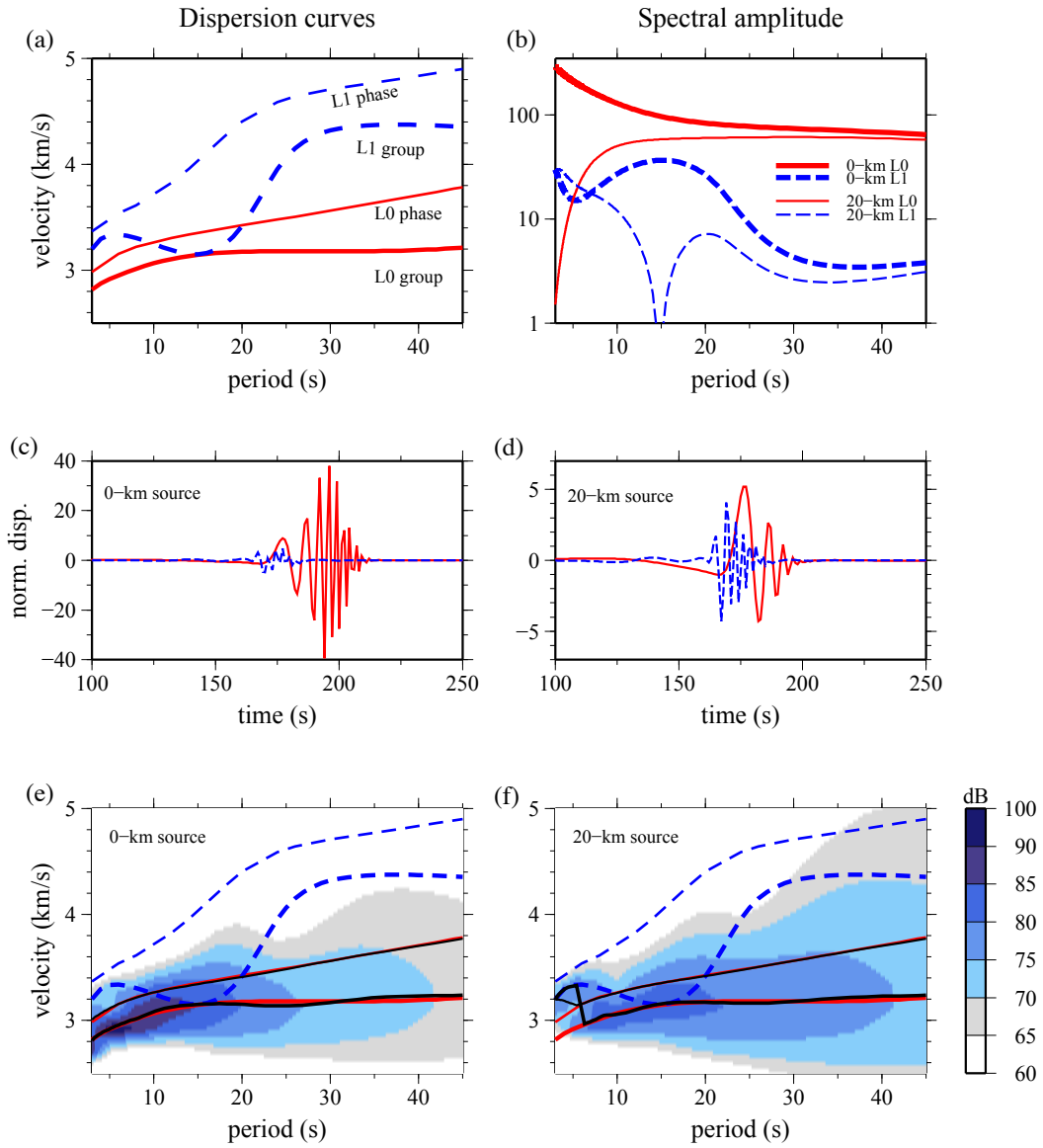

Figure 2.20. Synthetic results for the fundamental and higher mode Love waves. (a) Dispersion curves computed from an isotropic model based on the structure at location B in Fig. 2.1a. Red lines represent phase- and group- velocity dispersion curves of the fundamental model Love wave (L0) and dashed blue lines represent that of the first higher mode Love wave (L1). (b) Spectral amplitudes computed for a horizontal force at the surface (bold lines) or at 20 km depth (thin lines) for the fundamental Love wave (red lines) and first overtone Love wave (blue lines). (c) Green's function computed from the same model in (a) with a single horizontal force located at the surface (0-km depth). Red line indicates the fundamental Love wave; the dashed blue line is the first overtone Love wave. (d) Similar to (c), but computed with a single horizontal force located at 20-km depth. (e)-(f) Frequency-time analysis (FTAN) diagram for the superposition of the Green's functions shown in (c) and (d), respectively. Red and blue lines are the dispersion curves shown in (a) and black lines are the phase and group velocity dispersion curves measured using FTAN.

separately plotting the fundamental and first overtone Green's functions for a horizontal force. Figure 2.20e-f shows the FTAN diagrams for these two Green's functions. For the surface source, the overtone does not interfere with measurements of the fundamental mode group or phase speeds across the entire period band of the synthetic seismogram (2 – 45 sec). For the mid-crustal source, FTAN picks up the first overtone only at periods below ~6 sec and measures an unbiased fundamental mode at all longer periods. Similar results are found for force couples and double couples.

Although the physical cause of Love waves in ambient noise remains enigmatic, it is likely that they arise from processes near earth's surface. In this case the fundamental mode would probably be much stronger than the overtones and overtone interference in measuring fundamental mode Love wave group and phase speeds would probably be minimal at all periods. Even in the unlikely event that ambient noise Love waves were somehow generated at mid-crustal depths or there were some other means to de-amplify the fundamental relative to the overtone modes so that the relative amplitude of overtones and fundamental Love waves would be more commensurate, these synthetic results presented here show that the fundamental mode group and phase speeds can be measured accurately at periods above about 6 sec.

Rayleigh wave overtones have been observed quite robustly in ambient noise cross-correlations in ocean seismograph data [*Harmon et al*., 2007; *Yao et al*., 2011] and in basin resonances for waves coming on the continents [*Savage et al., 2013*] but only at periods below about 5 sec and for the basin resonances predominantly on the radial (non-vertical) component. They are also commonly observed at frequencies above 1 Hz in exploration settings [e.g., *Ritzwoller and Levshin, 2002*]. The period band of these observations does not intersect the

current study and Rayleigh wave overtones are also an unlikely cause of interference with our observations of fundamental mode radial anisotropy.

In conclusion, although the arguments presented here are not definitive, it is highly unlikely that overtones have interfered significantly with the measurement of fundamental mode Love or Rayleigh wave dispersion in the period band of our observations.

2.5.4.6 Conclusions about potential bias in the posterior distributions

We have tested how systematic changes to prior information and constraints imposed in the inversion affect the key model attributes that are interpreted in the paper; namely, the amplitude of mid-crustal Vs radial anisotropy and mid-crustal Voigt-averaged isotropic Vs. In particular, we tested the effect of changing the fixed amplitude of radial anisotropy in the upper mantle, the crustal thickness in the reference model, the Vp:Vs ratio in the crust, and the Vp radial anisotropy and η in the crust. In general, we find that the mid-crustal radial anisotropy will become more positive (i.e., Vsh will increase relative to Vsv) by reducing mantle radial anisotropy, increasing crustal thickness, increasing crustal Vp/Vs, and introducing a more realistic elastic tensor in the crust. Because crustal Vp radial anisotropy is expected to be anticorrelated with η [*Erdman et al.*, 2013], we show that the introduction of Vp radial anisotropy with η allowed to differ from unity has the effect of slightly increasing the estimate of mid-crustal Vs radial anisotropy. Similarly, isotropic shear wave speed Vs also depends to a certain extent on these choices, being inclined to increase with increasing crustal thickness and with decreasing Vp/Vs. The tests demonstrate, however, that the inference of both positive and negative mid-crustal radial anisotropy is robust and potential bias caused by physically realistic variations in prior information imposed in the inversion should lie within the stated uncertainties

of the key model attributes. In addition, we have argued that interference from Love wave (and Rayleigh wave) overtones is expected to affect estimates of crustal Vs anisotropy negligibly.

Improved constraints on crustal thickness and radial anisotropy in the mantle can be achieved by introducing receiver functions and longer period surface wave dispersion information from earthquake tomography, which are planned for the future. Vp radial anisotropy and η can be constrained better with improved knowledge of the petrologic composition of the Tibetan crust as more accurate scaling relationships between Vs anisotropy, Vp anisotropy and η are obtained. The observation of higher mode surface waves after earthquakes is another possible direction for improvements in the model. Providing improved constraints on crustal Vp/Vs may prove to be more challenging, however.

2.6 Discussion

Taking into account the estimated probabilities and the likelihood of bias discussed in Section 2.5 we now address two final questions: What is the most likely cause (or causes) of the radial anisotropy observed beneath and bordering eastern Tibet? Is there evidence for pervasive partial melt in the middle crust beneath eastern Tibet?

2.6.1 On the cause of positive and negative radial anisotropy

Four robust radially anisotropic features are observed. In the middle crust, positive radial anisotropy is observed beneath essentially all of (1) eastern Tibet and (2) the Sichuan Basin and (3) negative anisotropy is found beneath the Longmenshan region bordering eastern Tibet and the Sichuan Basin. (4) In the upper crust, negative radial anisotropy is observed beneath the Songpan-Ganzi terrane and parts of the Qiangtang and Chuandian terranes. We consider the cause of the mid-crustal observations first.

Earlier studies [*Shapiro et al*., 2004; *Huang et al*., 2010] have interpreted the observation of mid-crustal positive radial anisotropy beneath Tibet as evidence for the existence of anisotropic crustal minerals in the middle crust. Recent experimental results, however, have shown that continental crustal minerals such as quartz and feldspars act to dilute the anisotropic response of mica rich rocks [*Ward et al*., 2012]. This dilution effect may raise doubt into whether crystallographic preferred orientation (CPO) of continental crustal minerals alone can cause strong mid-crustal anisotropy. Open or filled fractures [*Leary et al*., 1990; *Crampin and Chastin*, 2003; *Figueiredo et al*., 2013], grain-scale effects [*Hall et al*., 2008], sedimentary layering [*Valcke et al*., 2006], other microstructural parameters [*Wendt et al*., 2003], and sills or lenses of partial melt [*Takeuchi et al*., 1968; *Kawakatsu et al*., 2009] have all been discussed as mechanisms to produce seismic anisotropy under certain conditions. Amongst these mechanisms, partial melt may provide the most viable alternative to CPO to produce mid-crustal radial anisotropy, The anisotropic effect of partial melt is less well understood and its ability to produce substantial radial anisotropy is more speculative than CPO. Thus, the observation of crustal radial anisotropy is still best seen as a mapping of the distribution of aligned crustal minerals – albeit with the caveat that the relative fractions of mica, feldspars, quartz, and amphibole remain poorly understood. In the middle crust we believe that the chief contributor to strong anisotropy is a sheet silicate such as mica (biotite, muscovite).

Even though individual mica crystals exhibit monoclinic symmetry, their tendency to form sheets causes them in aggregate to approximate the much simpler hexagonal symmetry [*Godfrey et al*., 2000; *Cholach et al*., 2005; *Cholach and Schmitt*, 2006; *Erdman et al*., 2013]. There is a unique symmetry axis in a hexagonal system and we call the plane that is perpendicular to this axis the foliation plane. The amplitude and sign of radial anisotropy reflect

the orientation of the symmetry axis (or foliation plane) along with the intrinsic strength of anisotropy, which is determined by mineral content and extent of alignment. The amplitude of azimuthal anisotropy is also affected by the orientation of the symmetry axis [*Levin and Park*, 1997; *Frederiksen and Bostock*, 2000]. Dipping or tilted symmetry axes are believed to be common in many geological settings [*Okaya and McEvilly*, 2003] and should produce a combination of radial and azimuthal anisotropy.

Figure 2.21 clarifies these expectations by rotating the elastic tensors measured from three crustal rock samples obtained at the Funeral Mountains, the East Humboldt Range, and the Ruby Mountains by *Erdman et al*. [2013] (and supplied by B. Hacker) through a set of orientations where the symmetry axis ranges from vertical ($\theta = 0°$, transverse isotropy) to horizontal ($\theta = 90°$). Similarly, the foliation plane ranges from horizontal to vertical. The result of this calculation is presented in Figure 2.21b and yields four general conclusions. Radial anisotropy (1) is positive (Vsh>Vsv) and its magnitude maximizes for a vertical symmetry axis ($\theta = 0°$), (2) falls to zero at an intermediate angle ~50º, (3) becomes negative as the symmetry axis exceeds ~50º, and (4) has its maximum negative magnitude between 60°-90° which is less than the maximum positive magnitude. Therefore, the observed amplitude of radial anisotropy is controlled by a combination of the intrinsic strength of anisotropy, which results from the density of anisotropic minerals and the constructive interference of their effects, and the angle that the symmetry axis makes relative to the local vertical direction. The observation of weaker radial anisotropy alone cannot be interpreted as evidence for a lower density of anisotropic minerals. However, the observation of strong radial anisotropy is evidence for the existence of anisotropic minerals aligned consistently to produce a substantial anisotropic effect. In addition, positive radial anisotropy indicates that the foliation plane is subhorizontal ($\theta < 10°$) to shallowly dipping

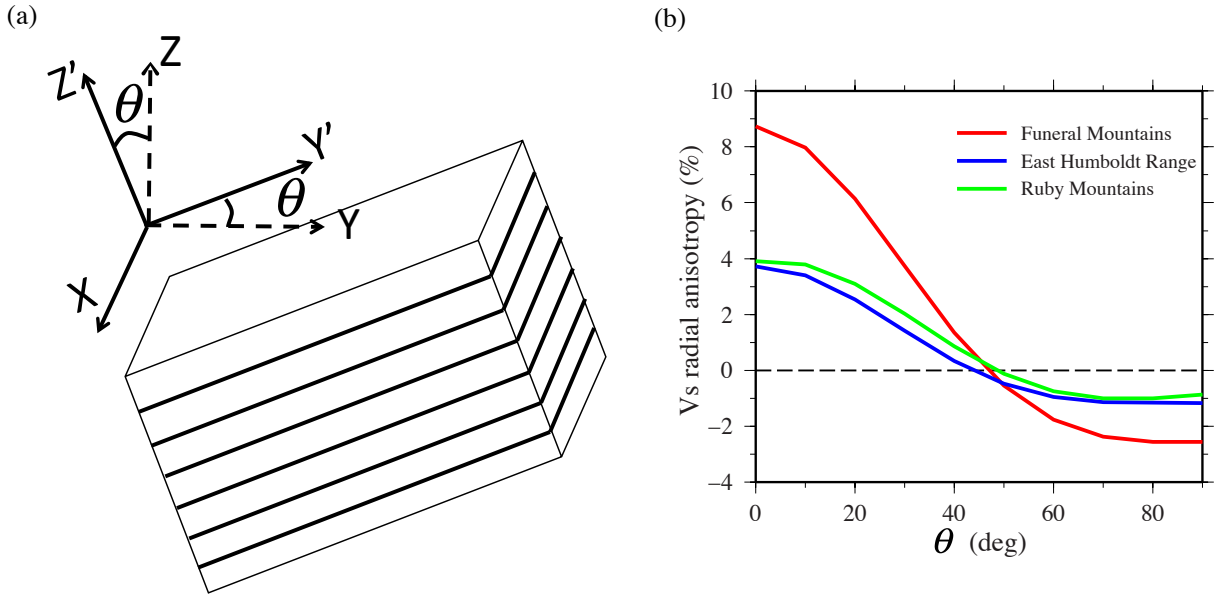

Figure 2.21. (a) Pictorial definition of the rotation angle θ for a hexagonally symmetric system. (b) Vs radial anisotropies, γ = (Vsh-Vsv)/Vs, plotted as a function of rotation angle θ, computed by re-orientating the elastic tensors of the crustal rock samples of *Erdman et al*. [2013]. Samples locations are identified by line color as indicated.

(10°-30°) and negative radial anisotropy implies that it is steeply dipping (60°-80°) to subvertical (80°-90°). Because the maximum negative amplitude of radial anisotropy is smaller than the maximum positive amplitude, negative anisotropy is a more difficult observation.

Based on these considerations, we conclude that the observations of positive mid-crustal radial anisotropy beneath eastern Tibet and beneath the Sichuan Basin imply the existence of planar mica sheets in the middle crust oriented systematically such that the foliation planes are shallowly dipping. We believe that the symmetry axes are not vertical because crustal azimuthal anisotropy is observed across Tibet [e.g., *Yao et al.,* 2010; *Xie et al.,* 2012]. Similarly, the observation of negative mid-crustal radial anisotropy along the Longmenshan region is taken as evidence for planar mica sheets oriented systematically such that the foliation plane is steeply dipping or subvertical. The orientation of the foliation plane (or symmetry axis) cannot be constrained accurately in the absence of information about azimuthal anisotropy, however.

The orientations of the mica sheets in the middle crust probably have dynamical causes. Other than to note that the micas probably orient in response to ductile deformation in the middle crust, we do not speculate on the nature of the deformation that produces this orientation. We do note that the dip angle of faults in the Longmenshan region between Tibet and the Sichuan Basin is high [*Chen and Wilson*, 1996] and that the 2008 Wenchuan earthquake ruptured a steep fault [*Zhang et al*., 2010]. The change in orientation of the mid-crustal foliation plane from shallowly dipping in eastern Tibet to steeply dipping or subvertical in the Longmenshan region may result from the resistance force applied by the rigid lithosphere underlying the Sichuan Basin.

The negative anisotropy observed in the shallow crust (~10 km) across the Songpan-Ganzi terrane and some other parts of eastern Tibet may also result from the CPO of shallower micaceous rocks. However, earthquakes occur to a depth of about 15-20 km within Tibet [*Zhang*

et al., 2010; *Sloan et al*., 2011], so the crust near 10 km depth where negative anisotropy is observed probably undergoes brittle deformation. Faults and cracks in the upper crust are associated with azimuthal anisotropy [*Sherrington et al*., 2004] and may also cause radial anisotropy. Negative anisotropy would result from the plane of cracks or faults having a substantial vertical component. We believe this is the most likely source of the observations of negative radial anisotropy in the shallow crust beneath parts of eastern Tibet, particularly the Songpan-Ganzi terrane.

2.6.2 Existence of pervasive partial melt in the middle crust beneath Tibet?

Even under ideal observational circumstances in which Vs would be exceptionally well constrained, it is difficult to interpret Vs in terms of the likelihood of partial melt. Consistent with the analysis of *Caldwell et al*. [2009], *Yang et al*. [2012] present a plausibility argument for partial melt setting on below about 3.4 km/s, but this threshold is exceptionally poorly determined and would be expected to vary as a function of crustal composition, wet or dry conditions, and anelastic Q. The average of the means of the posterior distributions of mid-crustal shear wave speed taken across eastern Tibet is about 3.427 ± 0.050 km/s. Thus, using the 3.4 km/s threshold value, the mean value of shear wave speed challenges the existence of pervasive mid-crustal partial melts across the entirety of eastern Tibet. There are, however, several discrete regions that prefer particularly low mid-crustal Vs. Figure 2.14b identifies the regions in which the inference that Vs < 3.4 km/s is highly probable (or nearly so): the northern Songpan-Ganzi terrane, the northern Chuandian terrane, and part of the central-to-northern Qiangtang terrane. Most of these regions are coincident with high conductance areas from MT studies [*Wei et al*., 2001; *Bai et al*., 2010]. The INDEPTH MT profile [*Wei et al*., 2001; *Unsworth et al*., 2004] displays a conductive zone starting at about 25 km depth in the central

Qiangtang terrane, and the conductor deepens both northward and southward. In the north Chuandian terrane, *Bai et al*. [2010] also observe a high conductive zone that begins at about 25 km depth.

Therefore, determining with certainty whether Vs lies either above or below 3.4 km/s is difficult using surface wave data alone. But, in summary, there is not compelling evidence that Vs is less than 3.4 km/s pervasively across all of eastern Tibet, although such low shear wave speeds are highly probable in three disjoint regions across the high plateau. Thus, assuming that Vs = 3.4 km/s is an appropriate proxy for the onset of partial melting, we would not expect partial melt to be a pervasive feature of eastern Tibet except in three disjoint regions (the northern Songpan-Ganzi terrane, the northern Chuandian terrane, and part of the central-to-northern Qiangtang terrane) where it should considered more probable. But this inference is highly uncertain due to the uncertainty of the threshold speed at which partial melt is likely to set on.

2.7 Conclusions

Based on Rayleigh (8 to 65 sec period) and Love (8 to 44 sec period) wave tomography using seismic ambient noise, we mapped phase velocities across eastern Tibet and surrounding regions using data recorded at PASSCAL and CEArray stations. A Bayesian Monte Carlo inversion method was applied to generate posterior distributions of the 3-D variation of Vsv and Vsh in the crust and uppermost mantle. Summarizing these distributions with their means and standard deviations at each depth and location, we showed that significant mid-crustal positive radial anisotropy (Vsh > Vsv) is observed across all of eastern Tibet with a spatially averaged amplitude of 4.8% ± 1.4% and terminates abruptly near the border of the high plateau. Weaker (-1.0% ± 1.4%) negative radial anisotropy (Vsh < Vsv) is observed in the shallow crust beneath

the Songpan-Ganzi terrane and in the middle crust (-2.8% ± 0.9%) near the border of the Tibetan plateau and the Sichuan Basin. Positive mid-crustal radial anisotropy (5.4% ± 1.4%) is observed beneath the Sichuan Basin. Shear wave speed in the middle crust is 3.427 ± 0.050 km/s averaged across eastern Tibet.

We also queried the posterior distributions to determine which structural attributes are highly probable and showed the following. (1) Positive mid-crustal radial anisotropy is highly probable beneath the eastern high plateau. Lower crustal radial anisotropy is determined more poorly than anisotropy in the middle crust. (2) Isotropic shear wave speeds below 3.4 km/s are possible across most of the high plateau, but are highly probable only beneath the northern Songpan-Ganzi, the northern Chuandian, and part of the Qiangtang terranes. (3) The crustal Vp/Vs ratio is a parameter that is fixed in the inversion, and we set it in the crystalline crust to that of a Poisson solid: Vp/Vs = 1.75. If a lower (higher) value were chosen, then the amplitude of radial anisotropy would have decreased (increased) and mid-crustal Vs would have gone up (down). Vertically averaged crustal Vp/Vs below 1.7 or above 1.8, however, would be hard to justify over large areas of Tibet and if crustal Vp/Vs ranges between these values the resulting change to radial anisotropy falls within estimated uncertainties.

A piece of evidence for partial melt in the middle crust would be shear wave speeds at 35 km depth less than about 3.4 km/s [*Yang et al*., 2012]. Although the maximum likelihood shear wave speed across Tibet at this depth is 3.43 km/s, Vs below 3.4 km/s cannot be formally ruled out particularly if the crystalline crustal Vp/Vs value is above 1.8. Such high values of Vp/Vs are characteristic of mafic mineralogy or partial melt, which are unlikely to extend vertically across the entire Tibetan crust, at least systematically over large areas. Therefore, in light of the uncertainty in the inference of partial melt from shear waves speeds, we do not find

incontrovertible evidence for mid-crustal partial melt existing pervasively across all of eastern Tibet. However, we do conclude that partial melt is most likely to exist in several discrete regions, notably the northern Songpan-Ganzi, the northern Chuandian, and part of the Qiangtang terranes, where Vs < 3.4 km/s at 35 km depth is highly probable.

We interpret observations of positive mid-crustal radial anisotropy beneath eastern Tibet and beneath the Sichuan Basin as evidence for planar mica sheets in the middle crust oriented systematically such that their foliation planes are shallowly dipping (10°-30° from horizontal) on average. Similarly, the observation of negative mid-crustal radial anisotropy in the Longmenshan region along the border separating Tibet from the Sichuan Basin is taken as evidence for planar mica sheets oriented systematically such that their foliation planes are steeply dipping (60°-80°) or subvertical (80°-90°). We do not speculate on the nature of the deformation that produces this orientation of the mica sheets, but do argue that the change in orientation of the mid-crustal foliation plane near the eastern boundary of Tibet from shallowly dipping to steeply dipping or subvertical may result from the resistance force applied by the rigid lithosphere underlying the Sichuan Basin. Finally, the negative anisotropy observed in the shallow crust beneath the Songpan-Ganzi terrane and some other parts of eastern Tibet may be caused by faults and cracks in the upper crust that have a substantial vertical component.

Some of the uncertainty in the estimates of radial anisotropy and in Voigt-averaged shear wave speed Vs results from poor knowledge of the Vp/Vs ratio in the crystalline crust, of the crustal Vp radial anisotropy and η, of crustal thickness, and of radial anisotropy in the uppermost mantle. Future improvements in estimates of crustal radial anisotropy and Vs will depend on developing improved constraints on these structures. Earthquake surface wave tomography would improve knowledge of radial anisotropy in the mantle and in the lowermost crust.

Receiver functions can be used to improve constraints on crustal thickness and perhaps also to provide information about the average Vp/Vs across the crust. Continued improvement in petrologic information about the the anisotropy of crustal rocks will provide tighter constraints on the scaling between Vp radial anisotropy, η, and Vs radial anisotropy.

CHAPTER III

INFERRING THE ORIENTED ELASTIC TENSOR FROM SURFACE WAVE OBSERVATIONS: PRELIMINARY APPLICATION ACROSS THE WESTERN US

Jiayi Xie[1], Michael H. Ritzwoller[1], S.J. Brownlee[2], and B.R. Hacker[3]

1 – Center for Imaging the Earth's Interior, Department of Physics, University of Colorado at Boulder, Boulder, CO 80309-0390, USA (jiayi.xie@colorado.edu)

2 – Department of Geology, Wayne State University, Detroit, MI 48202

3 – Department of Earth Science, UC Santa Barbara, CA USA 93106-9630

Abstract

Radial and azimuthal anisotropy in seismic wave speeds have long been observed using surface waves and are believed to be controlled by deformation within the Earth's crust and uppermost mantle. Although radial and azimuthal anisotropy reflect important aspects of anisotropic media, few studies have tried to interpret them jointly. We describe a method of inversion that interprets simultaneous observations of radial and azimuthal anisotropy under the assumption of a hexagonally symmetric elastic tensor with a tilted symmetry axis defined by dip and strike angles. We show that observations of radial anisotropy and the 2ψ component of azimuthal anisotropy for Rayleigh waves obtained using USArray data in the western US can be fit well under this assumption. Our inferences occur within the framework of a Bayesian Monte Carlo inversion, which yields a posterior distribution that reflects both variances of and covariances between all model variables, and divide into theoretical and observational results. Principal theoretical results include the following: (1) There are two distinct groups of models (Group 1, Group 2) in the posterior distribution in which the strike angle of anisotropy in the

crust (defined by the intersection of the foliation plane with earth's surface) is approximately orthogonal between the two sets. (2) The Rayleigh wave fast axis directions are orthogonal to the strike angle in the geologically preferred group of models in which anisotropy is strongly non-elliptical. (3) The estimated dip angle may be interpreted in two ways: as a measure of the actual dip of the foliation of anisotropic material within the crust, or as a proxy for another non-geometric variable, most likely a measure of the deviation from hexagonal symmetry of the medium. The principal observational results include the following: (1) Inherent S-wave anisotropy (γ) is fairly homogeneous vertically across the crust, on average, and spatially across the western US. (2) Averaging over the region of study and in depth, γ in the crust is approximately 4.1%±2%. γ in the crust is approximately the same in the two groups of models. (3) Dip angles in the two groups of models show similar spatial variability and display geological coherence. (4) Tilting the symmetry axis of an anisotropic medium produces apparent radial and apparent azimuthal anisotropies that are both smaller in amplitude than the inherent anisotropy of the medium, which means that most previous studies have probably underestimated the strength of anisotropy.

3.1 Introduction

The study of anisotropy using surface waves is primarily of interest to seismologists because surface waves provide a homogenous sampling of the Earth's crust and uppermost mantle over large areas. Robust inferences about anisotropy from surface waves are typically not restricted to small regions, allowing conclusions to be drawn broadly over a variety of geologic and tectonic settings (e.g., *Anderson and Regan,* 1983; *Ekström and Dziewoński*, 1998; *Gung et al*., 2003; *Smith et al*., 2004; *Kustowski et al*., 2008; *Nettles and Dziewoński*, 2008). Cross-correlations of ambient noise principally present relatively short and intermediate period surface waves for interpretation. Therefore, the introduction of ambient noise surface wave tomography has allowed for increasingly detailed information to be gained about the crust over broad regions (e.g., *Shapiro et al*., 2005; *Yao et al*., 2006; *Bensen et al*., 2009; *Moschetti et al*., 2010a; *Ritzwoller et al*., 2011; *Yang et al*., 2012; *Ekström*, 2013), and information about anisotropy from ambient noise mainly concerns the crust (e.g., *Huang et al*., 2010; *Moschetti et al*., 2010b; *Yao et al*., 2010; *Lin et al*., 2011; *Xie et al*., 2013). In this paper, surface wave observations obtained from both ambient noise and earthquakes will be used, and the principal focus will be on the means to infer crustal anisotropy.

Studies of seismic anisotropy using surface waves primarily take two forms. In the first, azimuthally averaged (transversely isotropic) Rayleigh and Love wave travel time (or dispersion) curves are studied to determine if they are consistent with an isotropic medium of propagation. If not, radial anisotropy (or polarization anisotropy) is introduced to the medium to resolve what is often called the "Rayleigh-Love discrepancy" (e.g., Forsyth, 1975; *Dziewonski and Anderson*, 1981; *Moschetti et al*., 2010b; *Xie et al*., 2013). In the second form, the directional dependence of surface wave travel times is used to determine azimuthal anisotropy (e.g., *Simons et al.,* 2002;

Marone and Romanowicz, 2007; *Yao et al.,* 2010; *Lin et al.,* 2011). In both cases, the anisotropy is typically interpreted to result from the mechanism of formation of the medium, either through (1) the crystallographic or lattice preferred orientation of anisotropic minerals (*Christensen*, 1984; *Ribe*, 1992) or (2) the anisotropic shape distribution of isotropic materials, such as laminated structure (*Backus*, 1962; *Kawakatsu et al*., 2009) or fluid filled cracks (*Anderson et al*., 1974; *Crampin*, 1984; *Babuška*, 1991). Indeed, one of the principal motivations to study seismic anisotropy is to understand the deformation that a medium was subject to during its formation and evolution.

The anisotropic properties of an elastic medium and the anisotropy of seismic wave speeds both depend on the detailed constitution of the elastic tensor and on its orientation. With several notable exceptions (e.g., *Montagner and Jobert*, 1988; *Dziewonski and Anderson*, 1981) most studies of seismic anisotropy with surface waves model only the polarization or azimuthal dependence of shear wave speeds and do not explicitly attempt to estimate the elastic tensor. Because, as we discuss below, the directional dependence of surface waves may be ambiguously related to the deformation of the transport medium, in order to understand the anisotropy that seismic waves exhibit and its relationship to the deformation that causes it, it is important to seek information about the (depth-dependent) elastic tensor within the crust and mantle together with its orientation. We refer to the anisotropic properties of a medium as "inherent anisotropy" when they are based on a measured (or inferred) elastic tensor with a known orientation. We use the term "inherent" as opposed to "intrinsic" anisotropy because the latter term often refers to anisotropy that results from a specific cause, namely, from crystal orientation (*Wang et al*., 2013; *Thomsen and Anderson*, 2015). Therefore, we use the term inherent as more general than intrinsic or extrinsic anisotropy, but not directly in conflict with these terms (e.g., *Wang et al*.,

2013). The term inherent may also be contrasted with "apparent" anisotropy, which would be inferred from observational studies that have not explicitly estimated the elastic tensor and its orientation.

A useful starting point on which to base estimates of the elastic tensor is the simplifying assumption that the medium possesses hexagonal symmetry. Such a medium has one symmetry axis, and if the symmetry axis is either vertical or horizontal the elastic tensor can be represented with five independent elastic moduli. A hexagonally symmetric medium with a vertical symmetry axis (z-axis in **Fig. 3.1**) is referred to as a vertical transversely isotropic medium or VTI medium. Such a medium is defined by five depth-dependent elastic parameters (A, C, N, L, F or η), where A and C are compressional moduli and N and L are shear moduli. In this case, the 6x6 elastic modulus matrix, $C_{\alpha\beta}$, the Voigt simplification of the elastic tensor, can be written as the following symmetric matrix:

$$ {}^{V}C_{\alpha\beta} = \begin{bmatrix} A & A-2N & F & 0 & 0 & 0 \\ A-2N & A & F & 0 & 0 & 0 \\ F & F & C & 0 & 0 & 0 \\ 0 & 0 & 0 & L & 0 & 0 \\ 0 & 0 & 0 & 0 & L & 0 \\ 0 & 0 & 0 & 0 & 0 & N \end{bmatrix} \tag{3.1} $$

where η = F/(A-2L) and the superscript V stands for vertical. With a vertical symmetry axis, a hexagonally symmetric medium will produce no azimuthal variation in surface wave speeds mainly because the C_{44} and C_{55} matrix elements are identical. A hexagonally symmetric elastic tensor may display either slow or fast symmetry. In the slow symmetry case, C < A and L < N, which is referred to as positive S-wave radial anisotropy and implies that Love waves are faster than predicted from an isotropic medium that fits Rayleigh wave speeds. Crustal rocks generally display slow symmetry and a finely layered medium also requires it (*Thomsen and*

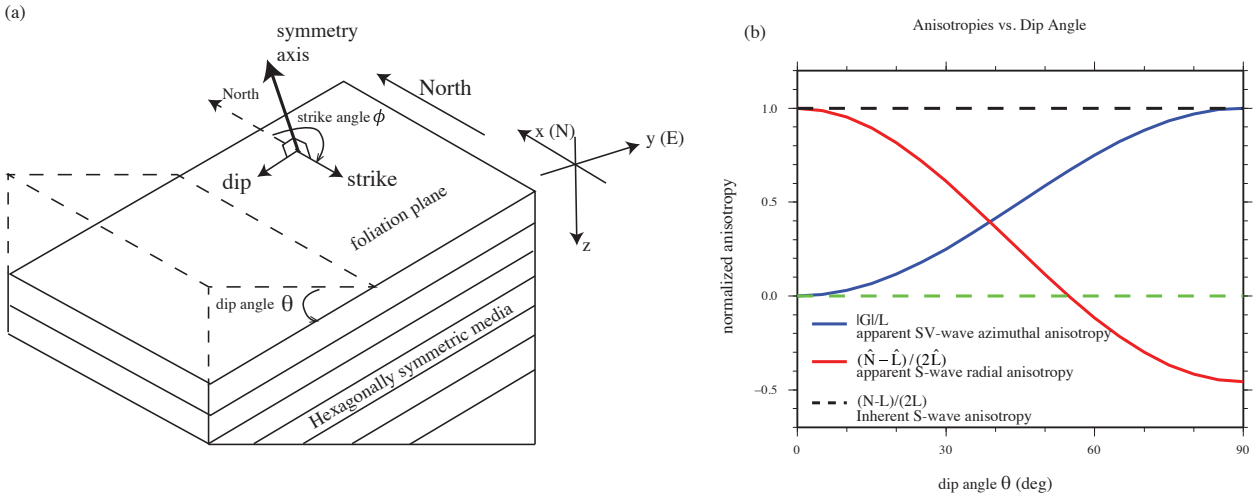

Figure 3.1. (a) Depiction of a tilted hexagonally symmetric medium with definitions of the foliation plane, symmetry axis, strike angle, and dip angle. (b) Illustrative computation of the variation of apparent S-wave radial ($\hat{\gamma}$, red curve) and SV-wave azimuthal (blue curve) anisotropy as a function of dip angle θ. All amplitudes are normalized by the amplitude of maximum inherent S-wave anisotropy, γ. These quantities are defined by Equations (3.9) and (11), and they are obtained by rotating a hexagonally symmetric elastic tensor based on the effective anisotropic medium theory (*Montagner and Nataf*, 1986). This figure aims to summarize qualitatively the variation of anisotropy with dip angle. Details (e.g., the absolute amplitude, the zero-crossing angle, and the number of crossing angles) depend on the elastic tensor.

Anderson, 2015; *Tatham et al*., 2008; *Brownlee et al*., 2011; *Erdman et al*., 2013). For the mantle, however, rocks abundant in olivine are sometimes considered hexagonally symmetric with a fast symmetry axis, because seismologists have assumed that the two slower olivine crystal axes scatter randomly perpendicular to the average fast axis (*Park and Levin*, 2002). However, melt-rich layers embedded in a meltless mantle (*Kawakatsu et al*., 2009; *Jaxybulatov et al*., 2014) probably have a slow symmetry axis.

In contrast, if a hexagonally symmetric medium has a horizontal symmetry axis (x-axis in **Fig. 3.1**), it is referred to as a HTI medium (horizontal transversely isotropic) and the elastic modulus matrix has the following form:

$$ {}^{H}C_{\alpha\beta} = \begin{bmatrix} C & F & F & 0 & 0 & 0 \\ F & A & A-2N & 0 & 0 & 0 \\ F & A-2N & A & 0 & 0 & 0 \\ 0 & 0 & 0 & N & 0 & 0 \\ 0 & 0 & 0 & 0 & L & 0 \\ 0 & 0 & 0 & 0 & 0 & L \end{bmatrix} \tag{3.2} $$

In this case, if N is larger than L ($C_{44} > C_{66}$) then there would be negative S-wave radial anisotropy, which is observed in the mantle beneath the mid-ocean ridges (e.g., *Ekström and Dziewoński*, 1998; *Zhou et al*., 2006; *Nettles and Dziewoński,* 2008) but is observed only rarely in the crust (e.g., *Xie et al*., 2013). Also, mainly because $C_{44} \neq C_{55}$, this elastic tensor would generate azimuthal variations in wave speeds.

Assumptions of either vertical or horizontal hexagonal symmetry are inconsistent with one another and cannot explain the widely observed co-existence of positive S-wave radial anisotropy along with azimuthal anisotropy (e.g., *Huang et al*., 2010; *Yao et al*., 2010; *Yuan and*

Romanowicz, 2010; *Yuan et al*., 2011; *Xie et al*., 2013; *Hacker et al., 2014*; *Burgos et al*., 2014), at least for the case of a slow symmetry axis. The purpose of this paper is to describe a method to interpret observations of radial and azimuthal anisotropy simultaneously under the assumption of a hexagonally symmetric elastic tensor with a tilted symmetry axis (**Fig. 3.1a**), as was first suggested by *Montagner and Nataf* (1988) and applied at a global scale across the Indian Ocean by *Montagner and Jobert*(1988). Such an assumption has been applied before to body wave observations (e.g., *Okaya and McEvilly*, 2003) as well as studies of the effect of mode-coupling on surface waves (e.g., *Yu and Park*, 1993).

The assumption of hexagonal symmetry is a starting point designed to reduce the number of free parameters that govern the anisotropic medium, which simplifies and accelerates the inverse problem. To describe the medium under this assumption at a given depth requires seven unknowns, the five moduli that govern the inherent characteristics of a hexagonally symmetric medium and two angles through which the elastic tensor is rotated: the dip and strike angles. There are, however, reasons to believe that crustal anisotropy, which is the primary focus of this paper, may display dominantly hexagonal symmetry. For example, strongly laminated or foliated rocks are nearly hexagonal in symmetry (*Okaya and McEvilly*, 2003) and lamination in the lower crust has been observed worldwide (*Meissner et al*., 2006). Also, the primary anisotropic mineral in the middle crust is probably mica (*Weiss et al*., 1999; *Meissner et al*., 2006), which displays approximate hexagonal symmetry. Therefore, if anisotropy derives from the CPO of anisotropic minerals, then mid-crustal anisotropy may be well approximated by an inherently hexagonally symmetric elastic tensor. However, as discussed later in the paper, amphiboles are also strongly anisotropic and may be the dominant anisotropic mineral in the lower crust, but are more orthorhombic than hexagonal in symmetry (*Meissner et al*., 2006; *Tatham et al*., 2008). If

amphiboles are a significant source of anisotropy, then what we estimate by assuming hexagonal symmetry may not have direct geologic relevance, but may yet contain information about the lower-order symmetry of the real elastic tensor, and inferences that are derived should be cognizant of this.

Two further comments will conclude this discussion. First, Rayleigh and Love waves are strongly sensitive only to four (N, L, θ, ϕ, as described later) of the seven unknowns that define a rotated hexagonally symmetric elastic medium. Therefore, a straightforward inversion for the elastic tensor is impractical using surface wave data alone. For this reason we cast the inverse problem in terms of a Bayesian Monte Carlo approach in which we estimate a range of elastic tensors that agree with the data. This allows us to estimate uncertainties in all variables as well as the covariances or correlations between them as represented by the "posterior distribution" at each location and depth. As discussed later, we find that certain elements of the elastic tensor are well determined, others are not, and the posterior distribution is bimodal in three important variables. Second, the assumption of hexagonal symmetry is actually not required for the method we present, but simplifies it significantly. We could have, for example, cast the inverse problem in terms of an un-tilted orthorhombic elastic tensor, but at the expense of introducing two additional free parameters.

Applications here are made using Rayleigh and Love wave dispersion maps from the western US obtained using the Transportable Array (TA) stations from EarthScope USArray. We obtain isotropic Rayleigh wave phase speed maps from 8 to 40 sec period from ambient noise data and from 24 to 90 sec period from earthquake data. Isotropic Love wave maps are taken from ambient noise data from 10 to 25 sec period and from earthquake data from 24 to 50 sec period. These observations produce azimuthally isotropic Rayleigh and Love wave phase speed

curves at each point on a 0.2°x0.2° grid across the study region. The 2ψ Rayleigh wave azimuthal anisotropy data are obtained from 10 to 40 sec from ambient noise data and 24 to 60 sec period from earthquake data, where ψ is the azimuth of propagation of the wave. No azimuthal anisotropy data from Love waves are used in this study. Love wave azimuthal variations are expected (and observed) to display dominantly 4ψ azimuthal variation, which is a much more difficult observation to make than the 2ψ azimuthal variation of Rayleigh waves.

In Section 3.2 we briefly describe the data we use and the observations from surface waves that serve as the input data for the inversion. In Section 3.3, we explain the theoretical background of the inversion, concentrating on the connections between surface wave observations and elastic constants. In Sections 3.4 and 3.5, the model parameterization and inversion are discussed. Finally, in Section 3.6, we present the inversion results and discuss possible physical implications of the estimated models.

3.2 Surface wave data

This paper is motivated by the need for a new inversion method, which is described in a later section, that self-consistently interprets observations of radial and azimuthal anisotropy of surface waves. The method is applied here to surface wave data obtained in a region that encompasses the western US and part of the central US, where USArray stations operated between the years 2005 and 2010. We use continuous ambient noise data to measure Rayleigh and Love wave phase speeds between station-pairs and data from earthquakes with Mw>5.0 to generate dispersion curves between event-station pairs. We follow the tomographic methods described by *Lin et al*. (2009) and *Lin and Ritzwoller* (2011) known as eikonal and Helmholtz

tomography to estimate phase velocity maps with uncertainties. Our region of study extends somewhat further eastward than these earlier studies, however, and we obtain Love wave dispersion maps in addition to Rayleigh wave maps.

At short periods, we use only ambient noise data and at very long periods only earthquake data, but there is an intermediate period range where ambient noise data and earthquake data are combined. The short period interval extends from 8 to 22 sec period where we apply eikonal tomography to produce the Rayleigh wave dispersion maps (*Lin et al*., 2009) from ambient noise. The period band of overlap of ambient noise and earthquake measurements for Rayleigh waves is broad, ranging from 24 - 40 sec period. Love wave measurements, however, only extend up to 25 sec period for ambient noise so overlap between ambient noise and earthquake measurements occurs only at 25 sec period. At longer periods (>40 sec for Rayleigh waves, > 25 sec for Love waves) earthquake data alone are used, with Rayleigh wave measurements extending to 90 sec period and Love wave measurements to 50 sec period. The signal-to-noise ratio is smaller at long periods for Love waves than for Rayleigh waves, which reduces the longest period that Love wave phase speed maps can be constructed. Following the recommendation of *Lin and Ritzwoller* (2011), we apply eikonal tomography up to 50 sec period but apply Helmholtz tomography, which accounts for finite frequency effects, at periods greater than 50 sec. Also following *Lin et al*. (2009), the uncertainties in the isotropic maps are scaled up to encompass the differences between the ambient noise and earthquake-derived maps.

An example of the output of eikonal (ambient noise data) and Helmholtz (earthquakes data) tomography for a point in the Basin and Range province (Point A, **Fig. 3.3a**) is shown in **Figure 3.2** in which the local azimuthal variation of Rayleigh wave phase velocity is presented at

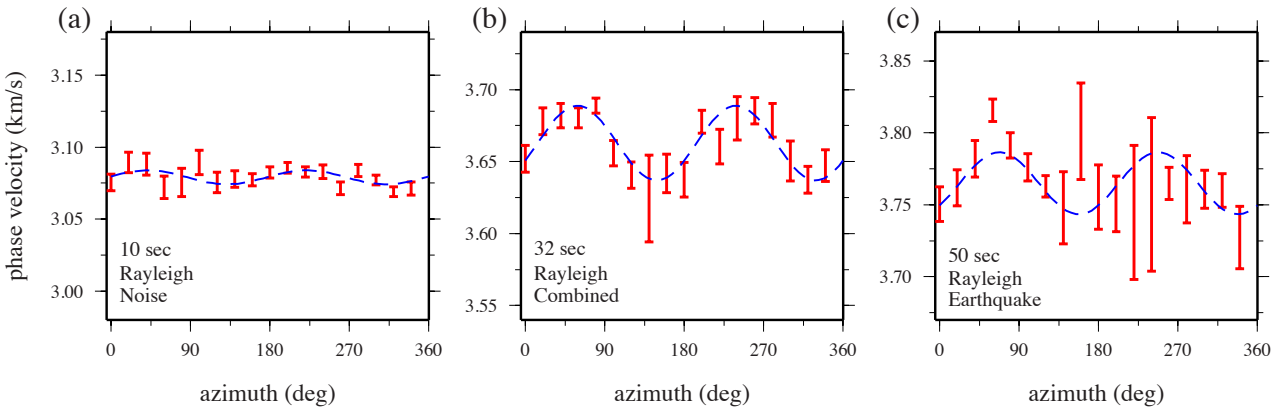

Figure 3.2. Examples of 10, 32, and 50 sec period Rayleigh wave phase velocity observations as a function of azimuth for location A identified in **Fig. 3.3a**, observed using ambient noise datra, ambient noise and earthquake data, and earthquake data, respectively. Blue dashed lines give the best fitting 2ψ curves, where ψ is the azimuth of wave propagation defined positive clockwise from North.

three periods, where results at 10 sec are from ambient noise, at 50 sec from earthquake data, and at 32 sec period from a combination of ambient noise and earthquake data. At each period for each location a truncated Fourier series is fit to the data to estimate the azimuthal dependence of phase velocity for both Rayleigh and Love waves:

$$c(T,\psi) = c_0(T)[1 + a_2\cos(2(\psi - \varphi_{FA})) + a_4\cos(4(\psi - \alpha))] \quad (3.3)$$

where T is period, ψ is the azimuth of propagation of the wave measured clockwise from north, c_0 is isotropic phase speed, φ_{FA} is what we call the 2ψ fast axis direction, α is an analogous phase angle for 4ψ variations in phase speed, and a_2 and a_4 are the relative amplitudes of the 2ψ and 4ψ anisotropy. Uncertainties in each of these quantities are determined at each location and period.

Examples of isotropic phase speed maps for Rayleigh and Love waves are presented **Figure 3.3**, where the short period maps (10 sec period) are determined from ambient noise, the long period maps (Rayleigh: 70 sec, Love: 45 sec) are from earthquake data, and the intermediate period maps are a combination of both data sets. Although azimuthally anisotropic phase speed maps are estimated for both Rayleigh and Love waves, we use only the 2ψ maps for Rayleigh waves here. Rayleigh wave azimuthal anisotropy is observed to be dominated by 180° periodicity (or 2ψ anisotropy) as expected for weakly anisotropic media (*Simth & Dahlen*, 1973). For Love waves, we use only the azimuthally isotropic phase speed maps because Love wave anisotropy is dominated by 90° periodicity (or 4ψ anisotropy), which is a more difficult observable that we choose not to invoke (comparing with Rayleigh wave, the observation of azimuthally dependent Love wave requires better azimuthal data coverage, while the horizontal component of the data is typically noisier than the vertical component). Examples of observations of Rayleigh wave azimuthal anisotropy are presented in **Figure 3.4** at three periods,

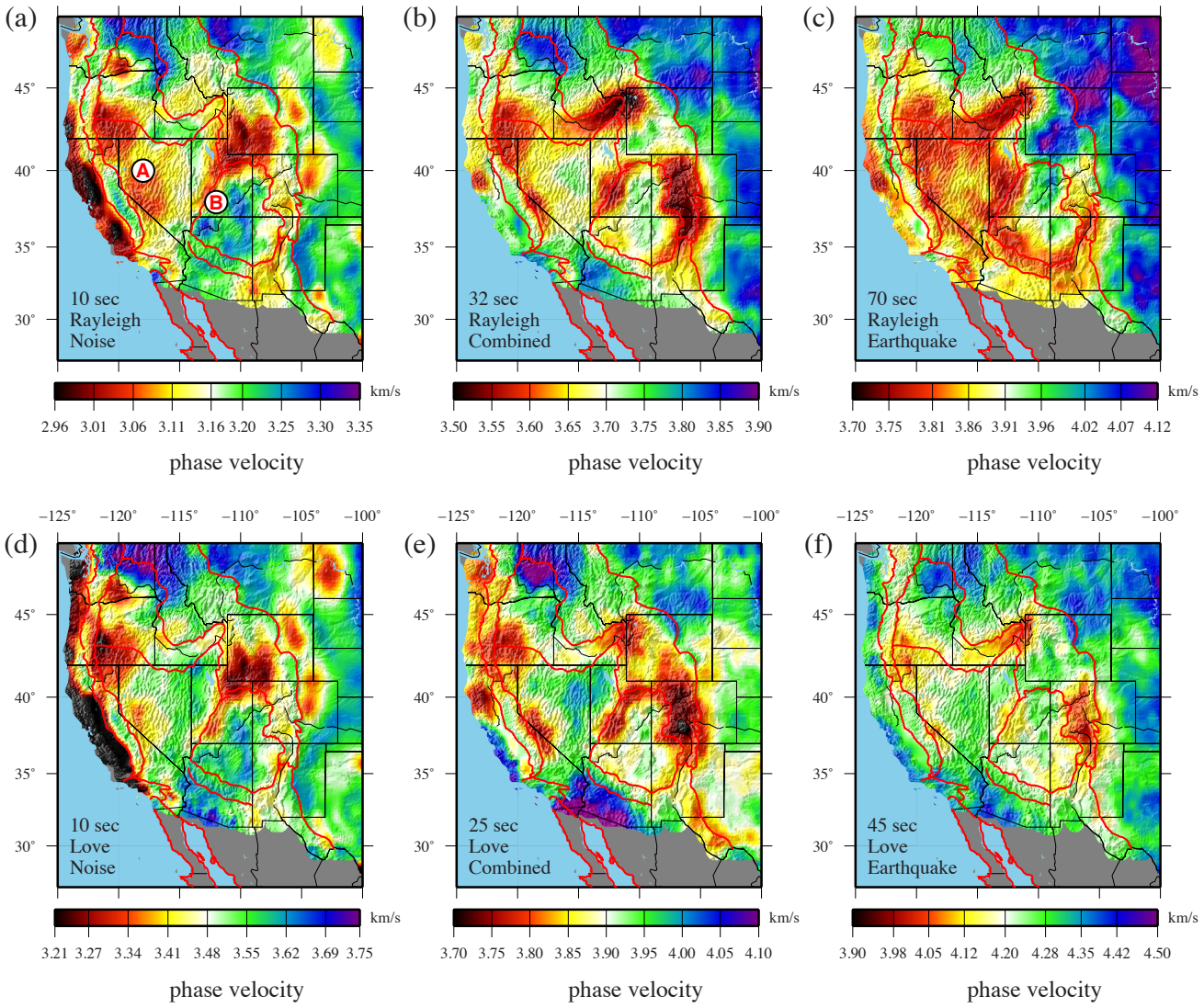

Figure 3.3. Examples of Rayleigh and Love wave isotropic phase speed maps. (a)-(c) Rayleigh wave phase speed maps at 10, 32, and 70 sec period derived from ambient noise data, the a combination of ambient noise and earthquake data, and earthquake data, respectively. (d)-(f) Love wave phase speed maps at 10, 25, and 45 sec period, similarly defined from ambient noise data, the a combination of ambient noise and earthquake data, and earthquake data, respectively.

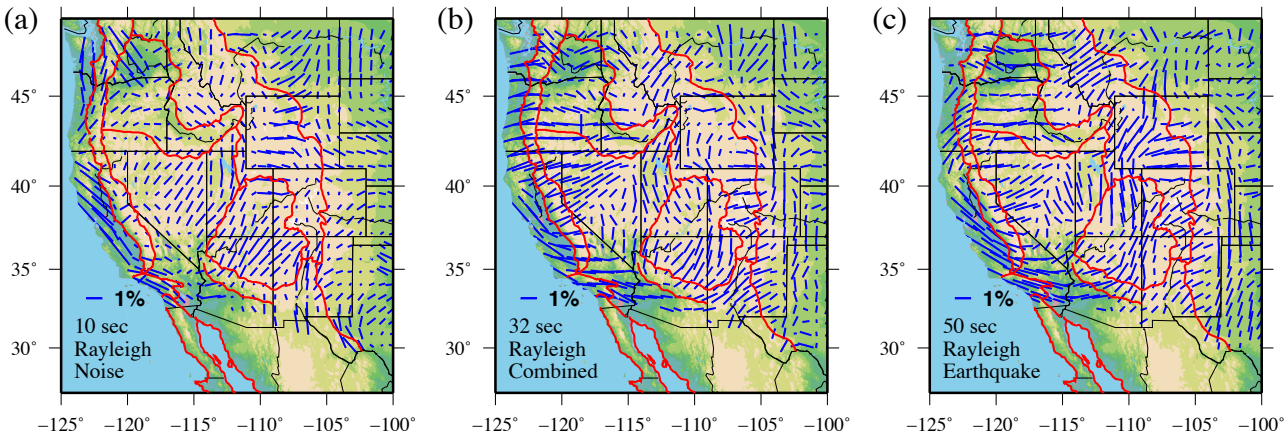

Figure 3.4. The observed Rayleigh wave 2ψ azimuthal anisotropy maps, where ψ is the azimuth of wave propagation defined positive clockwise from North. (a)-(c) Rayleigh wave azimuthal anisotropy maps at 10, 32, and 50 sec period derived from ambient noise data, the a combination of ambient noise and earthquake data, and earthquake data, respectively. The bars are Rayleigh wave fast directions with lengths representing the peak-to-peak amplitude (in percent).

where the length of each bar is the peak-to-peak amplitude of 2ψ anisotropy, $2a_2$, and the orientation of each bar is the fast axis direction φ_{FA}.

Examples of characteristic maps (Rayleigh: 32 sec period, Love: 25 sec period) of the estimated uncertainties in these quantities are presented in **Figure 3.5**. The spatially averaged uncertainties for the isotropic Rayleigh and Love wave speeds (**Fig. 3.5a,b**) are 8 m/s and 18 m/s, respectively, illustrating that Love wave uncertainties are typically more than twice as large as Rayleigh wave uncertainties. Uncertainties in the fast axis directions depend on the amplitude of azimuthal anisotropy and the regions of large uncertainty in **Figure 3.5c** occur where the amplitude of azimuthal anisotropy is small. The average peak-to-peak amplitude of 2ψ anisotropy for the 32 sec Rayleigh wave is approximately 0.8%, and for this amplitude the uncertainty of the fast axis direction averages about 8°. The uncertainty grows sharply as the amplitude of anisotropy reduces below about 0.5% and diminishes slowly as the amplitude grows above 1%. The average uncertainty in the amplitude of 2ψ anisotropy for the 32 sec Rayleigh wave is about 0.24%, which is less than 1/3 of the average amplitude of anisotropy. Thus, the amplitude of the 2ψ Rayleigh wave anisotropy is determined typically to better than 3σ.

From the maps of isotropic phase speed for Rayleigh and Love waves and the amplitude and fast axis direction of 2ψ anisotropy for Rayleigh waves (and their uncertainties), we generate at location on a 0.2°x0.2° grid in the study area isotropic phase speed curves (dispersion curves) for both Rayleigh and Love waves and 2ψ anisotropic period-dependent curves for Rayleigh waves. This raw material forms the basis for the later inversion for a 3D model. **Figure 3.6** presents examples for two locations (A: Basin and Range, B: Colorado Plateau identified in **Fig. 3.3a)** that illustrate how these curves can vary. For Point A, the fast azimuth of the Rayleigh

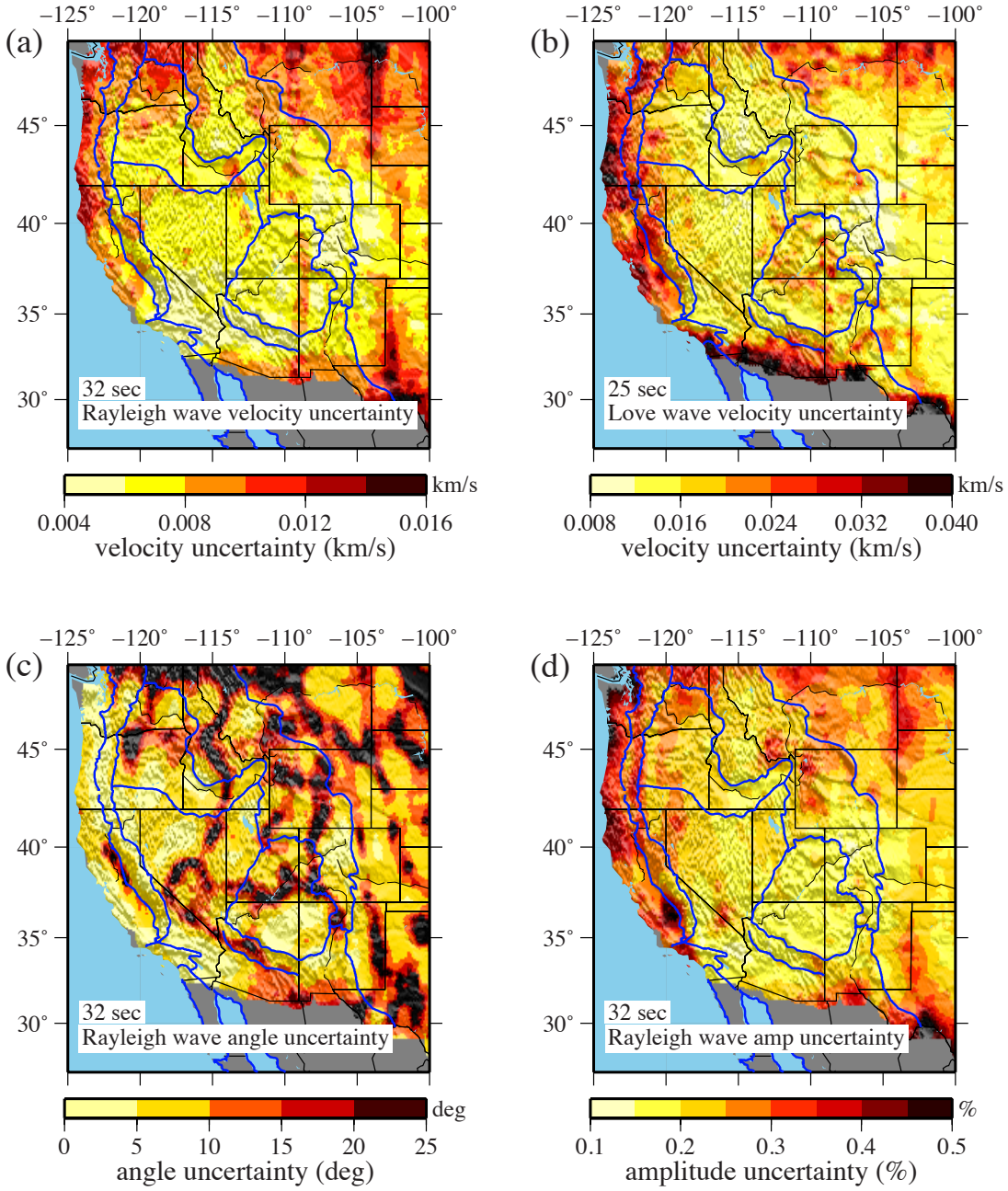

Figure 3.5. Uncertainty maps for (a) the isotropic Rayleigh wave phase speeds at 32 sec period, (b) the isotropic Love wave phase speed at 25 sec period, (c) the fast azimuth direction of Rayleigh wave azimuthal anisotropy at 32 sec period, and (d) the amplitude of Rayleigh wave azimuthal anisotropy at 32 sec period.

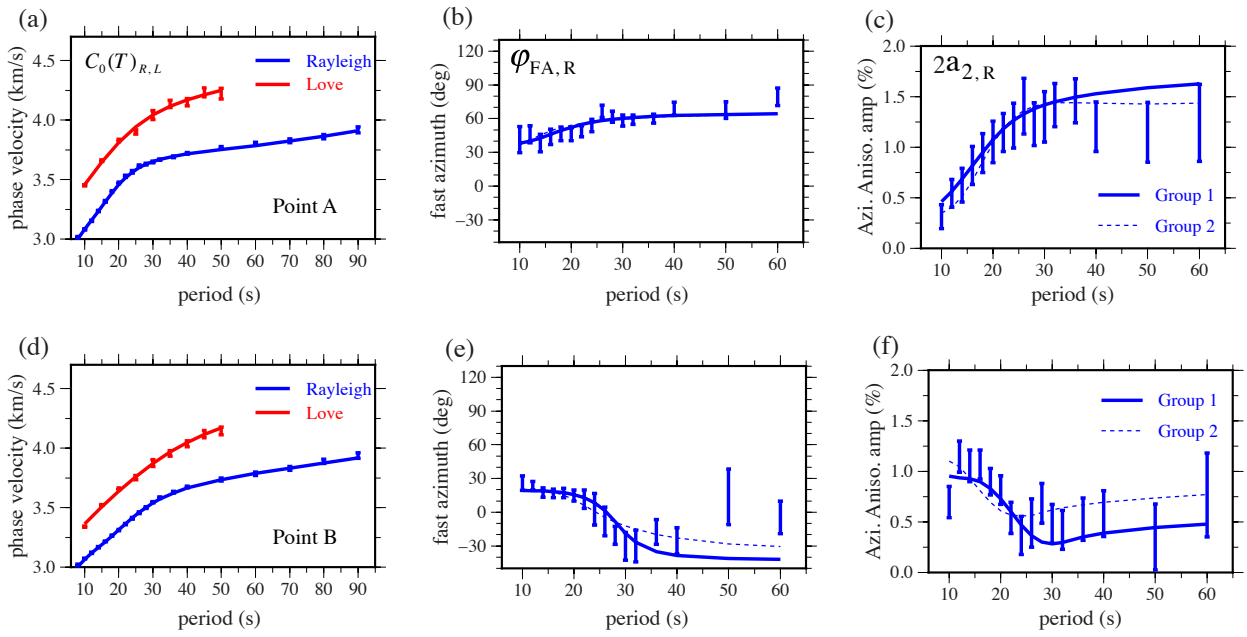

Figure 3.6. (a-c) The local dispersion curves for Point A in the Basin and Range province (identified in **Fig. 3.3a**). The local (a) phase speed, (b) fast azimuth direction, and (c) azimuthal anisotropy amplitude curves are presented as one-standard deviation error bars. Red error bars are the Love wave data and blue error bars are the Rayleigh wave data. The solid and dashed lines are the dispersion curves computed from the average of the posterior distribution for Point A: solid lines are from Group 1 models while dashed lines are from Group 2 models. (d-f) Similar to (a-c) but for Point B in the Colorado Plateau (**Fig. 3.3a**).

wave does not change strongly with period, but the amplitude of azimuthal anisotropy increases with period. In contrast, for Point B, the fast azimuth changes with period, but the amplitude of azimuthal anisotropy tends to decrease with period.

Similar data sets have been used previously to study the anisotropic structure of the western US. For example, *Moschetti et al*. (2010a, 2010b) used isotropic Rayleigh and Love wave phase speed dispersion curves such as those presented in **Figure 3.6a,d** to image apparent crustal radial anisotropy. *Lin et al*. (2011) used azimuthally anisotropic dispersion curves similar to those in **Figure 3.6b,c,e,f** to image the apparent crustal and uppermost mantle azimuthal anisotropy. These two data sets were interpreted separately, but here we attempt to explain both radial and azimuthal anisotropy simultaneously using tilted hexagonally symmetric media (**Fig. 3.1**).

3.3 The elastic tensor and surface wave anisotropy

In a linearly elastic medium, stress and strain are related by a linear constitutive equation, $\sigma_{ij} = C_{ijkl}\varepsilon_{kl}$, where C_{ijkl} is the elastic tensor that describes the behavior of the medium under strain and, therefore, determines the speed of seismic waves. Without loss of generality, the elastic tensor can be compacted into the 6x6 elastic modulus matrix, $C_{\alpha\beta}$, following the Voigt recipe (e.g., *Thomsen*, 1986). Although a general elastic tensor is described by 21 elastic moduli, hexagonal symmetry is often used to characterize earth materials due to its simplicity (e.g., *Dziewoński and Anderson*, 1981; *Montagner and Nataf, 1988*), and can approximate many media within the Earth (e.g., laminated structures, LPO of mica or micaceous rocks, alignment of olivine crystals along the a axis with randomly oriented b and c axes). The hexagonally symmetric elastic modulus matrices with vertical ($^{V}C_{\alpha\beta}$) and horizontal ($^{H}C_{\alpha\beta}$) symmetry axes

are presented in the Introduction. A general reorientation of the symmetry axis, which we call a tilt, is achieved by rotating ${}^{V}C_{\alpha\beta}$ through the dip and strike angles defined in **Figure 3.1a**, as described in the Appendix. The elastic constants for a tilted hexagonally symmetric medium can be characterized by seven independent parameters, five unique elastic constants (A,C,N,L,F) that describe the un-tilted hexagonally symmetric (transversely isotropic) elastic tensor, and two for the orientation of the symmetry axis (Montagner and Nataf, 1988).

For a model of the elastic tensor as a function of depth at a given location, the forward problem in which period and azimuth dependent Rayleigh and Love wave phase speed curves are computed is described in Appendix A. For weakly anisotropic media, surface wave velocities are only sensitive to 13 elements of the elastic tensor and the remaining 8 elements are in the null space of surface wave velocities (*Montagner and Nataf,* 1986). There is an additional symmetry in surface wave observations: phase speeds with dip angles of θ and $\pi-\theta$ (with constant ϕ) are indistinguishable, as are observations at strike angles of ϕ and $\pi+\phi$ (with constant θ). This means that surface wave observations cannot distinguish between the left-dipping foliation plane in **Figure 3.1a** from a right-dipping foliation plane that has been rotated about the z-axis by 180°.

Some terminology is needed to help distinguish between the properties of the anisotropic medium from observations of anisotropy with surface waves. By "inherent anisotropy" we mean the anisotropy of the untilted hexagonally symmetric elastic tensor given by the moduli A,C,N,L,F. We often summarize the inherent anisotropy of a hexagonally symmetric medium using the Thomsen parameters (*Thomsen*, 1986; *Helbig and Thomsen,* 2005; *Thomsen and Anderson*, 2015):

$$\varepsilon \equiv \frac{A-C}{2C} \approx \frac{V_{PH}-V_{PV}}{V_P} \tag{3.4}$$

$$\gamma \equiv \frac{N-L}{2L} \approx \frac{V_{SH}-V_{SV}}{V_S} \tag{3.5}$$

$$\delta \equiv \frac{(F+L)^2-(C-L)^2}{2C(C-L)} \approx \frac{F+2L-C}{C} \tag{3.6}$$

where ε is referred to as inherent "P-wave anisotropy" and γ is called inherent "S-wave anisotropy". A so-called "elliptical" anisotropic medium is one in which δ = ε, in which case P-wave and SH-wave fronts are elliptical and SV-wave fronts are spherical (*Thomsen*, 1986). As shown in the Appendix, upon tilting and reorienting in strike angle, a hexagonally symmetric elastic tensor can be decomposed into the sum of an azimuthally invariant (or effective transversely isotropic) tensor and an azimuthally anisotropic tensor. We refer to the moduli that compose the azimuthally invariant tensor ($\hat{A},\hat{C},\hat{N},\hat{L},\hat{F}$) as the "apparent" transversely isotropic moduli because these moduli govern the azimuthally averaged phase speeds of Rayleigh and Love waves. The Thomsen parameters can be recomputed using these moduli and they define apparent quasi-P wave and quasi-S wave radial anisotropy: $\hat{\varepsilon} \equiv (\hat{A}-\hat{C})/2\hat{C}$, $\hat{\gamma} \equiv (\hat{N}-\hat{L})/2\hat{L}$. As discussed later, previous observational studies of radial anisotropy have estimated apparent radial anisotropy rather than the inherent anisotropy of the medium if earth media are, in fact, not oriented with a vertical symmetry axis.

A tilted hexagonally symmetric elastic tensor will generate both radial and azimuthal anisotropy in surface waves. **Figure 3.1b** demonstrates how apparent SV-wave azimuthal and apparent S-wave radial anisotropy (Rayleigh-Love discrepancy) vary as a function of dip angle. Note that only the dip angle is changing so that the inherent anisotropy is constant as apparent

anisotropy changes. These curves are computed from a simple elastic tensor with a slow symmetry axis. For this model, the amplitude of azimuthal anisotropy increases with increasing dip angle (θ), and the apparent radial anisotropy decreases with increasing dip angle. When the dip angle is 0, there is strong positive apparent S-wave radial anisotropy but no azimuthal anisotropy. At some dip angle, the apparent radial anisotropy vanishes but the azimuthal anisotropy is non-zero. As the dip angle increases further, the apparent radial anisotropy becomes negative (meaning $\hat{L} > \hat{N}$) and azimuthal anisotropy attains its maximum value. This example is intended to qualitatively illustrate the trend with dip angle; the details (e.g., the absolute amplitude, the crossing point in dip angle, and the number of crossing points) depend on the elastic tensor itself (especially F or η).

The computation of Rayleigh and Love wave phase velocities from a given tilted hexagonally symmetric medium is discussed in the Appendix.

3.4 Model parameterization and constraints in the inversion

Our model parameterization, as well as the allowed variations in the model, are similar to those described by *Shen et al*., (2013a, 2013b) in the inversion of isotropic Rayleigh wave phase speeds and receiver functions for an isotropic apparent V_{SV} model of the crust and uppermost mantle in the western and central US. In fact, our model covers a subset of the region of Shen's model, which is the starting model for the inversion performed in this paper. Shen's model is isotropic with $V_S^0 = V_{SH} = V_{SV}$, $\eta^0 = 1$, and $V_P^0 = V_{PV} = V_{PH} = 2.0V_S$ in the sediments, $V_P^0 = V_{PV} = V_{PH} = 1.75V_S$ in the crystalline crust and mantle, density is computed through depth-dependent empirical relationships relative to V_S (*Christensen and Mooney*, 1995; *Brocher*,

2005), and the Q model is taken from the AK135 model (*Kennett et al*., 1995). Here, we fix the density and Q models to those values found by Shen.

In the crust and mantle we assume that the elastic tensor possesses hexagonal symmetry with orientation given by the dip and strike angles (**Fig. 1a**). The depth dependence of the elastic moduli A, C, N, L, and F (or V_{PV} ,V_{PH} , V_{SH} ,V_{SV} , and η) is represented by four B-splines in the crystalline crust from the base of the sediments to Moho, and five B-splines in the mantle from Moho to 200 km depth. Beneath 200 km the model is identical to AK135. The B-spline basis set imposes a vertical smoothing constraint on the model in both the crust and the mantle. If sedimentary thickness in Shen's model is less than 5 km, then the sediments are isotropic and are fixed to the 3D starting model (Shen et al. 2013b) in which the depth dependence of V_S is represented by a linear function. Otherwise, as described below, S-wave anisotropy is introduced in the sediments by varying V_{SH} .

In addition to the parameterization, there are model constraints that govern the allowed variations around the starting model (V_S^0 , V_P^0 , η^0) in the inversion (described in the next section). Because we perform a Monte Carlo inversion, which involves only forward modeling, the imposition of the constraints is straightforward as they affect only the choice of models that we compare with data; i.e., which models are used to compute the likelihood function. In the following, when referring to the seismic velocities ($V_{PV} = \sqrt{C/\rho}$, $V_{PH} = \sqrt{A/\rho}$, $V_{SV} = \sqrt{L/\rho}$, $V_{SH} = \sqrt{N/\rho}$) and $\eta = F/(A-2L)$ we mean the inherent elements of a hexagonally symmetric elastic tensor; that is, the inherent characteristics of the elastic tensor prior to tilting.

The constraints that are imposed during inversion are the following. (1) Constancy of tilt angles in the crust and mantle: At each location, the dip and strike angles (tilt angles θ, ϕ) that define the orientation of the symmetry axis of anisotropy are constant through the crystalline crust and constant through the mantle, although the crustal and mantle angles are allowed to differ from each other. (2) Range of model variables: The allowed variations of the elastic parameters in the crystalline crust and mantle relative to the starting model are as follows: $V_{SV} \pm 0.05V_S^0$, $V_{SH} \pm 0.15V_S^0$, $V_{PV} \pm 0.15V_P^0$, $V_{PH} \pm 0.15V_P^0$. In addition, in the crust $\eta_{\text{crust}} \in [0.6,1.1]$ and in the mantle it lies in the smaller range $\eta_{\text{mantle}} \in [0.85,1.1]$. Also, the tilt angles range through the following intervals: $\theta \in [0°,90°]$, $\phi \in [0°,180°]$. The reasons for the choice of the ranges of model variables are explained in subsequent paragraphs. (3) Sedimentary model: If sedimentary thickness is less than 5 km in Shen's model, the sedimentary part of the model remains unchanged (i.e., it is isotropic and identical to Shen's model). If the thickness is greater than 5 km, then only the V_{SH} part of the model is perturbed to introduce S-wave radial anisotropy with $\gamma \in [0,0.2]$; i.e., this is a maximum S-wave anisotropy of 20%. No tilt is introduced to the elastic tensor in the sediments. (4) V_P/V_S ratio: $V_P/V_S \approx (V_{PV} + V_{PH})/(V_{SV} + V_{SH}) \in [1.65,1.85]$. (5) Monotonicity constraint: V_{SV} , V_{SH} , V_{PV} , and V_{PH} each increase monotonically with depth in the crystalline crust. A monotonicity constraint is not imposed on η or on any of the variables in the mantle. (6) Positive inherent anisotropy: $V_{SH} > V_{SV}$, $V_{PH} > V_{PV}$. This indicates that our inverted hexagonally symmetric tensor has a slow symmetry axis (N>L, A>C, V_P and V_S are slower in the direction of symmetry axis and faster in the foliation plane). (7) Fixed points of the model: Density, sedimentary thickness, and crustal thickness are not changed relative to the starting model.

The constraints can be considered to fall into two groups, one group is based on prior knowledge and the other is introduced to simplify the model. The V_P/V_S ratio, positive anisotropy, and the fixed points of the model constraints are based on prior knowledge. For example, the inherent anisotropies are set to be positive (slow symmetry axis) because most crustal rock samples display slow velocities perpendicular to the foliation plane and fast velocities within the foliation plane, and anisotropy caused by layering requires positive inherent anisotropy (*Thomsen and Anderson*, 2015; *Tatham et al*., 2008; *Brownlee et al*., 2011; *Erdman et al*., 2013). In addition, we have tested negative inherent anisotropy (fast symmetry axis), which is probably consistent with crustal rocks abundant in quartz and amphibole, but this kind of medium cannot explain our observations across the region of study. We set the sedimentary thickness and crystalline crustal thickness constant based on the receiver function observations by *Shen et al*. (2013b). The V_P/V_S ratio is constrained to be within 1.65 to 1.85 because most observations of V_P/V_S fall in this range (e.g., *Lowry and Perez-Gussinye,* 2011; *Christensen*, 1996; *Buehler and Shearer*, 2014).

In contrast, constraints such as the vertically constant tilt angle in the crust and mantle and the monotonic increase of seismic wave speeds in the crust are used to simplify the resulting models. Everything else being equal, we prefer simpler models because they are more testable and falsifiable. For example, we could have parameterized the tilt angles as depth-varying and still fit our data. (In fact, there are always an infinite number of possible and more complex alternatives that include more ad hoc assumptions.) Without prior knowledge, more complex models can hardly be proven wrong because they can always fit the data. Besides, little can be learned from such complexities because they are not derived from the data. On the other hand, a simple model cannot always fit the data (e.g., a constant velocity profile cannot fit the dispersion

curves), so it is easier to prove wrong (if it is). When a model is too simple to fit the data, we then add complexity to the model or loosen constraints. Because this kind of added complexity is motivated by the data, it is more likely to provide information about the earth. Therefore, we view the vertically constant tilt angle and monotonicity constraints as hypotheses that we test empirically. If we are unable to fit aspects of the data acceptably, we will return and loosen these constraints to help fit the data. Otherwise, these constraints are kept to generate a simple model.

In summary, we seek an anisotropic model that is relatively close to the isotropic model of Shen, possesses hexagonally symmetric anisotropy with a slow symmetry axis of locally constant but geographically variable orientation in the crystalline crust and upper mantle, has only positive P-wave and S-wave anisotropy, a V_P/V_S ratio that varies around that of a Poisson solid, and possesses seismic velocities that increase with depth in the crust. Given the allowed variations in the elastic moduli, the maximum S-wave anisotropy (γ) considered in both the crust and mantle is 20%. Because Shen's model was constructed with Rayleigh wave data alone (and receiver functions) it only weakly constrains V_P and V_{SH}, but has rather strong constraints on the sedimentary and crustal thicknesses and V_{SV} in the crust. For this reason, we allow in our inversion wider variation in V_P and V_{SH} than in V_{SV}. η is allowed to vary through a wider range in the crust than in the mantle based on measurements of elastic tensors for crustal rocks (*Tatham et al., 2008; Brownlee et al*., 2011; *Erdman et al.,* 2013) and olivine (*Babuška*, 1991), which is believed to be the major contributor to mantle anisotropy, and also to be consistent with mantle elastic moduli in other studies (e.g., *Montagner and Anderson,* 1989). We do not allow sedimentary thickness or crustal thickness to vary at all because receiver functions are not used in our inversion. However, we find that in areas where the sediments are thicker than 5 km, radial anisotropy is needed in order to fit the data at short periods. In this case, we introduce only

S-wave anisotropy in the sediments (no P-wave anisotropy, no deviation of η from unity), which is probably physically unrealistic, so we do not interpret the resulting model of anisotropy in the sediments. However, regions where sediments are thicker than 5 km in Shen's model are relatively rare in the western US, being confined to a few regions, most notably southwestern Wyoming.

3.5 Bayesian Monte Carlo inversion

The data that are inverted are similar to those shown in **Figure 3.6** for two locations in the western US. We apply a Bayesian Monte Carlo method to invert the data at every location on a 1°x1° grid. The implementation of the inversion is very similar to the method described in detail by *Shen et al*. (2013a), but we do not apply receiver functions. We construct observations such as those in **Figure 3.6** on a 0.2°x0.2° grid. The isotropic model constructed by *Shen et al*. (2013b), which is our starting model, is constructed on the irregular grid given by the station locations where the receiver functions are defined. In contrast, we construct our model on a regular 1°x1° grid across the central and western US. At each grid point, the starting model in our inversion is Shen's model at the nearest station, which in some cases may be as much as 40 km away.

At each location the prior probability distribution is defined relative to Shen's model based on the constraints described in the previous section. The prior distribution guides the sampling of model space. A model is determined to be acceptable or not based on its likelihood function *L(m)*, which is related to the chi-squared misfit *S(m)* (*Shen et al*., 2013a; *Xie et al*., 2013). *L(m)* and *S(m)* are defined as follows:

$$L(m) = \exp(-\frac{1}{2}S(m)) \tag{3.7}$$

where

$$S(m) = \sum_i \frac{(D(m)_i^{predicted} - D_i^{observed})^2}{\sigma_i^2} \tag{3.8}$$

The chi-squared misfit *S(m)* measures the weighted difference between the observed and predicted dispersion curves, where the forward model is computed as described in the Appendix. The chi-squared misfit is composed of four terms, corresponding to the four curves at each location shown in **Figure 3.6**. The first two are for isotropic Rayleigh and Love waves. The other two are for the amplitude and fast-axis direction of Rayleigh wave azimuthal anisotropy. The only weights in the misfit function are the standard deviations of the measurements.

The model sampling process and acceptance criteria follow the procedure described *Xie et al*. (2013) where the partial derivatives are updated when each additional 200 models are accepted. Because the model sampling will not complete until at least 5000 models are initially accepted, the partial derivatives are updated at least 25 times during the sampling. After the sampling is complete, the entire set of initially accepted models is put through the selection process again to remove models with larger misfit (*Xie et al*., 2013). On average, models are accepted up to about twice the rms misfit of the best-fitting model. This reselected model set composes the (truncated) posterior probability distribution**,** which is the principal output of the inversion. The posterior distribution satisfies the constraints and observations within tolerances that depend on data uncertainties.

Figure 3.7 presents map views of the misfit for the best-fitting models (from Group1, defined below) across the study region. Here the misfit is defined as $\sqrt{S/N}$ where S is the chi-squared misfit defined in equation(3.8), and N is the number of observations. In general, our data

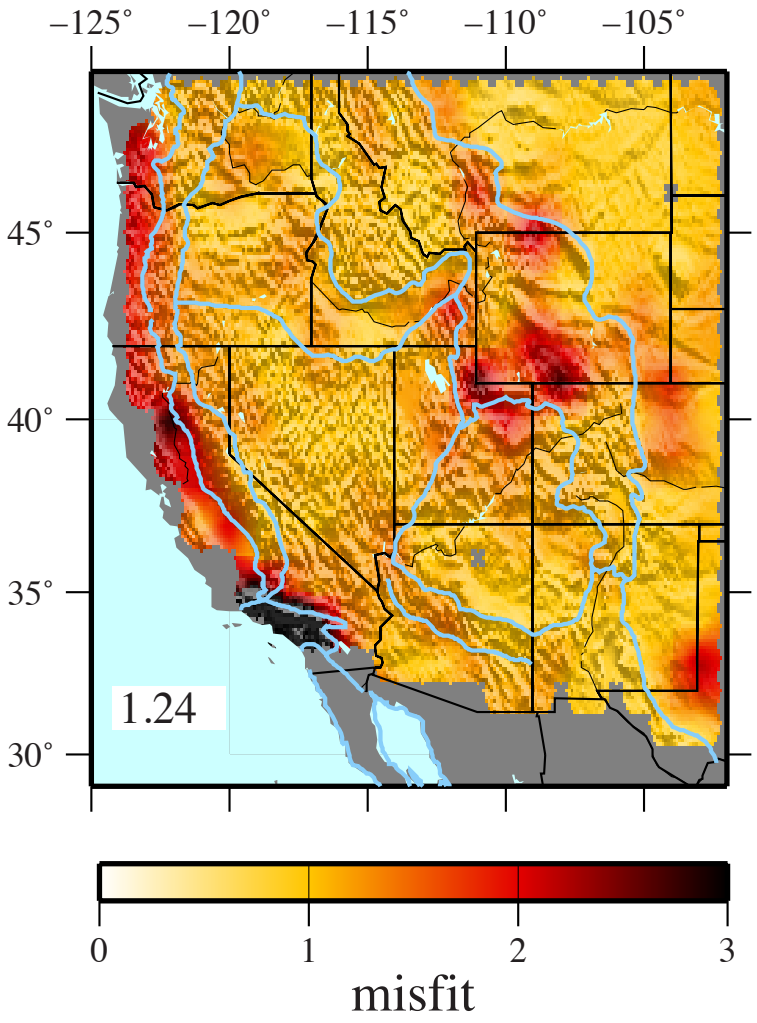

Figure 3.7. Map view of the misfit for the best-fitting models (from Group 1 models) across the study region. The misfit is defined as $\sqrt{S/N}$ where S is the chi-squared misfit defined in equation (3.8), and N is the number of observations. Average value across the map is inset.

can be well fit with an average misfit around 1.2. The misfit is larger along the coast and near the Green River Basin and other basins in southwestern Wyoming, where thick sediments exist. This indicates that our parameterization is not optimal in regions with thick sediments. In the future, we plan to improve the inversion in the sediments by incorporating the Rayleigh wave H/V ratio from ambient nosie (*Lin et al.,* 2012) that provide additional sensitivity to shallow structures. Misfit from Group 2 models is similar.

Examples of prior and posterior probability distributions for the inherent moduli at 20 km depth are shown in **Figures 3.8 and 3.9** for the same two locations for which we present the data in **Figure 3.6**. The prior distributions are strongly shaped by the model constraints and are displayed as white histograms in each panel. For example, V_{SV} displays a narrower prior distribution because only 5% perturbations relative to the starting model are sampled compared to 15% perturbations in V_{SH} , V_{PV} , and V_{PH} . The non-uniform shape of many of the distributions arises from constraints that tie model variables between different depths or of different types, such as the monotonicity constraint. The prior distributions for the dip and strike angles are uniform, however, because they are constant across the crust and, therefore, are not explicitly tied to choices of variables at different depths or of different types. The posterior distribution is wider for variables that are poorly constrained by the data (e.g.,V_{PH} , η) than for those that are well constrained (e.g., θ, ϕ, V_{SV} , V_{SH}). Note that the crustal dip and strike angles, θ and ϕ, are well constrained by the data in that their posterior distributions are relatively narrow. However, the posterior distribution of the crustal strike angle is bimodal, defining two model groups in which strike angles differ by 90°, on average. These two groups of models are presented as blue and red histograms in **Figures 3.8 and 3.9**. The physical cause of this bifurcation is discussed in **Section 3.6.2** below.

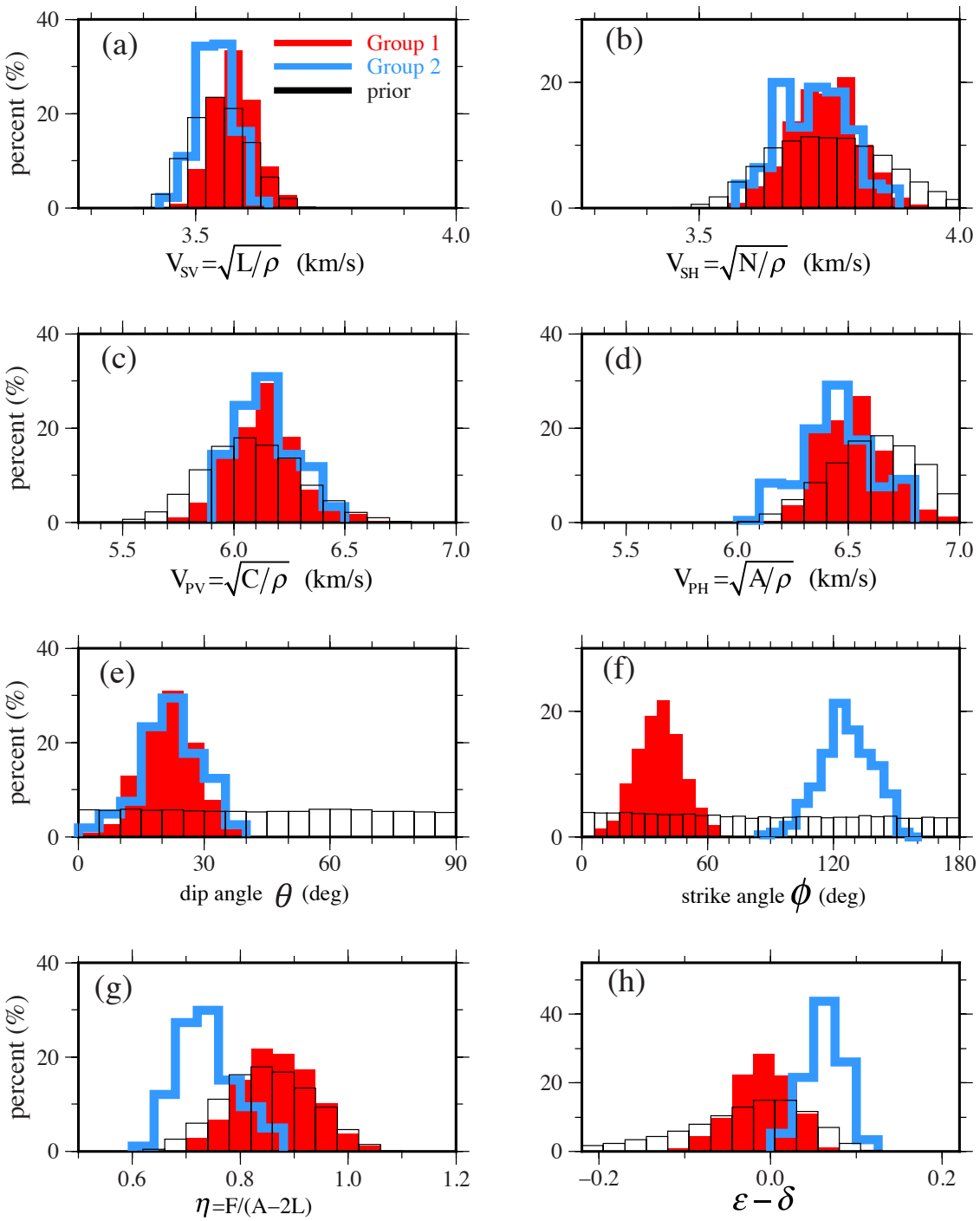

Figure 3.8. Prior and posterior distributions for several model parameters at 20 km depth for Point A (in the Basin and Range, **Fig. 3.3a**). White histograms shown with black lines indicate the prior distributions; both red and blue histograms are the posterior distributions but result from model groups 1 and 2, respectively.

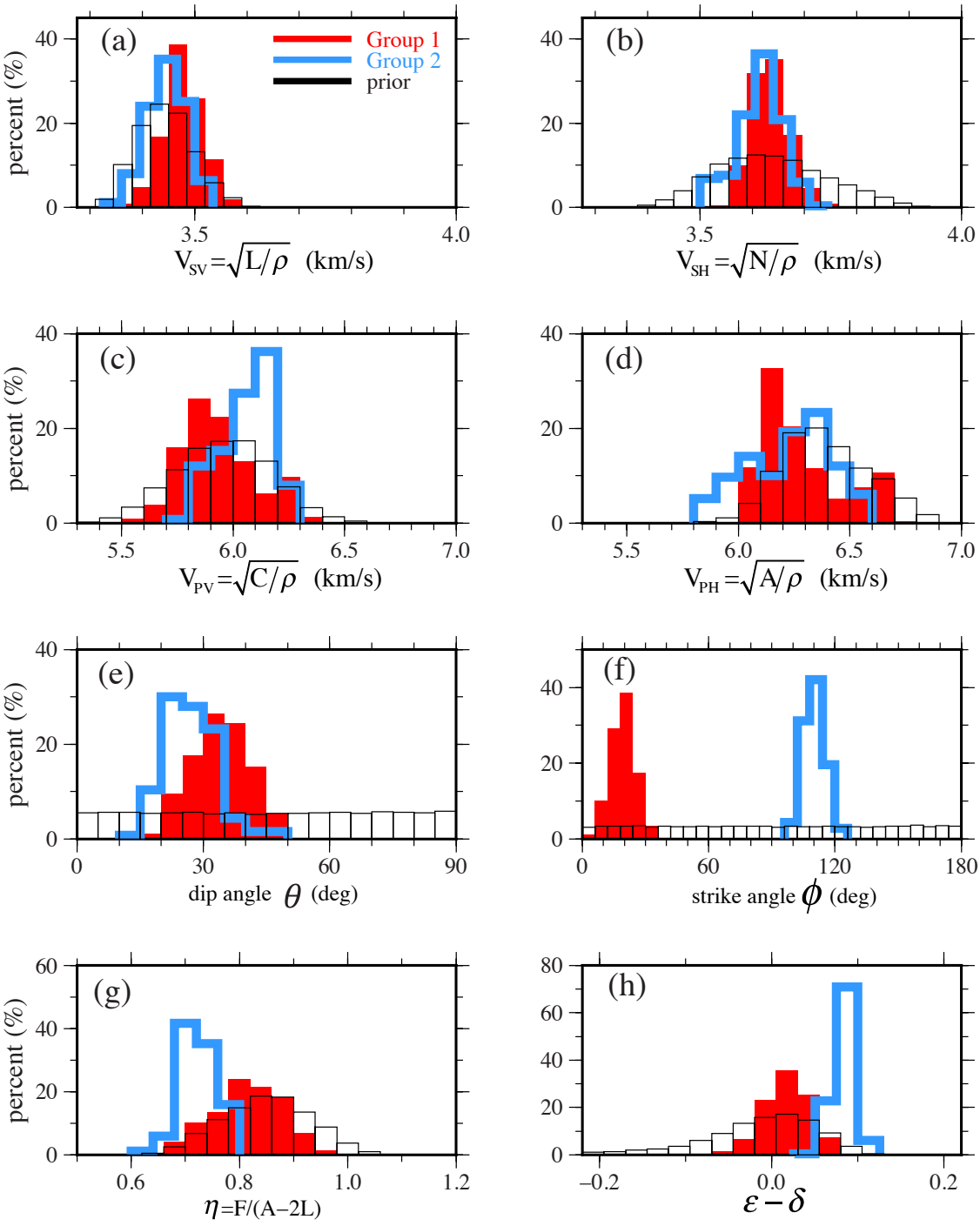

Figure 3.9. Similar to **Fig. 3.8** but for Point B in the Colorado Plateau (**Fig. 3.3a**).

We define "Group 1" (red histograms) to be the set of models with a crustal strike angle that approximately parallels the Rayleigh wave fast direction averaged between 10 sec and 22 sec period. "Group 2" is the set of models with a strike angle that is approximately orthogonal to the Rayleigh wave fast axis direction in this period range. There are subtle differences between the crustal moduli A, C, N, and L between the two groups, but much stronger differences in η, dip angle θ, and the non-ellipticality parameter (ε-δ). Typically, Group 1 has larger values of η and more nearly elliptical anisotropy ($\varepsilon \approx \delta$) in the crust, whereas Group 2 has smaller η and a more non-elliptical anisotropy. Also, Group 1 models tend to have a slightly larger crustal dip angle, on average. We believe that the bifurcation in model space is controlled fundamentally by η, which is poorly constrained in the prior distribution or by the data. The effect of the bifurcation on our conclusions also will be discussed further in the next section of the paper.

Ultimately, we summarize each posterior distribution by its mean and standard deviation, which define the final model and uncertainty at each depth, and for each model variable. **Table 3.1** presents these statistics for the posterior distributions shown in **Figures 3.8 and 3.9**. **Figure 3.10** presents vertical profiles of inherent V_{SV} and V_{SH} (related to the moduli L and N), showing the mean and standard deviation for Group 1 and Group 2 models separately at locations A and B in the Basin and Range and Colorado Plateau (**Fig. 3.3a**), respectively. Differences between the moduli of the two groups are discussed further below. These profiles are derived to fit the data presented in **Figure 3.6**, where we also show how well the data are fit by the mean model from each group (Group 1: solid lines, Group 2: dashed lines). The two groups fit the isotropic phase speed data nearly identically but do display small differences in the details of the fit to Rayleigh wave azimuthal anisotropy, although both fit within data uncertainties. The differences

Table 3.1. The mean and standard deviations for the posterior distributions in **Figures 3.8, 3.9**

		$\sqrt{L/\rho}$ $= V_{SV}$ (km/s)	$\sqrt{N/\rho}$ $= V_{SH}$ (km/s)	$\sqrt{C/\rho}$ $= V_{PV}$ (km/s)	$\sqrt{A/\rho}$ $= V_{PH}$ (km/s)	Dip angle θ (º)	Strike angle ϕ (º)	F/(A-2L)= η	Non-ellipticality $\varepsilon - \delta$
Point A $\rho = 2.79 g/cm^3$	Group 1	3.57 (0.04)	3.74 (0.06)	6.14 (0.15)	6.52 (0.15)	21 (6)	37 (12)	0.87 (0.07)	-0.01 (0.04)
	Group 2	3.54 (0.03)	3.72 (0.07)	6.15 (0.13)	6.47 (0.18)	22 (7)	126 (13)	0.74 (0.05)	0.06 (0.02)
Point B $\rho = 2.73 g/cm^3$	Group 1	3.48 (0.04)	3.63 (0.04)	5.94 (0.17)	6.28 (0.18)	34 (7)	19 (6)	0.82 (0.06)	0.02 (0.03)
	Group 2	3.45 (0.04)	3.61 (0.04)	6.06 (0.12)	6.24 (0.19)	27 (6)	110 (5)	0.72 (0.03)	0.08 (0.01)

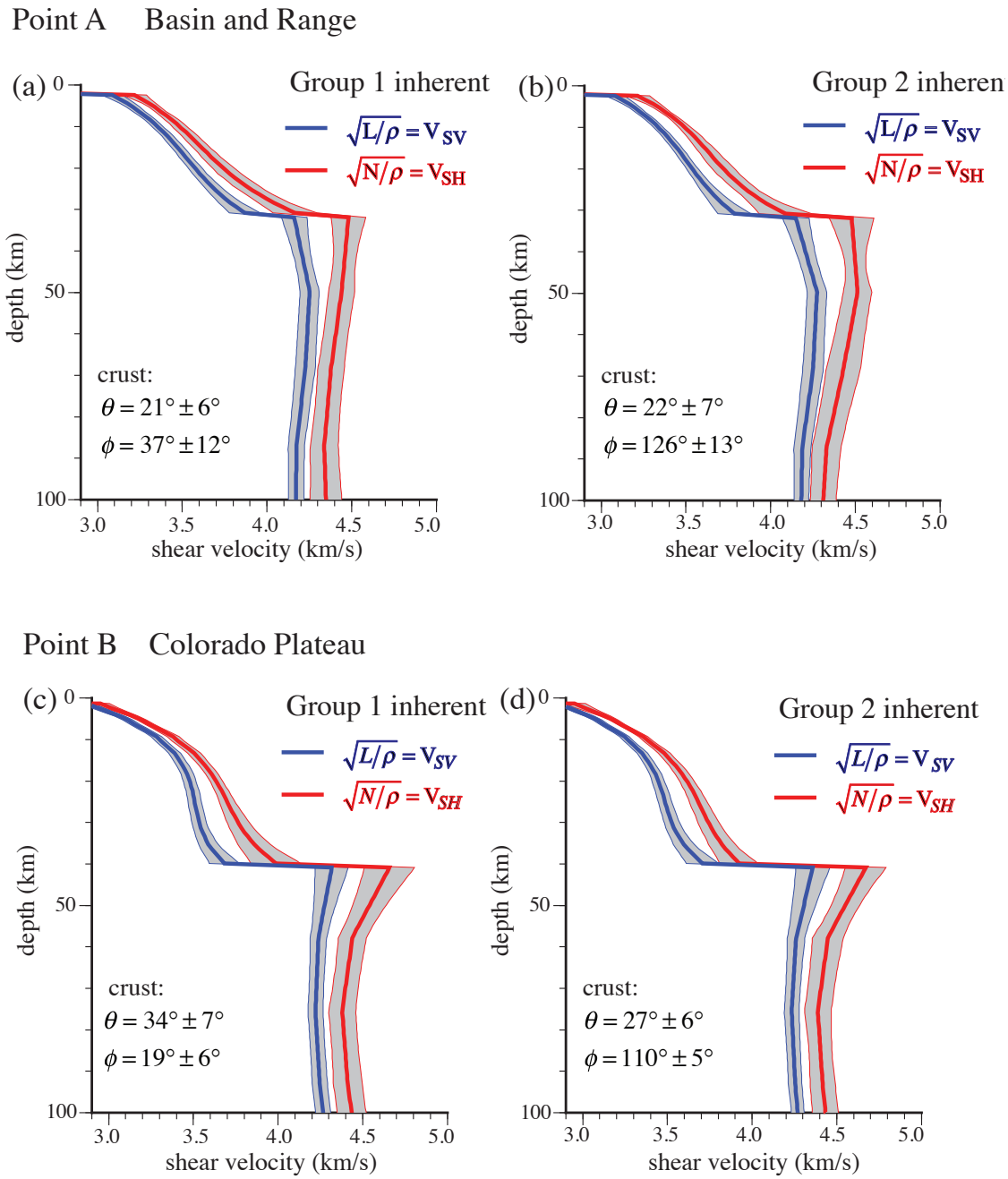

Figure 3.10. (a) Group 1 posterior distribution at Point A showing the inherent Vsv (blue) and Vsh (red), where the one-standard deviation extent of the posterior distribution is shown with the gray corridors and the average of each distribution is plotted with bold solid lines. (b) Same as (a), but for Group 2, Point A. (c) Same as (a), but for Group 1, Point B. (d) Same as (a), but for Group 2, Point B. Points A and B are identified in **Fig. 3.3a**.

in fit are largest for the amplitude of azimuthal anisotropy above 30 sec period where uncertainties in this variable grow. Note that both groups fit the fast azimuth direction of Rayleigh wave azimuthal anisotropy equally well, even though the strikes angles of the crustal anisotropy differ by 90°.

In addition, posterior covariances between model variables at a particular depth or different depths are also determined from the posterior distributions. In practice, we compute posterior correlation matrices in which the elements of the covariance matrix are normalized by the appropriate standard deviation, which normalizes the diagonal elements of the matrix to unity. We use the terms correlation and covariance interchangeably, however.

As an example, the posterior covariance matrix for five variables ($\gamma,\varepsilon,\delta,\theta,\phi$) at 20 km depth is presented in **Figure 3.11a** for a point in the Basin and Range province (point A in **Fig. 3.3a**). Most correlations are relatively weak, γ is negatively correlated with ε and δ, ε and δ are strongly positively correlated with each other in order to keep a relatively constant $\varepsilon-\delta$. Importantly, the dip angle θ has no correlation with other variables except δ. A correlation between these two variables is probably not surprising because δ affects the speed of waves propagating at an angle through the medium (oblique to the symmetry axis) and θ orients the medium.

Similarly, **Figure 3.11b-f** shows the posterior covariance matrix for each model variable with itself at different depths. This is again for point A in the Basin and Range province, where crustal thickness is about 31 km; depths greater than 31 km are in the mantle and shallower depths are in the crust. Most of the correlations in this case are positive. The correlation length (a measure of the rate of decay of the covariance with distance) in the crust is smaller than in the

mantle because the vertical resolution is better. The B-splines in the crust only span from the bottom of the sediments to the Moho (less than 30 km here), whereas in the mantle they span

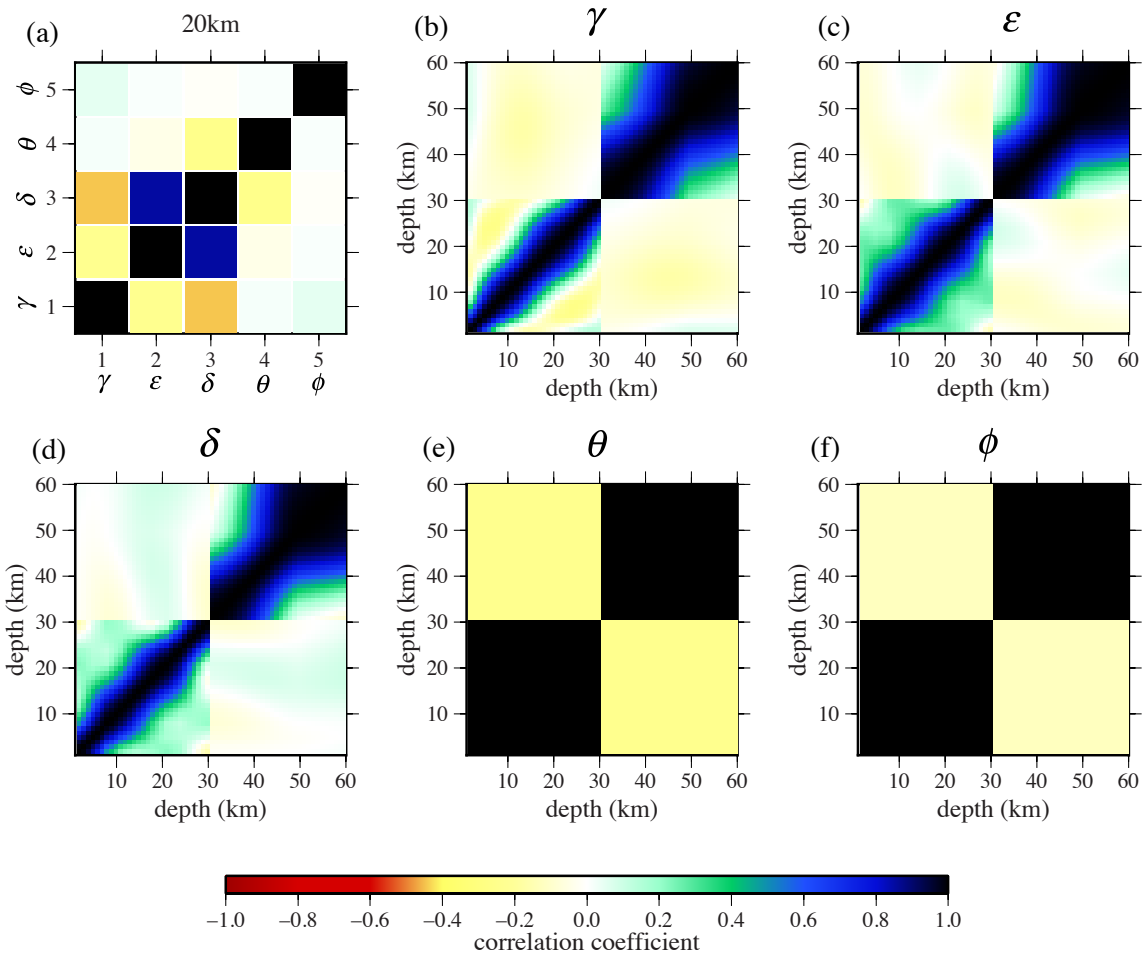

Figure 3.11. Aspects of the correlation (or normalized covariance) matrix observed at Point A. (a) The correlations between several model parameters at 20 km depth. (b) The correlations between γ at different depths. (c-f) Similar to (b), but for four other model parameters: ε, δ, θ, and ϕ. θ is the dip angle, ϕ is the strike angle, and γ, ε, δ are Thomsen parameters that summarize the elastic tensor.

about 170 km. The correlation length for γ is smaller than for ε and δ, indicating a better vertical resolution of γ.

Covariance matrices such as the examples presented here illuminate the implications of the parameterization and constraints imposed in the inversion, but we only interpret this information qualitatively; it is not used formally.

3.6 Results

Love wave phase speed dispersion curves extend only up to 50 sec period and the Rayleigh wave anisotropic dispersion curves also do not extend to very long periods. Thus, constraints on crustal structure are stronger than on the mantle. We have tested variations in mantle parameterizations and constraints, and found that changes affect estimated crustal structure within uncertainties. In the following, therefore, we will concentrate detailed discussion on the crustal part of our model, and will discuss mantle structure principally in a spatially averaged sense. Later work will specifically aim to improve and interpret the mantle model in a spatially resolved sense.

3.6.1 Crustal anisotropy across the western US

The results presented to this point are only for two locations, in the Basin and Range province and the Colorado Plateau (points A and B, **Fig. 3.3a**). We have applied the Bayesian Monte Carlo inversion described above to the US west of 100°W longitude and produced a 3D model of the tilted crustal elastic tensor (with uncertainties) on a 1°x1° grid across the region. The mean and standard deviation of aspects of the posterior distribution averaged across the crystalline crust (from the base of the sediments to Moho) are shown in **Figures 3.12** and **3.13**.

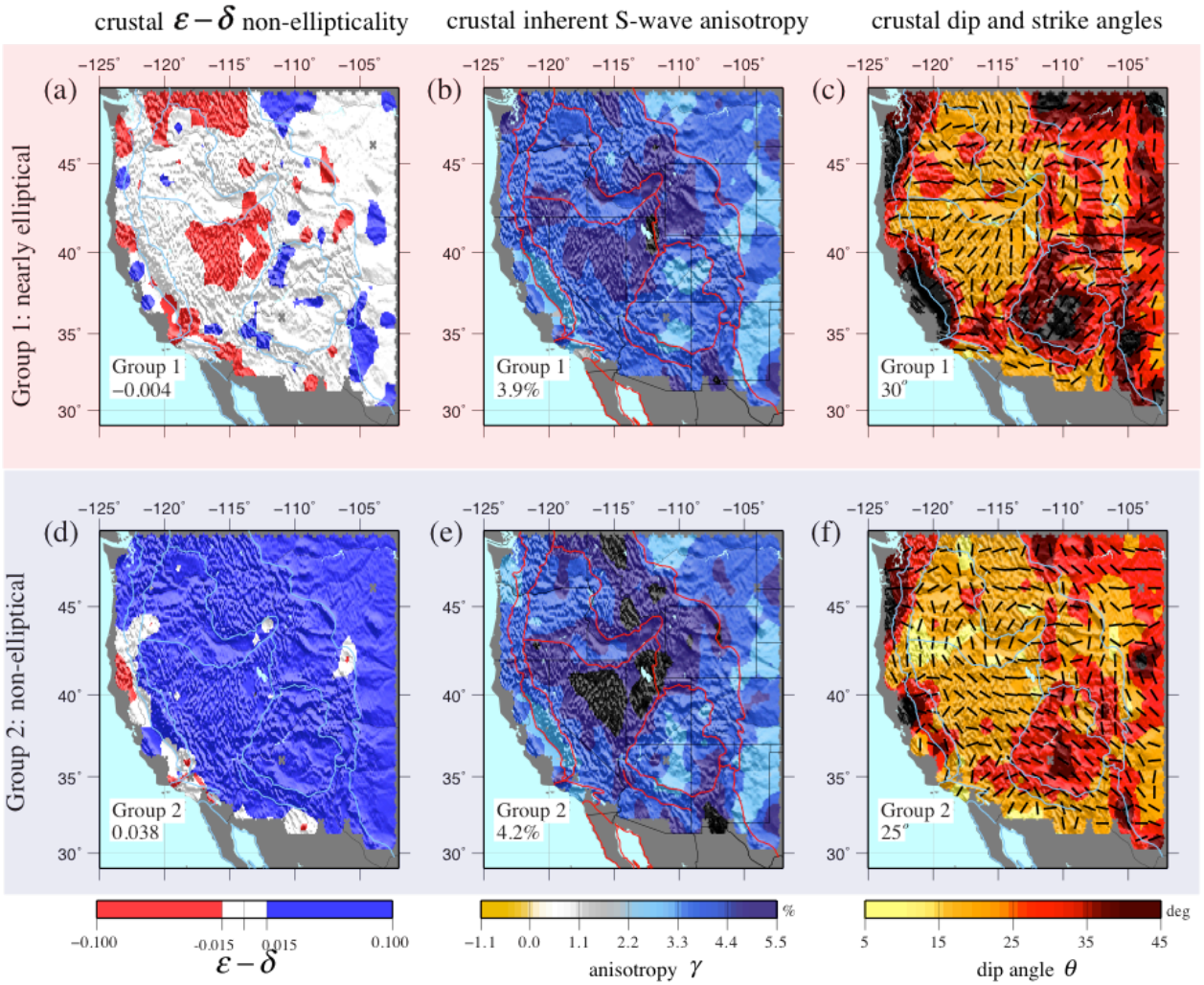

Figure 3.12. Map view of the crustal averaged non-ellipticality of anisotropy ($\varepsilon-\delta$), the crustal averaged inherent S-wave anisotropy (γ), the crustal dip (θ) and strike (ϕ) angles for Group 1 (a-c) and Group 2 (d-f) models. In (c) and (f), dip angles are represented by the background color and strike angle directions are given by the black bars. Average values across each map are inset.

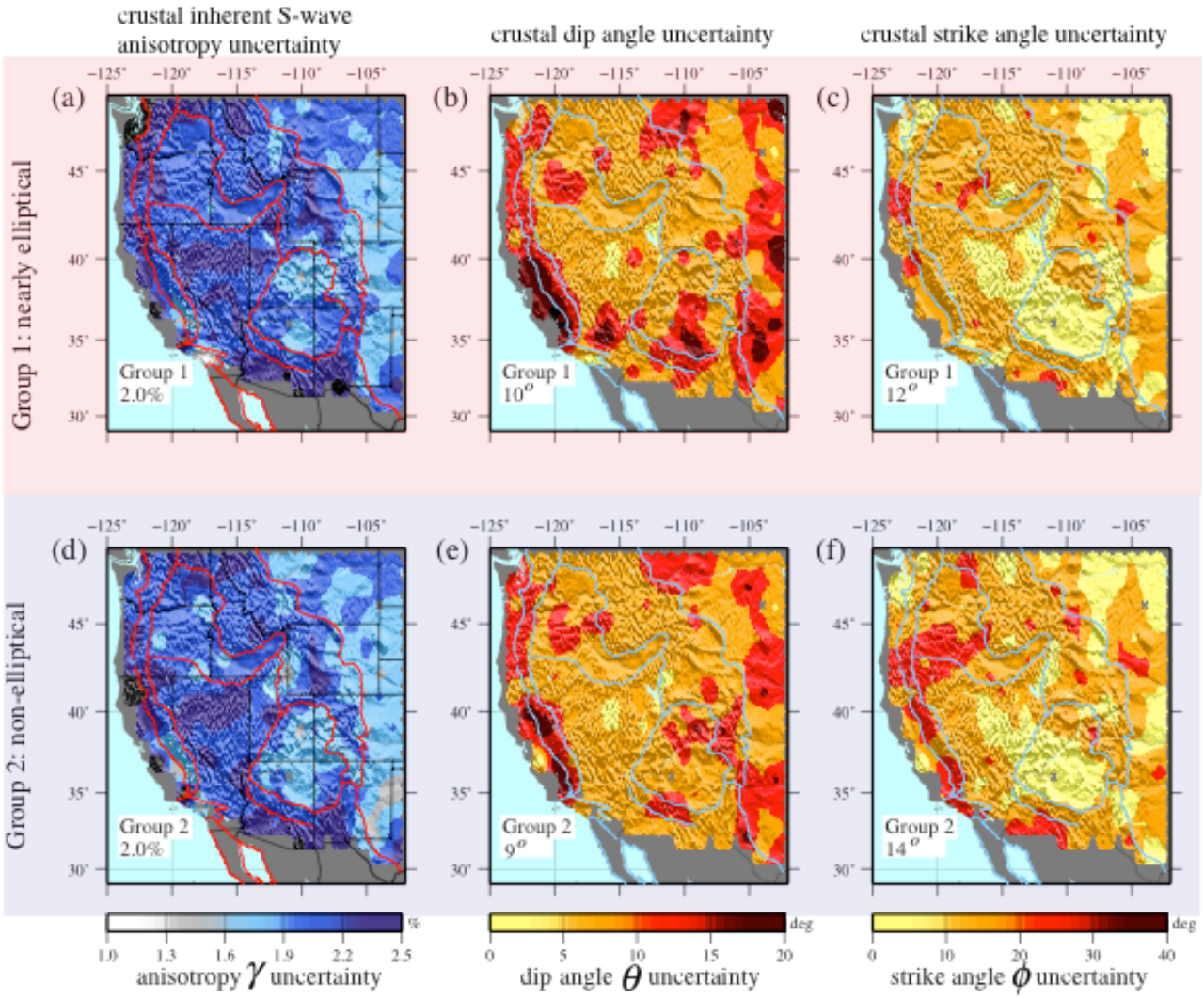

Figure 3.13. Local uncertainties for the model variables shown in **Fig. 3.12**. Average uncertainties across each map are inset.

As discussed above, the posterior distribution bifurcates at each location into two disjoint groups of models based on the strike angle, and we present results in the crust for both groups of models. For Group 1, crustal anisotropy is nearly elliptical meaning that the Thomsen parameters ε and δ, defined in equations (3.4) and (3.6), are nearly identical. **Figure 3.12a** shows that ε – δ is small across the entire western US for Group 1 models. We refer to ε – δ as the "non-ellipticality" parameter because values much larger than zero indicate the deviation from elliptical anisotropy. Group 2 models have more non-elliptical anisotropy as **Figure 3.12d** illustrates, and ε is generally greater than δ so that the non-ellipticality parameter is generally positive. The non-ellipticality parameter is about an order of magnitude larger for Group 2 than Group 1 models.

Although the elastic tensors in the two groups of models differ in the extent to which the anisotropy is non-elliptical, the geographical distribution and the amplitude of inherent S-wave anisotropy, given by the Thomsen parameter γ (eqn. (5)), are similar. This amplitude averages about 3.9% for Group 1 and 4.2% for Group 2 (**Fig. 3.12b,e**). The differences in γ between Groups 1 and 2 are within estimated uncertainties (**Fig. 3.13a,d**), which average about 2% across the region. On average, γ does not vary strongly with depth in the crust, as **Figure 3.14** illustrates. The error bars represent the inherent S-wave anisotropy at crustal depths normalized by local crustal thickness averaged across the study region. γ tends to be somewhat stronger in the shallow (~4%±2%) and deep (~6%±3%) crust than in the middle crust (~3%±2%), but the trend is weak and does not occur everywhere. The amplitude of inherent S-wave anisotropy is everywhere positive (as it is constrained to be), and is fairly homogeneous laterally across the western US. It is, however, largest in the Basin and Range province and smallest in the Colorado

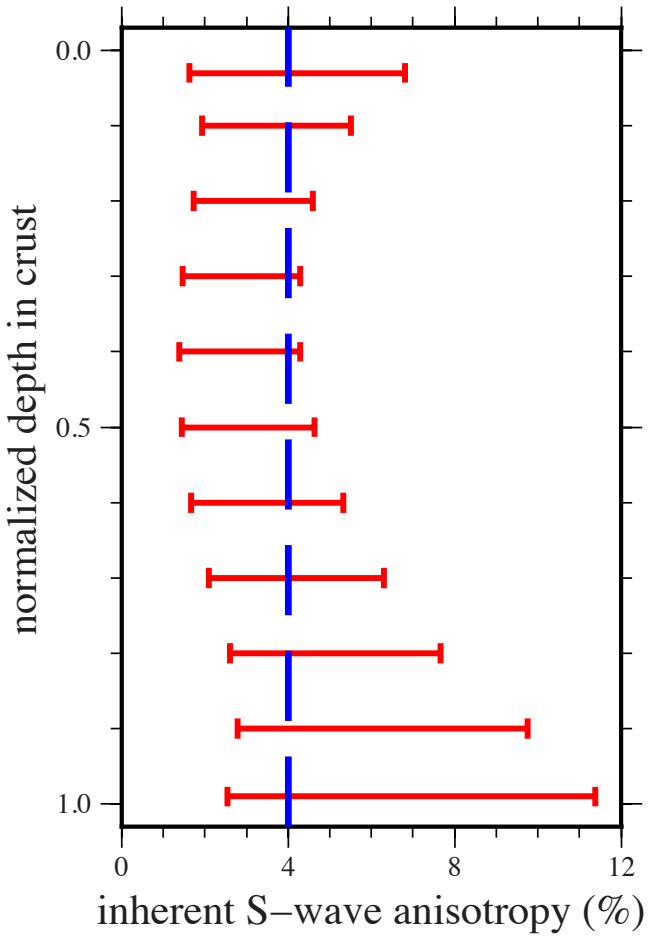

Figure 3.14. The spatially averaged inherent S-wave anisotropy (γ) as a function of depth in the crust, where depth is normalized by local crustal thickness. The middle of the error bar is the average value of γ, in percent, and the half width of the error bar is the spatial average of the one-standard deviation uncertainty. The blue dashed line indicates 4% anisotropy, which is the amplitude of anisotropy averaged over the whole crystalline crust and over the study region.

Plateau and the western Great Plains. The positivity constraint on γ, motivated by elastic tensors measured on crustal rocks, does not have to be relaxed anywhere to fit the data. γ is larger than its uncertainty across nearly the entire western US with the possible exception of some of the peripheral regions where uncertainties grow due to less than ideal data coverage. For this reason, we suggest that γ not be interpreted near the Pacific coast.

Compared with earlier estimates of (apparent) S-wave radial anisotropy across the western US (e.g., *Moschetti et al*., 2010a, 2010b), the amplitude of γ (inherent S-wave anisotropy) does not change as strongly across the region. This discrepancy is correlated with the difference between 'inherent' and 'apparent' anisotropy, and is discussed below in **Section 3.6.5**.

In contrast with γ, the dip angle θ does change appreciably across the study region and the dip and strike angles differ appreciably between the two model groups. Differences between dip angles, shown by varying the background coloration in **Figure 3.12c,f**, are somewhat subtle. The spatially averaged uncertainty in the dip angle across the western US is 9° to 10° for both model groups. The geographical distribution of the variation in dip angle is similar between the two groups of models, but models in Group 2 have dip angles that average about 25° whereas Group 1 models average about 30°. Recall that the dip angle in the elastic tensor is introduced to produce azimuthal anisotropy. Thus, elastic tensors with nearly elliptical anisotropy must be tilted more to fit the azimuthal anisotropy data than tensors with substantially non-elliptical anisotropy. The dip angle in the crust everywhere across the western US is less than about 70° and greater than about 10°, with the majority of the angles falling within the range of 10º and 45º. The Basin and Range province has a shallower dip whereas the Colorado Plateau has a steeper dip, on average.

There is a more prominent difference in strike angle than dip angle between the two groups of models. The strike angle directions for Group 1 and Group 2 models differ by 90°. This is a significant enough observation to warrant its own subsection, and is discussed further in **Sections 3.6.2 and 3.6.3**. Uncertainty in strike angle averages 12°-13° across the study region.

There are also significant differences between the two groups of models in η and the other Thomsen parameters, ε (inherent P-wave anisotropy) and δ. η averages about 0.83 ($\pm$0.08) for Group 1 models and 0.077 ($\pm$0.07) for Group 2. In addition, there are larger values of inherent P-wave anisotropy (ε) in Group 1 (8.1%$\pm$4.8%) than in Group 2 (6.6%$\pm$4.2%). Group 1 models have nearly elliptical anisotropy, so $\delta \approx \varepsilon$. Thus, for Group 1 models, δ is on average larger (8.5% $\pm$ 6.7%) than for Group 2 models (2.8% $\pm$ 5.3%). For Group 2 models $\delta \ll \varepsilon$, on average.

3.6.2 On the cause of the bifurcation in strike angle of crustal anisotropy

The fact that two groups of solutions with orthogonal strike angles both fit the crustal sensitive Rayleigh wave data may be explained in terms of the phase speed surface produced by different elastic tensors. The phase speed surface can be computed by solving the Christoffel equation. For waves traveling in any direction, there are always three mutually orthogonal wave solutions, one (quasi-) P wave and two (quasi-) S waves. Normally, the S wave with faster speed is called S_1, and the slower one is called S_2. Note that S_1 and S_2 should not be associated with SV or SH waves, because S_1 and S_2 are defined based on the wave speed instead of the polarization direction. The discussion below only aims to provide a qualitative understanding of the bifurcation. For more insight, more sophisticated forward computations would be required, which is beyond the scope of this paper.

Figure 3.15 shows the phase speed surface of P, S_1, and S_2 waves, together with the polarization direction of the S wave for two tilted elastic tensors with hexagonal symmetry, one is elliptical with a dip angle of 20° and strike angle of 210°, the other is non-elliptical with dip angle 20° and a strike angle 300°. Each surface plots a particular speed (Vs_1, Vs_2, P) for waves propagating in different directions. Each panel is a lower hemisphere plot so that horizontally propagating waves (surface waves) are sensitive to wave speeds at the edge of the diagram. These two tensors represent our Group 1 and Group 2 models that have different ellipticality of anisotropy and orthogonal strike angles. The most prominent feature of the non-elliptical tensor is that the polarization direction of the S1 wave suddenly changes from radial to tangential at some degree oblique to the symmetry axis. A Rayleigh wave that is propagating horizontally in a hexagonally symmetric medium with a shallow to moderate dip is mainly sensitive to the phase speed of the S_2 wave (Vs_2). In the following paragraphs, therefore, we will concentrate discussion on the speed Vs_2. We will demonstrate that the two groups of elastic tensors produce the same azimuthal pattern in wave speed Vs_2 even though their strikes angles differ by 90°.

In an elliptical hexagonally symmetric anisotropic medium (Group 1), the Vs_2 surface has its minimum value oblique to the symmetry axis. In a non-elliptical hexagonal material, the pattern of the Vs_2 surface is reversed: Vs_2 has its maximum value oblique to the symmetry axis. Because horizontally propagating Rayleigh waves only sample the outer margin of the wave speed surface, we plot the value of Vs_2 at the edge of the surface as a function of azimuth (**Fig. 3.16a**). We find that despite the orthogonal strike directions, the two groups of models produce similar azimuthal patterns of Vs_2, with the same fast axis directions. Group 1 models have their Vs_2 fast axis direction parallel to the strike angle of the elastic tensor, whereas Group 2 models have their fast axis directions orthogonal to the strike. This phenomenon results in the same fast

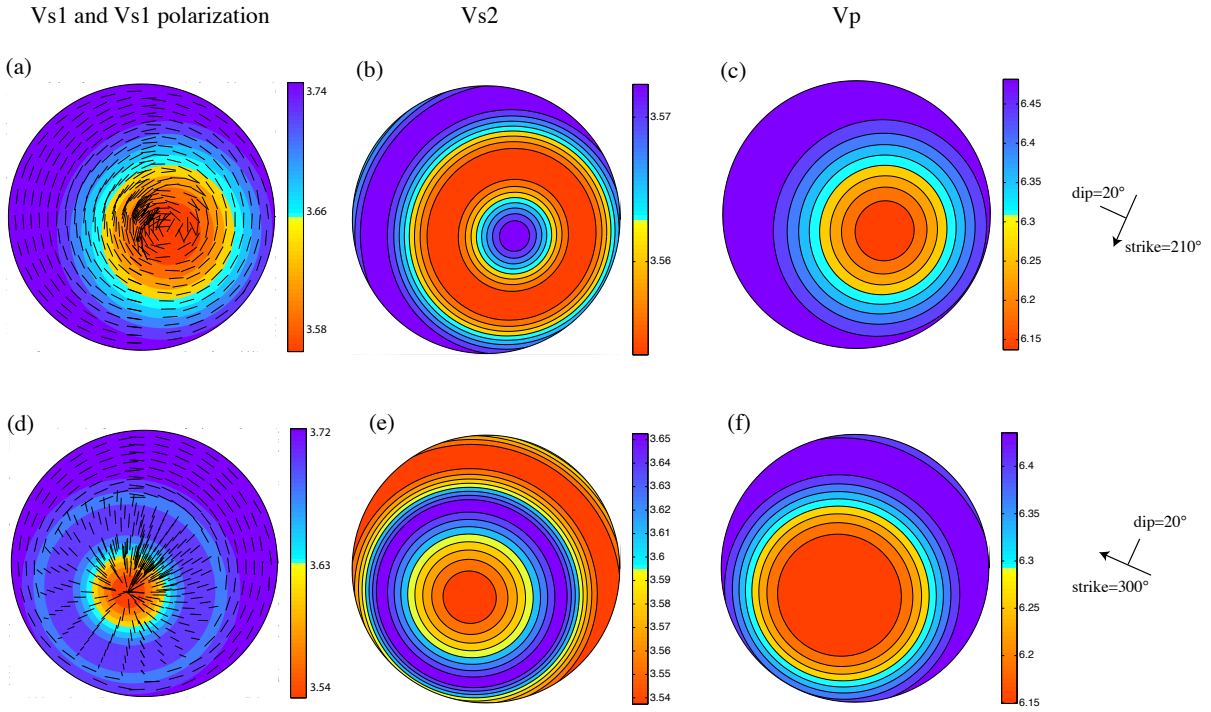

Figure 3.15. Phase velocity surfaces of Vs1, Vs2, and Vp for two elastic tensors with hexagonal symmetry: one is elliptical (a-c, represents a Group 1 model) and the other one is non-elliptical (d-f, represents a Group 2 model). Vs1 polarizations are indicated in (a) and (c) where the black bars are the projection of the Vs1 vector onto the plane of stereonet. The orientations of the two elastic tensor groups are shown at the right hand side of the figure.

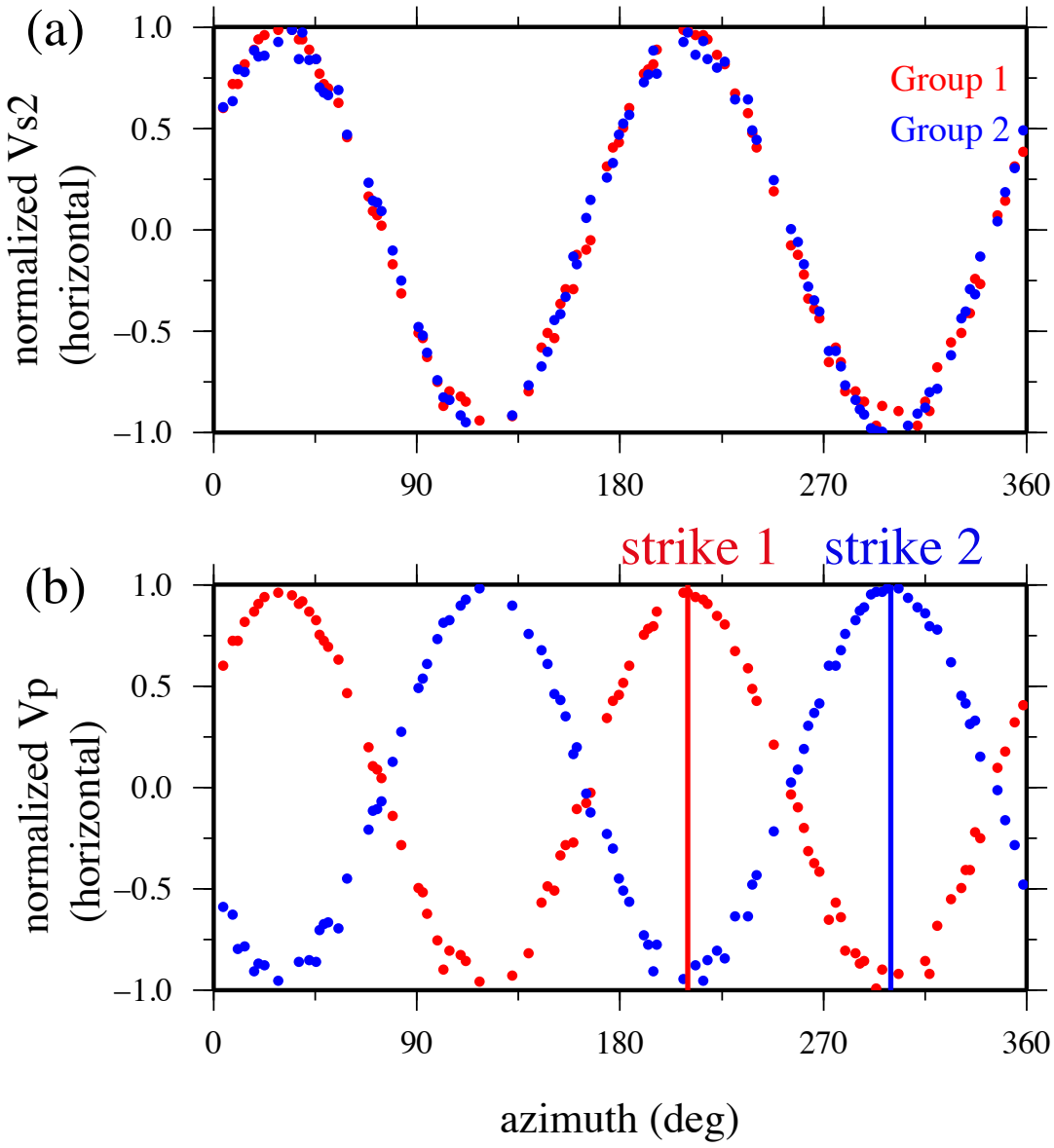

Figure 3.16. Azimuthal velocity variations of the horizontally propagating (a) S_2 wave and (b) P wave where all the velocities are normalized. The red and blue dots represent the velocities computed from the elastic tensor of Group 1 and Group 2, respectively (the velocities at the edge of **Fig. 3.15b, d**). The vertical lines in (b) indicate the strike direction, red for Group 1 and blue for Group 2.

direction for the Rayleigh waves, even when the orientation of the inherent elastic tensor is different. These results highlight the fact that the fast direction of Rayleigh wave is not necessarily parallel to the strike of anisotropy, but depends on a property of the medium, whether the anisotropy is elliptical or not. This phenomenon is similar to what Song and Kawakatsu (2012) found for shear-wave splitting.

In contrast with the propagation of S_2 waves, however, a horizontally propagating P wave is always fastest parallel to the strike of a dipping hexagonally symmetric elastic tensor (**Fig. 3.16b**). Therefore, a P wave's fast direction always indicates the strike direction.

In conclusion, for both groups of models the Rayleigh wave fast axis direction is the same even though the strike of the anisotropy differs by 90°. However, the P wave fast directions in the two groups will be orthogonal to each other, consistent with a 90˚ rotation of the strike. Therefore, observations of P wave anisotropy provide unambiguous information about the orientation of the strike angle of anisotropy, but Rayleigh wave travel times do not. In addition, observations from waves with near-vertical incidence angles, such as receiver functions (e.g., *Levin and Park*, 1997; *Savage*, 1998; *Bianchi et al*., 2008, 2010; *Liu and Niu*, 2012; *Schulte-Pelkum and Mahan*, 2014a, 2014b), may also provide unambiguous information about the orientation of the strike angle of anisotropy.

3.6.3 The strike angle of crustal anisotropy and the Rayleigh wave fast axis direction

As discussed in **Section 3.5** and earlier in this section, the posterior distribution divides into two disjoint groups of crustal models according to the estimated strike angle (ϕ) of anisotropy, which is defined in **Figure 3.1a**. The physical cause of this bifurcation is discussed in **Section 3.6.2**. Thus, at each spatial grid point there are two distinct distributions of elastic

tensors and orientations (or tilts) that fit the Rayleigh wave azimuthal anisotropy observations approximately equally well. For Group 1, the set of models with approximately elliptical anisotropy ($\varepsilon \approx \delta$) and typically larger value of η, the distribution of strike angles is shown in **Figure 3.12c**. These strike angles are very similar to the Rayleigh wave fast axis directions for waves that sample the crust (e.g., 10-20 sec period, **Fig 3.4a**). **Figure 3.17** illustrates this fact by plotting as blue dots the 16 sec period Rayleigh wave fast axis directions against the Group 1 strike angles (ϕ_1) at each location . The mean and standard deviation of the difference are 0.2° and 21.0°, respectively. The geographical distribution of the strike angles (and fast axis directions for crustal sensitive Rayleigh waves) are similar to those found by *Lin et al*. (2011), who discuss the geological coherence of the observations, so we forgo this discussion here.

The second group of models, Group 2, possesses strike angles that are distinct from Group 1, ε is typically significantly larger than δ, so the anisotropy is decidedly non-elliptical, and η is usually smaller than 0.8. As **Figure 3.17** also shows with red symbols, the strike angles of Group 2 (ϕ_2) are, on average, perpendicular to the strike angles of Group 1 (ϕ_1) such that the average angular difference and standard deviation are 90.2° and 8.8°, respectively. This distribution is tighter than the comparison with Rayleigh wave fast axis directions because Rayleigh wave fast axes at a particular period are measurements and are, therefore, noisy.

In summary, Rayleigh wave fast axis directions are ambiguously related to the strike of inherent crustal anisotropy. In fact, the fast axis direction will only parallel the strike direction if the crustal anisotropy is largely elliptical in nature. As petrological information has grown concerning the seismic anisotropy in the crust, evidence has mounted that crustal anisotropy is probably not strongly elliptical (e.g., *Tatham et al., 2008; Brownlee et al*., 2011; *Erdman et al.,* 2013). Thus, the geologically favored models are probably from Group 2. Therefore, crustal

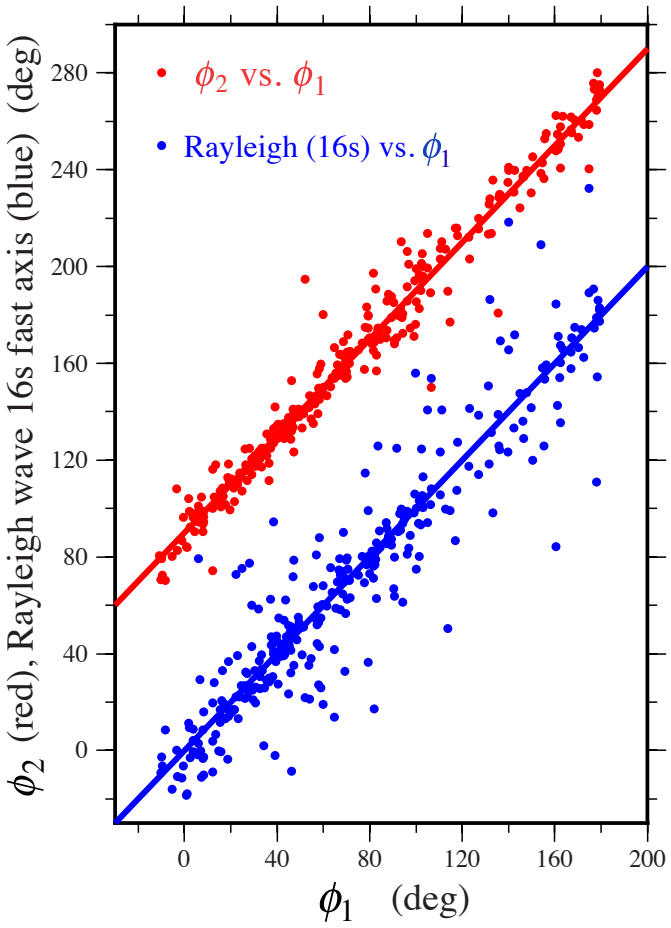

Figure 3.17. (Red dots) Comparison between the Group 2 strike angle (ϕ_2) and the Group 1 strike angle (ϕ_1) across the study region, where the red line represents $y=x+90°$. The strike angles in the two groups are approximately orthogonal. (Blue dots) Comparison between the fast azimuth of the Rayleigh wave at 16 sec period to the Group 1 strike angle, where the blue line represents $y=x$. Crustal sensitive Rayleigh wave fast axis directions are approximately parallel to Group 1 strike directions and perpendicular to Group 2 strike directions.

sensitive Rayleigh waves must only be used with caution to reveal the orientation of the geological features that are causing the anisotropy. It is probably more likely for the fast axis direction of crustal sensitive Rayleigh waves to point perpendicular to the strike direction than parallel to it. Similarly, assuming nearly-vertical shear waves, crustal shear wave splitting will have its fast axis in the direction of the Rayleigh-wave fast axis. Therefore, the fast splitting direction of crustal SKS is also more likely to point perpendicular to the strike direction than parallel to it.

To recover unambiguous information about the strike angle, other types of data need to be introduced. As discussed in **Section 3.6.2**, observations of crustal P wave anisotropy can resolve the ambiguity because the P wave fast direction is always parallel to the strike direction as can observations of anisotropy using receiver functions. Admittedly, however, these are difficult observation to make.

3.6.4 On the interpretation of the inferred dip angle

There are two alternative interpretations of the inferred dip angle, θ: that it is a measurement of the actual geometry of the foliation plane of material composing the crust or that it is a proxy for another potentially unknown non-geometric variable. We will first discuss the latter alternative.

First, it is possible that the observed dip angle is proxy for other variables. Even though our models are expressed in terms of a tilted hexagonally symmetric medium, crustal anisotropy may not actually be hexagonally symmetric, or the approximation to hexagonal symmetry may not be accurate everywhere. Crustal anisotropy may indeed possess lower order symmetry than hexagonal. Tilting a material can have the effect of decreasing the apparent symmetry of the material if viewed in the same coordinate system (*Okaya and McEvilly*, 2003). In principle,

therefore, a lower order of symmetry could be approximated by a higher order of symmetry (e.g., hexagonally symmetric) through tilting. It is possible that the efficacy of this approximation is enhanced by the fact that surface wave travel time data are insensitive to 8 of the 21 moduli that constitute a general elastic tensor (Appendix). It is conceivable, therefore, that the effect on our data that we interpret as a tilt (non-zero dip angle) could have resulted from the non-hexagonal component of the actual elastic tensor of the medium. What we would estimate in this case is an "apparent dip angle" that is proxy for the extent to which the medium deviates from hexagonal symmetry.

We have experimented with numerically fitting tilted hexagonally symmetric elastic tensors to nearly orthorhombic tensors from crustal rock samples (*Tatham et al., 2008; Brownlee et al*., 2011; *Erdman et al*., 2013) using only the 11 combinations to which observations of the 2ψ component of Rayleigh wave and the azimuthally isotropic Rayleigh and Love wave data are sensitive (Appendix). We estimate an apparent dip angle that measures the medium's deviation from hexagonal symmetry. Apparent dip angles resulting from this fit typically range between 15˚ to 25˚. The dip angles that we infer, therefore, may be a result of approximating orthorhombic or other lower-symmetry material with hexagonally symmetric tensors, in which case steeper dip angles would reflect a greater deviation from hexagonal symmetry.

Second, there is also likely to be at least some component of the inferred crustal elastic tensors related to the actual dip of the foliation of the material. In fact, variations in observed dip angles make geologic sense in some regions. For example, observed dips are shallow beneath the Basin and Range province, which is consistent with large-scale crustal extension along low-angle normal faults and horizontal detachment faults (e.g. *Xiao et al*. 1991; *Johnson and Loy*, 1992; *John and Foster*, 1993; *Malavieille* 1993). The steeper dip angles observed in California are also

consistent with a lower crust consisting of foliated Pelona-Orocopia-Rand schist (e.g. *Jacobson* 1983; *Jacobson et al*. 2007; *Chapman et al*. 2010), which was under-plated during Laramide flat-slab subduction (e.g. *Jacobson et al*., 2007). In other regions, such as beneath the Colorado Plateau, the potential geologic meaning of the steeper observed dip angles is less clear; perhaps the steeper dips are an indication of a change in crustal composition resulting in an elastic tensor with low symmetry.

3.6.5 Comparison with previous studies: Inherent versus apparent anisotropy

A tilted hexagonally symmetric elastic tensor will generate both apparent radial and azimuthal anisotropy in surface waves as demonstrated by **Figure 3.1b**. At a given depth, referencing the notation in the Appendix, we define apparent S-wave radial anisotropy as:

$$\hat{\gamma} = (\hat{N} - \hat{L})/2\hat{L} \tag{3.9}$$

where

$$\widehat{N} = (C_{11} + C_{22})/8 - C_{12}/4 + C_{66}/2 \qquad \hat{L} = (C_{44} + C_{55})/2 \tag{3.10}$$

We also define the amplitude of apparent SV-wave azimuthal anisotropy as:

$$|G|/L = \sqrt{G_c^2 + G_s^2}/L \tag{3.11}$$

where

$$G_c = (\delta C_{55} - \delta C_{44})/2 = (C_{55} - C_{44})/2 \tag{3.12}$$

$$G_s = \delta C_{45} = C_{45} \tag{3.13}$$

The components of the modulus matrix, $C_{\alpha\beta}$, are functions of the inherent elastic moduli (A,C,N,L,F) and tilt (θ,ϕ). The strength of inherent S-wave anisotropy is defined by equation (3.5).

As shown in **Figure 3.1b**, when the inherent elastic moduli (A,C,N,L,F) are fixed, variations in dip angle θ produce the variations in the apparent anisotropies. The amplitudes of apparent anisotropies are always smaller than the inherent anisotropy except for two extreme cases, $\theta = 0°$ and $\theta = 90°$. Thus, if earth structure has $\theta \in (0°,90°)$, then neither apparent radial nor apparent azimuthal anisotropy will reflect the real strength of anisotropy (inherent anisotropy) in the earth.

In studies of anisotropy based either on isotropic dispersion curves or azimuthally anisotropic dispersion curves alone, it is the apparent anisotropy instead of the inherent anisotropy that is estimated. For example, in studies of radial anisotropy using surface waves (e.g., *Moschetti et al*., 2010a, 2010b; *Xie et al*., 2013), only the azimuthally isotropic Rayleigh and Love wave dispersion curves are used to produce a transversely isotropic model, which produces no azimuthal anisotropy. Because the azimuthally isotropic dispersion curves are only sensitive to the effective transversely isotropic part of the elastic tensor ($\hat{A},\hat{C},\hat{N},\hat{L},\hat{F}$, Appendix), this transversely isotropic model is the effective transversely isotropic (ETI) part of our model. To prove this, we compute the ETI part of our model, from which the apparent S-wave radial anisotropy can be generated (**Fig. 3.18**). The apparent S-wave radial anisotropy for both Group 1 and Group 2 models are very similar to each other, they both change appreciably across the study region, with large amplitudes in the Basin and Range province and small amplitudes in the Colorado Plateau. This pattern is very similar to that observed by *Moschetti et*

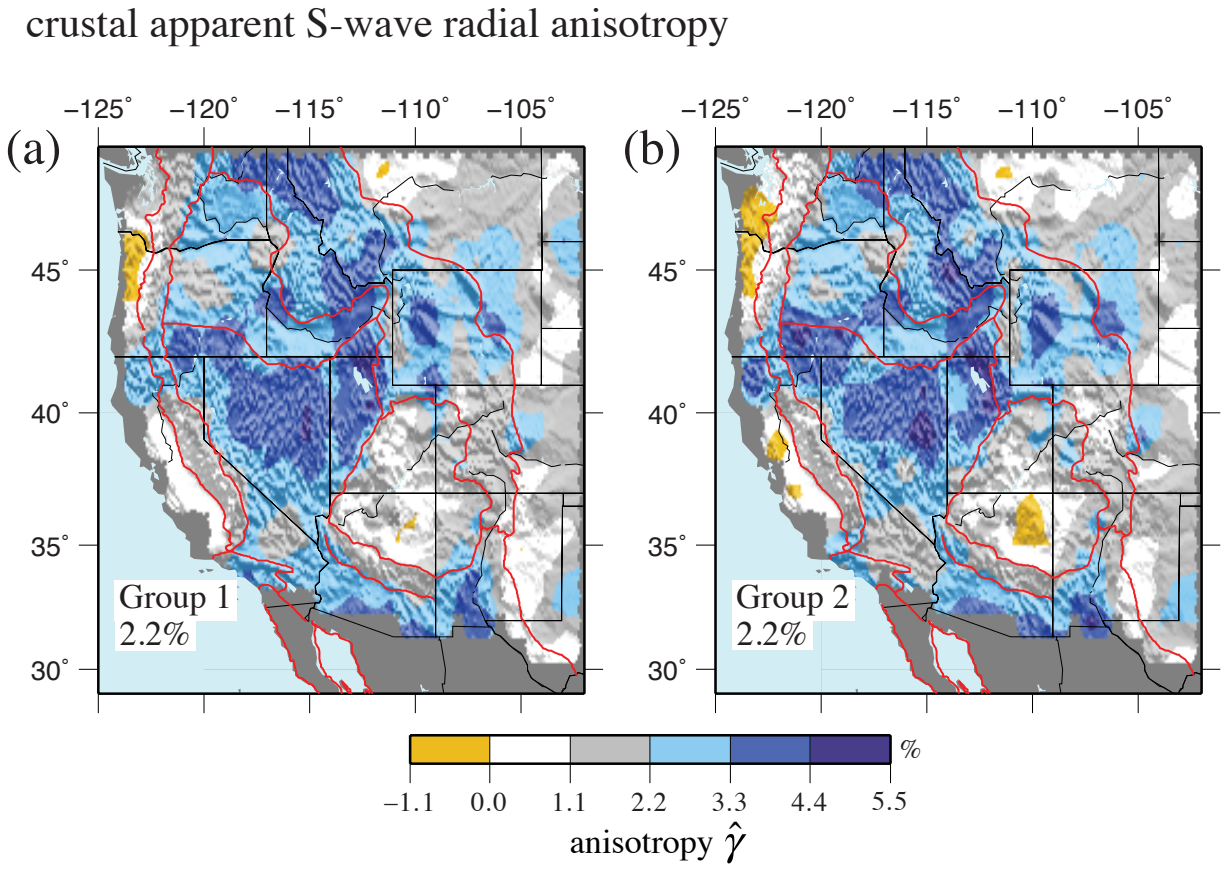

Figure 3.18. The mean of the posterior distribution of apparent S-wave radial anisotropy, $\hat{\gamma}$, averaged vertically across the crust for (a) Group 1 models and (b) Group 2 models. Average values across the crust and region of study are inset.

al. (2010b), and thus demonstrates that inversion with isotropic dispersion curves alone results in observations of apparent S-wave radial anisotropy, $\hat{\gamma}$. Similarly, inversion with azimuthally anisotropic dispersion curves alone results in apparent quasi-SV-wave azimuthal anisotropy (e.g., *Lin et al*., 2010).

The apparent radial and apparent azimuthal anisotropy reflect different aspects of the inherent elastic tensor and both mix information from the inherent elastic moduli and the orientation. As described in **Section 3.6.1**, the amplitude of $\hat{\gamma}$, the inherent S-wave anisotropy, does not change strongly across the region, and averages about 4%. In contrast, the amplitude of $\hat{\gamma}$, the apparent radial anisotropy, changes strongly across the region in a pattern similar to the variation of the dip angle θ , and averages to about 2%. Thus, the lateral variation of $\hat{\gamma}$ results mainly from the variation of θ , and does not reflect the strength of γ.

In most surface wave studies, only the apparent anisotropies are estimated. Therefore, the results depend on the unknown orientation of the medium (or the non-hexagonality of medium for which the dip angle may be a proxy), which limits their usefulness to constrain the elastic properties of the medium (e.g., the inherent S-wave anisotropy, γ).

3.6.6 Mantle anisotropy across the western US

Although the focus of this paper is on crustal anisotropy we present here a brief discussion of the mantle anisotropy that emerges from the inversion. **Figure 3.19** shows the prior and posterior distributions at 60 km depth at point A in the Basin and Range province. At this point, the mean of the posterior distribution is between 4-5% for both inherent S-wave (γ) and P-wave (ε) anisotropy, both the dip and strike angles are fairly well resolved with a mean dip angle of 27° (±7°) and strike angle of 66° (±8°), the mean of the posterior distribution for η is 0.96

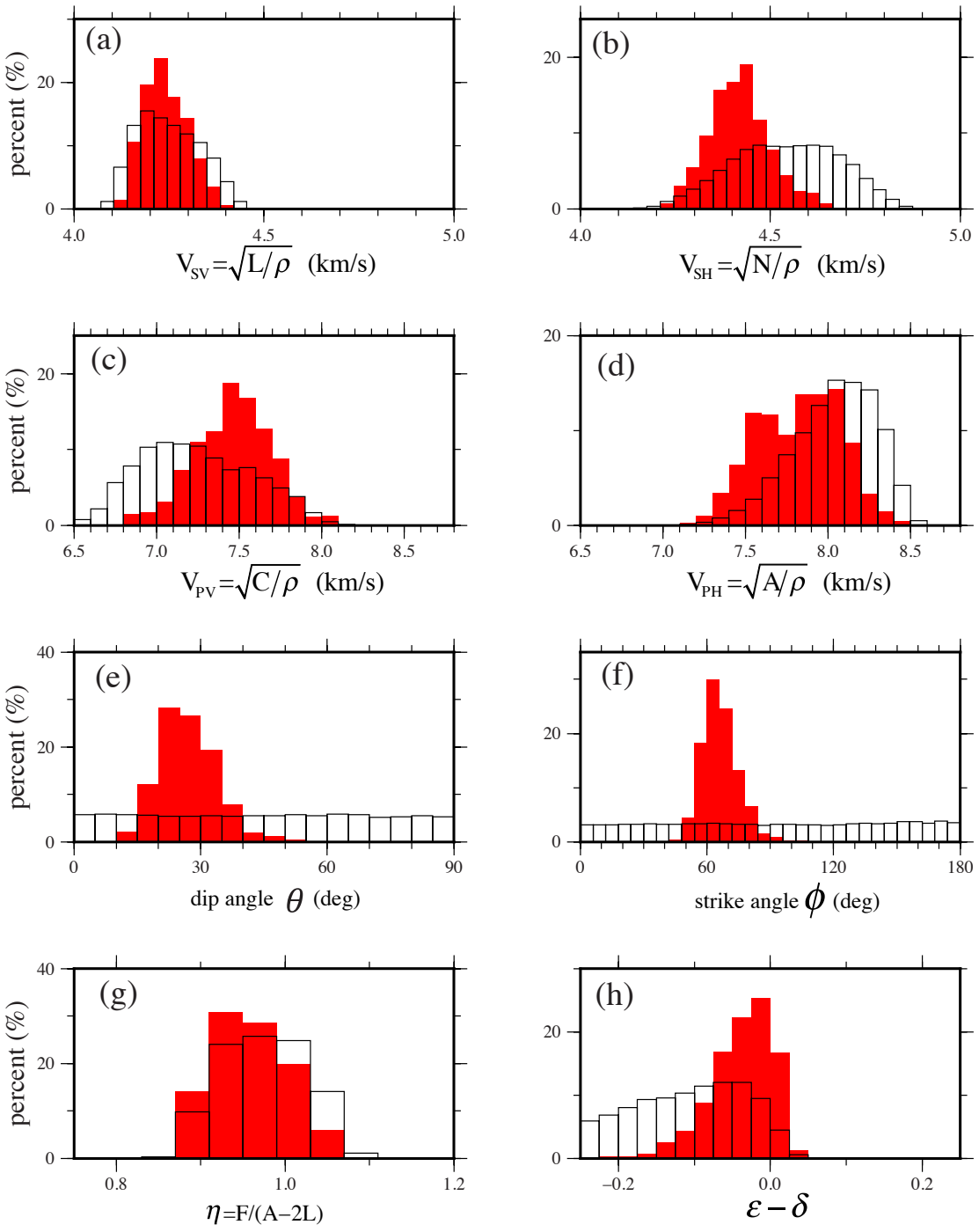

Figure 3.19. Prior and posterior distributions for several model parameters in the mantle at 60 km depth for Point A (in Basin and Range, identified in **Fig. 3.3a**). Similar to **Fig. 3.8**, white histograms indicate the prior distributions and red histograms represent the posterior distributions. Posterior distributions in the mantle are not bimodal as they are in the crust.

(±0.04) which is much higher than in the crust, and the anisotropy is indistinguishable from elliptical (ε-δ = -0.04 ± 0.06). The nearly elliptical nature of mantle anisotropy is also quite different from what we observe in the crust. This location is fairly typical of mantle anisotropy across the western US, as γ averages 4.4% (±2.6%) across the western US with an average dip angle of 21° (±8°). We note in passing that such a steep dip angle may result from a strong orthorhombic component to the mantle elastic tensors and may not result from the actual tilt of the medium. Because, unlike the crust, the posterior distribution in the mantle does not bifurcate according to strike angle, Rayleigh wave fast axis directions are unambiguously related to the strike angle in the mantle. Because mantle anisotropy is nearly elliptical (with η close to one), Rayleigh wave fast axes actually align with the strike angle rather than orthogonal to it. However, mantle strike angle is not everywhere well determined across the region as the average uncertainty is nearly 30°. The inability to resolve mantle strike angle unambiguously across the region with the current data set and method is one of the reasons we focus interpretation on crustal anisotropy here and we plan to return to mantle anisotropy in a later contribution.

3.7 Summary and Conclusions

The motivation for this paper is to present a method of inversion that explains surface wave observations of both radial and azimuthal anisotropy, which are seldom explained simultaneously. The method we present here inverts for the inherent properties of the medium represented by a hexagonally symmetric elastic tensor, with an arbitrarily oriented symmetry axis, which we refer to as "tilted". The elastic tensor itself at each depth is given by five elastic moduli (A, C, N, L, and F or η) and the tilt is defined by two rotation angles: the dip and strike, which are illustrated in **Figure 3.1a**. We refer to these moduli as "inherent", as they reflect the characteristics of the elastic tensor irrespective of its orientation.

We show that observations of radial anisotropy and the 2ψ component of azimuthal anisotropy for Rayleigh waves obtained using USArray in the western US can be fit well by tilted hexagonally symmetric elastic tensors in the crust and mantle, subject to the constraints listed in the text. The inversion that we apply is a Bayesian Monte Carlo method, which yields a posterior distribution that reflects both the data and prior constraints. The most noteworthy constraint is that the tilt angles (dip, strike) are constant in the crust and mantle, but may differ between the crust and mantle. The results are summarized as posterior distributions of smoothly depth-varying inherent (unrotated) moduli (A or V_{PH}, C or V_{PV}, N or V_{SH}, L or V_{SV}, and F or η) as well as dip and strike angles. The standard deviation of the posterior distribution defines the uncertainties in these quantities. Anisotropy can be summarized with the Thomsen parameters, inherent S-wave anisotropy (γ) and inherent P-wave anisotropy (ε), and either η or δ (which is the third Thomsen parameter).

Because the crust is constrained by the data better than the mantle and γ (inherent S-wave anisotropy) is determined more tightly than ε (inherent P-wave anisotropy), we focus interpretation on γ in the crust as well as the tilt angles. Major results include the following. (1) γ is fairly homogeneous vertically across the crust, on average, and spatially across the western US. (2) Averaging over the region of study and in depth, γ in the crust is approximately 4%±2%. (3) Crustal strike angles (ϕ) in the posterior distributions bifurcate into two sets of models that we refer to as Groups 1 and 2. Models in Group 1 have strike angles that approximately parallel crust-sensitive Rayleigh wave fast axis directions, and typically have larger values of η and nearly elliptical anisotropy (ε ≈ δ). Group 2 models have strike angles that are approximately orthogonal to crust-sensitive Rayleigh wave fast directions, smaller values of η, and more strongly non-elliptical anisotropy where typically ε > δ. Mantle strike angles do not bifurcate as

they do in the crust because of tighter constraints imposed on η in the inversion. (4) γ in the crust is approximately the same in the two groups of models. (5) Dip angles in the two groups of models vary spatially in similar ways and display geological coherence; for example, they are smaller in the Basin and Range province than in the Colorado Plateau or the Great Plains. However, in Group 1 they are slightly larger than in Group 2, averaging 30°±10° in Group 1 and 25°±9° in Group 2. (6) Rayleigh wave fast axis directions are ambiguously related to the strike of anisotropy, but recent studies of the anisotropy of crustal rocks (e.g., *Tatham et al., 2008; Brownlee et al*., 2011; *Erdman et al*., 2013) imply that the crustal anisotropy is probably not nearly elliptical, which favors Group 2 models. Therefore, under the assumption that crustal anisotropy is approximately hexagonally symmetric with an arbitrary tilt, Rayleigh wave fast axis directions for crustal sensitive Rayleigh waves will be oriented orthogonal rather than parallel to the strike of anisotropy. Interpretation of Rayleigh wave fast axis directions in terms of crustal structure must be performed with caution. (7) The estimated dip angle may be interpreted in two alternative ways. It is either an actual measure of the dip of the foliation plane of anisotropic material within the crust, or it is proxy for another non-geometric variable, most likely a measure of the deviation from hexagonal symmetry of the medium. (8) By attempting to estimate the inherent moduli that compose the elastic tensor of the crust (and mantle), our approach differs from earlier studies that produce measurements of "apparent" moduli. Because tilting a medium produces apparent radial and apparent azimuthal anisotropies that are both smaller than the inherent anisotropy in amplitude, previous studies have tended to underestimate the strength of anisotropy.

In the future, we intend to improve long period data in order to produce improved results for the mantle and apply the method more generally to observations of surface wave anisotropy

in the US and elsewhere. It will also be desirable to apply increasingly strong constraints on allowed anisotropy and continue to revise the interpretation of results as more information accrues about crustal anisotropy from laboratory measurements on crustal rocks. In particular, it may make sense to experiment with more general theoretical models of anisotropy in the inversion, perhaps by considering a mixture of elastic tensors with hexagonal and orthorhombic symmetry. Ultimately, we aim to interpret the results in terms of petrological models that agree with the inferred elastic tensor.

Appendix for Chapter III. The Forward Problem: Computation of period and azimuthally variable phase speeds for an arbitrarily oriented hexagonally symmetric elastic tensor

Given an elastic tensor that varies with depth at a given location, we seek to compute how Rayleigh and Love wave phase velocities change with period T and azimuth ψ. The code MINEOS (*Masters et al.,* 2007) computes period dependent Rayleigh and Love wave phase speeds at high accuracy for a transversely isotropic medium; i.e., a medium with hexagonal symmetry and a vertical symmetry axis. Instead, we are interested in a medium whose elastic properties are given by an elastic tensor for a hexagonally symmetric medium with an arbitrarily oriented symmetry axis.

First, let the moduli A, C, N, L, and F represent the elastic tensor at a particular depth for a hexagonally symmetric medium with a vertical symmetry axis, given by Equation (3.1) in the Introduction. Four of the five moduli are directly related to P and S wave speeds for waves propagating perpendicular or parallel to the symmetry axis using the following relationships: $A = \rho V_{PH}^2$, $C = \rho V_{PV}^2$, $L = \rho V_{SV}^2$, $N = \rho V_{SH}^2$. Here, ρ is density, V_{PH} and V_{PV} are the speeds of P waves propagating horizontally and vertically respectively, V_{SV} is the speed of the S wave propagating horizontally and polarized vertically or propagating vertically and polarized horizontally, and V_{SH} is the speed of the S wave that is propagating in a horizontal direction and polarized horizontally. The modulus $F = \eta(A - 2L)$ affects the speed of waves propagating oblique to the symmetry axis and controls the shape of the shear wave phase speed surface (*Okaya and Christensen*, 2002). For an isotropic medium, $A = C$, $L = N$, $F = A - 2L$, $\eta = 1$.

Next, rotate the tensor in Equation (3.1) through the two angles, θ (the dip angle) and ϕ (the strike angle), defined in **Figure 3.1a**, to produce the modulus matrix $C_{\alpha\beta}(\theta,\phi)$. We refer to a

general reorientation of the symmetry axis as a tilt, which is achieved by pre- and post-multiplying the elastic modulus matrix by the appropriate Bond rotation matrix and its transpose, respectively (e.g, *Auld*, 1973; *Carcione*, 2007), which act to rotate the 4th-order elasticity tensor appropriately. The order of the rotations matters because the rotation matrices do not commute: first a counter-clockwise rotation through angle θ around the x-axis is applied followed by a second counter-clockwise rotation through angle ϕ around the z-axis. The rotation can fill all components of the modulus matrix but will preserve its symmetry:

$$C_{\alpha\beta}(\theta,\phi)=\begin{bmatrix} C_{11} & C_{12} & C_{13} & C_{14} & C_{15} & C_{16} \\ C_{12} & C_{22} & C_{23} & C_{24} & C_{25} & C_{26} \\ C_{13} & C_{23} & C_{33} & C_{34} & C_{35} & C_{36} \\ C_{14} & C_{24} & C_{34} & C_{44} & C_{45} & C_{46} \\ C_{15} & C_{25} & C_{35} & C_{45} & C_{55} & C_{56} \\ C_{16} & C_{26} & C_{36} & C_{46} & C_{56} & C_{66} \end{bmatrix} \tag{A1}$$

Montagner and Nataf (1986) showed that this modulus matrix may be decomposed into an effective transversely isotropic (azimuthally independent) part, $C_{\alpha\beta}^{ETI}$, and an azimuthally anisotropic part, $C_{\alpha\beta}^{AA}$, as follows:

$$C_{\alpha\beta}(\theta,\phi)=\begin{bmatrix} \hat{A} & \hat{A}-2\hat{N} & \hat{F} & 0 & 0 & 0 \\ \hat{A}-2\hat{N} & \hat{A} & \hat{F} & 0 & 0 & 0 \\ \hat{F} & \hat{F} & \hat{C} & 0 & 0 & 0 \\ 0 & 0 & 0 & \hat{L} & 0 & 0 \\ 0 & 0 & 0 & 0 & \hat{L} & 0 \\ 0 & 0 & 0 & 0 & 0 & \hat{N} \end{bmatrix}+\begin{bmatrix} \delta C_{11} & \delta C_{12} & \delta C_{13} & \delta C_{14} & \delta C_{15} & \delta C_{16} \\ \delta C_{12} & \delta C_{22} & \delta C_{23} & \delta C_{24} & \delta C_{25} & \delta C_{26} \\ \delta C_{13} & \delta C_{23} & \delta C_{33} & \delta C_{34} & \delta C_{35} & \delta C_{36} \\ \delta C_{14} & \delta C_{24} & \delta C_{34} & \delta C_{44} & \delta C_{45} & \delta C_{46} \\ \delta C_{15} & \delta C_{25} & \delta C_{35} & \delta C_{45} & \delta C_{55} & \delta C_{56} \\ \delta C_{16} & \delta C_{26} & \delta C_{36} & \delta C_{46} & \delta C_{56} & \delta C_{66} \end{bmatrix} \tag{A2}$$

where $\hat{A}=3(C_{11}+C_{22})/8+C_{12}/4+C_{66}/2$, $\hat{C}=C_{33}$, $\hat{N}=(C_{11}+C_{22})/8-C_{12}/4+C_{66}/2$, $\hat{L}=(C_{44}+C_{55})/2$, and $\hat{F}=(C_{13}+C_{23})/2$

Equations (3.1) and (A2) present a clear definition of what we call the "inherent" and "apparent" elastic moduli, respectively. The inherent moduli are A,C,N,L,F from the elastic tensor with a vertical symmetry axis and the apparent moduli are $\hat{A},\hat{C},\hat{N},\hat{L},\hat{F}$ from the effective transversely isotropic part of the rotated elastic tensor.

We seek expressions for the period dependence of the phase speed for both Rayleigh and Love waves as well as the 2ψ azimuthal dependence for Rayleigh waves because these are the observations we make. This computation is based on the introduction of a transversely isotropic reference elasticity tensor composed of the depth dependent reference moduli A_0,C_0,N_0,L_0,F_0. The code MINEOS will compute Rayleigh and Love wave phase speed curves for the reference model ($c_0^R(T),c_0^L(T)$). Then we define the effective transversely isotropic moduli relative to this reference:

$$\hat{A} = A_0 + \delta\hat{A},\ \hat{C} = C_0 + \delta\hat{C},\ \hat{N} = N_0 + \delta\hat{N},\ \hat{L} = L_0 + \delta\hat{L},\ \text{and}\ \hat{F} = F_0 + \delta\hat{F}\ .$$

In this case, Montagner and Nataf present the required expressions for Rayleigh and Love wave phase speeds, which break into contributions from the reference moduli, the perturbation by the effective transversely isotropic (ETI) moduli relative to the reference moduli, and the azimuthally anisotopic (AA) moduli:

$$c_R(T,\psi) = c_0^R(T) + \delta c_R^{ETI}(T) + \delta c_R^{AA}(T,\psi) \tag{A3}$$

$$c_L(T,\psi) = c_0^L(T) + \delta c_L^{ETI}(T) \tag{A4}$$

where

$$\delta c_R^{ETI}(T) = \int_0^\infty \left\{ \delta\hat{A}\frac{\partial c_R}{\partial A}\bigg|_0 + \delta\hat{C}\frac{\partial c_R}{\partial C}\bigg|_0 + \delta\hat{L}\frac{\partial c_R}{\partial L}\bigg|_0 + \delta\hat{F}\frac{\partial c_R}{\partial F}\bigg|_0 \right\} dz \tag{A5}$$

$$\delta c_L^{ETI}(T) = \int_0^\infty \left\{ \delta\hat{N}\frac{\partial c_L}{\partial N}\bigg|_0 + \delta\hat{L}\frac{\partial c_L}{\partial L}\bigg|_0 \right\} dz \tag{A6}$$

$$\delta c_R^{AA}(T,\psi) = \int_0^{\infty} \left\{ B_c \cos 2\psi + B_s \sin 2\psi \right) \frac{\partial c_R}{\partial A}\bigg|_0 + (G_c \cos 2\psi + G_s \sin 2\psi) \frac{\partial c_R}{\partial L}\bigg|_0 + (H_c \cos 2\psi + H_s \sin 2\psi) \frac{\partial c_R}{\partial F}\bigg|_0 \right\} dz \quad \text{(A7)}$$

The depth-dependent moduli B_c, B_s, G_c, G_s, H_c, and H_s are linear combination of the components of the azimuthally variable part of the elastic modulus matrix in Equation (A2), $\delta C_{\alpha\beta}^{AA}$, as follows: $B_c = (\delta C_{11} - \delta C_{22})/2$, $B_s = \delta C_{16} + \delta C_{26}$, $G_c = (\delta C_{55} - \delta C_{44})/2$, $G_s = \delta C_{54}$, $H_c = (\delta C_{13} - \delta C_{23})/2$, and $H_s = \delta C_{36}$. Note that the azimuthally independent and 2ψ variations in surface wave phase speeds are sensitive only to 13 of the elements of the elastic tensor, and notably only the (1,6), (2,6), (3,6), (4,5) elements of the elastic tensor outside of the nine elements occupied under transverse isotropy. The other 8 elements of the elastic tensor ((1,4), (1,5), (2,4), (2,5), (3,4), (3,5), (4,6), (5,6)) are in the null space of surface wave phase speed measurements.

Montagner and Nataf present explicit formulas for the partial derivatives in Equations (A5) – (A7) in terms of normal mode eigenfunctions. Instead of using these expressions we recast the problem by computing the partial derivatives numerically which are computed relative to the reference model. The partial derivatives in the expression for the azimuthal term, $\delta c_R^{AA}(T,\psi)$ are equal to the partial derivatives of the azimuthally-independent terms ($c_0^R(T), c_0^L(T)$) with respect to the corresponding transversely isotropic parameters (A, C, F, L, N). This feature facilitates the forward computation because the azimuthal dependence of surface wave speeds can be computed using only the partial derivatives with respect to the five elastic parameters of a transversely isotropic medium, which can be achieved using the MINEOS code (*Masters et al*., 2007). **Figure A3.1** presents the sensitivity of Rayleigh and Love wave phase

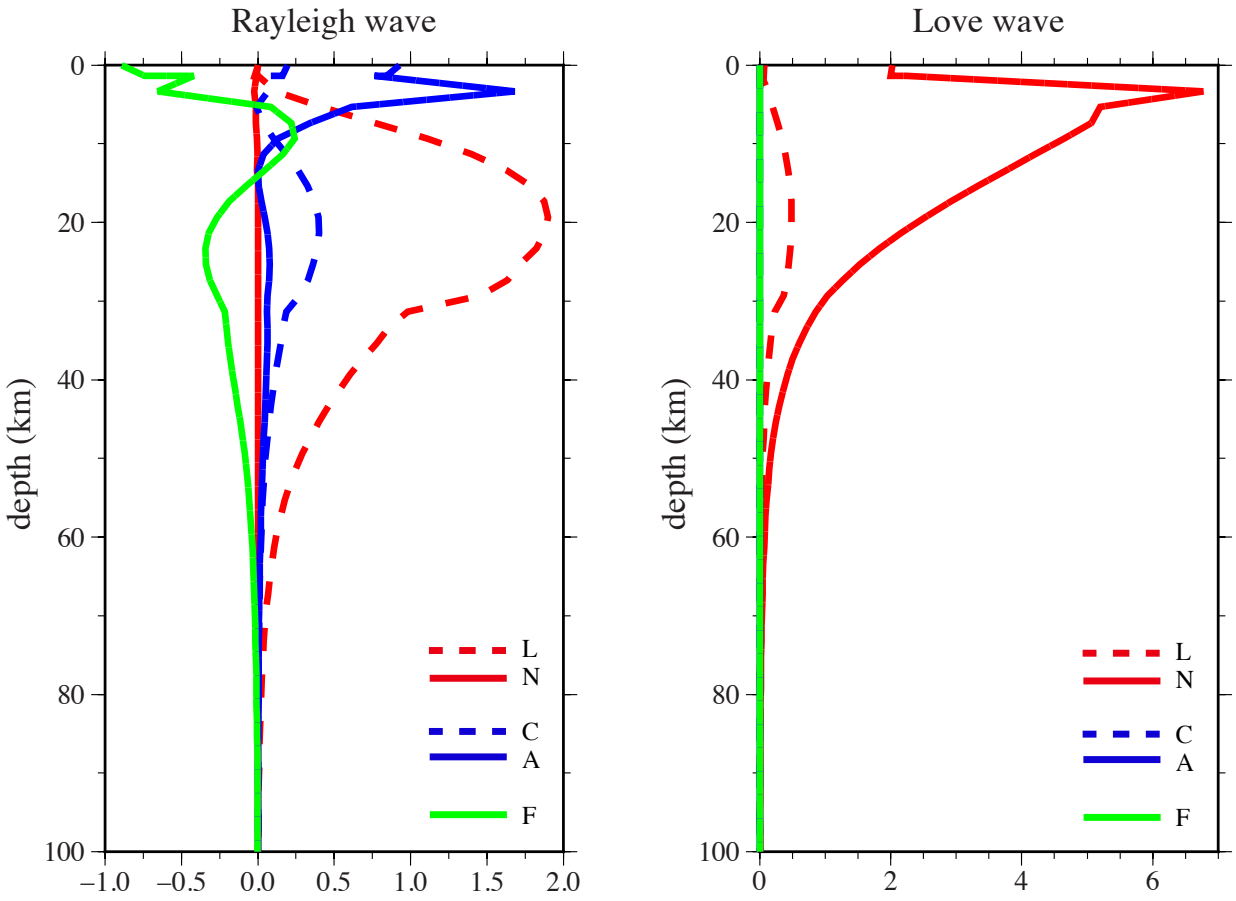

Figure A3.1. Example sensitivity kernels for Rayleigh and Love wave phase speeds at 20 sec period to perturbations in L, N, C, A, and F as a function of depth.

speeds at 20 sec period to perturbations in L, N, C, A, and F as a function of depth. Love waves are sensitive almost exclusively to N, being only weakly sensitivity to L, and completely insensitive to C, A, or F. In contrast, Rayleigh waves are sensitive to all of the parameters except N.

We represent the depth variation of the moduli by defining each on a discrete set of nodes distributed with depth and linearly interpolating the moduli between each node (**Fig. A3.2**). With this approach, we compute the partial derivatives using MINEOS by linear finite differences and convert the integrals to sums in Equations (A5) – (A7). The method is more accurate for Rayleigh than for Love waves and at longer rather than at shorter periods. For example, a constant 10% relative perturbation in the modulus N ($(\hat{N} - N_0)/N_0 = 0.1$, which is 5% in V_{SH}) across the entire crust produces an error in the computed Love wave phase speed of less than 0.1% except at periods less than 10 sec where it is only slightly larger. For Rayleigh waves, a similar constant 10% perturbation in L ($(\hat{L} - L_0)/L_0 = 0.1$, 5% in V_{SV}) results in an error less than 0.05% at all periods in this study. These errors are more than an order of magnitude smaller than final uncertainties in estimated model variables and, therefore, can be considered negligible.

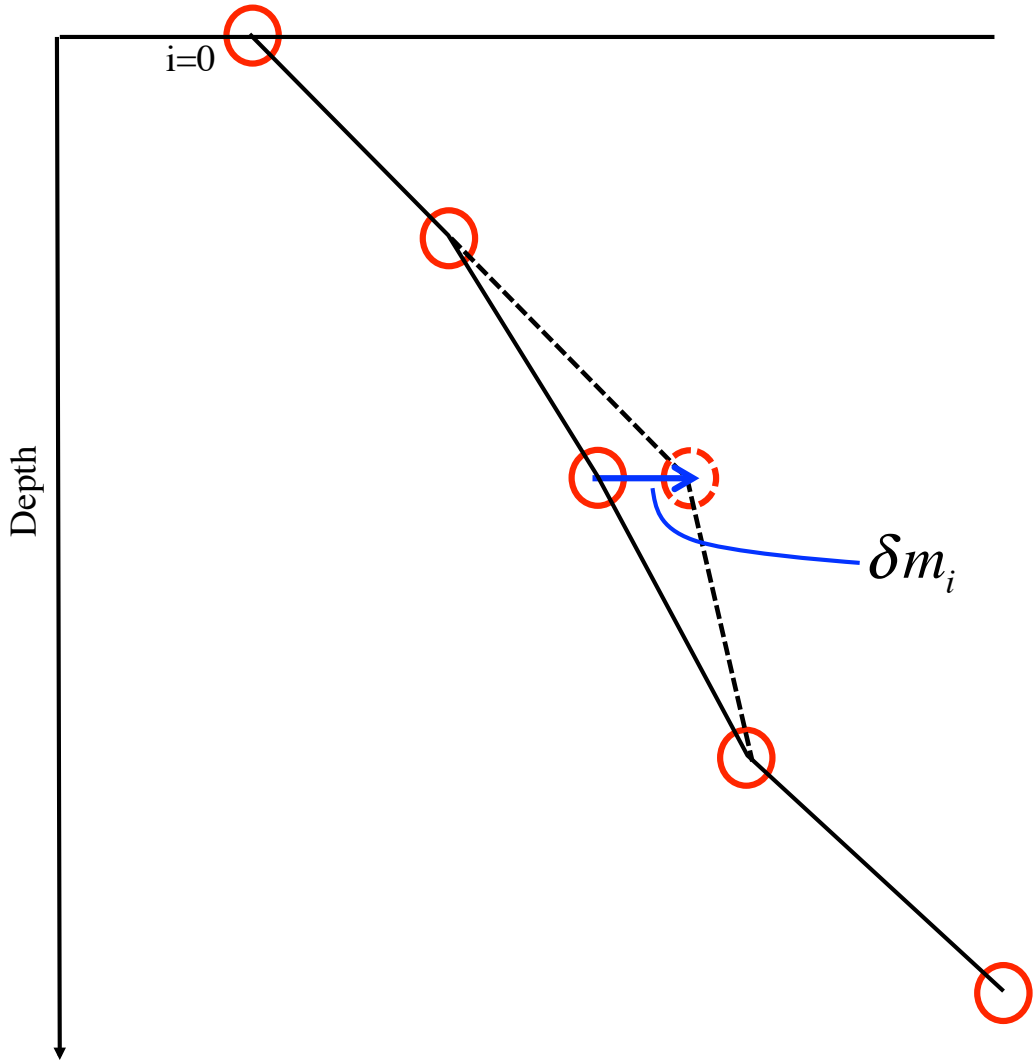

Figure A3.2. Illustration of the model discretization. At each grid point, the model profile is represented by a vertical set of nodes. Each model parameter is perturbed at each node as shown to compute the depth sensitivity of surface wave data.

CHAPTER IV
CRUSTAL ANISOTROPY ACROSS EASTERN TIBET AND SURROUNDINGS MODELED AS A DEPTH-DEPENDENT TILTED HEXAGONALLY SYMMETRIC MEDIUM

Jiayi Xie[1], Michael H. Ritzwoller[1], W. Shen[1,2], Weitao Wang[3]

1- Department of Physics, University of Colorado at Boulder, Boulder, CO 80309, USA

2 – now at Department of Earth and Planetary Sciences, Washington University, St. Louis, MO 63130

3 - Institute of Geophysics, Chinese Earthquake Administration, Beijing 100045 China

Abstract

Two types of surface wave anisotropy are observed regularly by seismologists but are only rarely interpreted jointly: apparent radial anisotropy, which is the difference in propagation speed between horizontally and vertically polarized waves inferred from Love and Rayleigh waves, and apparent azimuthal anisotropy, which is the directional dependence of surface wave speeds (usually Rayleigh waves). We show that a new data set of Love and Rayleigh wave isotropic phase speeds and Rayleigh wave azimuthal anisotropy observed within and surrounding eastern Tibet can be explained simultaneously by modeling the crust as a depth-dependent tilted hexagonally symmetric (THS) medium. We specify the THS medium with depth-dependent hexagonally symmetric elastic tensors tilted and rotated through dip and strike angles and estimate these quantities using a Bayesian Monte Carlo inversion to produce a 3-D model of the crust and uppermost mantle on a 0.5°x0.5° spatial grid. In the interior of eastern Tibet and in the Yunnan-Guizhou plateau, we infer a steeply dipping THS upper crustal medium overlying a shallowly dipping THS medium in the middle-to-lower crust. Such vertical stratification of anisotropy may reflect a brittle to ductile transition in which shallow fractures and faults control

upper crustal anisotropy and the crystal preferred orientation of anisotropic (perhaps micaceous) minerals governs the anisotropy of the deeper crust. In contrast, near the periphery of the Tibetan Plateau the anisotropic medium is steeply dipping throughout the entire crust, which may be caused by the reorientation of the symmetry axes of deeper crustal anisotropic minerals as crustal flows are rotated near the borders of Tibet.

4.1. Introduction

The high Tibetan Plateau has resulted from the collision of India with Eurasia over the past 45 million years [*Molnar and Tapponnier*, 1975; *Jolivet et al*., 1990; *Le Fort,* 1975]. How the plateau has deformed in response to the collision and how it has deformed surrounding regions remains subject to debate, and has inspired a wide range of tectonic models. Hypotheses have included deformation via rigid blocks [e.g., *Tapponnier et al*., 2001], the continuous deformation of the entire lithosphere [e.g., *Molnar and Tapponnier*, 1975; *Houseman and England*, 1993], and flow in the lower crust [e.g., *Royden et al*., 1997].

As suggested by heat flow measurements [*Francheteau et al*., 1984] and thermo-kinematic models [*Bollinger et al*., 2006], the thickened Tibetan crust is believed to be hot, which implies a significant weakness of the middle and lower crust [*Francheteau et al*., 1984; *Nelson et al*., 1996; *Clark and Royden*, 2000; *Beaumont et al*., 2001]. In addition, earthquakes are mainly confined to the upper crust of Tibet where brittle deformation occurs [e.g., *Chu et al*., 2009; *Zhang et al*., 2010; *Sloan et al*., 2011], seismic tomography has identified low velocity zones in the middle to lower crust [e.g., *Yao et al*., 2008; *Yang et al*., 2012; *Xie et al*., 2013], and receiver function studies observe velocity jumps in the middle crust [e.g., *Kind et al*., 2002; *Nabelek et al*., 2009; *Li et al*., 2011; *Deng et al*., 2015]. Some researchers take these results as evidence for a viscously deforming deeper crust [e.g., *Clark and Royden*, 2000; *Beaumont et al*., 2001], which may imply a decoupling between the upper crust and the underlying mantle. Partial melt in the middle crust may also be a common feature of central Tibet [e.g., *Hacker et al*., 2014]. On the other hand, some authors argue that the Tibetan lithosphere is deforming as a coherent unit [e.g., *England and Molnar*, 1997], at least in southern Tibet [*Copley et al*., 2011].

In this paper, we investigate the state of the upper and middle-to-lower crust of Tibet

based on inferences about seismic anisotropy. There have been a number of previous studies of crustal anisotropy across Tibet based on surface waves from ambient noise or earthquake data. Radial anisotropy is the difference in propagation speed between horizontally and vertically polarized waves, inferred from Love and Rayleigh waves, respectively. Crustal radial anisotropy has been mapped across parts of Tibet by, for example, *Shapiro et al*. [2004], *Chen et al*. [2009], *Huang et al*. [2010], *Duret et al*. [2010], *Guo et al*. [2012*], Xie et al*. [2013], *Agius and Lebedev* [2014], and *Tan et al*. [2015]. Azimuthal anisotropy characterizes how propagation speed varies with azimuth. The Rayleigh wave azimuthal anisotropy of the crust also has been mapped by *Wei et al*. [2008], *Yao et al*. [2010], and *Pandey et al*. [2015].

The novelty of the current study lies in its simultaneous interpretation of observations of radial and azimuthal anisotropy from surface waves by estimating the depth-dependent oriented elastic tensor in the crust. *Xie et al*. [2015], influenced by much earlier studies of *Montagner and Nataf* [1986, 1988] *and Montagner and Jobert* [1988], presents a method to infer the oriented elastic tensor from such observations by imposing the constraint that the elastic tensor possesses hexagonal symmetry with an orientation (described by dip and strike angles, **Fig. 4.1**) that is constant throughout the crust. They conclude that only one dip angle (and strike angle) is needed at each location across the relatively thin crust that composes the western US. However, the Tibetan crust is much thicker and many studies have observed significant vertical complications in crustal structure, such as a significant mid-crustal discontinuities [e.g., *Kind et al*., 2002; *Nábělek et al*., 2009; *Li et al*., 2011; *Deng et al*., 2015] and crustal low velocity zones [e.g., *Kind et al*., 1996; *Cotte et al*., 1999; *Rapine et al*., 2003; *Shapiro et al*., 2004; *Xu et al*., 2007; *Yao et al*., 2008; *Caldwell et al*., 2009; *Guo et al*., 2009; *Li et al*., 2009; *Acton et al*., 2010; *Jiang et al*., 2011; *Xie et al*., 2013; *Deng et al*., 2015]. Here, we consider the effects that such complications

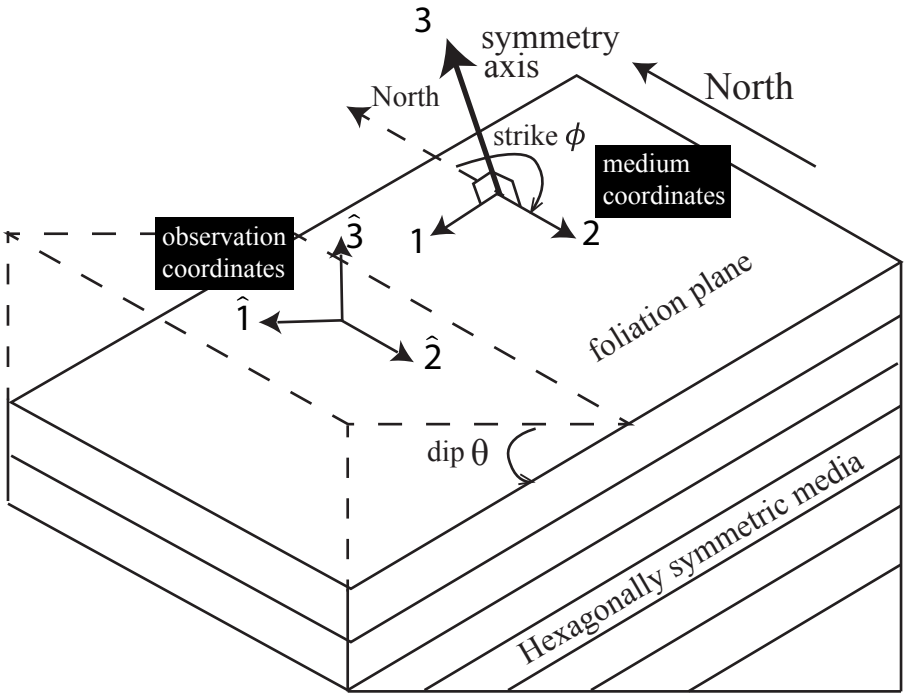

Figure 4.1. Depiction of a tilted hexagonally symmetric medium (THS), showing the foliation plane, the strike and dip angles, and the symmetry axis. The medium coordinates (x_1, x_2, x_3) and the observing coordinates ($\hat{x}_1, \hat{x}_2, \hat{x}_3$) are also shown.

might have on the inference of the oriented elastic tensor across eastern Tibet and adjacent regions.

Estimating the oriented elastic tensor interests us because it may provide insight into the geometry of foliation of material that composes the Tibetan crust, which may provide new constraints on deformation. In particular, estimates of the elastic tensor for the crust of Tibet may provide new information about the difference or similarity between the Tibetan upper and middle-to-lower crust.

In discussing anisotropy it is important to keep in mind two different coordinate frames (**Fig. 4.1**): the frame in which the observations are made and the frame defined by the symmetry axis of the medium. We define the elastic tensor in the coordinate frame of the medium (x_1, x_2, x_3), in which the 3-axis aligns with the symmetry axis and the coordinate pair (x_1, x_2) spans the foliation plane. We refer to anisotropy defined in this frame as "*inherent*". In this frame, a hexagonally symmetric medium possesses no azimuthal anisotropy, where azimuth is defined in terms of rotation about the symmetry axis. In contrast, the coordinate system of observation is represented by the three-components of seismometers at the Earth's surface ($\hat{x}_1, \hat{x}_2, \hat{x}_3$) in which the 3-axis lies normal to the Earth's surface. In this frame, observations of anisotropy depend on how the components of the elastic tensor, composed of the inherent elastic moduli, are affected by the tilt of the medium (or the rotation of the symmetry axis). We refer to measurements of anisotropy and inferences drawn from them in the observational frame as "*apparent*". Most studies of anisotropy based on surface waves have reported measurements and models of particular aspects of apparent anisotropy, such as radial and azimuthal anisotropy. In particular, azimuthal anisotropy is a commonly observed property.

The purpose of this paper is to address the following questions with a focus on eastern

Tibet and surrounding areas: (1) First, can information about anisotropy contained in surface wave travel times observed across Tibet be fit with the oriented elastic tensor model, in the same way as similar data were fit in the western US by *Xie et al*. [2015]? (2) Second, is there a difference in anisotropy between the upper crust and middle-to-lower crust across Tibet? Specifically, is a single orientation for the elastic tensor at all depths in the crust sufficient to fit the observations? (3) Finally, does the nature and vertical distribution of anisotropy across Tibet differ from that across surrounding regions?

In order to address these questions, we combine data from three networks across parts of China and Tibet: the China Earthquake Array (CEArray), the China Array deployed in and around Yunnan Province, and the PASSCAL installations in Tibet (**Fig. 4.2b**). Based on recordings from these stations we obtain Rayleigh and Love wave phase velocity measurements from ambient noise by assimilating phase velocity measurements from previous studies and also updating Love wave phase velocity maps by introducing new observations. Rayleigh wave phase velocity maps for Tibet were previously presented by *Yang et al*. [2012], *Xie et al*. [2013] and later by *Shen et al*. [2016] who produced an isotropic and azimuthally anisotropic data set of observed surface wave phase speeds from ambient noise that covers most of China. These studies ultimately yield an integrated data set of Rayleigh wave phase speed measurements and maps, which we incorporate here. The new measurements we incorporate include both the isotropic and azimuthally anisotropic components of Rayleigh wave phase speeds (**Fig. 4.3**). *Xie et al* [2013] present isotropic Love wave phase speed maps for Tibet. Here, we add new measurements of Love wave phase speeds based on ambient noise recorded at 438 China Array stations in and around Yunnan Province, and produce updated Love wave phase speed maps.

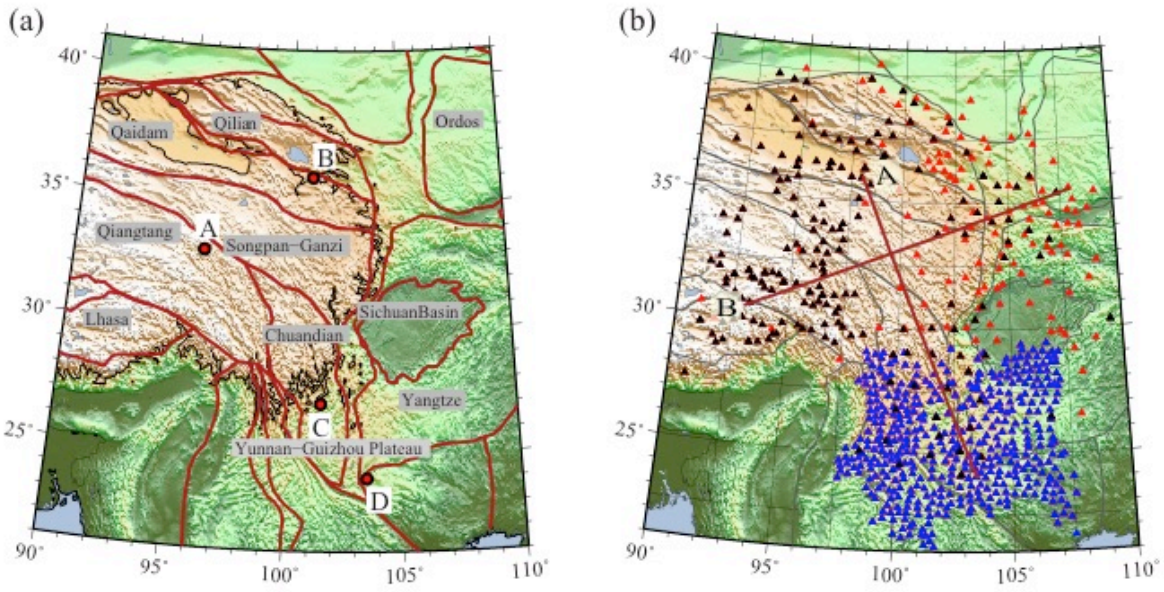

Figure 4.2. (a) Reference map of the study region in which 3 km topography isolines are presented (black lines) along with the boundaries of major geological units (red lines). Points A - D indicate sample locations referenced in **Figs. 4.5, 4.8-4.11, 4.17,** and **4.21**. (b) Locations of seismic stations used in this study: CEArray stations (red triangles), China Array stations around Yunnan province (blue triangles), and PASSCAL stations (black triangle). The two profiles (A, B) are used in **Figs. 4.14** and 4.**19**.

The remainder of this paper is separated into five principal sections. In section 4.2, we briefly describe the data used in our inversion, which is period-dependent surface wave phase speeds extracted from Rayleigh and Love wave tomography, including data sensitivity and uncertainties. In section 4.3, we clarify the terminology and concepts that underlie our work, particularly as related to the notions of inherent and apparent anisotropy. In section 4.4 we describe the model parameterization and constraints applied in the Bayesian Monte Carlo inversion. In section 4.5, we describe the model of the depth-dependent tilted elastic tensor in the crust that explains this data set and present views with horizontal maps and vertical profiles of the estimated dip and inherent strength of anisotropy and their uncertainties. In section 4.6, we provide views of apparent anisotropy to aid comparison with previous studies and discuss the physical and geological significance of the results.

4.2 Data

4.2.1 Measurements

In this study, we combine new ambient noise based Love wave phase velocity measurements with previously observed Rayleigh and Love wave phase speed measurements obtained from cross-correlations of continuous ambient noise data. First, for Rayleigh waves, we incorporate the subset of the maps of isotropic and azimuthally anisotropy phase velocities from *Shen et al*. [2016] that covers our study area. *Shen et al*. [2016] produce isotropic Rayleigh wave phase speed maps (8 to 50 sec period) using ray theoretic tomography [*Barmin et al*., 2001], and simultaneously estimate maps of azimuthal anisotropy. Second, we also incorporate the isotropic Love wave phase speed measurements obtained by *Xie et al*. [2013] using ambient noise cross-correlations based on CEArray and PASSCAL data. Finally, we introduce new Love wave phase speed measurements obtained from cross-correlations of ambient noise recorded at the 438 China Array stations centered on Yunnan Province. The Love wave phase velocity measurements for each cross-correlation station pair are measured using automated frequency-time analysis (FTAN) [*Levshin and Ritzwoller*, 2001; *Bensen et al*., 2007] as in the study of *Xie et al*. [2013]. We apply ray theoretic tomography [*Barmin et al*., 2001] to generate azimuthally variable and isotropic Love wave phase velocity maps from 8 to 40 sec period. As described below, we only interpret the isotropic component of the resulting Love wave maps here.

In a weakly anisotropic medium, the azimuthal dependence of phase velocity for a Rayleigh wave has the following form [*Smith and Dahlen*, 1973]:

$$c(T,\psi) = c_0(T)[1 + a_2\, cos\big(2(\psi - \varphi_{FA})\big) + a_4 cos\,(4(\psi - \alpha))] \qquad (4.1)$$

where T is period, ψ is the azimuth of propagation of the wave measured clockwise from north,

$c_0(T)$ is the isotropic phase speed, φ_{FA} is the 2ψ fast axis orientation, α is an analogous angle for the 4ψ variation in phase velocity, and a_2 and a_4 are the relative amplitudes of the 2ψ and 4ψ anisotropy. Based on theoretical arguments [*Smith and Dahlen*, 1973; *Montagner and Nataf*, 1986] and observations [e.g., *Lin and Ritzwoller*, 2011; *Lin et al*., 2011; *Xie et al*., 2015], the 2ψ term (180° periodicity) is understood to dominate the Rayleigh wave azimuthal variation, so we will only present the 2ψ signal here for Rayleigh waves. However, Love wave azimuthal anisotropy is dominated by the 4ψ term (90° periodicity), which means that exceptionally good azimuthal coverage is required for Love wave anisotropy to be measured reliably. Because the azimuthal coverage is not ideal across much of Tibet and because Love wave observations are typically noisier than Rayleigh wave observations, we do not use the azimuthal anisotropy observed for Love waves in the inversion presented here. The observations of Love wave azimuthal anisotropy help to insure that the isotropic Love wave phase speeds are not biased by azimuthal anisotropy.

We produce isotropic phase speed maps for Love waves (8 to 40 sec period) and Rayleigh waves (8 to 50 sec period), and 2 ψ azimuthal anisotropy maps for Rayleigh waves (8 to 50 sec period). The difference between the isotropic parts of Love and Rayleigh wave phase speeds is shown in **Figure 4.3a,b** at periods of 10 sec and 30 sec. Love wave phase speeds are everywhere faster than Rayleigh wave speeds in the period band of measurement, but the difference between Love and Rayleigh wave speeds (referred to as $C_{Love} - C_{Rayleigh}$ in **Fig. 4.3**) depends on period and location. Examples of Rayleigh wave azimuthally anisotropic phase velocity maps are presented in **Figure 4.3c,d** at 10 sec and 30 sec period, where the length of each bar is the amplitude of 2ψ anisotropy (a_2 in equation 4.1, in percent), and the orientation of each bar is the fast-axis orientation (φ_{FA} in equation 4.1). The azimuthal anisotropy has large

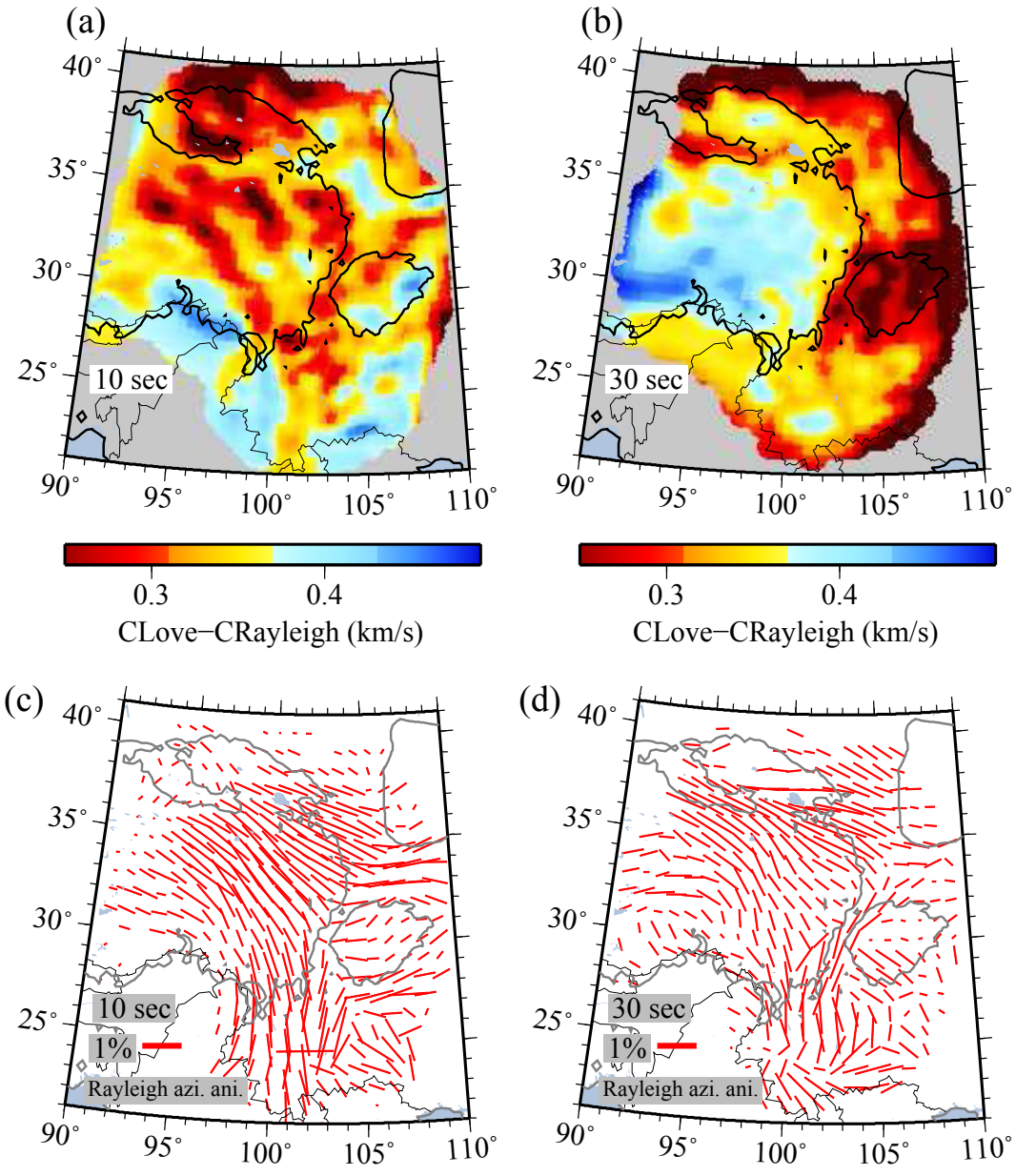

Figure 4.3. (a, b) Examples of the Love-Rayleigh phase speed difference ($C_{Love} - C_{Rayleigh}$) across the study region at periods of 10 and 30 sec. (c, d) The observed Rayleigh wave 2ψ (180° periodicity) azimuthal anisotropy maps at 10 and 30 sec periods. The red bars identify Rayleigh wave fast orientations with lengths proportional to the amplitude in percent (a_2 in eqn. (4.1)).

amplitudes within Tibet and in the Yunnan-Guizhou plateau south of the Sichuan basin. At short periods, fast axis directions generally follow the orientations of surface faults.

4.2.2 Data sensitivity

The differences between Love and Rayleigh wave phase speeds shown in **Figure 4.3a,b** reflect the amplitude of the Rayleigh-Love discrepancy in our observations and provide information about the depth distribution of S-wave anisotropy. The Rayleigh-Love discrepancy is a measure of the inability of a simply parameterized isotropic model to fit Rayleigh and Love wave dispersion curves simultaneously. The introduction of radial anisotropy, or the speed difference between horizontally polarized (V_{SH}) and vertically polarized (V_{SV}) waves in a transversely isotropic medium (TI) (hexagonally symmetric medium with a vertical symmetry axis), is one way to resolve the Rayleigh-Love discrepancy. In general, the phase speed difference between Love and Rayleigh waves increases within the eastern Tibetan Plateau up to about a period of 30 s, and decreases or remains nearly constant with period outside of the Plateau. Procedurally, we specify anisotropy with the elastic tensor and its orientation, and use the notation V_{PV}, V_{PH}, V_{SH}, and V_{SV} only when speaking of a TI medium. In a medium with a tilted symmetry axis, we will specify anisotropy exclusively in terms of the Love moduli A, C, N, L, and F.

Synthetic examples of the difference between Love and Rayleigh wave phase speeds are shown in **Figure 4.4a,b**. Four models of the depth distribution of the difference between Vsh and Vsv in a TI medium are shown in **Figure 4.4a** and the resulting differences between Love and Rayleigh wave phase speeds ($C_{Love} - C_{Rayleigh}$) are shown in **Figure 4.4b**, which depend strongly on the amplitude and depth distribution of the difference V_{SH} - V_{SV}. For example, comparing the

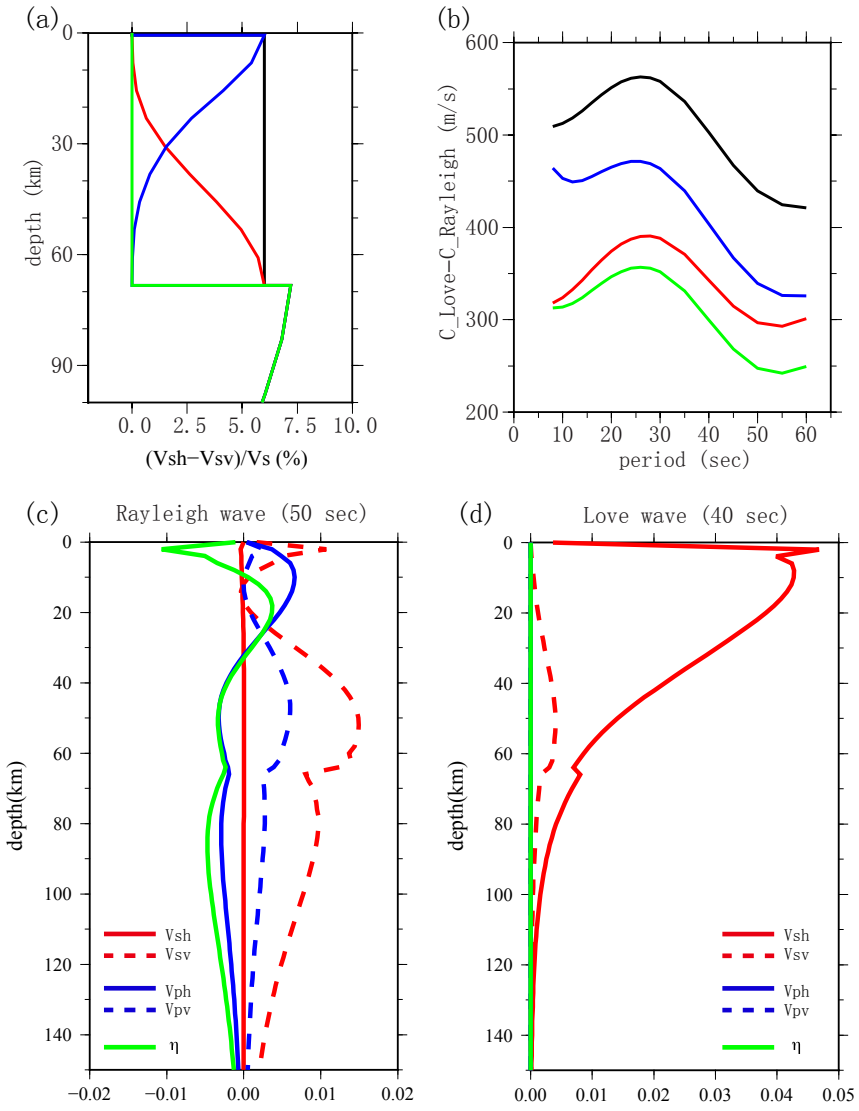

Figure 4.4. (a, b) Simulations that illustrate the effect of changes in a hexagonally symmetric medium with a vertical symmetry axis (VHS medium) on the Love-Rayleigh phase speed difference. (a) Four types of structures with different amplitudes of radial anisotropy ($V_{SH} - V_{SV}$ in %) in the crust. (b) The Love-Rayleigh phase speed differences ($C_{Love} - C_{Rayleigh}$) computed from the structures shown in (a). (c, d) Example unnormalized sensitivity kernels for Rayleigh and Love wave phase velocities for a VHS medium: 50 s period for Rayleigh waves with perturbations in Vsv, Vsh, Vpv, Vph, and η, as a function of depth, and 40 s period for Love waves with perturbations in Vsh and Vsv.

two models in which one is isotropic (green line, **Fig. 4.4a**) and the other has a depth constant radial anisotropy ($V_{SH} - V_{SV} = 5\%$, black line, **Fig. 4.4b**) in the crust, there is a difference in C_{Love} - $C_{Rayleigh}$ of more than 200 m/s, which is a very large effect. The concentration of radial anisotropy in progressively narrower and deeper depth ranges in the crust has a progressively decreasing effect on the Love – Rayleigh phase speed difference. The shapes of the curves in **Figure 4.4b** depend on several factors. The period of the peak difference between Love and Rayleigh wave phase speeds depends largely on crustal thickness. The negative slope of the curves at periods longer than the peak period occurs because the Rayleigh wave becomes sensitive to the mantle at shorter periods than the Love wave. The upward curve at long periods occurs because of increasing sensitivity of Love waves to mantle anisotropy.

As discussed further in section 4.3, a TI medium can be characterized with five elastic moduli. Rayleigh and Love waves are differentially sensitive to these five moduli, which can be represented with the Love parameters A, C, N, L, and F or Vsv, Vsh, Vpv, Vph, and η. As **Figure 4.4c,d** illustrates, Rayleigh waves are predominantly sensitive to Vsv and Love waves are almost entirely sensitive to Vsh. Rayleigh waves also possess substantial sensitivity to η and to both Vpv and Vph, although the Vpv and Vph sensitivities tend to cancel one another which results in a sensitivity to Vpv that is much weaker and more shallow than to V_{SV}. Love waves are sensitive to shallower structures than Rayleigh waves at a given period, the effect of which is amplified in this study because our Love wave measurements only extend up to 40 s period whereas the Rayleigh waves extend to 50 s. The sensitivity kernels in **Figure 4.4c,d** are at the longest periods of this study. Love wave phase speed sensitivity at 40 s period extends only to about 50 km depth (at 25% of the maximum amplitude of the sensitivity curve) whereas Rayleigh wave sensitivity at 50 s period extends to greater than 100 km (based on the same

relative amplitude criterion). This difference in depth sensitivity of Love and Rayleigh waves has implications for the reliability of estimates of anisotropy, as discussed in section 4.6.3.1.

In the inversion for the elastic tensor the differential sensitivity of Rayleigh and Love waves to the elastic moduli allows only some of the moduli to be estimated well. This is complicated further by the need to estimate the dip and rotation angles for the elastic tensor. Much of the point of the Bayesian Monte Carlo inversion procedure described later is to estimate the relative precision with which the different moduli and rotation angles can be estimated.

4.2.3 Uncertainty estimates

Because eikonal tomography [*Lin et al*., 2009] models off great circle propagation and provides an estimate of uncertainty, everything else being equal we would prefer to use it rather than the traditional ray theoretic tomography that we apply here [*Barmin et al*., 2001]. However, eikonal tomography does not perform well in the presence of spatial gaps in the station coverage such as those found in eastern Tibet. Such spatial gaps prevent us from constructing accurate phase velocity maps and uncertainty estimates using eikonal tomography across much of the study region. Thus, our uncertainty estimates for the isotropic phase velocity maps (Love and Rayleigh waves) and azimuthal anisotropy maps (Rayleigh wave) are based on the spatially averaged 1σ uncertainty estimates obtained by applying eikonal tomography where the method does work in the region of study. Where eikonal tomography does not work well we scale up the spatially averaged uncertainty. To do this we are motivated by the procedure described at greater length by *Shen et al*. [2016]. We scale the measurement uncertainties based on some combination of three factors: resolution, ray-path azimuthal coverage, and the amplitude of azimuthal anisotropy. The uncertainties for Rayleigh and Love wave isotropic phase speed maps are scaled using resolution alone as a guide, as described by *Shen et al* [2016]. The uncertainty

for Rayleigh wave azimuthal anisotropy amplitude is scaled using both resolution and azimuthal coverage. Uncertainty for the Rayleigh wave azimuthal anisotropy fast axis is scaled using all three factors. Examples of uncertainties in measured quantities are presented as one standard deviation error bars in **Figure 4.5**.

4.2.4 Dispersion curves

From the Love wave (8 – 40 s period) and Rayleigh wave (8 – 50 s period) isotropic phase speed maps, the Rayleigh wave azimuthal anisotropy maps, and their uncertainties, we generate at all locations on a 0.5°×0.5° grid across the study region isotropic phase speed curves for both Rayleigh and Love waves and period-dependent curves of the amplitude and fast axis orientation of Rayleigh wave azimuthal anisotropy. These four local curves form the basis for the 3-D model inversion described later in the paper.

Figure 4.5 presents examples of these local dispersion curves at the four locations identified in the **Figure 4.2a** (A: eastern Tibet, B: Qilian terrane, C: Chuandian terrane just off the Tibetan plateau, E: Yunnan-Guizhou plateau). Instead of showing the Love and Rayleigh wave isotropic phase speed curves separately, we present the difference between them as in the simulation results presented in **Figure 4.4b**, although in the inversion they are used as two independent observations. Phase speed differences are presented as error bars, defined as the quadratic sum of the estimated uncertainties of the Rayleigh and Love wave phase speeds at each location. As shown in **Figure 4.5a**, within Tibet the difference between Love and Rayleigh wave phase speeds increases rapidly to peak at about 30 s and decreases slowly at longer periods. Outside of Tibet (**Fig. 4.5d,g,j**) the difference increases at short periods less rapidly than in Tibet, peaks at a shorter period, and then decreases either quicker or remains flat with period. A comparison of the synthetic curves in **Figure 4.4b** with the observations in **Figures 5a,d,g,j**

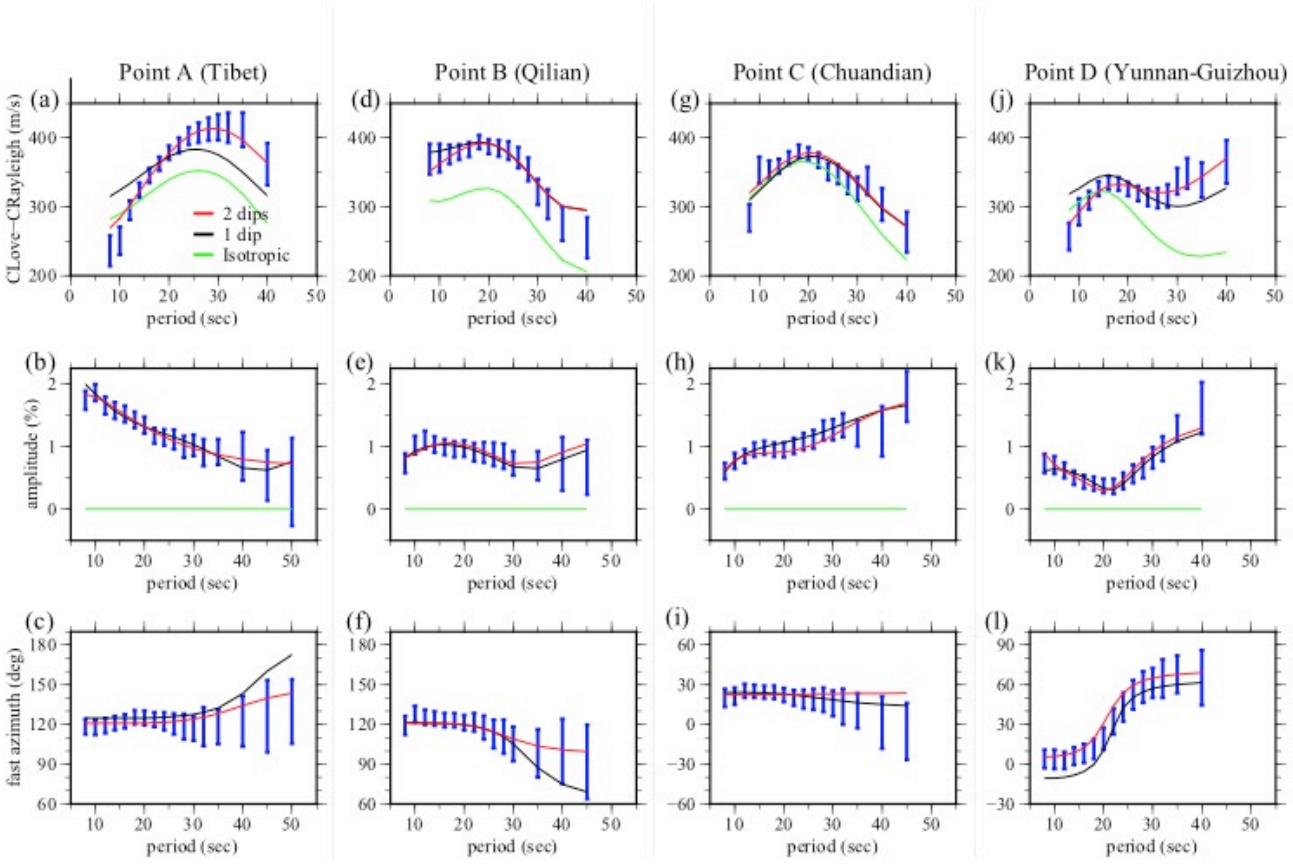

Figure 4.5. Surface wave measurements presented as 1σ error bars illustrating model fits at four locations: eastern Tibet (Point A), Qilian terrane (Point B), Chuandian terrane (Point C), and Yunan-Guizhou plateau (Point D) identified in **Fig. 4.2a**. (a,d,g,j) Love minus Rayleigh wave phase speed. (b,e,h,k) Amplitude of Rayleigh wave azimuthal anisotropy (coefficient a_2 in eqn. (4.1)). (c,f,i,l) Rayleigh wave fast axis orientation. The solid lines are curves computed from the best fitting model at the location using three model parameterizations: isotropic model (green lines), tilted hexagonally symmetric (THS) model with a constant dip angle in the crust (black lines), and THS model with two dip angles in the crust (red lines). Aspects of the THS models with two crustal dip angles are shown in **Fig. 4.11**.

provides hints to the depth distribution of radial anisotropy in Tibet and regions surrounding it.

In addition, the middle and bottom rows of **Figure 4.5** show the period dependent curves for the amplitude and fast axis orientation of Rayleigh wave 2ψ azimuthal anisotropy, respectively. The features of these curves vary dramatically from place to place. For example, at Point A (eastern Tibet), the amplitude of Rayleigh wave azimuthal anisotropy decreases with period and the Rayleigh wave fast azimuth does not change strongly with period. In contrast, at Point B (Qilian terrane), the amplitude of Rayleigh wave azimuthal anisotropy remains flat with period but the Rayleigh wave fast azimuth decreases moderately with period. At Points C and D, azimuthal anisotropy changes in still different ways with period. At Point C the amplitude of anisotropy increases with period and at Point D the fast axis orientation differs appreciably between short and long periods, which indicates a change in the orientation of anisotropy with depth.

4.3 Background: Terminology for a Hexagonally Symmetric Medium

The spatially dependent isotropic and azimuthally anisotropic phase velocity measurements described above provide information about the isotropic and anisotropic properties of the crust and uppermost mantle. The properties of an elastic medium and seismic wave velocities depend on the depth-dependent constitution and orientation of the elastic tensor, which consists of 21 independent components for a general anisotropic medium. Simplifications are needed in order to constrain aspects of the elastic tensor. A useful starting point is the assumption that the medium possesses hexagonal symmetry, which at each depth is described by five unique elastic moduli known as the Love moduli: A, C, N, L, F [*Montagner and Nataf*, 1988; *Xie et al*., 2015]. A and C are compressional moduli and N and L are shear moduli. The

Voigt simplification of the elastic tensor is the 6x6 elastic modulus matrix, $C_{\alpha\beta}$, which for a hexagonally symmetric medium with a vertical symmetry axis is given by:

$$ {}^{V}C_{\alpha\beta} = \begin{bmatrix} A & A-2N & F & 0 & 0 & 0 \\ A-2N & A & F & 0 & 0 & 0 \\ F & F & C & 0 & 0 & 0 \\ 0 & 0 & 0 & L & 0 & 0 \\ 0 & 0 & 0 & 0 & L & 0 \\ 0 & 0 & 0 & 0 & 0 & N \end{bmatrix} \tag{4.2} $$

where the V superscript denotes "vertical" for the orientation of the symmetry axis. With a vertical symmetry axis, a hexagonally symmetric medium will produce no azimuthal variation is surface wave speeds. A hexagonally symmetric medium may possess either a slow or fast symmetry axis; the slow symmetry case occurs when C < A and L < N, which crustal rocks generally display and finely layered media require [e.g. *Brownlee et al*., 2011*; Erdman et al*., 2013; *Thomsen and Anderson*, 2015]. Fast symmetry implies that C > A and L > N.

A hexagonally symmetric medium with a vertical symmetry axis (transversely isotropic, TI) is unique in that the 3-axis of the medium coordinates (symmetry axis) coincides with the 3-axis of the observing coordinates (vertical direction), as defined in **Figure 4.1**. For a TI medium, four of the five Love moduli are directly related to P and S wave speeds for waves propagating vertically or horizontally in the Earth: $A = \rho V^2_{PH}$, $C = \rho V^2_{PV}$, $L = \rho V^2_{SV}$, $N = \rho V^2_{SH}$.. Here ρ is density, V_{PH} and V_{PV} are the speeds of P waves propagating horizontally and vertically in the Earth, V_{SV} is the speed of the S wave propagating horizontally and polarized vertically or propagating vertically and polarized horizontally, and V_{SH} is the speed of the S wave that is propagating in a horizontal direction and polarized horizontally. The modulus $F = \eta(A - 2L)$ affects the speed of waves propagating oblique to the symmetry axis and controls the shape of

the shear wave phase speed surface [*Okaya and Christensen*, 2002]. For an isotropic medium, $A = C, L = N, F = A - 2L, \eta = 1$.

Hexagonally symmetric earth media may have a non-vertical, tilted and rotated symmetry axis as illustrated in **Figure 4.1**, where the tilt is denoted by the dip angle θ and the rotation by the strike angle ϕ. We use the notation V_{PH}, V_{PV}, V_{SV}, and V_{SH} only when discussing a medium with a vertical symmetry axis or an isotropic medium. With a tilted symmetry axis, we will use the notation A, C, N, L, and F (or η = F/(A-2L)) to represent the elements of the elastic tensor. We also introduce the following terminology: VHS for a hexagonally symmetric medium with a vertical symmetry axis, HHS for a hexagonally symmetric medium with a horizontal symmetry axis and THS for a hexagonally symmetric medium with a tilted symmetry axis.

A rotation of the medium will rotate the elastic tensor in equation (4.2) to produce the modulus matrix $C_{\alpha\beta}(\theta,\phi)$. We refer to a general reorientation of the symmetry axis as a tilt, which is achieved by pre- and post-multiplying the elastic modulus matrix by the appropriate rotation matrix and its transpose, respectively [e.g, *Auld*, 1973; *Carcione*, 2007], which act to rotate the 4th-order elasticity tensor appropriately. The rotation can fill all components of the modulus matrix but will preserve its symmetry:

$$C_{\alpha\beta}(\theta,\phi) = \begin{bmatrix} C_{11} & C_{12} & C_{13} & C_{14} & C_{15} & C_{16} \\ C_{12} & C_{22} & C_{23} & C_{24} & C_{25} & C_{26} \\ C_{13} & C_{23} & C_{33} & C_{34} & C_{35} & C_{36} \\ C_{14} & C_{24} & C_{34} & C_{44} & C_{45} & C_{46} \\ C_{15} & C_{25} & C_{35} & C_{45} & C_{55} & C_{56} \\ C_{16} & C_{26} & C_{36} & C_{46} & C_{56} & C_{66} \end{bmatrix} \tag{4.3}$$

Montagner and Nataf [1986] showed that this modulus matrix may be decomposed into

azimuthally independent and azimuthally dependent parts as follows:

$$C_{\alpha\beta}(\theta,\phi)=\begin{bmatrix} \hat{A} & \hat{A}-2\hat{N} & \hat{F} & 0 & 0 & 0 \\ \hat{A}-2\hat{N} & \hat{A} & \hat{F} & 0 & 0 & 0 \\ \hat{F} & \hat{F} & \hat{C} & 0 & 0 & 0 \\ 0 & 0 & 0 & \hat{L} & 0 & 0 \\ 0 & 0 & 0 & 0 & \hat{L} & 0 \\ 0 & 0 & 0 & 0 & 0 & \hat{N} \end{bmatrix}+\begin{bmatrix} \delta C_{11} & \delta C_{12} & \delta C_{13} & \delta C_{14} & \delta C_{15} & \delta C_{16} \\ \delta C_{12} & \delta C_{22} & \delta C_{23} & \delta C_{24} & \delta C_{25} & \delta C_{26} \\ \delta C_{13} & \delta C_{23} & \delta C_{33} & \delta C_{34} & \delta C_{35} & \delta C_{36} \\ \delta C_{14} & \delta C_{24} & \delta C_{34} & \delta C_{44} & \delta C_{45} & \delta C_{46} \\ \delta C_{15} & \delta C_{25} & \delta C_{35} & \delta C_{45} & \delta C_{55} & \delta C_{56} \\ \delta C_{16} & \delta C_{26} & \delta C_{36} & \delta C_{46} & \delta C_{56} & \delta C_{66} \end{bmatrix} \quad (4.4)$$

where $\hat{A}=3(C_{11}+C_{22})/8+C_{12}/4+C_{66}/2$, $\hat{C}=C_{33}$, $\hat{N}=(C_{11}+C_{22})/8-C_{12}/4+C_{66}/2$, $\hat{L}=(C_{44}+C_{55})/2$, and $\hat{F}=(C_{13}+C_{23})/2$. The carat over the symbols indicates that the moduli are azimuthal averages, and can be thought of as the apparent radially anisotropic moduli that would be observed in the observational coordinates. Apparent azimuthally averaged seismic velocities can be defined similarly ($\hat{V}_{sh}=(\hat{N}/\rho)^{1/2}, \hat{V}_{sv}=(\hat{L}/\rho)^{1/2}, \hat{V}_{ph}=(\hat{A}/\rho)^{1/2}, \hat{V}_{sv}=(\hat{C}/\rho)^{1/2}$).

As discussed in the Introduction, it is important to distinguish between the coordinates used to describe the medium's properties and the coordinates in which the observations are made. We define anisotropy in the coordinate system of the medium in which the 3-axis is parallel to the medium's symmetry axis and the 1- and 2-axes lie in the foliation plane as shown in **Figure 4.1**. In these coordinates, the five Love moduli completely describe the anisotropy, and because the medium is hexagonally symmetric there is no (inherent) azimuthal anisotropy. Following *Xie et al*. [2015], we refer to anisotropy in the coordinate frame of the medium as "inherent". To describe the anisotropy fully, we include the medium's orientation by specifying the dip and strike angles. Thomsen (1986) defined useful summaries of inherent anisotropy:

$$\gamma \equiv \frac{N-L}{2L} \qquad \varepsilon \equiv \frac{A-C}{2C} \qquad \delta \approx \frac{F+2L-C}{C} \quad (4.5)$$

where, in particular, we refer to γ as "inherent S-wave anisotropy". In contrast, in the

observational coordinates the description of anisotropy is "apparent". The azimuthally averaged elastic tensor, given by the first matrix on the right-hand-side of (4.4), summarizes the apparent radial anisotropy of the medium, which depends both on the inherent moduli and the dip angle. As defined by *Xie et al*. [2015], a useful summary is the apparent S-wave radial anisotropy:

$$\hat{\gamma} \equiv \frac{\left(\hat{N} - \hat{L}\right)}{2\hat{L}}, \tag{4.6}$$

where, as in equation (4.4), the carat over a symbol indicates that the quantity is apparent. Apparent S-wave radial anisotropy is what most studies refer to simply as "radial anisotropy" [e.g., *Shapiro et al*., 2004; *Xie et al*., 2015]. Although there is no inherent azimuthal anisotropy in our model, apparent Rayleigh (or SV) wave azimuthal anisotropy emerges in the observational frame by tilting the medium, which we represent with dimensionless amplitude:

$$\hat{\Gamma} \equiv \frac{\left((C_{55} - C_{44})^2 + (C_{45})^2\right)^{1/2}}{2\hat{L}} \tag{4.7}$$

and direction $\hat{\varphi}_{FA} = \frac{1}{2}\tan^{-1}(C_{45}/(C_{55} - C_{44}))$. $\hat{\Gamma}$ is equivalent to $|G|/2L$ used in other studies [e.g., *Yao et al*., 2010; *Lin et al*., 2011; *Yuan et al*., 2011; *Xie et al*., 2015].

Thus, the anisotropy of a THS medium can be described completely in terms of the inherent Love moduli and the dip angle. Alternately, it can be described partially by the apparent radial and azimuthal anisotropy, which depend on the inherent anisotropy and tilt. In particular, for the same inherent elastic tensor, the nature of the apparent anisotropy will depend on the orientation of the medium. **Figure 4.6** demonstrates qualitatively how apparent SV-wave (or Rayleigh wave) azimuthal anisotropy, $\hat{\Gamma}$, and apparent S-wave radial anisotropy, $\hat{\gamma}$, will vary as a function of the dip angle of the symmetry axis. These curves are computed from a simple

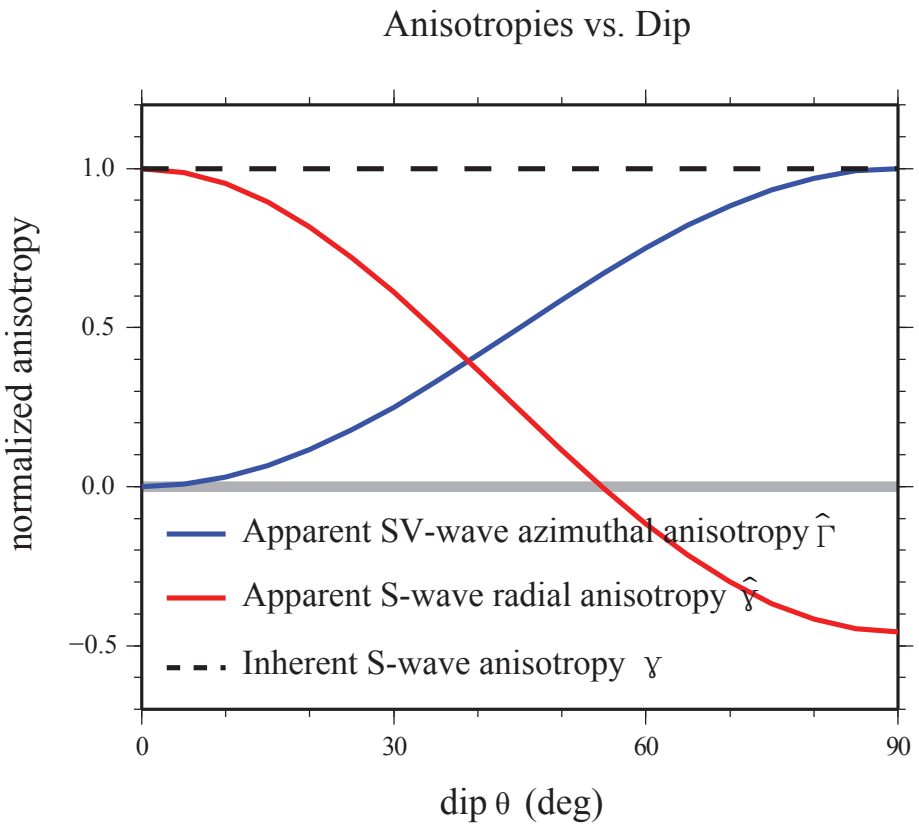

Figure 4.6. Variation of apparent S-wave radial anisotropy $\hat{\gamma}$ (red curve) and apparent SV-wave azimuthal anisotropy $\hat{\Gamma}$ (blue curve) as a function of dip angle θ. The inherent S-wave anisotropy γ is constant and normalized to unity. This computation results from a simplified hexagonally symmetric elastic tensor, details of these functions will depend on the form of the elastic tensor.

elastic tensor with a slow vertical symmetry axis with inherent S-wave anisotropy γ normalized to unity. For this model, the amplitude of apparent azimuthal anisotropy $\hat{\Gamma}$ increases monotonically with increasing dip angle θ, and the apparent radial anisotropy $\hat{\gamma}$ decreases with increasing dip. When the foliation plane is flat or equivalently the symmetry axis is vertical (dip θ=0°), there is strong positive apparent S-wave radial anisotropy but no azimuthal anisotropy. As the dip angle increases, the apparent radial anisotropy becomes negative and azimuthal anisotropy attains its maximum value.

Observations of strong positive apparent radial anisotropy but low amplitude apparent azimuthal anisotropy are consistent with a subhorizontal foliation plane and a slow nearly vertical symmetry axis (i.e., a VHS medium). In contrast, observations of a strongly negative apparent radial anisotropy and strong azimuthal anisotropy are consistent with a subhorizontal symmetry axis (i.e., a HHS medium). Simultaneous observations of intermediate values of radial and azimuthal anisotropy are consistent with a tilted symmetry axis (i.e., a THS medium). Therefore, technically, with surface wave observations, we can invert for a description of the THS medium. However, because surface waves are strongly sensitive only to some of the seven depth-depdendent variables that describe the THS medium, a straightforward inversion is impractical with surface wave data alone. Following *Xie et al*. [2015], we employ a Bayesian Monte Carlo inversion method to estimate distributions of THS media that agree with the data. Such posterior distributions reflect both variances within and covariances between all model variables. Here, we present models in terms of inherent anisotropy and the dip and strike angles, but because most studies present apparent radial anisotropy and apparent azimuthal anisotropy we also convert our results into these quantities to aid comparison with other studies (section 4.6.1).

4.4 Model Specification: Parameterization and Constraints

Figure 4.7 schematically represents the model parameterization, which is similar in many respects to the parameterization applied by *Xie et al*. [2015]. Like *Xie et al*. [2015] we parameterize the crust in terms of a depth-varying THS medium that is described by seven inherent parameters (A, C, N, L, F, strike ϕ and dip θ) (**Fig. 4.1**). The depth dependences of the elastic moduli A, C, N, L, and F are represented by five B-splines in the crystalline crust from the base of the sediments to Moho. For *Xie et al*. [2015], at each location, the dip and strike angles (tilt angles θ, ϕ) that define the orientation of the symmetry axis of anisotropy are constant through the crystalline crust. Here, however, we introduce a discontinuity in the crust that allows the dip angle to jump smoothly from values above and below a mid-crustal dip boundary set at one third of the crystalline crustal thickness at each location. The strike angle, however, remains constant throughout the crust. Like *Xie et al*. [2015] we assume the sediments to be isotropic. We constrain crustal anisotropy to have a slow symmetry axis consistent with studies of crustal petrology as discussed in section 4.6.2.2. In addition, the introduction of a fast symmetry axis tends to be incompatible with the frequency dependence of our observations.

We introduce the mid-crustal discontinuity in dip angle because we find that we are unable to fit our observations over large areas, particularly in Tibet, without it. **Figure 4.5** illustrates this point. The difference between Love and Rayleigh wave phase speeds at Point A in Tibet (**Fig. 4.5a**) cannot be fit with a model in which the dip angle is constant in the crust (black line), but can be fit when we allow dip angle to change once discontinuously in the crust (red line). We choose the value of one third of the crustal thickness as the location of the discontinuity in accordance with the study of *Deng et al*. [2015], who observed a discontinuity at about this depth in northern Tibet based on joint inversion of surface wave dispersion and

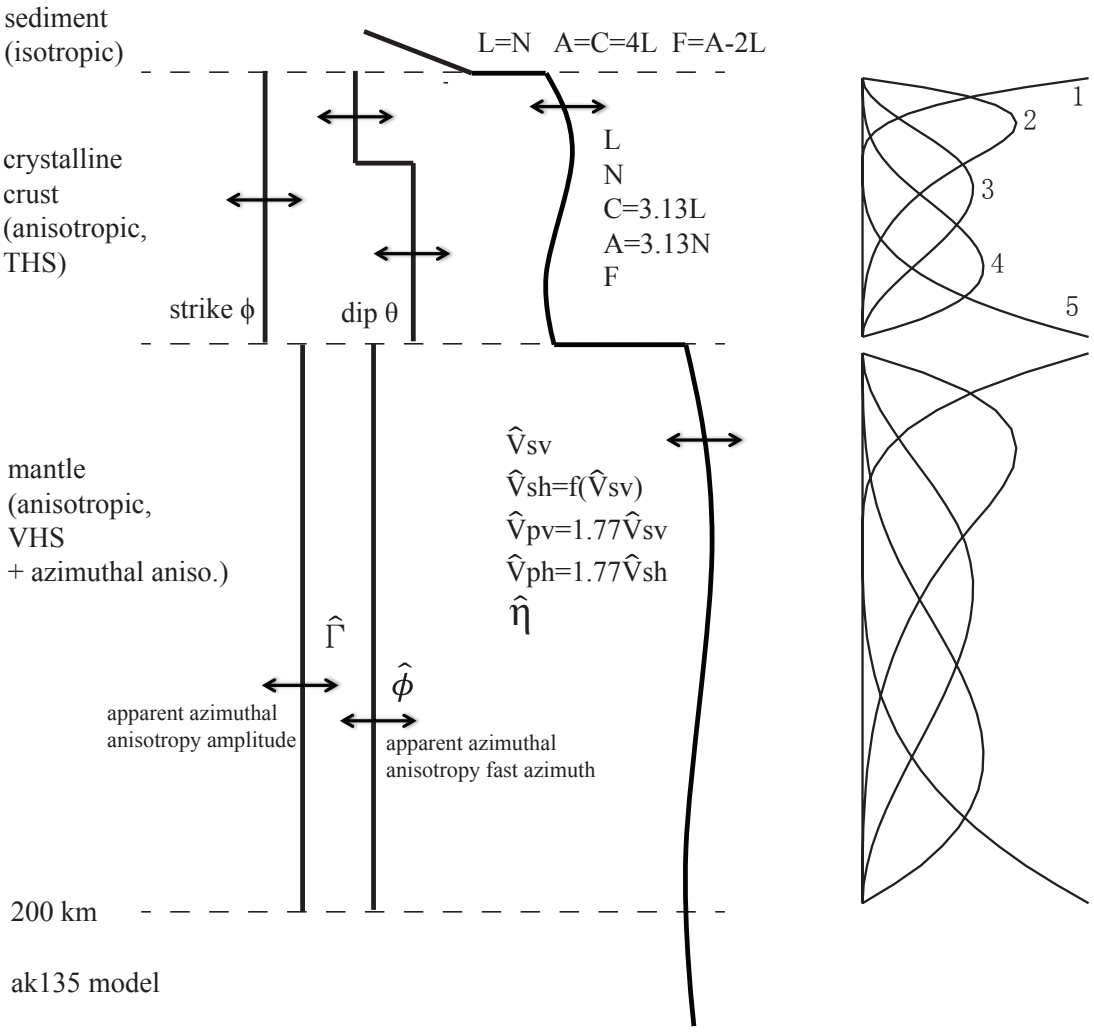

Figure 4.7. Model parameterization. Sedimentary structure is isotropic with shear and compressional velocities increasing linearly with depth. The crystalline crust is an anisotropic THS medium described by seven depth-dependent parameters: five inherent elastic moduli, dip angle, and strike angle. The elastic moduli change smoothly with depth and are represented with five B-splines. Strike is constant within the crystalline crust and dip is allowed to change once within the crystalline crust at a depth of one-third of the crustal thickness. The uppermost mantle is modeled as a VHS anisotropic medium plus apparent azimuthal anisotropy and is described by seven parameters: five apparent elastic moduli ($\hat{V}_{SV}, \hat{V}_{SH}, \hat{V}_{PV}, \hat{V}_{PH}, \hat{\eta}$) and two parameters to represent apparent azimuthal anisotropy ($\hat{\Gamma}, \hat{\phi}$). Mantle apparent radial anisotropy $\hat{\gamma}$ is constrained to be 4.5% and the amplitude of mantle apparent azimuthal anisotropy is constant with depth.

receiver function data. In contrast, in some areas the data can be fit by the model with a constant crustal dip, such as Points B and C in the Qilian and Chuandian terranes (**Fig. 4.5b,g**). At Point D in the Yunnan-Guizhou plateau (**Fig. 4.5j**), two crustal dip angles are needed to fit the data but the misfit produced by the single dip model is not as large as within Tibet.

We use the China reference model produced by Shen et al. [2016] as the crustal reference around which perturbations are applied in the inversion. This is an isotropic model based on Rayleigh wave data, which most strongly constrain the elastic modulus L (related to V_{SV} in a TI medium). We use the model to define a reference for the four elastic moduli and density: $A_0(r)$, $C_0(r)$, $N_0(r)$, $L_0(r)$, and $\rho_0(r)$, where r is the radius within the Earth. Also, we use it to define sedimentary structure (seismic velocities and density increase linearly with depth and thickness), Moho depth, and Q(r), which we do not change in the inversion.

Based on data sensitivity (e.g., **Fig. 4.4c,d**), we apply several prior constraints to the seven depth-dependent parameters that describe the oriented elastic tensor. We apply weaker constraints on parameters that are highly data sensitive, and stronger constraints on parameters to which the data have little sensitivity. Therefore, the shear moduli L and N are relatively weakly constrained, and are perturbed within the range of $L_0(1\pm0.3)$. In contrast, the compressional moduli are strongly constrained, and we set $C = (1.77)^2 L \approx 3.13N$ where 1.77 is the Vp/Vs ratio, and similarly we set $A=(1.77)^2 N$. Thus, the inherent P-wave anisotropy $\varepsilon = (A-C)/2C$ equals inherent S-wave anisotropy $\gamma = (N-L)/2L$. The modulus $\eta = F/(A-2L)$ is freely perturbed within [0.8,1.1]. This is a narrower range for η than used by *Xie et al*. [2015] (in that work $\eta \in [0.6,1.1]$) in order to eliminate the in strike angle. *Xie et al*. [2015] found that two groups of models with orthogonal strike directions fit the data equally well, and these two groups of models have similar inherent S-wave anisotropy and dip but different values of η. Therefore, reducing the

range of η eliminates this bifurcation and simplifies the resulting models. We discuss the impact of this constraint on the strike angle in section 4.5.2. The dip angle θ and strike angle ϕ range between 0° and 90°.

Because Love wave sensitivity is shallower than Rayleigh wave sensitivity (**Fig. 4.4c,d**) at a given period, the amplitude of inherent S-wave anisotropy γ is poorly determined in the Tibetan lowermost crust. This is illustrated in **Figure 4.8**, which shows the results of three inversions of the same data in Tibet (Point A) but with different constraints on γ: (a) $\gamma \geq 0$ throughout the crust, (b) $\gamma > 0$ throughout the crust but $\gamma = 0$ at the base of the crust, and (c) $0 \leq \gamma \leq 10\%$ throughout the crust. These constraints produce very different estimates of γ below 50 km depth in the crust. In particular, without a constraint beyond the positivity constraint ($\gamma \geq 0$), the estimate of γ in the lowermost crust of Tibet becomes unstable. For this reason, we seek a small amplitude model here and apply the constraint that $0 \leq \gamma \leq 10\%$ throughout the crust across the entire study region. The result of this constraint is that γ will tend to be approximately constant with depth in the lowermost crust of Tibet.

It is with some trepidation that we have modeled the sediments as isotropic because Tibet is surrounded by large basins where there is strong evidence of anisotropy. However, because the model of *Shen et al. [2016]* is based exclusively on Rayleigh wave data it does not provide a particularly accurate reference for sedimentary structure, in particular sedimentary thickness. Thus, inferences we might draw here about sedimentary anisotropy would be suspect. In order to constrain the structure of the sediments better, additional data such as receiver functions or the H/V ratio, which are more sensitive to the shallower depths, should be added. We discuss sedimentary anisotropy in section 4.6.2.3 where we provide evidence that the sediments are strongly anisotropic, so much so that we are forced to eliminate the amplitude constraint on γ in

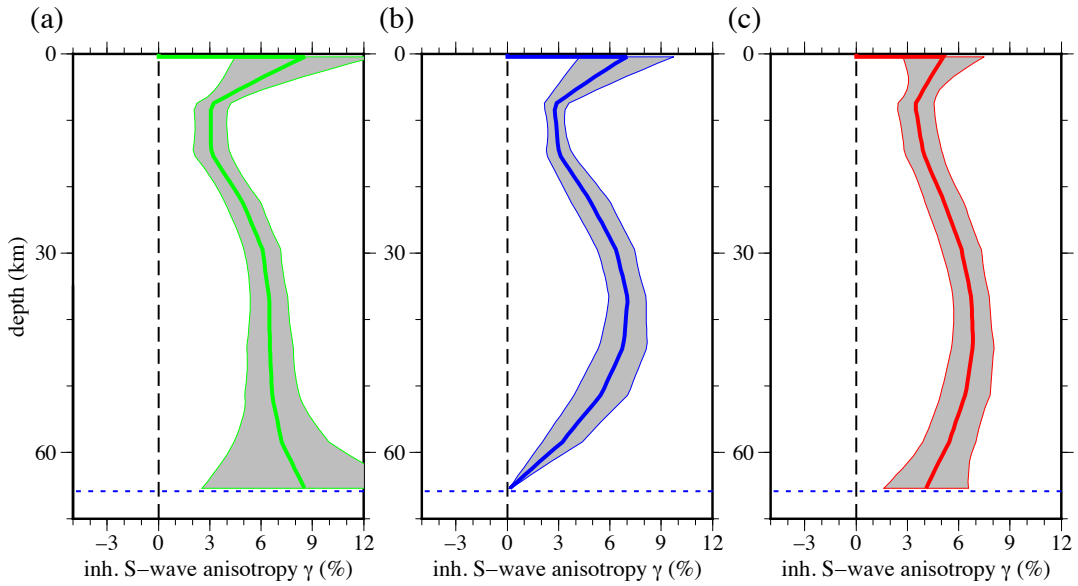

Figure 4.8. Mean (solid colored lines) and standard deviation (grey corridor) of posterior distributions of inherent S-wave anisotropy (γ) at Point A in Tibet showing the vertical variation of this quantity with different constraints applied in the inversion: (a) $\gamma \geq 0$ across the crust, (b) $\gamma \geq 0$ across the crust but γ is set to 0 at the base of the crust, similar to *Xie et al. (*2013); and (c) $0 \leq \gamma \leq 10\%$ across the entire crust as done in this paper. γ is not well constrained by our observations below 50 km depth.

the sediments. However, modeling them as isotropic does not affect our primary conclusions, although it does mean that we are not able to fit our data well within the basins.

In terms of the mantle parameterization, it is not clear if hexagonal symmetry with a slow symmetry axis is physically appropriate to represent mantle anisotropy. If mantle anisotropy is produced by the lattice-preferred orientation (LPO) of olivine, then the mantle could be modeled either as hexagonally symmetric with a fast symmetry axis or as orthorhombic, depending on whether the two slower olivine crystal axes scatter randomly or not [*Christensen*, 1984]. In contrast, if the mantle anisotropy is caused by partial melt, then mantle anisotropy could be modeled either as hexagonally symmetric with a slow symmetry axis or orthorhombic, depending on the shape of the melt pockets [e.g., *Thomsen and Anderson,* 2015]. In any case, because our surface wave observations extend only up to 50 sec period they poorly constrain mantle anisotropy beneath Tibet. Tests of several different mantle parameterizations and constraints show, however, that changes in the parameterization affect estimated crustal structures within the estimated uncertainties.

For these reasons, we parameterize mantle anisotropy (**Fig. 4.7**) simply in terms of apparent quantities rather than inherent properties, and beneath 200 km the model is set to be AK135 [*Kennett et al.,* 1995], which is isotropic. In particular, we describe the mantle as a VHS medium plus additional apparent azimuthal anisotropy. In this case, mantle radial anisotropy decouples from azimuthal anisotropy and both are the apparent quantities. We estimate $\hat{V}_{sv}$ as a free parameter in the uppermost mantle, represent it with five B-splines, and allow it to vary within the range $\hat{V}_{sv0}(1 \pm 0.15)$, where the reference value $\hat{V}_{sv0}$ is from *Shen et al.* [2016]. We compute $\hat{V}_{sh}$ from $\hat{V}_{sv}$ by assuming a constant value of $\hat{\gamma} = 4.5\%$, a value that is consistent with

the average of mantle apparent radial anisotropy across the study region determined by *Shapiro et al*. [2004]. This is presented in **Figure 4.7** as $\hat{V}_{SH} = f(\hat{V}_{SV})$, which should be read "$\hat{V}_{SH}$ is a function of $\hat{V}_{SV}$". We also estimate the apparent amplitude of azimuthal anisotropy $\hat{\Gamma}$ (eqn. (4.7)) and the local fast direction $\hat{\varphi}$, both of which are set to be constant with depth in the mantle. We further set $\hat{V}_{PV} = 1.77\hat{V}_{SV}$ and $\hat{V}_{PH} = 1.77\hat{V}_{SH}$, which sets apparent P-wave anisotropy equal to apparent S-wave anisotropy. $\hat{\eta}$ is freely varying within the range [0.8,1.1]. Because we do not infer any inherent properties of the mantle anisotropy we do not show mantle anisotropy in plots of inherent anisotropy. However, plots of apparent anisotropy do include mantle anisotropy. In any event, we will focus our discussion on the crustal part of the model.

4.5. Results

The Bayesian Monte Carlo inversion is based on the observed data (described in section 4.2), a forward computation algorithm (described by *Xie et al*. [2015] in detail), a starting model, and prior information consisting of constraints on the model. As discussed in section 4.4, the starting model comes from *Shen et. al. [2016],* which is an isotropic Vsv model derived exclusively from Rayleigh waves, and the constraints guide the formation of the prior distribution at each location.

The Bayesian Monte Carlo inversion method is very similar to that described in a series of recent papers by *Shen et al*. [2013a,b] and elsewhere [e.g., *Shapiro and Ritzwoller*, 2002; *Zheng et al*., 2011; *Yang et al*., 2012; *Zhou et al*., 2012; *Shen et al*., 2013c; *Tian et al*., 2013; *Xie et al*., 2013; *Deng et al*., 2015; *Kang et al*., 2015*; Shen et al*., 2015; *Shen and Ritzwoller*, 2016]. Here, we invert the data at every location on a 0.5° x 0.5° grid and produce a set of models that define the posterior distribution of models that fit the data acceptably. We summarize each posterior distribution by its mean, which we refer to as the "mean model", and standard deviation, which together define the final model with an estimate of uncertainty at each depth and for each model variable. We present the model here in terms of the inherent elastic tensor and its orientation (dip and strike). A discussion of the apparent anisotropy that results from this representation occurs in section 4.6.1. Examples of marginal posterior distributions of selected model characteristics are presented in **Figures 4.9** and 4.**10** for 10 km and 30 km depth, respectively, and are discussed further below.

4.5.1 Example results at four locations

We first present the results of the inversion of the data presented in **Figure 4.5** at the four locations identified in **Figure 4.2a**: Point A in eastern Tibet, Point B in the Qilian terrane north

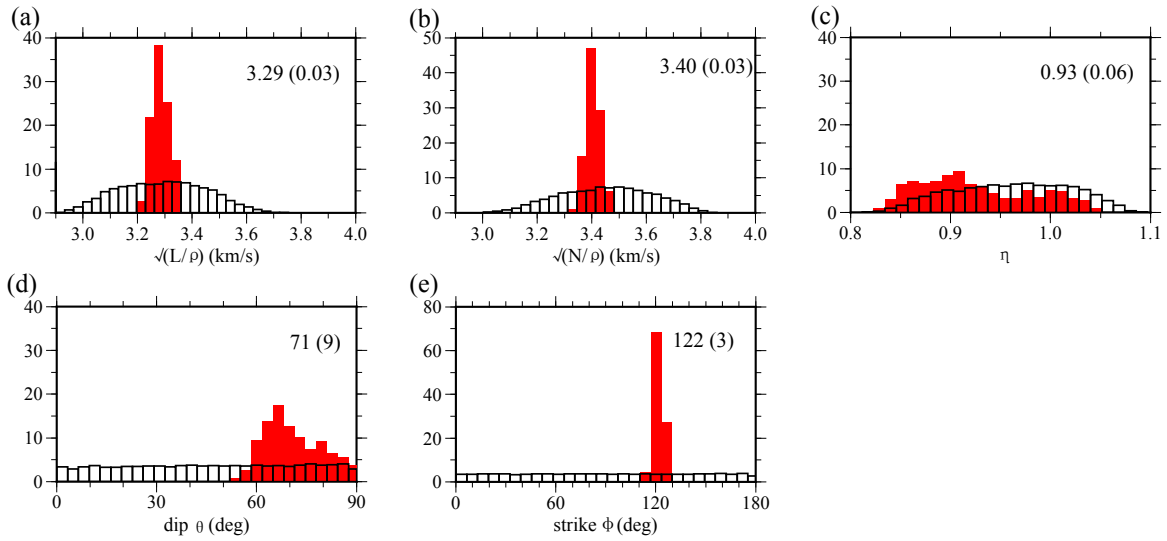

Figure 4.9. Example comparison of prior and posterior marginal distributions from the Bayesian Monte Carlo inversion for five example model parameters at 10 km depth for Point A in Tibet (**Fig. 4.2a**). White histograms are the prior marginal distributions and red histograms are the posterior marginal distributions. The average and standard deviation of the posterior distributions are presented on each plot.

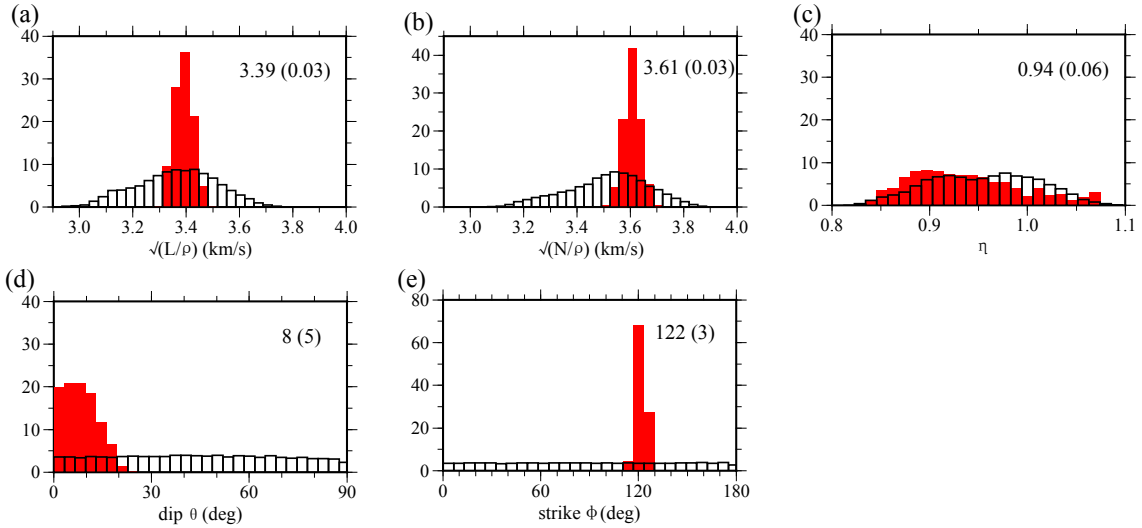

Figure 4.10. Similar to **Fig. 4.9**, but at 30 km depth, again for Point A in Tibet.

of Tibet, Point C in the central Chuandian terrane just off southeastern edge of the Tibetan plateau, and Point D in the Yunnan-Guizhou plateau.

At Point A, the Love-Rayleigh phase velocity difference increases with period, while the amplitude of Rayleigh wave azimuthal anisotropy decreases with period (**Figure 4.5a-c**). **Figure 4.5a-c** shows that the data are fit well (red lines) by the mean model with the parameterization that allows two different dip angles in the crust. The fit delivered by the mean models produced from inversions with two other parameterizations are also shown in **Figure 4.5a-c**: an isotropic model (green lines) and a model with a constant dip angle throughout the crust (black lines). Neither of these models can fit the Love wave and Rayleigh wave phase speeds simultaneously across most of Tibet. This provides the primary justification for the introduction of the discontinuity in dip angle in the middle crust in our parameterization.

Aspects of the posterior distributions at Point A are presented in **Figures 4.9** and 4.**10**, which display marginal distributions for inherent $\sqrt{L/\rho}$, $\sqrt{N/\rho}$, η, dip angle θ, and strike angle ϕ at depths of 10 km and 30 km. These are five of the seven parameters that describe the elastic tensor and its orientation at each depth. The other two (compressional moduli A, C) are scaled from the shear moduli L and N and are, therefore, not shown. At both depths L and N are well constrained; the standard deviations of the posterior distributions are less than about 1% at both 10 km and 30 km depth. The strike angle is constant in the crust and is also well constrained, with a standard deviation of about 3°. In contrast, η is not well constrained at either depth, which tends to be true across the study region. The most notable difference between the two depths is the very different dip angle at 10 km (71°±9°) compared with 30 km (8°±5°). The foliation plane dips steeply in the upper crust and is sub-horizontal in the lower crust at this location in eastern Tibet, and across most of Tibet, as we will show. In the lower crust here, the

foliation plane is observationally indistinguishable from horizontal (i.e., the symmetry axis is indistinguishable from vertical).

This information can be viewed in a different way in **Figure 4.11** in which one standard deviation bounds around the mean of the posterior distribution are presented as a function of depth for the dip angle and inherent S wave anisotropy, γ (eqn. (4.5)). The change in the dip angle with crustal depth is shown for Point A in Tibet in **Figure 4.11a** and γ is seen in **Figure 4.11b** to range from 3-5% in the uppermost crust (depth < 10 km), to about 7% at 40 km depth, and then decrease with depth to ~4-5% in the lowermost crust.

At Point B, which is located in the Qilian terrane just north of Tibet, the isotropic model also does not fit the data (**Fig. 4.5d-f**), thus crustal anisotropy is also required outside of Tibet. However, the data can be fit with either model in which we allow the dip angle to change in the middle crust or constrain it to be constant throughout the crust. The reason for this is seen in **Figure 4.11c**, which shows that the dip angle is essentially indistinguishable between the upper and lower crust at this location (~40°). **Figure 4.11d** shows that γ is approximately constant with depth, averaging about 4% across the crust at this location.

At Point C, the data differ from those at both Points A and B in that the Love-Rayleigh phase speed difference can nearly be fit with an isotropic model (**Fig. 4.5g**; indicating near-zero apparent radial anisotropy). However, the high amplitude of azimuthal anisotropy guarantees the existence of crustal anisotropy. Similar to Point B, the dip angle (~60°) at Point C does not change strongly with depth across the crust (**Fig. 4.11e**), but the dip angle is steeper than at Point B. The amplitude of inherent S-wave anisotropy γ averages between 2% and 3% across most of the crust (**Fig. 4.11f**), which is weaker than at Points A and B.

Crustal anisotropy at Point D is more similar to Tibet in that two dip angles are needed to

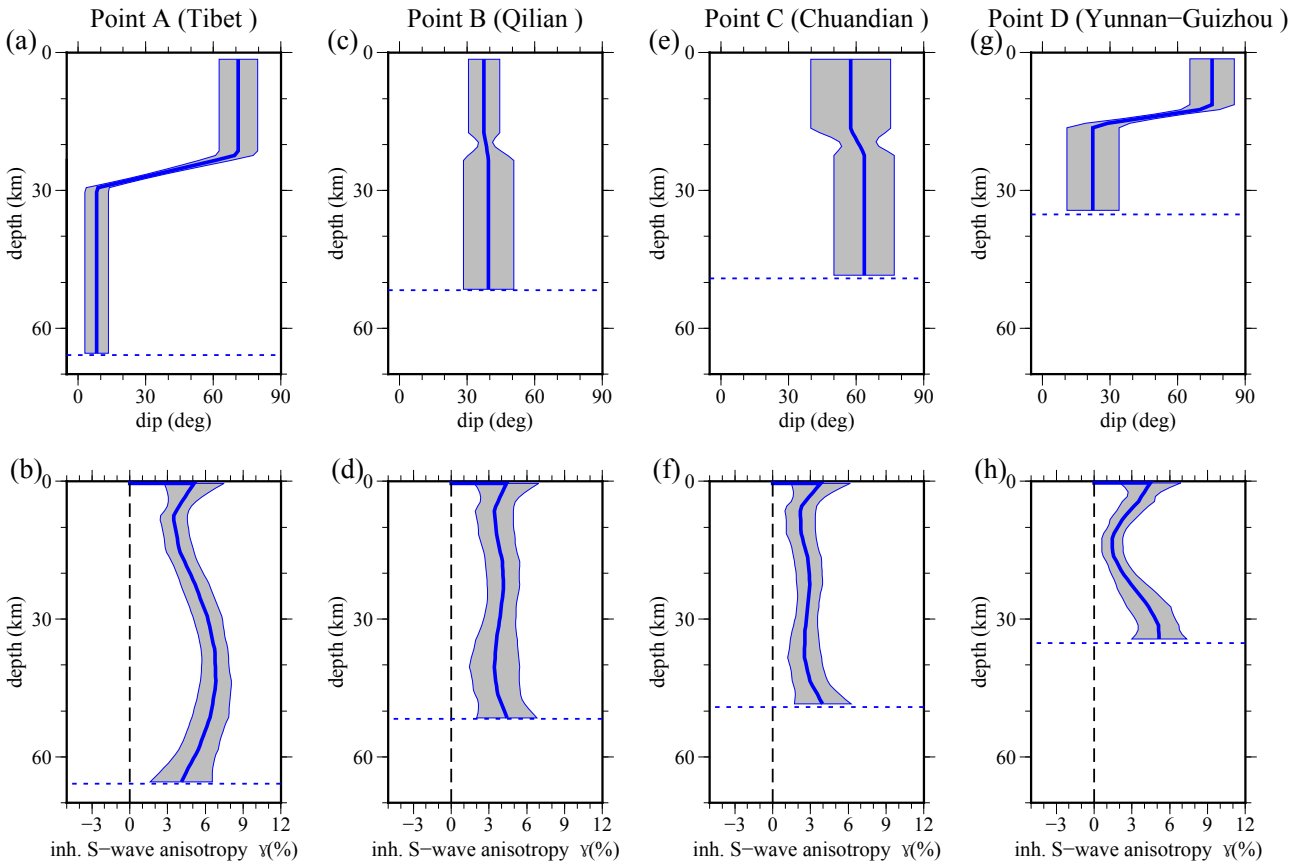

Figure 4.11. Posterior distributions of inherent anisotropic variables at Points A –D (**Fig. 4.2a**) showing (a,c,e,g) the vertical variation of the dip angle θ and (b,d,f,h) the inherent S-wave anisotropy γ. The one-standard deviation extent of the posterior distribution is shown at each depth with the grey corridor and the average is plotted with bold black solid lines. Only the crystalline crustal part of the model is shown because sediments are isotropic and the mantle is parameterized in terms of apparent moduli, so no inherent property is inferred.

fit the data shown in **Figure 4.5j-l**. Although the dip angle (**Fig. 4.11g**) in the upper crust is similar to that in Tibet (>70°), the dip angle in the lower crust is larger (~20°) and is distinguishable from zero. Thus, the lower crustal foliation plane in the Yunnan-Guizhou plateau is not as horizontal as beneath Tibet, but is shallowly dipping. Also, the vertical distribution of inherent S-wave anisotropy at Point D (**Fig. 4.11h**) differs from Tibet. The anisotropy in Tibet is strong throughout the crust, whereas beneath the Yunnan-Guizhou plateau it is concentrated in the uppermost (~4%) and lowermost crust (~5%) with a minimum at a depth of about 15 km (~1.5%).

In section 4.6.1, we discuss the apparent crustal anisotropy computed from the inherent anisotropy and dip angle discussed here, as well as apparent mantle anisotropy.

4.5.2 Results across the entire region: mean of the posterior distribution

Aspects of the resulting model (dip angle θ, inherent S wave anisotropy γ), defined as the mean of the posterior distribution at each depth, are shown in **Figure 4.12** at depths of 10 km and 30 km in the crust. These depths bracket the discontinuity in dip angle across the entire study region. The estimated strike of anisotropy, which is constant with depth within the crust, is shown in **Figure 4.13a** in which the orientation of the bars indicates the strike orientation (ϕ). As described in Section 4.4, we have deliberately narrowed the allowed range of η by eliminating small η values; thus our resulting models approximately possess so-called elliptical anisotropy [e.g., *Thomsen*, 1986; *Xie et al*., 2015]. As a consequence, the crustal strike orientation generally follows the Rayleigh wave fast axis orientation at short periods (**Fig. 4.3c**). However, as discussed by Xie et al. [2015], if η is allowed to vary broadly enough there will be two subsets of models in the posterior distribution with orthogonal strike angles. We circumvented this bifurcation by constraining the η to be relatively large. Nevertheless, at each location there is

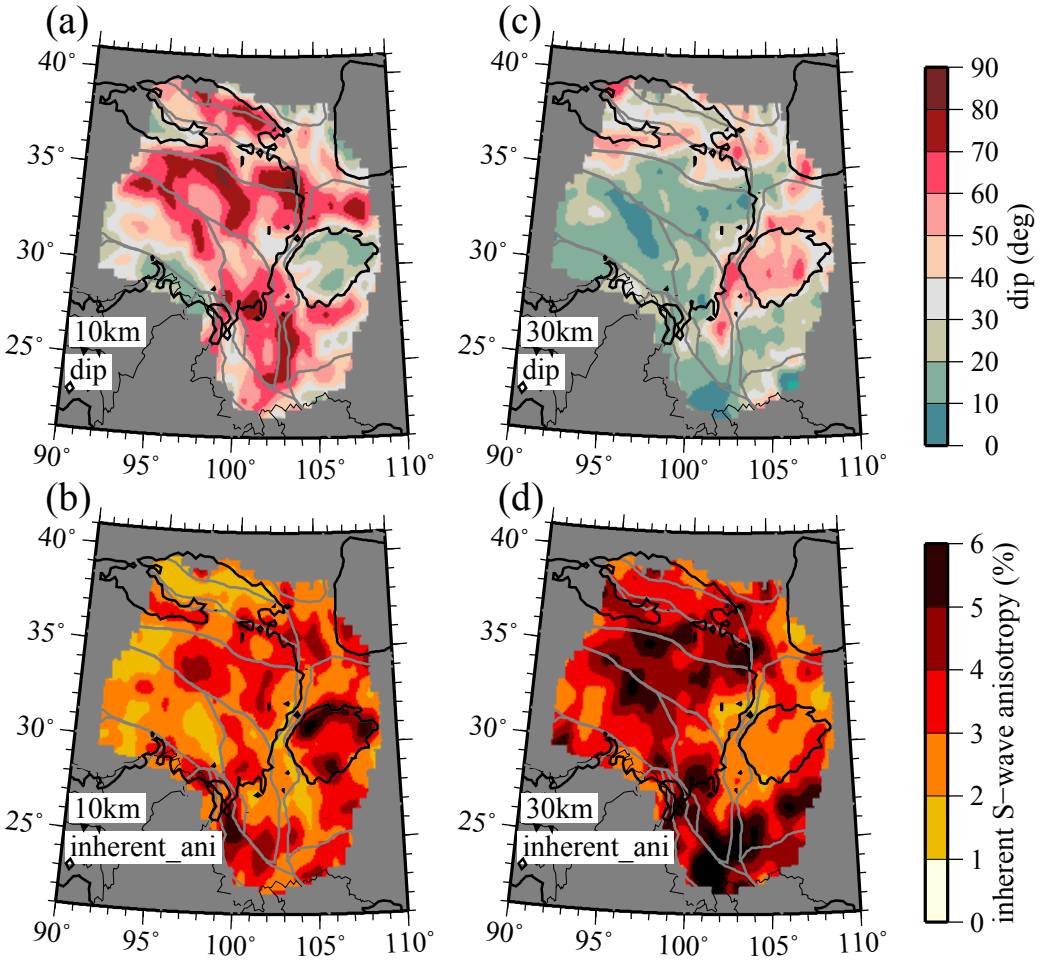

Figure 4.12. Map views of the dip angle θ and inherent S-wave anisotropy γ, respectively, at depths of: (a, b) 10 km and (c, d) 30 km.

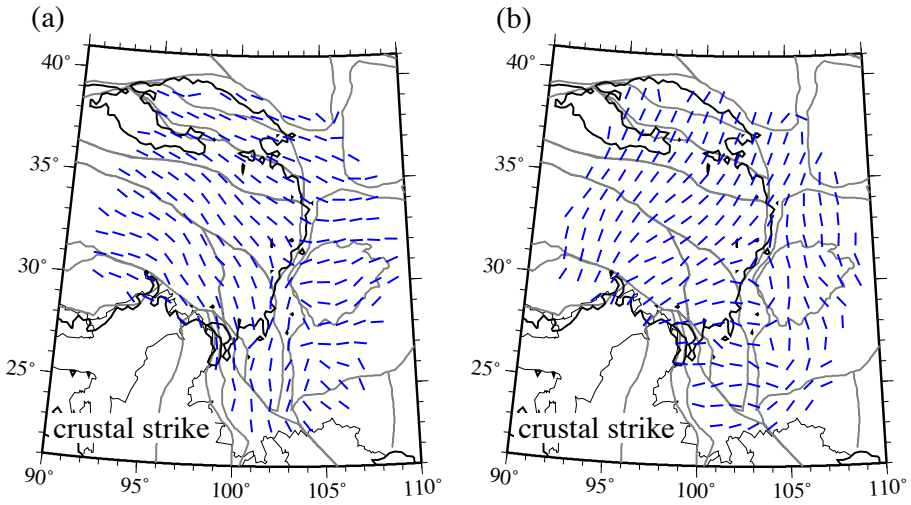

Figure 4.13. (a) The orientation of the local crustal strike angle ϕ determined here, which is constant vertically throughout the crust, is shown with blue bars. (b) Crustal strike orientation perpendicular to the results shown in (a), acknowledging the ambiguity in the estimate of the crustal strike angle.

another strike orientation that is consistent with our data, which we show in **Figure 4.13b**. We note that if the dip angle is small so that the foliation plane is nearly horizontal, the strike angle loses its significance.

At 10 km depth (**Fig. 4.12a,b**), the foliation plane in the upper crust is steeply dipping across most of the study region, including the Tibetan plateau and its surroundings. In contrast, the Qaidam basin, Ordos block, southern Tibet, and the Sichuan basin are characterized by shallow dip angles in the shallow crust. The inherent S-wave anisotropy (**Fig. 4.12b**) ranges from ~2% to ~6% across most of the study region. Inherent S-wave anisotropy in the shallow crust is not noticeably stronger in Tibet than in its surrounding areas. Because the sediments in the model are isotropic, anisotropy in the sediments may bias γ to larger values at 10 km depth beneath the deep sediments of the Sichuan and Qaidam basins.

At 30 km depth (**Fig. 4.12c,d**), the interior of eastern Tibet has a sub-horizontal foliation plane that is largely indistinguishable from a VHS medium. Near the boundaries of the Tibetan plateau, particularly between Tibet and the western Yangtze craton (including the Sichuan Basin) and in the Qilian terrane north of Tibet, the medium is moderately to steeply dipping in the middle to lower crust (**Fig. 4.12c**). The inherent S-wave anisotropy (**Fig. 4.12d**) is relatively large across the entire region of study with amplitudes ranging from about 3% to 6%. The strongest inherent S-wave radial anisotropy is observed in the interior of eastern Tibet and the Yunnan-Guizhou plateau south of the Sichuan basin. Weaker inherent S-wave anisotropy is observed near the eastern boundary of the Tibetan plateau and in the Sichuan basin and Ordos block. At most places, γ grows with depth in the crust but not beneath the major basins.

For a more complete view of crustal anisotropy, two vertical profiles of crustal inherent S-wave anisotropy and dip angle are presented in **Figure 4.14**. The locations of the two profiles

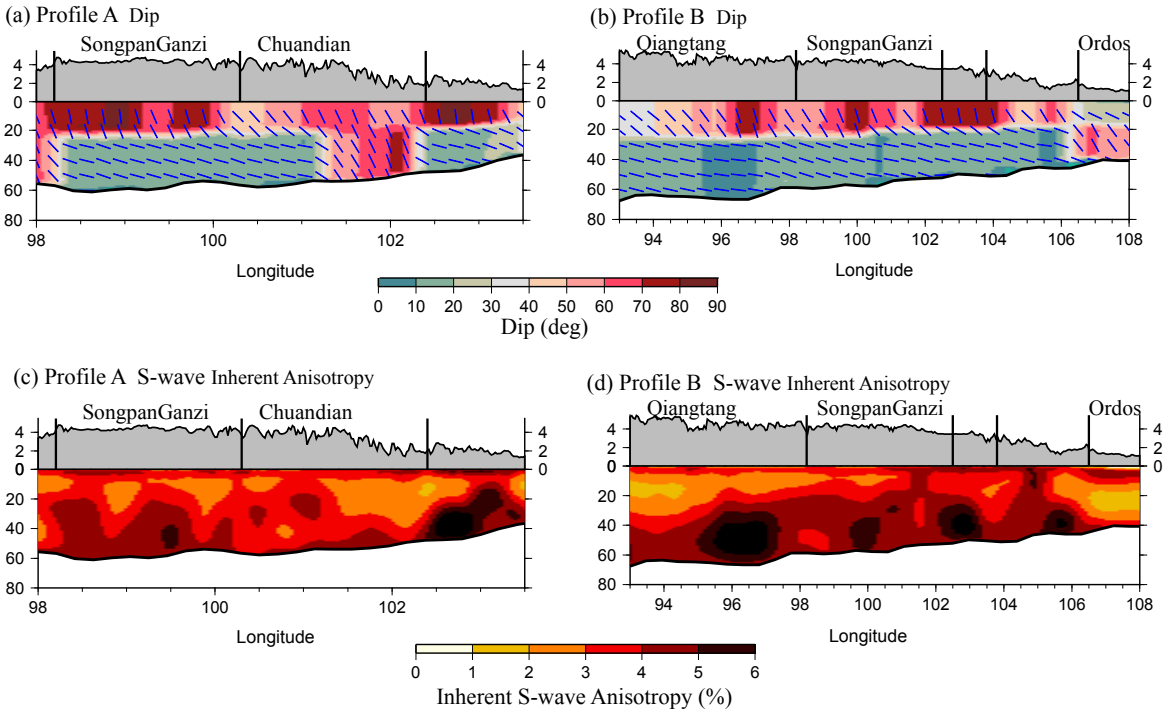

Figure 4.14. Vertical transects of inherent S-wave anisotropy γ and dip angle θ along profiles A and B identified in **Fig. 4.2b**. In (a) and (b) dip angle is color-coded and the orientation of the foliation plane is presented with short blue bars. In (c) and (d), γ is color-coded in percent. Only the crustal part of the model is presented because the mantle is parameterized in terms of apparent moduli.

are shown in **Figure 4.2b**. Profile A starts just north of the Kunlun fault east of the Qaidam basin, runs through the Songpan-Ganzi terrane of eastern Tibet and the Chuandian terrane, off the southeastern margin of Tibet, and into the Yunnan-Guizhou plateau. Profile B runs from the boundary between the Lhasa and Qiantang terranes in eastern Tibet, through the Qiangtang and Songpan-Ganzi terranes, and northeast off the Tibetan plateau to terminate just within the Ordos block. **Figures 14a** and **14b** present the dip angles along these profiles in two ways: color-coded and also with orientation bars that lie along the foliation plane at 50 km lateral intervals. The vertical bifurcation of the dip angle between the steeply dipping upper and shallowly dipping lower crust is the most striking feature of both profiles. The principal exception occurs near the southeastern border of Tibet where steeping dipping anisotropy appears throughout the entire crust (**Fig. 4.14a**). **Figures 14c** and **14d** present inherent S-wave anisotropy (γ) and illustrates that along these profiles γ tends to grow with depth in the crust. In general γ is more homogeneous laterally than vertically, although it is smaller beneath the Ordos block than elsewhere along these profiles. As discussed earlier, γ is poorly estimated below 50 km depth.

Because the lower crustal dip angle is small across most of the study region, the strike angle for the lower crust has little significance. This may be one of the reasons why a single strike angle at each location across crust suffices to fit the data in Tibet. As discussed in section 4.6.1, this is related to the fact that there is very low amplitude apparent azimuthal anisotropy in the lower crust of Tibet.

Discussion of the interpretation of these results is delayed until section 4.6.2. Comparison with apparent radial and azimuthal anisotropy, which are the more commonly estimated quantities in surface wave studies, is found in section 4.6.1. We also show γ at 5 km above Moho in section 4.6.3.1 while discussing the vertical distribution of the amplitude of inherent

anisotropy.

4.5.3 Data misfit

The misfit to the data (Rayleigh wave phase speeds, Love wave phase speeds, amplitude and fast axis directions of Rayleigh wave azimuthal anisotropy) is presented as the square root of the reduced chi-squared misfit in **Figure 4.15**. Specifically, misfit is defined as follows. For model m, let S(m) be the reduced chi-square:

$$S(m) = \frac{1}{N}\sum_{i=1}^{N}\frac{(D(m)_i - D_i)^2}{\sigma_i^2} \tag{4.8}$$

where D_i is the observation of datum i, $D(m)_i$ is that datum predicted from model m, σ_i is the standard deviation of datum i, and N is the total number of observations. The error bars in **Figure 4.5** illustrate the nature and number of the observations and their standard deviations. The misfit presented in **Figure 4.15** is the square root of *S(m)* across the study region. A value of unity would indicate that the data are fit on average at the level of one standard deviation. The data across most of the region are fit at a level better than 1.5 standard deviations, with the exception of the large sedimentary basins (Sichuan, Qaidam). To fit the data in the basins we would need to introduce anisotropy to the sediments, which complicates the inversion and is beyond the scope of this paper.

4.5.4 Results across the entire region: standard deviation of the posterior distribution

As discussed by *Shen and Ritzwoller* [2016], it is not entirely straightforward how to use the posterior distribution to quantify model uncertainty. They argue that the standard deviation of the posterior distribution does not provide an estimate of the effect of systematic errors and provides an over-estimate of the effect of non-systematic errors. They go on to quantify

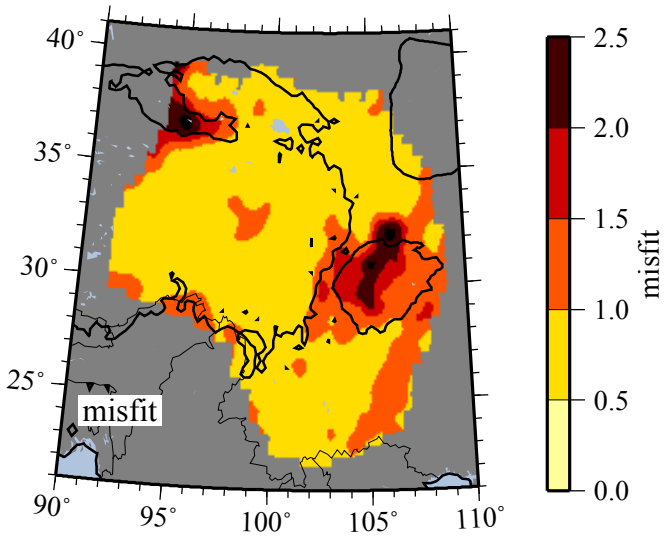

Figure 4.15. Geographic variation in data misfit produced by the best-fitting model at each location. Misfit is defined as the square root of the reduced chi-squared value at each location (eqn. (4.8)).

non-systematic errors in several different ways and estimate that the standard deviation of the posterior distribution over-estimates the effect of non-systematic errors by about a factor of 4. Here, we present the standard deviation of the posterior distribution to guide the use of the model and refer to it as model uncertainty, but it should be understood that this uncertainty does not include potential systematic contributions and is probably a very conservative estimate of non-systematic error.

The standard deviation of the posterior distribution (uncertainty) is shown in **Figure 4.1**6 at depths of 10 and 30 km for dip angle and inherent S-wave anisotropy γ. The uncertainty for dip lies between 5° and 15° at both 10 and 30 km depths in most regions remote to the Sichuan and Qaidam basins (**Figures 16a,b**). (The uncertainty beneath the basins is magnified because the data cannot be fit as well there due to the fact that we have not included anisotropy in the sediments.) In contrast, as shown in **Figure 4.16e**, the standard deviation of the posterior distribution for the strike angle is smaller, averaging about 7° outside the basins, but is larger near the periphery of our study region where the fast axis directions of Rayleigh waves are less well constrained. One reason the strike uncertainty is smaller than the dip uncertainty is because the strike angle is constrained to be constant within the crust, whereas the dip angle is allowed to change within the crust. A second reason is that strike is constrained in a direct way by observations of the Rayleigh wave fast azimuth, whereas the dip angle trades off with the inherent elastic moduli and together they are less directly constrained by our observations. The average value of 7° is close to the uncertainty for Rayleigh wave fast azimuth at short periods (e.g., **Figures 5c,f,i,l**).

The average uncertainty for inherent S-wave anisotropy (γ) is about 1.2% at 10 km depth and slightly larger at 30 km depth (**Figures 16c,d**). At both depths, the uncertainty is larger

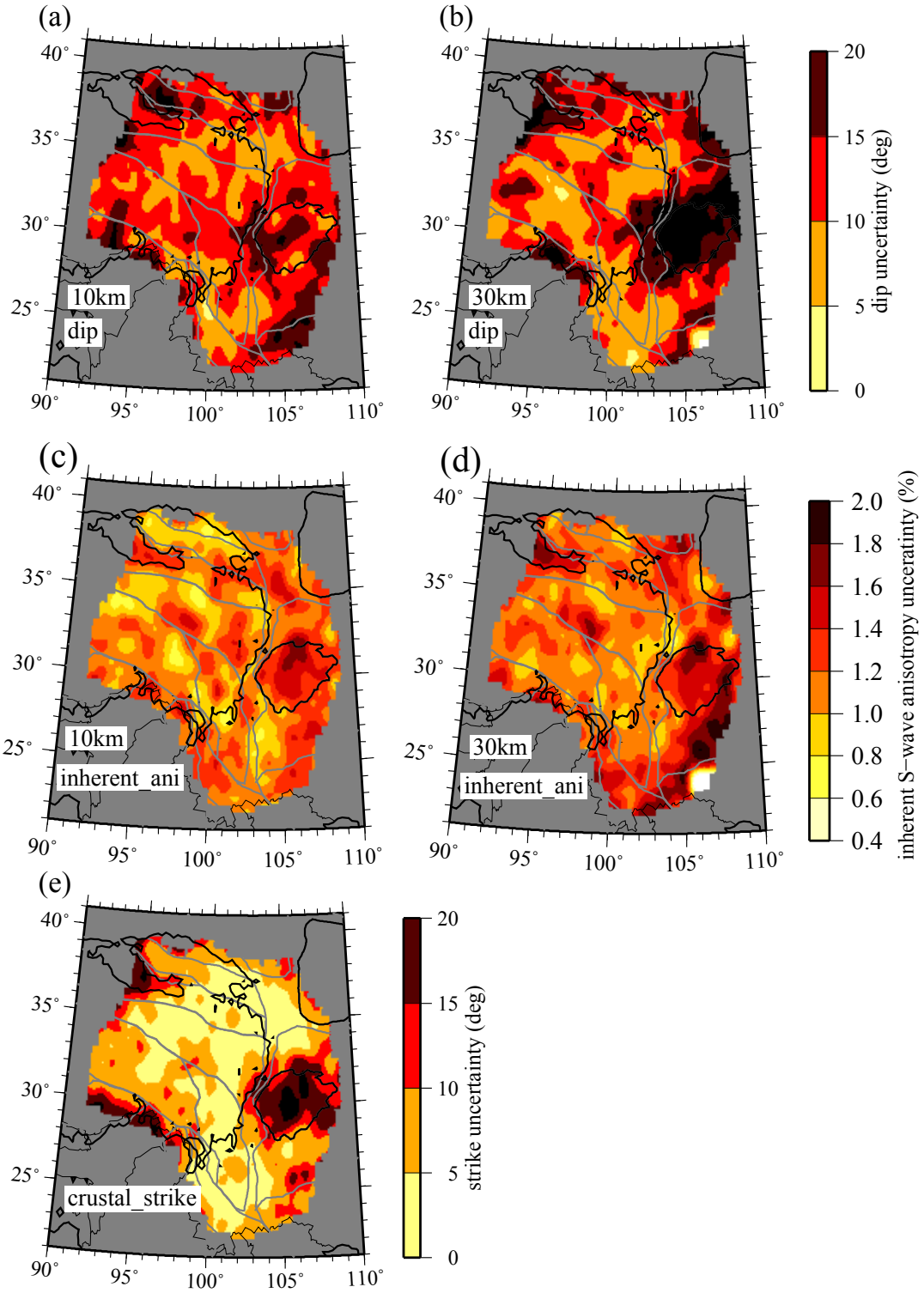

Figure 4.16. Map views of the standard deviation of the posterior distribution for (a,b) dip angle θ and (c,d) inherent S-wave anisotropy γ at depths of 10 km and 30 km, respectively. (e) Standard deviation of the posterior distribution for strike angle, which is constant in the crust.

outside of Tibet. At 30 km depth, the uncertainty is extremely large in the southeastern part of the study region. This is because uncertainty grows near to the Moho due to trade-offs across the interface. The Moho lies between 35 and 40 km where large uncertainties exist in γ. The estimated uncertainty in γ at 5 km above Moho is shown and discussed in section 4.6.3.1. Formally, it is larger at this depth than shallower in the crust but the result we show later actually underestimates uncertainty below 50 km depth because it reflects the weak anisotropy constraint ($\gamma \leqslant 10\%$), which stabilizes the inversion below a depth of 50 km and reduces the uncertainty estimate.

4.6 Discussion

4.6.1 Model presented in terms of apparent anisotropy

In section 4.5, we present the estimated THS model in terms of the mean of the posterior distribution of the inherent elastic moduli and orientation at each depth. Particular emphasis is placed on the inherent S-wave anisotropy γ (eqn. (4.5)) and the dip and strike angles (θ,ϕ) that describe the orientation of the medium because these are the variables that are best constrained by surface wave data. The inherent representation of anisotropy presents the elastic tensor in the coordinate frame of the medium as shown in **Figure 4.1**. In the medium frame, the 3-axis of the coordinate system aligns with the symmetry axis of the medium and there is no azimuthal anisotropy. However, in the coordinate system of observation the 3-axis lies normal to the Earth's surface and observations of anisotropy depend on how components of the elastic tensor are affected by the tilt of the medium. When a hexagonally symmetric medium is tilted, both apparent S-wave radial anisotropy ($\hat{\gamma}$, eqn. (4.6)) and apparent SV-wave azimuthal anisotropy ($\hat{\Gamma}$, eqn. (4.7)) may be observed. Indeed, most studies of anisotropy using surface waves have described anisotropy in terms of $\hat{\gamma}$ [e.g., *Shapiro et al*., 2004; *Panning and Romanowicz*, 2006; *Marone et al*., 2007; *Nettles and Dziewoński*, 2008; *Duret et al*., 2010; *Huang et al*., 2010; *Moschetti et al*., 2010; *Yuan et al*., 2011; *Xie et al*., 2013; *French and Romanowicz*, 2014] or $\hat{\Gamma}$ [e.g., *Simons et al*., 2002; *Marone and Romanowicz*, 2007; *Yao et al*., 2010; *Lin et al*., 2011; *Yuan et al*., 2011; *Pandey et al*., 2015]. As discussed by *Xie et al*. [2015] the apparent values can be computed from the inherent values. In order to aid comparison with other studies, we summarize here the apparent S-wave radial anisotropy and apparent azimuthal anisotropy computed from the estimated inherent elastic tensor and its orientation.

Figure 4.17 presents results for crustal apparent radial anisotropy $\hat{\gamma}$ and apparent azimuthal $\hat{\Gamma}$ anisotropy at the same locations shown for inherent S-wave anisotropy γ and dip angle θ in **Figure 4.11**. **Figure 4.17** also presents results for $\hat{\gamma}$ and $\hat{\Gamma}$ in the mantle because we parameterize the mantle in terms of apparent quantities. Mantle apparent radial anisotropy $\hat{\gamma}$ is set to 4.5% at all locations, although $\hat{V}_{SV}$ and apparent azimuthal anisotropy $\hat{\Gamma}$ change spatially.

Apparent radial anisotropy is qualitatively similar in the crust at Points A and D (**Fig. 4.17a,g**), being weakly negative in the upper crust and more strongly positive in the lower crust. $\hat{\gamma}$ attains a maximum value of about 7% at about 45 km depth at Point A and is negative (-1.5%) in the upper crust. Because the foliation plane of the lower crust is sub-horizontal across most of Tibet, inherent S-wave anisotropy γ and apparent radial anisotropy $\hat{\gamma}$ in the lower crust are very similar at Point A (**Figs. 11b, 17a**). Also at Points A and D, apparent azimuthal anisotropy $\hat{\Gamma}$ dominantly arises from the upper crust. Apparent azimuthal anisotropy is indistinguishable from zero in Tibetan lower crust (**Fig. 4.17b**), thus the lower crustal strike angle has little significance.

At Points B and C, $\hat{\gamma}$ is approximately constant in the crust. At Point C it is indistinguishable from zero even although the inherent anisotropy γ averages about 3%. This is caused by a dip angle of about 60° across the entire crust, a value that lies near the zero-crossing of anisotropy shown in **Figure 4.6**. $\hat{\Gamma}$ also is approximately constant with depth in the crust at Points B and C.

Mantle apparent radial anisotropy (4.5%) tends to be stronger than crustal radial anisotropy except at Point A in Tibet where lower crustal $\hat{\gamma}$ reaches 7%. At Point A in Tibet,

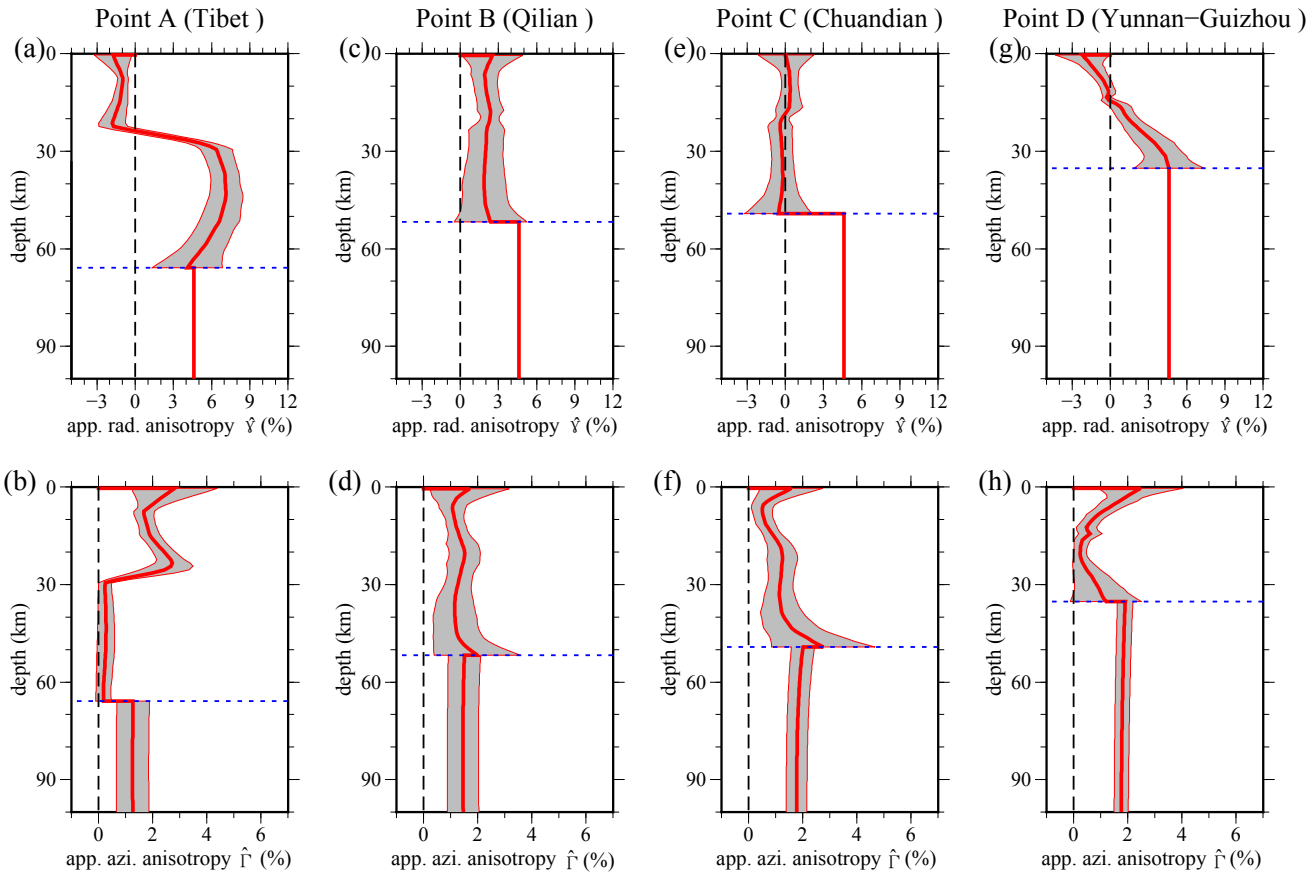

Figure 4.17. Posterior distributions of apparent radial ($\hat{\gamma}$) and apparent azimuthal ($\hat{\Gamma}$) anisotropy defined similarly to **Fig. 4.11** for comparison.

upper crustal apparent azimuthal anisotropy (2-3%) is stronger than mantle apparent azimuthal anisotropy (~1.2%).

Horizontal slices at depths of 10 km and 30 km are presented for the apparent quantities $\hat{\gamma}$ and $\hat{\Gamma}$ in **Figure 4.18**, to contrast with the inherent quantities γ and θ found in **Figure 4.12**. Negative $\hat{\gamma}$ commonly coincides with large $\hat{\Gamma}$ in the shallow crust, again due to large dip angle and is explained by **Figure 4.6**. Similarly, in the deep crust large $\hat{\gamma}$ coincides with small $\hat{\Gamma}$ due to a shallow dip angle. Finally, vertical transects of the apparent quantities $\hat{\gamma}$ and $\hat{\Gamma}$ are presented in **Figure 4.19** for comparison with the inherent quantities plotted in **Figure 4.14**.

Compared with inherent S-wave anisotropy γ, the apparent radial anisotropy $\hat{\gamma}$ (**Fig. 4.18a,c; 19a,b**) displays much stronger lateral variations because it reflects variations in dip angle in addition to inherent anisotropy. The steep dip angle in the upper crust (**Fig. 4.12a**) produces negative apparent radial anisotropy (apparent V_{SH} < apparent V_{SV}) across much of the study region (e.g., **Fig. 4.18a**), with the principal exceptions occurring beneath large sedimentary basins. **Figure 4.19** shows that the negative apparent anisotropy in the upper crust extends beneath much of both vertical profiles. Such negative $\hat{\gamma}$ values was observed across parts of Tibet by *Xie et al*. [2013], who interpreted them as evidence for steeply dipping fractures or faults in the shallow Tibetan crust. Due to the shallow lower crustal dip angles across much of the study region, γ and $\hat{\gamma}$ are similar in the lower crust. Thus across much of the region, **Figure 4.12c** is similar to **Figure 4.18c**, with the notable exceptions being in regions with steep lower crustal dip angles such as the regions flanking Tibet. Profile A in **Figure 4.19a** illustrates one of these exceptions (longitudes between 101.3° and 102.5°) and shows that negative apparent radial anisotropy extends throughout the crust in the central-to-southern part of the Chuandian terrane

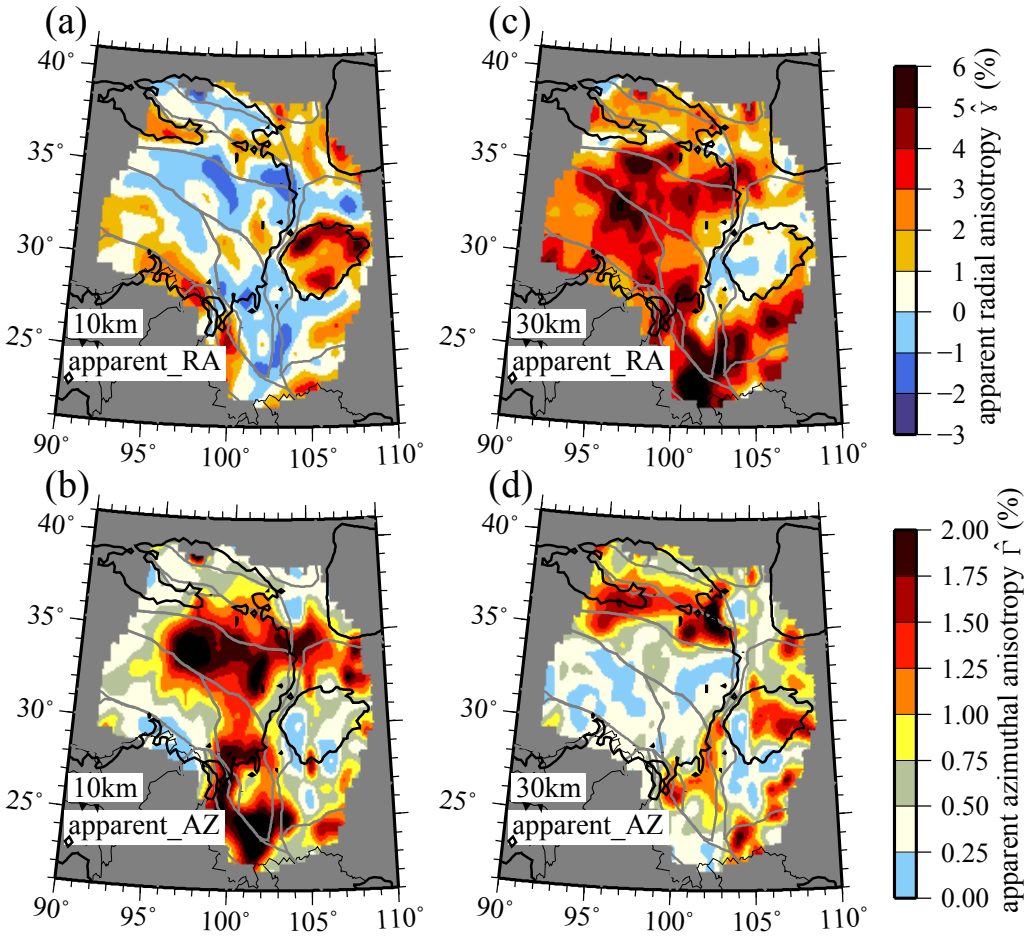

Figure 4.18. Map views of apparent radial ($\hat{\gamma}$) and apparent azimuthal ($\hat{\Gamma}$) anisotropy defined similarly to **Fig. 4.12** for comparison.

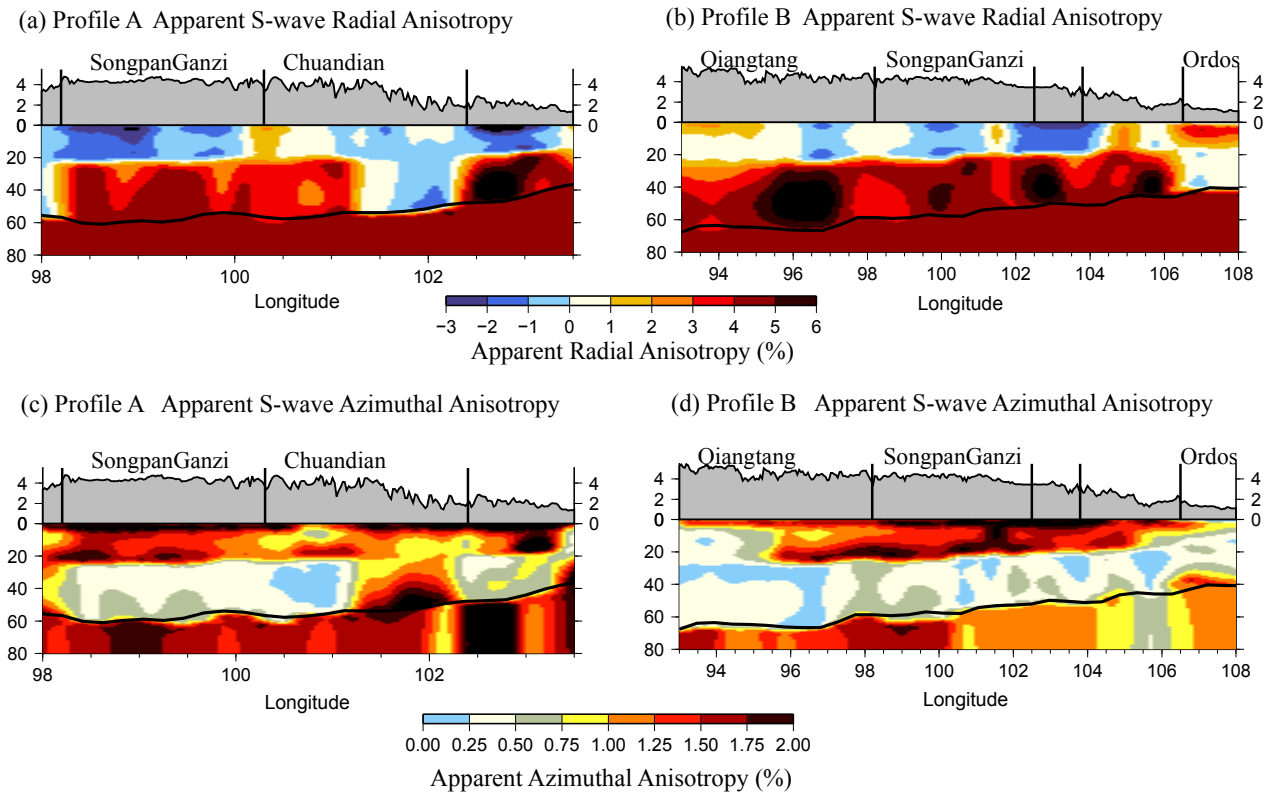

Figure 4.19. Vertical transects of apparent radial ($\hat{\gamma}$) and apparent azimuthal ($\hat{\Gamma}$) anisotropy defined similarly to **Fig. 4.14** for comparison.

near the southeast border of Tibet.

Azimuthal anisotropy is not an inherent property of the elastic tensor, but reflects the directional dependence of Rayleigh wave speeds that results from the amplitude of inherent anisotropy and the tilting of the medium. When the dip angle is small, as it is across much of the lower crust of Tibet (**Fig. 4.12c**), the apparent azimuthal anisotropy is minimal (**Fig. 4.18d**). In contrast, lower crustal apparent azimuthal anisotropy (**Fig. 4.18a**) is particularly strong near the periphery of Tibet where the lower crustal dip angle is steep. Unlike the lower crust, the upper crust is steeply dipping across much of the study region, so upper crustal apparent azimuthal anisotropy is also strong across most of the region (**Fig. 4.18b**). Apparent azimuthal anisotropy, being strong in the upper crust and weak in the lower crust at most locations, is seen clearly in the two vertical profiles in **Figure 4.19c,d**.

In summary, apparent azimuthal $\hat{\Gamma}$ and radial $\hat{\gamma}$ anisotropy bifurcate vertically in most of the study region. Apparent azimuthal anisotropy is strong principally in the upper crust whereas apparent radial anisotropy is strong mostly in the lower crust. The principal exception to this bifurcation lies predominantly near the periphery of Tibet, where the dip angle is nearly constant throughout the crust.

4.6.2 Geological and physical significance

4.6.2.1 Regionalization

The results presented here illustrate that the inferred crustal anisotropy is of two principal types that segregate into the two regions depicted in **Figure 4.20**: Region 1 (red color, Tibet and the Yunnan-Guizhou plateau region) and Region 2 (blue color, regions near the periphery of Tibet). The sedimentary basins define a third region that we do not discuss here.

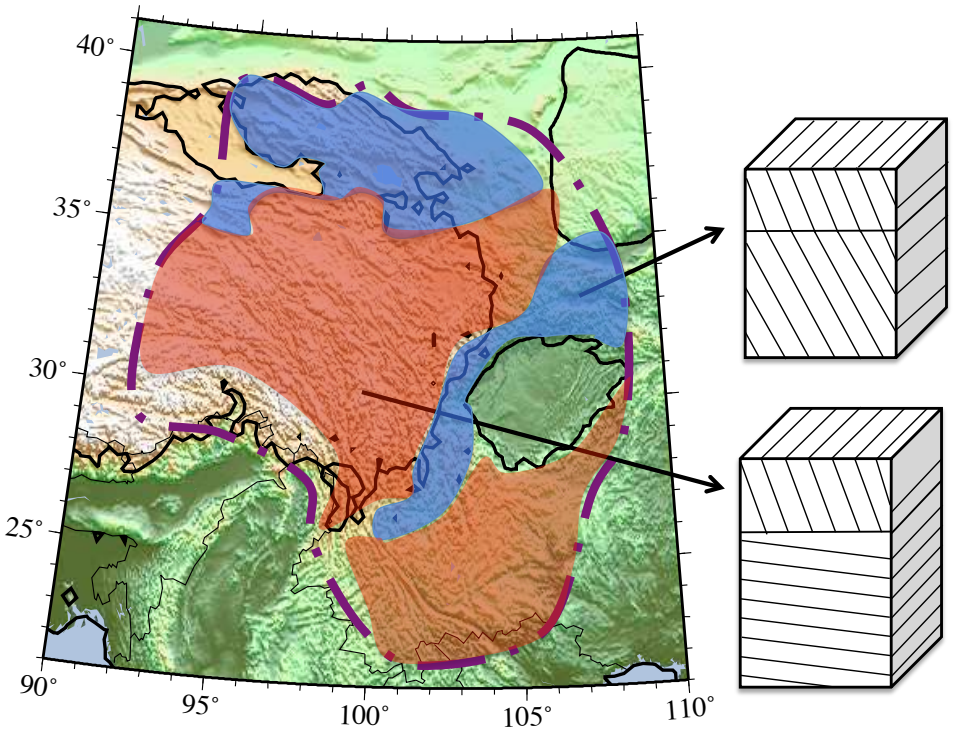

Figure 4.20. Regionalization of anisotropy in the final 3-D model. The dashed line indicates the study region. The blue shaded regions are characterized by moderately to steeply dipping foliations throughout the entire crust. The red shaded regions have foliations dipping steeply in the upper crust overlying a sub-horizontally foliated middle-to-lower crust.

Region 1: In the interior of eastern Tibet, the upper crust has a steeply dipping foliation plane, which generates negative apparent radial anisotropy, and the middle-to-lower crust has a sub-horizontal foliation in which the dip angle θ is often indistinguishable from zero. This results in a large positive apparent Vs radial anisotropy in the lower crust. Tibet itself has high seismicity with earthquakes occurring to a depth of about 15-20 km within Tibet [*Chu et al*., 2009; *Zhang et al*., 2010; *Sloan et al*., 2011]. Therefore, the upper crust to this depth probably undergoes brittle deformation. Steeply dipping foliation could result from fractures or faults that are sub-vertical or steeply dipping. In contrast, the nearly horizontal foliation plane of the middle-to-lower crust may result from the deeper crust undergoing predominantly horizontal ductile deformation in which melt-rich layers or planar mica sheets form in response to the deformation. Interestingly, this pattern of anisotropy is not unique to Tibet, but is also observed south of the Sichuan basin in the Yunnan-Guizhou Plateau.

Region 2: Near the boundary of eastern Tibet and regions north of Tibet, such as the Qilian terrane, there is a depth constant moderate dip angle through the entire crust that results in negative to slightly positive apparent radial anisotropy throughout the crust. From Region 1 to Region 2, the orientation of the middle-to-lower crustal foliation plane rotates from horizontal to moderately or steeply dipping. This lateral change of orientation may result from resistance forces applied by the rigid and relatively undeformed Sichuan basin, Yangtze craton and Ordos block.

4.6.2.2 Physical significance

Our principal results are represented with a pair of variables at each location and depth from which we can compute apparent radial and azimuthal anisotropy: inherent S-wave

anisotropy γ and dip angle θ. These variables allow us to predict the primary aspects of our observations. However, there are many constraints and assumptions underlying these results. Perhaps most significant amongst these is the assumption that the elastic tensor at all depths in the crust possesses hexagonal symmetry with a slow symmetry axis.

There are reasons to believe that hexagonal symmetry is a reasonable assumption for the crust. The cause of crustal anisotropy is related to shape preferred orientation (SPO) and lattice- or crystal-preferred orientation (CPO) of Earth's materials. In the crust, SPO can be caused by fluid-filled cracks and layering of materials with different compositions [e.g., *Crampin et al.,* 1984], and both situations can be approximated with a hexagonally symmetric medium with a slow symmetry axis. Other than SPO, another possible cause of seismic anisotropy is CPO of the crystallographic axes of elastically anisotropic minerals. Mica and amphibole are primary candidates for crustal anisotropy [*Mainprice and Nicolas,* 1989]. With increasing mica content, a deformed rock becomes anisotropic and tends to be approximately hexagonally symmetric with a slow symmetry axis [*Shao et al*., 2016; *Weisss et al*., 1999]. *Weiss et al*. [1999] argues that most deep crustal rocks are quasi-hexagonal, although some studies [e.g., *Tatham et al.,* 2008] conclude that the deep continental crust contains little mica, and amphibole is a more plausible explanation for deep crustal anisotropy. The presence of amphibole would reduce a rock's overall symmetry from hexagonal to a lower symmetry such as orthorhombic [*Shao et al.,* 2016]. Therefore, in many cases, a hexagonally symmetric medium with a slow symmetry axis is a reasonable approximation for crustal material, and in this circumstance the inferred dip and strike angles probably represent the orientation of the foliated anisotropic materials in the crust. But in the presence of abundant amphiboles, orthorhombic rather than hexagonal symmetry may be more appropriate. In this case, for example, it would not clear how to interpret the estimated dip

angle, which could be understood a proxy for deviation from hexagonal symmetry.

Even when hexagonal symmetry is an appropriate assumption for the anisotropy of crustal rocks, the dip and strikes angles shown in **Figures 4.12** and 4.**14** represent only one of several possible orientations that are consistent with surface wave data. *Xie et al. [2015]* point out that there are two principal ambiguities in orientation that arise using surface wave data alone to estimate a depth-dependent THS model. First, there is the dip ambiguity that results from a symmetry or a pure geometrical trade-off. Surface waves are not capable of distinguishing between structures with dip angle θ and angle 180° - θ (i.e., left dipping and right dipping). As a result, surface waves cannot distinguish between a structure that dips only toward one-side from a fold that is composed of a combination of left- and right-dipping foliations. Secondly, there is the strike ambiguity. Surface waves do not distinguish between anisotropic structures that differ in strike angle by 90°. This is not a geometrical symmetry but emerges because of covariances between the elastic moduli, and is related to the so-called ellipticity of the elastic tensor, as discussed in *Xie et al*. [2015]. We have eliminated this ambiguity by narrowing the range of η considered but show both strike angles in **Figure 4.13**. The limitation we imposed on the allowed η values does not affect our principal conclusions. However, it will be important in the future to attempt to distinguish between the two strike angles by invoking other data (e.g., receiver function observations).

4.6.2.3 Sedimentary basins

As discussed in section 4.4, we parameterized sedimentary basins as isotropic even though our data present evidence that the sediments are anisotropic, as seen clearly by significant data misfit under the Sichuan and Qaidam basins in **Figure 4.15**.

Figure 4.21 presents a comparison of the results of inversion of our data at a point in the

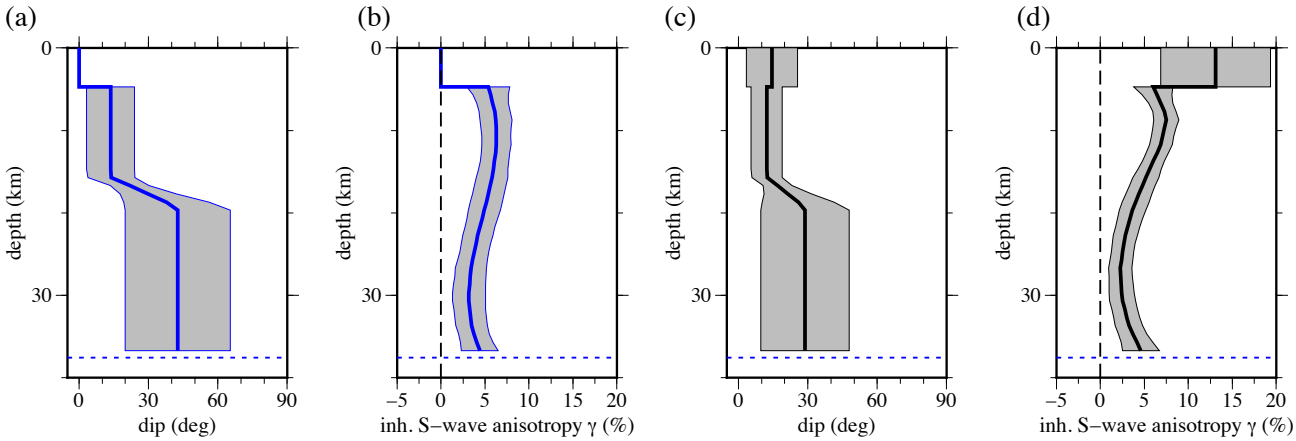

Figure 4.21. (a-b) Posterior distributions of estimated dip angle θ and inherent S-wave anisotropy γ for a point in the Sichuan basin (105°, 31°) presented as in **Fig. 4.11** with no anisotropy in the sediments. (c-d) Posterior distributions at the same location where anisotropy and an independent dip angle is allowed in the sediments.

Sichuan basin (105°, 31°) with (**Fig. 4.21c,d**) and without (**Fig. 4.21a,b**) anisotropy in the sediments. Misfit ($S^{1/2}$, equation 4.8) reduces from 3.44 to 1.40 with the introduction of anisotropy in the sediments at this point. The inherent anisotropy in the sediments is exceptionally strong (~13%) and the dip angle is shallow. Thus, the sediments dominantly produce apparent radial anisotropy with little associated apparent azimuthal anisotropy. Including anisotropy in the sediments does not strongly change inherent S-wave anisotropy in the crystalline crust (**Fig. 4.21a**,**c**) It does, however, reduce the lower crustal dip angle by about 10°, which more strongly segregates anisotropy between the upper and lower crust. However, these changes are within the estimated uncertainties. These results are similar to what we find at other locations within the Sichuan and Qaidam basins where surface wave observations are reliable and the sediments are thicker than 2 km in the reference model.

We conclude, therefore, that the specification of isotropic sediments changes our estimates of inherent S-wave anisotropy and dip angle in the crystalline crust within stated uncertainties, and does not modify the primary conclusions of the study. In the future, parameterizing the sediments to include anisotropy is recommended, but in doing so it is also advisable to include other constraints on sedimentary structure such as receiver functions or Rayleigh wave H/V to improve the estimate of sedimentary thickness. Uncertainties in the thickness of sediments directly affect estimates of the inherent anisotropy of the sediments. For example, at the point shown in **Figure 4.21**, our reference model [*Shen et al.,* 2016] indicates a sedimentary thickness of about 4 km. If the sediments were actually thicker, then the estimate of the inherent S-wave anisotropy would be smaller. Uncertainty in sedimentary thickness is one of the reasons we do not highlight structure in the basins in this paper.

4.6.3 Comparison with other studies

4.6.3.1 Vertical distribution of anisotropy in the crust

Figure 4.14c,d shows that the strength of inherent S-wave anisotropy is stronger in the middle-to-lower crust than in the upper crust across the study region. A comparison of **Figures 12b** and **12d** similarly shows this trend. To illustrate this trend, **Figure 4.22a** presents inherent S-wave anisotropy 5 km above Moho. Inherent S-wave anisotropy in the deep crust is similar to the middle crust, but stronger than the shallow crust. **Figures 18a,c, 19a,b,** and **22c** illustrate that the same trend holds for apparent radial anisotropy.

The nearly constant apparent radial anisotropy from middle to lower crust is different from the study of *Xie et al*. [2013], which concluded that apparent radial anisotropy is strongest in the middle crust. The difference between these two studies is due to two factors: (1) Love wave observations at periods below 40 sec are only weakly sensitive the shear wave speeds in the lower crust of Tibet. As a consequence, inherent S-wave anisotropy γ is poorly determined in the lowermost crust (**Fig. 4.8a**). (2) The study of *Xie et al*. [2013] and the current paper have different parameterization and place different constraints on anisotropy in the crust. *Xie et al*. [2013] uses the azimuthally invariant parts of Rayleigh and Love waves to invert for the apparent radial anisotropy $\hat{\gamma}$ without inferring the inherent properties, and $\hat{\gamma}$ is constrained to be 0 at the Moho. In contrast, the current study infers the inherent properties (e.g., γ, θ, Φ) from which apparent radial anisotropy $\hat{\gamma}$ is then derived. Here, we require $0 \leq \gamma \leq 10\%$ and the discontinuity in θ determines the resulting $\hat{\gamma}$. The result is that *Xie et al*. [2013] attempts to find a model that fits their data while minimizing lower crustal anisotropy whereas the current study applies the weak anisotropy constraint across the entire crust. The differences between the results of these two studies illustrate that the strength of anisotropy below about 50 km depth cannot be determined by the data alone, but is shaped largely by constraints imposed in the inversion.

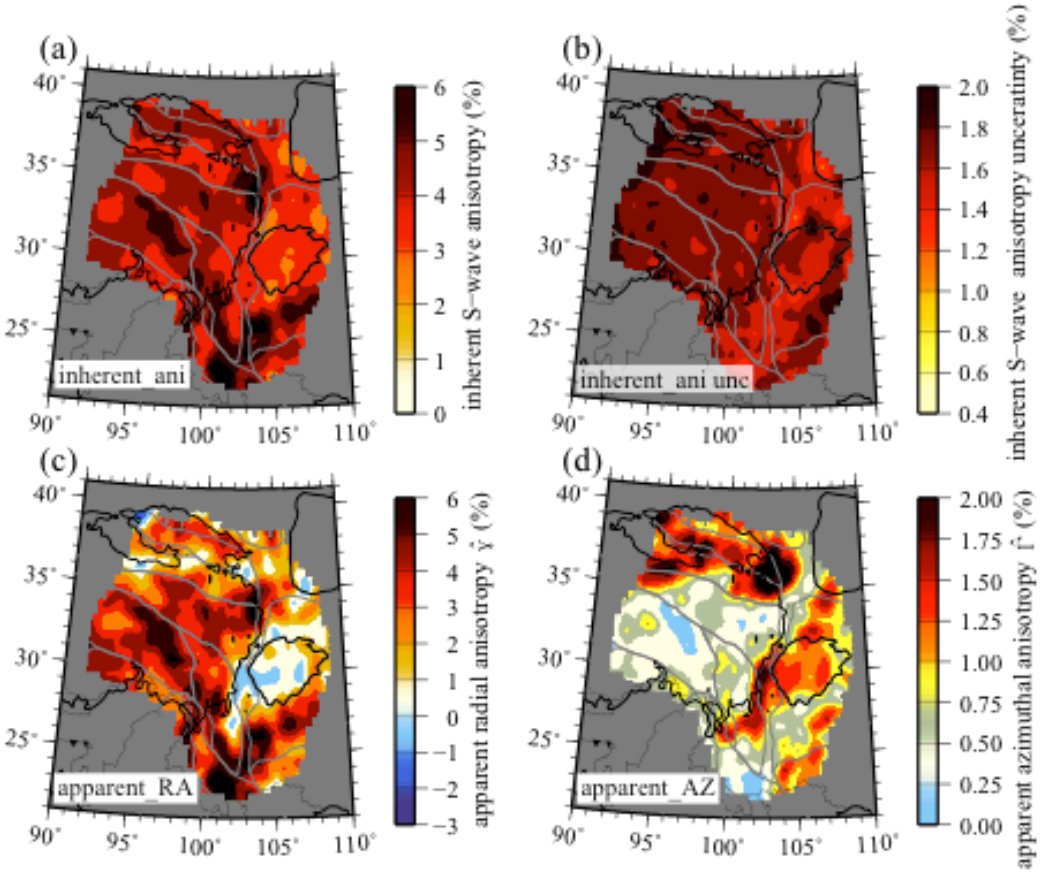

Figure 4.22. Aspects of inherent and apparent anisotropy estimated at a depth 5 km above the Moho: (a) inherent S-wave anisotropy γ, (b) standard deviation of the posterior distribution for γ, (c) apparent radial anisotropy $\hat{\gamma}$, and (d) apparent azimuthal anisotropy $\hat{\Gamma}$.

Better determination of the amplitude of inherent S-wave anisotropy in the Tibetan lower crust will require Love wave observations at periods longer than 40 s. Such measurements will probably derive from earthquake based observations rather than ambient noise.

4.6.3.2 Other aspects of the model

Many studies of Tibet might meaningfully be compared with the results we present here. We briefly discuss comparisons with three general types of studies: (1) studies that have identified differences between northern and southern Tibet, (2) studies that attempt to draw conclusions about the vertical distribution of strain near the southeast border of Tibet in the Chuandian terrane or Yunnan-Guizhou plateau, and (3) receiver function studies that attempt to produce information about crustal anisotropy.

(1) Differences between northern and southern Tibet have been widely observed in other studies. Shear wave splitting studies [e.g., *McNamara et al.,* 1994; *Huang et al.,* 2000; *Hirn et al.,* 1995] find a systematic rotation of the fast azimuth from southern to northern Tibet. Compared with southern Tibet, slower shear wave speeds [e.g., *Yang et al.,* 2012] and slower Pn velocities [e.g.,*McNamara et al*., 1997] are observed in northern Tibet. Some studies [e.g., *Huang et al*., 2000; *Nabelek et al*., 2009] suggest that 32°N marks the northern end of the subducted Indian plate. Although our study region only covers the eastern part of Tibet, we also observe differences between northern and southern Tibet on the western side of our study region. For example, compared with the southern part of our study region (Qiangtang terrane), the northern part (Songpan-Ganzi) has a steeper upper crustal dip angle (**Figures 12a, 14b**) and stronger middle crustal inherent anisotropy (**Figure 4.12d, 14d**).

(2) In southeastern Tibet (near the Chuandian terrane and the Yunnan-Guizhou plateau) the deformation mechanism remains under debate. Shear wave splitting studies observe a sharp

transition in mantle anisotropy across about 25°N latitude. North of this boundary the fast polarization orientation is mostly North-South, which is consistent with surface strain, while in the south the fast polarization orientation changes suddenly to East-West, which deviates from the surface strain [*Sol et al*., 2007; *Lev et al.,* 2006]. Such deviation was used as evidence for the decoupling between the crust and mantle near the southeastern edge of Tibet because shear wave splitting is mainly caused by mantle anisotropy.

We find a similar pattern of spatial variation in Rayleigh wave fast axis orientations in this region. For the northern part of southeastern Tibet, Rayleigh wave fast axes are nearly constant with period lying within about 20° of North-South (e.g., **Figure 4.5i** Point C), while south of 25°N latitude the fast azimuth is more complicated. It remains oriented North-South at short periods but changes to more nearly East-West at longer periods (e.g., **Figure 4.5l** Point D; **Figures 3c,d).** In our model, the crustal strike typically follows the Rayleigh wave fast azimuth at short periods (**Figures 3c, 13a**), and the mantle fast azimuth follows the Rayleigh wave fast azimuth at long periods.

We tend not to attribute the different fast axis orientations between the crust and upper mantle to decoupling between crustal and mantle strains for the following reasons. First, as pointed out by *Wang et al.* [2008] and *Fouch and Rondenay* [2006], anisotropy may manifest in the crust and mantle in very different ways for the same stress geometry. For example, crustal open cracks might align orthogonal to the direction of maximum extension, while in the mantle the fast direction of relatively dry olivine might align parallel to the maximum extension direction. Secondly, the possible existence of water or melt could make the interpretation more complicated [e.g., *Kawakatsu et al*., 2009; *Holtzman et al.*, 2003]. Moreover, as discussed in section 4.6.2.2 and by *Xie et al.* [2015], the Rayleigh wave fast azimuth and strike orientations of

anisotropy are ambiguously related to one another if non-ellipticity of anisotropy is taken into account. Therefore, it is hazardous to draw conclusions on the coupling or decoupling of the crust and mantle deformation based on seismic anisotropy observations alone. However, *Shen et al.* [2005] argue that southeastern Tibet has a weak lower crust underlying a stronger, highly fragmented upper crust by analyzing GPS data. This could provide a possible mechanism to decouple the upper crust from the upper mantle.

(3) The tilted hexagonally symmetric (THS) model that we produce is qualitatively similar to that inferred by some receiver function studies. For example, in central Tibet, *Ozacar and Zandt* [2004] used receiver functions to study the tilt of crustal anisotropy, and found that near-surface anisotropy has a steeply dipping fabric (~60°-80°), while mid-crustal anisotropy has a shallowly dipping fabric (~18°). This result qualitatively agrees with our findings across most of eastern Tibet. In addition, the strike angles of our THS model (and the fast directions of the short period Rayleigh waves) are parallel to the fast axis orientations revealed by the Moho Ps splitting near the eastern edge of the high plateau [e.g., *Sun et al*., 2015; *Kong et al.,* 2016]. *Sun et al*. [2015] further suggested that lower crustal flow may extrude upward into the upper crust along the steeply dipping strike faults under the Longmenshan area at the edge of the Sichuan Basin (Figure 4.9 in their paper), resulting in the surface uplift of the Longmenshan. Our observation of a rapid change of dip angle of the THS system from subhorizontal to subvertical beneath the same area (**Fig. 4.12c**) is consistent with this suggestion.

4.7 Summary and Conclusions

With ambient noise data recorded at CEArray, China Array, and PASSCAL stations that are located across eastern Tibet and adjacent areas, we measure Love and Rayleigh wave isotropic phase speeds and Rayleigh wave azimuthal anisotropy. In order to explain these observations jointly, we apply a method that inverts for an anisotropic medium represented by a depth-dependent tilted hexagonally symmetric (THS) elastic tensor. We perform the inversion with a Bayesian Monte Carlo method that produces depth-dependent marginal posterior distributions for the five inherent elastic moduli (A, C, N, L, and F or η) as well as dip and strike angles on a 0.5°x0.5° spatial grid. The final 3-D model is composed of the mean and standard deviation of each of these model variables.

The paper is motivated by the three questions listed in the Introduction, which are answered here. (1) Observations of apparent radial and apparent azimuthal anisotropy from surface waves can, indeed, be fit well with the oriented hexagonally symmetric elastic tensor model, analogous to the fit of similar data across the western US [*Xie et al.,* 2015]. The principal exception to this finding is that to fit the data well within the Sichuan and Qaidam basins, we would have needed to introduce very strong anisotropy into the sediments (**Fig. 4.21**), which was beyond the scope of this paper. (2) In contrast to results in the western US, we find that the data across much of the study region could not be fit with a single orientation for the elastic tensor at all depths in the crust. Specifically, we find that two dip angles (one in the upper crust and the other in the middle to lower crust) are needed in Tibet and the Yunnan-Guizhou plateau. However, a single strike angle in the crust does suffice to allow the data to be fit near the periphery of Tibet. (3) The vertical distribution of anisotropy within Tibet is similar to that beneath the Yunnan-Guizhou plateau, but both regions differ from the periphery of Tibet where

only a single dip angle is need.

Our results, therefore, segregate the area of study into two regions based on crustal anisotropy. Region 1 includes the interior of eastern Tibet and the Yunnan-Guizhou plateau. In this region, steeply dipping upper crust overlies shallowly dipping middle to lower crust and inherent S-wave anisotropy γ (eqn. (4.5)) is strong throughout the crust with larger amplitudes in the middle-to-lower crust. As a result, the apparent radial anisotropy $\hat{\gamma}$ (eqn. (4.6)) and apparent azimuthal anisotropy $\hat{\Gamma}$ (eqn. (4.7)) bifurcate vertically. $\hat{\gamma}$ tends to be weak and negative in the upper crust and is strong and positive in the middle-to-lower crust while $\hat{\Gamma}$ is strong mostly in the upper crust. The steep dip to the symmetry axis in the upper crust may result from fractures or faults that are sub-vertical or steeply dipping. In contrast, the sub-horizontal or shallow dipping symmetry axes in the middle-to-lower crust may result from ductile deformation that aligns the orientation of anisotropic minerals such as mica. Region 2 covers the edge of eastern Tibet and regions north of Tibet where the foliation across entire crust has a moderate to steep dip angle and inherent S-wave anisotropy γ does not change strongly with depth. As a result, apparent radial anisotropy $\hat{\gamma}$ is negative to slightly positive through the entire crust, and apparent azimuthal anisotropy $\hat{\Gamma}$ is strong throughout the crust. The more steeply dipping foliation planes may be caused by the reorientation of anisotropic minerals as crustal flows rotate and shear near the border of Tibet, which may result from resistance forces imposed by the more rigid and relatively undeformed surroundings to Tibet.

In the future, the introduction of other data sets may improve the current inversion, which is based exclusively on surface waves from ambient noise. Such information could provide new insight into crustal and mantle deformation and the generation of more realistic petrologic

models that agree with the elastic tensors inferred. (1) Azimuthal variations in receiver functions [e.g., *Levin and Park, 1997,1998*; *Ozacar and Zandt, 2004; 2009*; *Schulte-Pelkum and Mahan, 2014a,b*] as well as the splitting of the P-to-S converted phase [e.g., *Rumpker et al., 2014*; *Sun et al., 2015a*] can provide important point constraints on crustal anisotropy and could also help to identify depths at which crustal anisotropy changes dip angle. In some areas receiver function waveforms observe clear azimuthal variations, and these waveforms could be inverted simultaneously for the layered THS system [e.g., *Ozacar and Zandt et al.,* 2004; *Schulte-Pelkum and Mahan,* 2014a] together with surface wave data. (2) Rayleigh wave H/V ratio provides sensitivity to the velocity structure at shallow depths (upper ~5km), and would help to resolve anisotropy in the sedimentary basins. (3) Shear wave splitting, both SKS and the splitting of Moho converted P-to-S phases, could be combined with surface wave data to provide additional constraints on the depth-integrated amplitude of apparent azimuthal anisotropy [e.g., *Lin et al.,* 2010; *Montagner* et al., 2000]. (4) In addition, longer period surface wave measurements are needed to improve estimates of mantle anisotropy, including the type of anisotropy (e.g., hexagonal symmetry with a fast or slow symmetry axis, orthorhombic symmetry) and the orientation of the anisotropic media.

CHAPTER V

CONCLUSION AND FUTURE PLAN

5.1 Summary and conclusions

In this thesis, I have developed an oriented elastic tensor inversion method that explains different aspects of the surface wave observations simultaneously in terms of a tilted hexagonally symmetric medium. The surface wave measurements from large arrays, the development of this method, and its application to W. US, and E. Tibet form the major components of this thesis.

The oriented elastic tensor inversion method inverts for the inherent properties of the medium represented by a hexagonally symmetric elastic tensor, with an arbitrarily oriented symmetry axis, which I refer to as 'tilted'. The elastic tensor at each depth is described by 5 elastic moduli (A, C, N, L and F) and the tilt is defined by 2 rotation angles: the dip and strike, which are illustrated in Figure 1.1b. In total, 7 depth dependent parameters describe this tilted hexagonally symmetric medium (or THS). We refer to the 5 elastic moduli as 'inherent', as they reflect the characteristics of the elastic tensor irrespective of its orientation. Limited by the fact that surface wave data are strongly sensitive to part of the 7 unknowns, a straightforward inversion for the THS is impractical using surface wave data alone. Therefore, we cast the inversion problem in terms of a Bayesian Monte Carlo approach in which we estimate a range of elastic tensors that agree with the data.

Comparing with traditional practices, this new approach possesses some significant advantages. First, different aspects of surface wave measurements are used simultaneously to obtain one simple and self-consistent model. Inferences about the inherent elastic properties of the medium are obtained and apparent properties can then be derived, however, traditionally very

few studies try to infer the inherent properties or the orientations of the medium. Second, the Bayesian Monte Carlo inversion enables the assumptions and prior constraints on the model to be clearly presented in terms of prior distributions. Besides, this process utilizes the uncertainties from surface wave measurements, and naturally propagates the data uncertainty into the model uncertainty.

The major conclusions drawn from the thesis are summarized here.

- With large arrays, high quality surface wave measurements with error estimates can be obtained. We have performed extensive seismic data processing on continuous data recorded at seismic arrays in US and China. In the US, I use over 800 Transportable Array (TA) stations of Earthscope/USArray deployed from 2005 to 2010, and in China, ~ 800 stations from arrays deployed by different agencies between 2000 and 2012 are compiled through collaborations with multiple scientists. These data are processed to perform surface wave tomography, and measurements of Love wave speeds and azimuthally varying Rayleigh wave speeds together with their uncertainties are constructed. Chapter II, III and IV describe aspects of the data processing, and details of data quality control can be found in *Zhou et al*. [2012], which is not included in this thesis.

- Overall, the oriented elastic tensor inversion method explains the surface wave data well in both W. US and E. Tibet, subject to the constraints listed in Chapters III and IV.

- In W. US, the tilt angles (dip, strike) are constrained to be depth-constant in the crust.

Inherent S-wave anisotropy is fairly homogeneous vertically across the crust, on average, and spatially across the W. US. And the orientations of the hexagonally symmetric medium are geologically correlated.

The estimated dip may be interpreted in two alternative ways. It is either an actual measure of the dip of the foliation plane of anisotropic material within the crust, or it is proxy for another non-geometric variable, most likely a measure of deviation from hexagonal symmetry. First, it is possible that the observed dip angle is proxy for other variables. Even though our models are expressed in terms of a tilted hexagonally symmetric medium, the approximation to hexagonal symmetry may not be accurate everywhere. Therefore, the dip may be a result of approximating orthorhombic or other lower-symmetry material with hexagonal symmetry. Second, it is likely to be at least some component of dip is related to the actual dip of the foliation of the material. In fact, spatial variations of dip make geologic sense in some regions. For example, observed dip are shallow beneath the Basin and Range province, which is consistent with large-scale crustal extension along low-angle normal faults and horizontal detachment faults. The steeper dips observed in California are also consistent with a lower crust consisting of foliated schist.

There are two groups of THS fit the data equally well; one group has nearly elliptical anisotropy while the other group has non-elliptical anisotropy, and their strikes orthogonal to each other. Therefore, interpretation of surface wave (Rayleigh wave) fast axis direction in terms of crustal structure must be performed with caution.

- In E. Tibet, THS with depth-constant orientation cannot explain the data in some regions (e.g., part of E. Tibet and part of Yunnan-Guizhou Plateau). Therefore, THS with depth-

varying orientation is introduced to solve this problem. The dip is allowed to be different between the upper 1/3 and lower 2/3 of the crust, while the strike is constrained to be the same through the entire crust.

Our results segregate the area of study into two regions:

Region 1 includes the interior of E. Tibetan Plateau and the Yunnna-Guizhou plateau. In this region, steeply dipping upper crust overlies shallowly dipping middle to lower crust and inherent S-wave anisotropy is strong throughout the crust with larger amplitudes in the middle to lower crust. As a result, the apparent radial anisotropy and apparent azimuthal anisotropy bifurcate vertically. Apparent radial anisotropy tends to be negative in the upper crust and is strong and positive in the middle-to-lower crust while apparent azimuthal anisotropy is strong mostly in the upper crust. The steep dip to the symmetry axis in the upper crust may result from cracks or faults that are sub-vertical or steeply dipping. In contrast, the sub-horizontal or shallow dipping symmetry axes in the middle-to-lower crust may result from ductile deformation that aligns the orientations of anisotropic minerals such as mica.

Region 2 covers the edge of eastern Tibet and regions north of Tibet where the entire crust has a moderate to steep dip angle and inherent S-wave anisotropy does not change strongly with depth. As a result, apparent radial anisotropy is negative to slightly positive through the entire crust, and apparent azimuthal anisotropy is strong throughout the crust. The more steeply dipping foliation planes may be caused by the reorientation of anisotropic minerals as crustal flows rotate and shear near the border of Tibet, which may result from resistance forces imposed by the rigid and relatively undeformed

surroundings to Tibet.

5.2 Future work

There are a few works that can be proposed for the future:

- Add different data to the inversion. (1) Receiver functions could help to determine intra-crustal discontinuities related to features such as a mid-crustal low velocity zone, and also help to identify depths at which crustal anisotropy changes dip angle. In some areas receiver function waveforms observe clear azimuthal variations, and these waveforms could be inverted simultaneously for the layered THS system [e.g., *Ozacar and Zandt et al.,* 2004; *Schulte-Pelkim and Mahan* 2015] together with surface wave data. (2) Rayleigh wave H/V ratio provides sensitivity to the velocity structure at shallow depths (upper ~5km), and would help to resolve anisotropy in the sedimentary basins. (3) Shear wave splitting, both SKS and the splitting of Moho converted P-to-S phases, could be combined with surface wave data to provide additional constraints on the depth-integrated amplitude of apparent azimuthal anisotropy.
- Investigate more about elliptical and non-elliptical anisotropy. The concept of non-elliptical anisotropy is not well recognized in the global seismology, while it is commonly used in the field of petrology and exploration geophysics. The effect of non-elliptical anisotropy on the seismic waves is not well understood in global seismology, and could be an interesting area for future study.
- Move beyond hexagonal symmetry. As discussed in both Chapter III and Chapter IV, although we assume the crustal material to be hexagonally symmetric following the

traditional simplification, there are reasons to believe that the crustal material is more complex than hexagonally symmetry. And there are papers talking about effect of orthorhombic symmetry [e.g., *Tsvankin*, 1997]. Therefore, as quality and quantity of seismic data increases, moving beyond hexagonal symmetry may be the future direction, as it may provide more accurate description of the Earth's elastic property.

- Improve long period data. Upper mantle anisotropy provides important information on the dynamic of the lithosphere, therefore, it would be interesting to apply this oriented elastic tensor method to image mantle anisotropy. However, some of the assumptions I made in the crust are probably not appropriate for the mantle. For example, unlike mica the anisotropy related to olivine is probably orthorhombic in symmetry or hexagonal in symmetry but with a fast symmetry axis.
- Understand how anisotropy scales up. Petrology studies provide important information on understanding the seismic anisotropy. However, the study of petrology and seismology are at very different scales, and it is unclear how does large scale structures (e.g., fold) affect the overall anisotropy measured by seismic data.
- Ultimately, one may aim to interpret the results in terms of petrological models that agree with the inferred elastic tensors.

BIBLIOGRAPHY

Acton, C. E., K. Priestley, V. K. Gaur, and S. S. Rai (2010), Group velocity tomography of the Indo-Eurasian collision zone, *J. Geophys. Res. Solid Earth*, *115*(B12), B12335, doi:10.1029/2009JB007021.

Agius, M. R., and S. Lebedev (2014), Shear-velocity structure, radial anisotropy and dynamics of the Tibetan crust, *Geophys. J. Int.*, *199*(3), 1395–1415, doi:10.1093/gji/ggu326.

Aki, K. and K. Kaminuma (1963), Phase velocity of Love waves in Japan, 1, Love wave from the Aleutian shock of March 9, 1957, *Bull. Earthquake Res. Inst. Univ. Tokyo*, 41, 243-260.

Anderson, D. L. (1961), Elastic wave propagation in layered anisotropic media, *J. Geophys. Res.*, *66*(9), 2953–2963, doi:10.1029/JZ066i009p02953.

Anderson, D. L., and J. Regan (1983), Uppermantle anisotropy and the oceanic lithosphere, *Geophys. Res. Lett.*, *10*(9), 841–844, doi:10.1029/GL010i009p00841.

Anderson, D. L., B. Minster, and D. Cole (1974), The effect of oriented cracks on seismic velocities, *J. Geophys. Res.*, *79*(26), 4011–4015, doi:10.1029/JB079i026p04011.

Auld, B. A. (1973), *Acoustic fields and waves in solids*, Wiley.

Babuška, V. (1991), *Seismic Anisotropy in the Earth*, Modern approaches in geophysics v. 10, Kluwer Academic Publishers, Dordrecht, The Netherlands ; Boston.

Backus, G. E. (1962), Long-wave elastic anisotropy produced by horizontal layering, *J. Geophys. Res.*, *67*(11), 4427–4440, doi:10.1029/JZ067i011p04427.

Barmin, M. P., M. H. Ritzwoller, and A. L. Levshin (2001), A Fast and Reliable Method for Surface Wave Tomography, *Pure Appl. Geophys.*, *158*(8), 1351–1375, doi:10.1007/PL00001225.

Beaumont, C., R. A. Jamieson, M. H. Nguyen, and B. Lee (2001), Himalayan tectonics explained by extrusion of a low-viscosity crustal channel coupled to focused surface denudation, *Nature*, *414*(6865), 738–742, doi:10.1038/414738a.

Beghein, C., and J. Trampert (2004), Probability density functions for radial anisotropy from fundamental mode surface wave data and the Neighbourhood Algorithm, *Geophys. J. Int.*, *157*(3), 1163–1174, doi:10.1111/j.1365-246X.2004.02235.x.

Bensen, G. D., M. H. Ritzwoller, M. P. Barmin, A. L. Levshin, F. Lin, M. P. Moschetti, N. M. Shapiro, and Y. Yang (2007), Processing seismic ambient noise data to obtain

reliable broad-band surface wave dispersion measurements, *Geophys. J. Int.*, *169*(3), 1239–1260, doi:10.1111/j.1365-246X.2007.03374.x.

Bensen, G. D., M. H. Ritzwoller, and Y. Yang (2009), A 3-D shear velocity model of the crust and uppermost mantle beneath the United States from ambient seismic noise, *Geophys. J. Int.*, *177*(3), 1177–1196, doi:10.1111/j.1365-246X.2009.04125.x.

Bianchi, I., N. Piana Agostinetti, P. De Gori, and C. Chiarabba (2008), Deep structure of the Colli Albani volcanic district (central Italy) from receiver functions analysis, *J. Geophys. Res. Solid Earth*, *113*(B9), B09313, doi:10.1029/2007JB005548.

Bianchi, I., J. Park, N. Piana Agostinetti, and V. Levin (2010), Mapping seismic anisotropy using harmonic decomposition of receiver functions: An application to Northern Apennines, Italy, *J. Geophys. Res. Solid Earth*, *115*(B12), B12317, doi:10.1029/2009JB007061.

Bokelmann, G. H. R. (2002), Convection-driven motion of the North American craton: Evidence from P-wave anisotropy, *Geophys. J. Int.*, *148*(2), 278–287, doi:10.1046/j.1365-246X.2002.01614.x.

Bollinger, L., P. Henry, and J. Avouac (2006), Mountain building in the Nepal Himalaya: Thermal and kinematic model, *Earth Planet. Sci. Lett.*, *244*(1-2), 58–71, doi:10.1016/j.epsl.2006.01.045.

Brocher, T. M. (2005), Empirical relations between elastic wavespeeds and eensity in the Earth's crust, *Bull. Seismol. Soc. Am.*, *95*(6), 2081–2092, doi:10.1785/0120050077.

Brownlee, S. J., B. R. Hacker, M. Salisbury, G. Seward, T. A. Little, S. L. Baldwin, and G. A. Abers (2011), Predicted velocity and density structure of the exhuming Papua New Guinea ultrahigh-pressure terrane, *J. Geophys. Res. Solid Earth*, *116*(B8), B08206, doi:10.1029/2011JB008195.

Burgos, G., J.-P. Montagner, E. Beucler, Y. Capdeville, A. Mocquet, and M. Drilleau (2014), Oceanic lithosphere-asthenosphere boundary from surface wave dispersion data, *J. Geophys. Res. Solid Earth*, *119*(2), 1079–1093, doi:10.1002/2013JB010528.

Caldwell, W. B., S. L. Klemperer, S. S. Rai, and J. F. Lawrence (2009), Partial melt in the upper-middle crust of the northwest Himalaya revealed by Rayleigh wave dispersion, *Tectonophysics*, *477*(1–2), 58–65, doi:10.1016/j.tecto.2009.01.013.

Carcione, J. J. M. (2007), *Wave Fields in Real Media: Wave Propagation in Anisotropic, Anelastic, Porous and Electromagnetic Media*, Elsevier.

Champion, M. E. S., N. J. White, S. M. Jones, and K. F. Priestley (2006), Crustal velocity structure of the British Isles; a comparison of receiver functions and wide-angle seismic data, *Geophys. J. Int.*, *166*(2), 795–813, doi:10.1111/j.1365-246X.2006.03050.x.

Chapman, A. D., S. Kidder, J. B. Saleeby, and M. N. Ducea (2010), Role of extrusion of the Rand and Sierra de Salinas schists in Late Cretaceous extension and rotation of the southern Sierra Nevada and vicinity, *Tectonics*, *29*(5), TC5006, doi:10.1029/2009TC002597.

Chen, Y., J. Badal, and Z. Zhang (2009), Radial anisotropy in the crust and upper mantle beneath the Qinghai-Tibet Plateau and surrounding regions, *J. Asian Earth Sci.*, *36*(4–5), 289–302, doi:10.1016/j.jseaes.2009.06.011.

Christensen, N. I. (1984), The magnitude, symmetry and origin of upper mantle anisotropy based on fabric analyses of ultramafic tectonites, *Geophys. J. Int.*, *76*(1), 89–111, doi:10.1111/j.1365-246X.1984.tb05025.x.

Christensen, N. I., and W. D. Mooney (1995), Seismic velocity structure and composition of the continental crust: A global view, *J. Geophys. Res. Solid Earth*, *100*(B6), 9761–9788, doi:10.1029/95JB00259.

Chu, R., L. Zhu, and D. V. Helmberger (2009), Determination of earthquake focal depths and source time functions in central Asia using teleseismic P waveforms, *Geophys. Res. Lett.*, *36*, doi:10.1029/2009GL039494.

Clark, M. K., and L. H. Royden (2000), Topographic ooze: Building the eastern margin of Tibet by lower crustal flow, *Geology*, *28*(8), 703–706, doi:10.1130/0091-7613(2000)28<703:TOBTEM>2.0.CO;2.

Copley, A., J.-P. Avouac, and B. P. Wernicke (2011), Evidence for mechanical coupling and strong Indian lower crust beneath southern Tibet, *Nature*, *472*(7341), 79–81, doi:10.1038/nature09926.

Cotte, N., H. Pedersen, M. Campillo, J. Mars, J. F. Ni, R. Kind, E. Sandvol, and W. Zhao (1999), Determination of the crustal structure in southern Tibet by dispersion and amplitude analysis of Rayleigh waves, *Geophys. J. Int.*, *138*(3), 809–819, doi:10.1046/j.1365-246x.1999.00927.x.

Crampin, S. (1984), Effective anisotropic elastic constants for wave propagation through cracked solids, *Geophys. J. Int.*, *76*(1), 135–145, doi:10.1111/j.1365-246X.1984.tb05029.x.

Crampin, S., and D. W. King (1977), Evidence for anisotropy in the upper mantle beneath Eurasia from the polarization of higher mode seismic surface waves, *Geophys. J. Int.*, *49*(1), 59–85, doi:10.1111/j.1365-246X.1977.tb03701.x.

Deng, Q., P. Zhang, Y. Ran, X. Yang, W. Min, and Q. Chu (2003), Basic characteristics of active tectonics of China, *Sci. China Ser. Earth Sci.*, *46*(4), 356–372, doi:10.1360/03yd9032.

Deng, Y., W. Shen, T. Xu, and M. H. Ritzwoller (2015), Crustal layering in northeastern Tibet: a case study based on joint inversion of receiver functions and surface wave dispersion, *Geophys. J. Int.*, *203*(1), 692–706, doi:10.1093/gji/ggv321.

Duret, F., N. M. Shapiro, Z. Cao, V. Levin, P. Molnar, and S. Roecker (2010), Surface wave dispersion across Tibet: Direct evidence for radial anisotropy in the crust, *Geophys. Res. Lett.*, *37*(16), L16306, doi:10.1029/2010GL043811.

Dziewonski, A. M., and D. L. Anderson (1981), Preliminary reference Earth model, *Phys. Earth Planet. Inter.*, *25*(4), 297–356, doi:10.1016/0031-9201(81)90046-7.

Ekström, G. (2013), Love and Rayleigh phase-velocity maps, 5–40 s, of the western and central USA from USArray data, *Earth Planet. Sci. Lett.*, doi:10.1016/j.epsl.2013.11.022.

Ekstrom, G., and A. M. Dziewonski (1998), The unique anisotropy of the Pacific upper mantle, *Nature*, *394*(6689), 168–172, doi:10.1038/28148.

England, P., and P. Molnar (1997), Active deformation of Asia: From kinematics to dynamics, *Science*, *278*(5338), 647–650, doi:10.1126/science.278.5338.647.

Erdman, M. E., B. R. Hacker, G. Zandt, and G. Seward (2013), Seismic anisotropy of the crust: electron-backscatter diffraction measurements from the Basin and Range, *Geophys. J. Int.*, *195*(2), 1211–1229, doi:10.1093/gji/ggt287.

Forsyth, D. W. (1975), The Early Structural Evolution and Anisotropy of the Oceanic Upper Mantle, *Geophys. J. Int.*, *43*(1), 103–162, doi:10.1111/j.1365-246X.1975.tb00630.x.

Forsyth, D. W., and A. Li (2005), Array Analysis of Two-Dimensional Variations in Surface Wave Phase Velocity and Azimuthal Anisotropy in the Presence of Multipathing Interference, in *Seismic Earth: Array Analysis of Broadband Seismograms*, edited by A. Levander and G. Nolet, pp. 81–97, American Geophysical Union.

Fouch, M. J., and S. Rondenay (2006), Seismic anisotropy beneath stable continental interiors, *Phys. Earth Planet. Inter.*, *158*(2–4), 292–320, doi:10.1016/j.pepi.2006.03.024.

Fouch, M. J., K. M. Fischer, E. M. Parmentier, M. E. Wysession, and T. J. Clarke (2000), Shear wave splitting, continental keels, and patterns of mantle flow, *J. Geophys. Res. Solid Earth*, *105*(B3), 6255–6275, doi:10.1029/1999JB900372.

Francheteau, J., C. Jaupart, S. X. Jie, K. Wen-Hua, L. De-Lu, B. Jia-Chi, W. Hung-Pin, and D. Hsia-Yeu (1984), High heat flow in southern Tibet, *Nature*, *307*(5946), 32–36, doi:10.1038/307032a0.

Frederiksen, A. W., H. Folsom, and G. Zandt (2003), Neighbourhood inversion of teleseismic Ps conversions for anisotropy and layer dip, *Geophys. J. Int.*, *155*(1), 200–212, doi:10.1046/j.1365-246X.2003.02043.x.

French, S. W., and B. A. Romanowicz (2014), Whole-mantle radially anisotropic shear velocity structure from spectral-element waveform tomography, *Geophys. J. Int.*, *199*(3), 1303–1327, doi:10.1093/gji/ggu334.

Gaherty, J. B., and T. H. Jordan (1995), Lehmann Discontinuity as the Base of an Anisotropic Layer Beneath Continents, *Science*, *268*(5216), 1468–1471, doi:10.1126/science.268.5216.1468.

Gee, L. S., and T. H. Jordan (1992), Generalized seismological data functionals, *Geophys. J. Int.*, *111*(2), 363–390, doi:10.1111/j.1365-246X.1992.tb00584.x.

Gung, Y., M. Panning, and B. Romanowicz (2003), Global anisotropy and the thickness of continents, *Nature*, *422*(6933), 707–711, doi:10.1038/nature01559.

Guo, Z., X. Gao, H. Yao, J. Li, and W. Wang (2009), Midcrustal low-velocity layer beneath the central Himalaya and southern Tibet revealed by ambient noise array tomography, *Geochem. Geophys. Geosystems*, *10*(5), Q05007, doi:10.1029/2009GC002458.

Guo, Z., X. Gao, W. Wang, and Z. Yao (2012), Upper- and mid-crustal radial anisotropy beneath the central Himalaya and southern Tibet from seismic ambient noise tomography, *Geophys. J. Int.*, *189*(2), 1169–1182, doi:10.1111/j.1365-246X.2012.05425.x.

Hacker, B. R., M. H. Ritzwoller, and J. Xie (2014), Partially melted, mica-bearing crust in Central Tibet, *Tectonics*, *33*(7), 2014TC003545, doi:10.1002/2014TC003545.

Helbig, K., and L. Thomsen (2005), 75-plus years of anisotropy in exploration and reservoir seismics: A historical review of concepts and methods, *GEOPHYSICS*, *70*(6), 9ND–23ND, doi:10.1190/1.2122407.

Hess, H. H. (1964), Seismic Anisotropy of the Uppermost Mantle under Oceans, *Nature*, *203*(4945), 629–631, doi:10.1038/203629a0.

Hirn, A. et al. (1995), Seismic anisotropy as an indicator of mantle flow beneath the Himalayas and Tibet, *Nature*, *375*(6532), 571–574, doi:10.1038/375571a0.

Holtzman, B. K., D. L. Kohlstedt, M. E. Zimmerman, F. Heidelbach, T. Hiraga, and J. Hustoft (2003), Melt Segregation and Strain Partitioning: Implications for Seismic Anisotropy and Mantle Flow, *Science*, *301*(5637), 1227–1230, doi:10.1126/science.1087132.

Houseman, G., and P. England (1993), Crustal thickening versus lateral expulsion in the Indian-Asian continental collision, *J. Geophys. Res. Solid Earth*, *98*(B7), 12233–12249, doi:10.1029/93JB00443.

Huang, H., H. Yao, and R. D. van der Hilst (2010), Radial anisotropy in the crust of SE Tibet and SW China from ambient noise interferometry, *Geophys. Res. Lett.*, *37*, 5 PP., doi:201010.1029/2010GL044981.

Huang, W.-C. et al. (2000), Seismic polarization anisotropy beneath the central Tibetan Plateau, *J. Geophys. Res. Solid Earth*, *105*(B12), 27979–27989, doi:10.1029/2000JB900339.

Jacobson, C. E. (1983), Structural geology of the Pelona Schist and Vincent thrust, San Gabriel Mountains, California, *Geol. Soc. Am. Bull.*, *94*(6), 753–767, doi:10.1130/0016-7606(1983)94<753:SGOTPS>2.0.CO;2.

Jacobson, C. E., M. Grove, A. Vućić, J. N. Pedrick, and K. A. Ebert (2007), Exhumation of the Orocopia Schist and associated rocks of southeastern California: Relative roles of erosion, synsubduction tectonic denudation, and middle Cenozoic extension, *Geol. Soc. Am. Spec. Pap.*, *419*, 1–37, doi:10.1130/2007.2419(01).

Jaxybulatov, K., N. M. Shapiro, I. Koulakov, A. Mordret, M. Landès, and C. Sens-Schönfelder (2014), A large magmatic sill complex beneath the Toba caldera, *Science*, *346*(6209), 617–619, doi:10.1126/science.1258582.

Jiang, M., S. Zhou, E. Sandvol, X. Chen, X. Liang, Y. J. Chen, and W. Fan (2011), 3-D lithospheric structure beneath southern Tibet from Rayleigh-wave tomography with a 2-D seismic array, *Geophys. J. Int.*, *185*(2), 593–608, doi:10.1111/j.1365-246X.2011.04979.x.

John, B. E., and D. A. Foster (1993), Structural and thermal constraints on the initiation angle of detachment faulting in the southern Basin and Range: The Chemehuevi Mountains case study, *Geol. Soc. Am. Bull.*, *105*(8), 1091–1108, doi:10.1130/0016-7606(1993)105<1091:SATCOT>2.3.CO;2.

Johnson, R. A., and K. L. Loy (1992), Seismic reflection evidence for seismogenic low-angle faulting in southeastern Arizona, *Geology*, *20*(7), 597–600, doi:10.1130/0091-7613(1992)020<0597:SREFSL>2.3.CO;2.

Jolivet, L., P. Davy, and P. Cobbold (1990), Right-lateral shear along the Northwest Pacific Margin and the India-Eurasia Collision, *Tectonics*, *9*(6), 1409–1419, doi:10.1029/TC009i006p01409.

Kang, D., W. Shen, J. Ning, and M. H. Ritzwoller (2015), Seismic evidence for lithospheric modification associated with intracontinental volcanism in Northeastern China, *Geophys. J. Int.*, *204*(1), 215–235, doi:10.1093/gji/ggv441.

Kawakatsu, H., P. Kumar, Y. Takei, M. Shinohara, T. Kanazawa, E. Araki, and K. Suyehiro (2009), Seismic evidence for sharp lithosphere-asthenosphere boundaries of oceanic plates, *Science*, *324*(5926), 499–502, doi:10.1126/science.1169499.

Kawasaki, I., and F. Kon'no (1984), Azimuthal Anisotropy of Surface Waves and the Possible Type of the Seismic Anisotropy Due to Preferred Orientation of Olivine in the Uppermost Mantle Beneath the Pacific Ocean, *J. Phys. Earth*, *32*(3), 229–244, doi:10.4294/jpe1952.32.229.

Kennett, B. L. N., E. R. Engdahl, and R. Buland (1995), Constraints on seismic velocities in the Earth from traveltimes, *Geophys. J. Int.*, *122*(1), 108–124, doi:10.1111/j.1365-246X.1995.tb03540.x.

Kind, R., G. L. Kosarev, L. I. Makeyeva, and L. P. Vinnik (1985), Observations of laterally inhomogeneous anisotropy in the continental lithosphere, *Nature*, *318*(6044), 358–361, doi:10.1038/318358a0.

Kind, R., J. Ni, W. J. Zhao, J. X. Wu, X. H. Yuan, L. S. Zhao, E. Sandvol, C. Reese, J. Nabelek, and T. Hearn (1996), Evidence from earthquake data for a partially molten crustal layer in southern Tibet, *Science*, *274*(5293), 1692–1694, doi:10.1126/science.274.5293.1692.

Kind, R. et al. (2002), Seismic Images of Crust and Upper Mantle Beneath Tibet: Evidence for Eurasian Plate Subduction, *Science*, *298*(5596), 1219–1221, doi:10.1126/science.1078115.

Kong, F., J. Wu, K. H. Liu, and S. S. Gao (2016), Crustal anisotropy and ductile flow beneath the eastern Tibetan Plateau and adjacent areas, *Earth Planet. Sci. Lett.*, *442*, 72–79, doi:10.1016/j.epsl.2016.03.003.

Kustowski, B., G. Ekström, and A. M. Dziewoński (2008), Anisotropic shear-wave velocity structure of the Earth's mantle: A global model, *J. Geophys. Res. Solid Earth*, *113*(B6), B06306, doi:10.1029/2007JB005169.

Laske, G. and G. Masters (1997), A global digital map of sediment thickness, *EOS Trans. AGU,* 78, F483.

Laske, G., and G. Masters (1998), Surface-wave polarization data and global anisotropic structure, *Geophys. J. Int.*, *132*(3), 508–520, doi:10.1046/j.1365-246X.1998.00450.x.

Le Fort, P. (1975). "Himalayas, the collided range: Present Knowledge of the continental arc". *American Journal of Science* 275A: 1–44

Lev, E., M. D. Long, and R. D. van der Hilst (2006), Seismic anisotropy in Eastern Tibet from shear wave splitting reveals changes in lithospheric deformation, *Earth Planet. Sci. Lett.*, *251*(3–4), 293–304, doi:10.1016/j.epsl.2006.09.018.

Levin, V., and J. Park (1997a), Crustal anisotropy in the Ural Mountains Foredeep from teleseismic receiver functions, *Geophys. Res. Lett.*, *24*(11), 1283–1286, doi:10.1029/97GL51321.

Levin, V., and J. Park (1997b), P-SH conversions in a flat-layered medium with anisotropy of arbitrary orientation, *Geophys. J. Int.*, *131*(2), 253–266, doi:10.1111/j.1365-246X.1997.tb01220.x.

Levin, V., W. Menke, and J. Park (1999), Shear wave splitting in the Appalachians and the Urals: A case for multilayered anisotropy, *J. Geophys. Res. Solid Earth*, *104*(B8), 17975–17993, doi:10.1029/1999JB900168.

Levshin, A. L., and M. H. Ritzwoller (2001), Automated Detection, Extraction, and Measurement of Regional Surface Waves, *Pure Appl. Geophys.*, *158*(8), 1531–1545, doi:10.1007/PL00001233.

Li, H., W. Su, C.-Y. Wang, and Z. Huang (2009), Ambient noise Rayleigh wave tomography in western Sichuan and eastern Tibet, *Earth Planet. Sci. Lett.*, *282*(1–4), 201–211, doi:10.1016/j.epsl.2009.03.021.

Lin, F.-C., and M. H. Ritzwoller (2011), Helmholtz surface wave tomography for isotropic and azimuthally anisotropic structure, *Geophys. J. Int.*, *186*(3), 1104–1120, doi:10.1111/j.1365-246X.2011.05070.x.

Lin, F.-C., M. H. Ritzwoller, and R. Snieder (2009), Eikonal tomography: surface wave tomography by phase front tracking across a regional broad-band seismic array, *Geophys. J. Int.*, *177*(3), 1091–1110, doi:10.1111/j.1365-246X.2009.04105.x.

Lin, F.-C., M. H. Ritzwoller, Y. Yang, M. P. Moschetti, and M. J. Fouch (2011), Complex and variable crustal and uppermost mantle seismic anisotropy in the western United States, *Nat. Geosci.*, *4*(1), 55–61, doi:10.1038/ngeo1036.

Lin, F.-C., B. Schmandt, and V. C. Tsai (2012), Joint inversion of Rayleigh wave phase velocity and ellipticity using USArray: Constraining velocity and density structure in the upper crust, *Geophys. Res. Lett.*, *39*(12), L12303, doi:10.1029/2012GL052196.

Liu, H., and F. Niu (2012), Estimating crustal seismic anisotropy with a joint analysis of radial and transverse receiver function data, *Geophys. J. Int.*, *188*(1), 144–164, doi:10.1111/j.1365-246X.2011.05249.x.

Li, X., D. Wei, X. Yuan, R. Kind, P. Kumar, and H. Zhou (2011), Details of the Doublet Moho Structure beneath Lhasa, Tibet, Obtained by Comparison of P and S Receiver Functions, *Bull. Seismol. Soc. Am.*, *101*(3), 1259–1269, doi:10.1785/0120100163.

Mainprice, D., and A. Nicolas (1989), Development of shape and lattice preferred orientations: application to the seismic anisotropy of the lower crust, *J. Struct. Geol.*, *11*(1–2), 175–189, doi:10.1016/0191-8141(89)90042-4.

Mainprice, D., and P. G. Silver (1993), Interpretation of SKS-waves using samples from the subcontinental lithosphere, *Phys. Earth Planet. Inter.*, *78*(3), 257–280, doi:10.1016/0031-9201(93)90160-B.

Mainprice, D. (2007), Seismic anisotropy of the deep Earth from a mineral and rock physics perspective, in Treatise in Geophysics, 2, 437-492, Schubert, G., ed. Elsevier, Oxford.

Masters, G., M. P. Barmine, and S. Kientz (2007), Mineos user's manual, in Computational Infrastructure for Geodynamics, Calif. Inst. of Technol., Pasadena

Malavieille, J. (1993), Late Orogenic extension in mountain belts: Insights from the basin and range and the Late Paleozoic Variscan Belt, *Tectonics*, *12*(5), 1115–1130, doi:10.1029/93TC01129.

Marone, F., and B. Romanowicz (2007), The depth distribution of azimuthal anisotropy in the continental upper mantle, *Nature*, *447*(7141), 198–201, doi:10.1038/nature05742.

Marone, F., Y. Gung, and B. Romanowicz (2007), Three-dimensional radial anisotropic structure of the North American upper mantle from inversion of surface waveform data, *Geophys. J. Int.*, *171*(1), 206–222, doi:10.1111/j.1365-246X.2007.03465.x.

McEvilly, T. V. (1964), Central U.S. crust—Upper mantle structure from Love and Rayleigh wave phase velocity inversion, *Bull. Seismol. Soc. Am.*, *54*(6A), 1997–2015.

Mcnamara, D., T. Owens, P. Silver, and F. Wu (1994), Shear-Wave Anisotropy Beneath the Tibetan Plateau, *J. Geophys. Res.-Solid Earth*, *99*(B7), 13655–13665, doi:10.1029/93JB03406.

McNamara, D. E., W. R. Walter, T. J. Owens, and C. J. Ammon (1997), Upper mantle velocity structure beneath the Tibetan Plateau from Pn travel time tomography, *J. Geophys. Res. Solid Earth*, *102*(B1), 493–505, doi:10.1029/96JB02112.

Mechie, J., R. Kind, and J. Saul (2011), The seismological structure of the Tibetan Plateau crust and mantle down to 700 km depth, *Geol. Soc. Lond. Spec. Publ.*, *353*(1), 109–125, doi:10.1144/SP353.7.

Mechie, J. et al. (2012), Crustal shear (S) velocity and Poisson's ratio structure along the INDEPTH IV profile in northeast Tibet as derived from wide-angle seismic data, *Geophys. J. Int.*, *191*(2), 369–384, doi:10.1111/j.1365-246X.2012.05616.x.

Meissner, R., W. Rabbel, and H. Kern (2006), Seismic lamination and anisotropy of the Lower Continental Crust, *Tectonophysics*, *416*(1–4), 81–99, doi:10.1016/j.tecto.2005.11.013.

Molnar, P., and P. Tapponnier (1975), Cenozoic Tectonics of Asia: Effects of a Continental Collision, *Science*, *189*(4201), 419–426, doi:10.1126/science.189.4201.419.

Montagner, J.-P., and D. L. Anderson (1989a), Constrained reference mantle model, *Phys. Earth Planet. Inter.*, *58*(2–3), 205–227, doi:10.1016/0031-9201(89)90055-1.

Montagner, J.-P., and D. L. Anderson (1989b), Petrological constraints on seismic anisotropy, *Phys. Earth Planet. Inter.*, *54*(1–2), 82–105, doi:10.1016/0031-9201(89)90189-1.

Montagner, J.-P., and N. Jobert (1988), Vectorial tomography—II. Application to the Indian Ocean, *Geophys. J.*, *94*(2), 309–344, doi:10.1111/j.1365-246X.1988.tb05904.x.

Montagner, J.-P., and H.-C. Nataf (1986), A simple method for inverting the azimuthal anisotropy of surface waves, *J. Geophys. Res.*, *91*(B1), 511, doi:10.1029/JB091iB01p00511.

Montagner, J.-P., and H.-C. Nataf (1988), Vectorial tomography—I. Theory, *Geophys. J.*, *94*(2), 295–307, doi:10.1111/j.1365-246X.1988.tb05903.x.

Montagner, J.-P., and T. Tanimoto (1991), Global upper mantle tomography of seismic velocities and anisotropies, *J. Geophys. Res. Solid Earth*, *96*(B12), 20337–20351, doi:10.1029/91JB01890.

Montagner, J.-P., D.-A. Griot-Pommera, and J. Lavé (2000), How to relate body wave and surface wave anisotropy?, *J. Geophys. Res.*, *105*(B8), 19015–19,027, doi:10.1029/2000JB900015.

Moschetti, M. P., M. H. Ritzwoller, F.-C. Lin, and Y. Yang (2010a), Crustal shear wave velocity structure of the western United States inferred from ambient seismic noise and earthquake data, *J. Geophys. Res.*, *115*, 20 PP., doi:2010 10.1029/2010JB007448.

Moschetti, M. P., M. H. Ritzwoller, F. Lin, and Y. Yang (2010b), Seismic evidence for widespread western-US deep-crustal deformation caused by extension, *Nature*, *464*(7290), 885–889, doi:10.1038/nature08951.

Nábělek, J., G. Hetényi, J. Vergne, S. Sapkota, B. Kafle, M. Jiang, H. Su, J. Chen, B.-S. Huang, and the H.-C. Team (2009), Underplating in the Himalaya-Tibet Collision Zone Revealed by the Hi-CLIMB Experiment, *Science*, *325*(5946), 1371–1374, doi:10.1126/science.1167719.

Nelson et al. (1996), Partially Molten Middle Crust Beneath Southern Tibet: Synthesis of Project INDEPTH Results, *Science*, *274*(5293), 1684–1688.

Nettles, M., and A. M. Dziewoński (2008), Radially anisotropic shear velocity structure of the upper mantle globally and beneath North America, *J. Geophys. Res.*, *113*, 27 PP., doi:200810.1029/2006JB004819.

Nishizawa, O., and T. Yoshino (2001), Seismic velocity anisotropy in mica-rich rocks: an inclusion model, *Geophys. J. Int.*, *145*(1), 19–32, doi:10.1111/j.1365-246X.2001.00331.x.

Okaya, D., N. Christensen, D. Stanley, T. Stern, and S. I. G. T. (SIGHT) W. Group (1995), Crustal anisotropy in the vicinity of the Alpine Fault Zone, South Island, New Zealand, *N. Z. J. Geol. Geophys.*, *38*(4), 579–583, doi:10.1080/00288306.1995.9514686.

Okaya, D. A., and N. I. Christensen (2002), Anisotropic effects of non-axial seismic wave propagation in foliated crustal rocks, *Geophys. Res. Lett.*, *29*(11), 2–1–2–4, doi:10.1029/2001GL014285.

Okaya, D. A., and T. V. McEvilly (2003), Elastic wave propagation in anisotropic crustal material possessing arbitrary internal tilt, *Geophys. J. Int.*, *153*(2), 344–358, doi:10.1046/j.1365-246X.2003.01896.x.

Ozacar, A. A., and G. Zandt (2004), Crustal seismic anisotropy in central Tibet: Implications for deformational style and flow in the crust, *Geophys. Res. Lett.*, *31*(23), L23601, doi:10.1029/2004GL021096.

Ozacar, A. A., and G. Zandt (2009), Crustal structure and seismic anisotropy near the San Andreas Fault at Parkfield, California, *Geophys. J. Int.*, *178*(2), 1098–1104, doi:10.1111/j.1365-246X.2009.04198.x.

Pandey, S., X. Yuan, E. Debayle, F. Tilmann, K. Priestley, and X. Li (2015), Depth-variant azimuthal anisotropy in Tibet revealed by surface wave tomography, *Geophys. Res. Lett.*, *42*(11), 2015GL063921, doi:10.1002/2015GL063921.

Panning, M., and B. Romanowicz (2006), A three-dimensional radially anisotropic model of shear velocity in the whole mantle, *Geophys. J. Int.*, *167*(1), 361–379, doi:10.1111/j.1365-246X.2006.03100.x.

Park, J., and V. Levin (2002), Seismic Anisotropy: Tracing Plate Dynamics in the Mantle, *Science*, *296*(5567), 485 –489, doi:10.1126/science.1067319.

Poli, P., H. A. Pedersen, and M. Campillo (2013), Noise directivity and group velocity tomography in a region with small velocity contrasts: the northern Baltic shield, *Geophys. J. Int.*, *192*(1), 413–424, doi:10.1093/gji/ggs034.

Raitt, R. W., G. G. Shor, T. J. G. Francis, and G. B. Morris (1969), Anisotropy of the Pacific upper mantle, *J. Geophys. Res.*, *74*(12), 3095–3109, doi:10.1029/JB074i012p03095.

Rapine, R., F. Tilmann, M. West, J. Ni, and A. Rodgers (2003), Crustal structure of northern and southern Tibet from surface wave dispersion analysis, *J. Geophys. Res. Solid Earth*, *108*(B2), 2120, doi:10.1029/2001JB000445.

Readman, P. W., F. Hauser, B. M. O'Reilly, and V. C. Do (2009), Crustal anisotropy in southwest Ireland from analysis of controlled source shear-wave data, *Tectonophysics*, *474*(3–4), 571–583, doi:10.1016/j.tecto.2009.04.029.

Ribe, N. M. (1992), On the relation between seismic anisotropy and finite strain, *J. Geophys. Res. Solid Earth*, *97*(B6), 8737–8747, doi:10.1029/92JB00551.

Ritzwoller, M., and A. Levshin (2002), Estimating shallow shear velocities with marine multicomponent seismic data, *GEOPHYSICS*, *67*(6), 1991–2004, doi:10.1190/1.1527099.

Ritzwoller, M. H., F.-C. Lin, and W. Shen (2011), Ambient noise tomography with a large seismic array, *Comptes Rendus Geosci.*, *343*(8–9), 558–570, doi:10.1016/j.crte.2011.03.007.

Royden, L. H., B. C. Burchfiel, R. W. King, E. Wang, Z. Chen, F. Shen, and Y. Liu (1997), Surface Deformation and Lower Crustal Flow in Eastern Tibet, *Science*, *276*(5313), 788–790, doi:10.1126/science.276.5313.788.

Rümpker, G., A. Kaviani, and K. Latifi (2014), Ps-splitting analysis for multilayered anisotropic media by azimuthal stacking and layer stripping, *Geophys. J. Int.*, *199*(1), 146–163, doi:10.1093/gji/ggu154.

Savage, M. K. (1998), Lower crustal anisotropy or dipping boundaries? Effects on receiver functions and a case study in New Zealand, *J. Geophys. Res. Solid Earth*, *103*(B7), 15069–15087, doi:10.1029/98JB00795.

Savage, M. K. (1999), Seismic anisotropy and mantle deformation: What have we learned from shear wave splitting?, *Rev. Geophys.*, *37*(1), 65–106, doi:10.1029/98RG02075.

Savage, M. K., F.-C. Lin, and J. Townend (2013), Ambient noise cross-correlation observations of fundamental and higher-mode Rayleigh wave propagation governed by basement resonance, *Geophys. Res. Lett.*, *40*(14), 3556–3561, doi:10.1002/grl.50678.

Schlue, J. W., and L. Knopoff (1977), Shear-wave polarization anisotropy in the Pacific Basin, *Geophys. J. Int.*, *49*(1), 145–165, doi:10.1111/j.1365-246X.1977.tb03706.x.

Schulte-Pelkum, V., and K. H. Mahan (2014a), A method for mapping crustal deformation and anisotropy with receiver functions and first results from USArray, *Earth Planet. Sci. Lett.*, *402*, 221–233, doi:10.1016/j.epsl.2014.01.050.

Schulte-Pelkum, V., and K. H. Mahan (2014b), Imaging Faults and Shear Zones Using Receiver Functions, *Pure Appl. Geophys.*, 1–25, doi:10.1007/s00024-014-0853-4.

Shao, T., S. Ji, S. Oya, K. Michibayashi, and Q. Wang (2016), Mica-dominated seismic properties of mid-crust beneath west Yunnan (China) and geodynamic implications, *Tectonophysics*, doi:10.1016/j.tecto.2016.04.024.

Shapiro, N. M., and M. Campillo (2004), Emergence of broadband Rayleigh waves from correlations of the ambient seismic noise, *Geophys. Res. Lett.*, *31*(7), n/a–n/a, doi:10.1029/2004GL019491.

Shapiro, N. M., and M. H. Ritzwoller (2002), Monte-Carlo inversion for a global shear-velocity model of the crust and upper mantle, *Geophys. J. Int.*, *151*(1), 88–105, doi:10.1046/j.1365-246X.2002.01742.x.

Shapiro, N. M., M. H. Ritzwoller, P. Molnar, and V. Levin (2004), Thinning and flow of Tibetan crust constrained by seismic anisotropy, *Science*, *305*(5681), 233–236, doi:10.1126/science.1098276.

Shapiro, N. M., M. Campillo, L. Stehly, and M. H. Ritzwoller (2005), High-Resolution Surface-Wave Tomography from Ambient Seismic Noise, *Science*, *307*(5715), 1615–1618, doi:10.1126/science.1108339.

Shen, W., and M. H. Ritzwoller (2016), Crustal and uppermost mantle structure beneath the United States, *J. Geophys. Res. Solid Earth*, 2016JB012887, doi:10.1002/2016JB012887.

Shen, W., M. H. Ritzwoller, and V. Schulte-Pelkum (2013a), A 3-D model of the crust and uppermost mantle beneath the Central and Western US by joint inversion of receiver functions and surface wave dispersion, *J. Geophys. Res. Solid Earth*, *118*(1), 262–276, doi:10.1029/2012JB009602.

Shen, W., M. H. Ritzwoller, and V. Schulte-Pelkum (2013b), Crustal and uppermost mantle structure in the central U.S. encompassing the Midcontinent Rift, *J. Geophys. Res. Solid Earth*, *118*(8), 4325–4344, doi:10.1002/jgrb.50321.

Shen, W., M. H. Ritzwoller, V. Schulte-Pelkum, and F.-C. Lin (2013c), Joint inversion of surface wave dispersion and receiver functions: a Bayesian Monte-Carlo approach, *Geophys. J. Int.*, *192*(2), 807–836, doi:10.1093/gji/ggs050.

Shen, W., M. H. Ritzwoller, D. Kang, Y. Kim, F.-C. Lin, J. Ning, W. Wang, Y. Zheng, and L. Zhou (2016), A seismic reference model for the crust and uppermost mantle beneath China from surface wave dispersion, *Geophys. J. Int.*, ggw175, doi:10.1093/gji/ggw175.

Sherrington, H. F., G. Zandt, and A. Frederiksen (2004), Crustal fabric in the Tibetan Plateau based on waveform inversions for seismic anisotropy parameters, *J. Geophys. Res. Solid Earth*, *109*(B2), B02312, doi:10.1029/2002JB002345.

Silver, P. G., and W. W. Chan (1988), Implications for continental structure and evolution from seismic anisotropy, *Nature*, *335*(6185), 34–39, doi:10.1038/335034a0.

Simons, F. J., R. D. Van Der Hilst, J.-P. Montagner, and A. Zielhuis (2002), Multimode Rayleigh wave inversion for heterogeneity and azimuthal anisotropy of the Australian upper mantle, *Geophys. J. Int.*, *151*(3), 738–754, doi:10.1046/j.1365-246X.2002.01787.x.

Sloan, R. A., J. A. Jackson, D. McKenzie, and K. Priestley (2011), Earthquake depth distributions in central Asia, and their relations with lithosphere thickness, shortening and extension, *Geophys. J. Int.*, *185*(1), 1–29, doi:10.1111/j.1365-246X.2010.04882.x.

Smith, D. B., M. H. Ritzwoller, and N. M. Shapiro (2004), Stratification of anisotropy in the Pacific upper mantle, *J. Geophys. Res. Solid Earth*, *109*(B11), B11309, doi:10.1029/2004JB003200.

Smith, G. P., and G. Ekström (1999), A global study of Pn anisotropy beneath continents, *J. Geophys. Res. Solid Earth*, *104*(B1), 963–980, doi:10.1029/1998JB900021.

Smith, M. L., and F. A. Dahlen (1973), The azimuthal dependence of Love and Rayleigh wave propagation in a slightly anisotropic medium, *J. Geophys. Res.*, *78*(17), 3321–3333, doi:10.1029/JB078i017p03321.

Sol, S. et al. (2007), Geodynamics of the southeastern Tibetan Plateau from seismic anisotropy and geodesy, *Geology*, *35*(6), 563–566, doi:10.1130/G23408A.1.

Song, T.-R. A., and H. Kawakatsu (2012), Subduction of oceanic asthenosphere: Evidence from sub-slab seismic anisotropy, *Geophys. Res. Lett.*, *39*(17), L17301, doi:10.1029/2012GL052639.

Sun, X., X. Bao, M. Xu, D. W. Eaton, X. Song, L. Wang, Z. Ding, N. Mi, D. Yu, and H. Li (2014), Crustal structure beneath SE Tibet from joint analysis of receiver functions and Rayleigh wave dispersion, *Geophys. Res. Lett.*, *41*(5), 2014GL059269, doi:10.1002/2014GL059269.

Sun, Y., J. Liu, K. Zhou, B. Chen, and R. Guo (2015), Crustal structure and deformation under the Longmenshan and its surroundings revealed by receiver function data, *Phys. Earth Planet. Inter.*, *244*, 11–22, doi:10.1016/j.pepi.2015.04.005.

Su, W., C. Wang, and Z. Huang (2008), Azimuthal anisotropy of Rayleigh waves beneath the Tibetan Plateau and adjacent areas, *Sci. China Ser. Earth Sci.*, *51*(12), 1717–1725, doi:10.1007/s11430-008-0137-x.

Takeo, A., K. Nishida, T. Isse, H. Kawakatsu, H. Shiobara, H. Sugioka, and T. Kanazawa (2013), Radially anisotropic structure beneath the Shikoku Basin from broadband

surface wave analysis of ocean bottom seismometer records, *J. Geophys. Res. Solid Earth*, *118*, doi:10.1002/jgrb.50219.

Takeuchi, H., Y. Hamano, and Y. Hasegawa (1968), Rayleigh- and Love-wave discrepancy and the existence of magma pockets in the upper mantle, *J. Geophys. Res.*, *73*(10), 3349–3350, doi:10.1029/JB073i010p03349.

Tanimoto, T., and D. L. Anderson (1985), Lateral heterogeneity and azimuthal anisotropy of the upper mantle: Love and Rayleigh waves 100–250 s, *J. Geophys. Res. Solid Earth*, *90*(B2), 1842–1858, doi:10.1029/JB090iB02p01842.

Tan, J., H. Li, X. Li, M. Zhou, L. Ouyang, S. Sun, and D. Zheng (2015), Radial anisotropy in the crust beneath the northeastern Tibetan Plateau from ambient noise tomography, *J. Earth Sci.*, *26*(6), 864–871, doi:10.1007/s12583-015-0543-x.

Tapponnier, P., X. Zhiqin, F. Roger, B. Meyer, N. Arnaud, G. Wittlinger, and Y. Jingsui (2001), Oblique Stepwise Rise and Growth of the Tibet Plateau, *Science*, *294*(5547), 1671–1677, doi:10.1126/science.105978.

Tatham, D. J., G. E. Lloyd, R. W. H. Butler, and M. Casey (2008), Amphibole and lower crustal seismic properties, *Earth Planet. Sci. Lett.*, *267*(1–2), 118–128, doi:10.1016/j.epsl.2007.11.042.

Thomsen, L. (1986), Weak elastic anisotropy, *Geophysics*, *51*(10), 1954–1966, doi:10.1190/1.1442051.

Thomsen, L., and D. L. Anderson (2015), Weak elastic anisotropy in global seismology, in *Geological Society of America Special Papers*, vol. 514, pp. 39–50, Geological Society of America.

Tian, Y., W. Shen, and M. H. Ritzwoller (2013), Crustal and uppermost mantle shear velocity structure adjacent to the Juan de Fuca Ridge from ambient seismic noise, *Geochem. Geophys. Geosystems*, *14*(8), 3221–3233, doi:10.1002/ggge.20206.

Trampert, J., and A. J. H. Woodhouse (2001), Assessment of global phase velocity models, *Geophys. J. Int.*, *144*(1), 165–174, doi:10.1046/j.1365-246x.2001.00307.x.

Trampert, J., and J. H. Woodhouse (1995), Global phase velocity maps of Love and Rayleigh waves between 40 and 150 seconds, *Geophys. J. Int.*, *122*(2), 675–690, doi:10.1111/j.1365-246X.1995.tb07019.x.

Tsvankin, I. (1997), Anisotropic parameters and P-wave velocity for orthorhombic media, *Geophysics*, *62*, 1292–1309.

Unsworth, M., W. Wenbo, A. G. Jones, S. Li, P. Bedrosian, J. Booker, J. Sheng, D. Ming, and T. Handong (2004), Crustal and upper mantle structure of northern Tibet imaged with

magnetotelluric data, *J. Geophys. Res. Solid Earth*, *109*(B2), B02403, doi:10.1029/2002JB002305.

Valcke, S. L. A., M. Casey, G. E. Lloyd, J.-M. Kendall, and Q. J. Fisher (2006), Lattice preferred orientation and seismic anisotropy in sedimentary rocks, *Geophys. J. Int.*, *166*(2), 652–666, doi:10.1111/j.1365-246X.2006.02987.x.

Vergne, J., G. Wittlinger, Q. Hui, P. Tapponnier, G. Poupinet, J. Mei, G. Herquel, and A. Paul (2002), Seismic evidence for stepwise thickening of the crust across the NE Tibetan plateau, *Earth Planet. Sci. Lett.*, *203*(1), 25–33, doi:10.1016/S0012-821X(02)00853-1.

Vergne, J., G. Wittlinger, V. Farra, and H. Su (2003), Evidence for upper crustal anisotropy in the Songpan-Ganze (northeastern Tibet) terrane, *Geophys. Res. Lett.*, *30*(11), 1552, doi:10.1029/2002GL016847.

Villaseñor, A., M. H. Ritzwoller, A. L. Levshin, M. P. Barmin, E. R. Engdahl, W. Spakman, and J. Trampert (2001), Shear velocity structure of central Eurasia from inversion of surface wave velocities, *Phys. Earth Planet. Inter.*, *123*(2-4), 169–184, doi:10.1016/S0031-9201(00)00208-9.

Vinnik, L. P., V. Farra, and B. Romanowicz (1989), Azimuthal anisotropy in the earth from observations of SKS at GEOSCOPE and NARS broadband stations, *Bull. Seismol. Soc. Am.*, *79*(5), 1542–1558.

Vinnik, L. P., L. I. Makeyeva, A. Milev, and A. Y. Usenko (1992), Global patterns of azimuthal anisotropy and deformations in the continental mantle, *Geophys. J. Int.*, *111*(3), 433–447, doi:10.1111/j.1365-246X.1992.tb02102.x.

Wang, C.-Y., L. M. Flesch, P. G. Silver, L.-J. Chang, and W. W. Chan (2008), Evidence for mechanically coupled lithosphere in central Asia and resulting implications, *Geology*, *36*(5), 363–366, doi:10.1130/G24450A.1.

Wang, C.-Y., L. Zhu, H. Lou, B.-S. Huang, Z. Yao, and X. Luo (2010), Crustal thicknesses and Poisson's ratios in the eastern Tibetan Plateau and their tectonic implications, *J. Geophys. Res.*, *115*(B11), B11301, doi:10.1029/2010JB007527.

Wang, N., J.-P. Montagner, A. Fichtner, and Y. Capdeville (2013), Intrinsic versus extrinsic seismic anisotropy: The radial anisotropy in reference Earth models, *Geophys. Res. Lett.*, *40*(16), 4284–4288, doi:10.1002/grl.50873.

Ward, D., K. Mahan, and V. Schulte-Pelkum (2012), Roles of quartz and mica in seismic anisotropy of mylonites, *Geophys. J. Int.*, *190*(2), 1123–1134, doi:10.1111/j.1365-246X.2012.05528.x.

Weiss, T., S. Siegesmund, W. Rabbel, T. Bohlen, and M. Pohl (1999), Seismic Velocities and Anisotropy of the Lower Continental Crust: A Review, *Pure Appl. Geophys.*, *156*(1-2), 97–122, doi:10.1007/s000240050291.

Wei, W. et al. (2001), Detection of widespread fluids in the Tibetan crust by magnetotelluric studies, *Science*, *292*(5517), 716–719, doi:10.1126/science.1010580.

Wendt, A. S., I. O. Bayuk, S. J. Covey-Crump, R. Wirth, and G. E. Lloyd (2003), An experimental and numerical study of the microstructural parameters contributing to the seismic anisotropy of rocks, *J. Geophys. Res. Solid Earth*, *108*(B8), 2365, doi:10.1029/2002JB001915.

Xiao, H.-B., F. A. Dahlen, and J. Suppe (1991), Mechanics of extensional wedges, *J. Geophys. Res. Solid Earth*, *96*(B6), 10301–10318, doi:10.1029/91JB00222.

Xie, J., M. H. Ritzwoller, W. Shen, Y. Yang, Y. Zheng, and L. Zhou (2013), Crustal radial anisotropy across Eastern Tibet and the Western Yangtze Craton, *J. Geophys. Res. Solid Earth*, *118*(8), 4226–4252, doi:10.1002/jgrb.50296.

Xie, J., M. H. Ritzwoller, S. J. Brownlee, and B. R. Hacker (2015), Inferring the oriented elastic tensor from surface wave observations: preliminary application across the western United States, *Geophys. J. Int.*, *201*(2), 996–1021, doi:10.1093/gji/ggv054.

Xu, L., S. Rondenay, and R. D. van der Hilst (2007a), Structure of the crust beneath the southeastern Tibetan Plateau from teleseismic receiver functions, *Phys. Earth Planet. Inter.*, *165*(3–4), 176–193, doi:10.1016/j.pepi.2007.09.002.

Xu, Y., Z. Li, and S. W. Roecker (2007b), Uppermost mantle structure and its relation with seismic activity in the central Tien Shan, *Geophys. Res. Lett.*, *34*(10), L10304, doi:10.1029/2007GL029708.

Yang, Y., and M. H. Ritzwoller (2008), Characteristics of ambient seismic noise as a source for surface wave tomography, *Geochem. Geophys. Geosystems*, *9*(2), n/a–n/a, doi:10.1029/2007GC001814.

Yang, Y. et al. (2010), Rayleigh wave phase velocity maps of Tibet and the surrounding regions from ambient seismic noise tomography, *Geochem. Geophys. Geosystems*, *11*(8), Q08010, doi:10.1029/2010GC003119.

Yang, Y., M. H. Ritzwoller, Y. Zheng, W. Shen, A. L. Levshin, and Z. Xie (2012), A synoptic view of the distribution and connectivity of the mid-crustal low velocity zone beneath Tibet, *J. Geophys. Res.*, *117*, 20 PP., doi:201210.1029/2011JB008810.

Yao, H., R. D. Van Der Hilst, and M. V. De Hoop (2006), Surface-wave array tomography in SE Tibet from ambient seismic noise and two-station analysis - I. Phase velocity maps, *Geophys. J. Int.*, *166*(2), 732–744, doi:10.1111/j.1365-246X.2006.03028.x.

Yao, H., C. Beghein, and R. D. van der Hilst (2008), Surface-wave array tomography in SE Tibet from ambient seismic noise and two-station analysis - II. Crustal and upper-mantle structure, *Geophys. J. Int.*, *173*, 205–219.

Yao, H., R. D. van der Hilst, and J.-P. Montagner (2010), Heterogeneity and anisotropy of the lithosphere of SE Tibet from surface wave array tomography, *J. Geophys. Res.*, *115*(B12), B12307, doi:10.1029/2009JB007142.

Yao, H., P. Gouédard, J. A. Collins, J. J. McGuire, and R. D. van der Hilst (2011), Structure of young East Pacific Rise lithosphere from ambient noise correlation analysis of fundamental- and higher-mode Scholte-Rayleigh waves, *Comptes Rendus Geosci.*, *343*(8–9), 571–583, doi:10.1016/j.crte.2011.04.004.

Yuan, H., and B. Romanowicz (2010), Lithospheric layering in the North American craton, *Nature*, *466*(7310), 1063–1068, doi:10.1038/nature09332.

Yuan, H., B. Romanowicz, K. M. Fischer, and D. Abt (2011), 3-D shear wave radially and azimuthally anisotropic velocity model of the North American upper mantle, *Geophys. J. Int.*, *184*(3), 1237–1260, doi:10.1111/j.1365-246X.2010.04901.x.

Yue, H. et al. (2012), Lithospheric and upper mantle structure of the northeastern Tibetan Plateau, *J. Geophys. Res.*, *117*(B5), B05307, doi:10.1029/2011JB008545.

Yu, Y., and J. Park (1993), Upper mantle anisotropy and coupled-mode long-period surface waves, *Geophys. J. Int.*, *114*(3), 473–489, doi:10.1111/j.1365-246X.1993.tb06981.x.

Zandt, G., and C. J. Ammon (1995), Continental crust composition constrained by measurements of crustal Poisson's ratio, *Nature*, *374*(6518), 152–154, doi:10.1038/374152a0.

Zhang, P., Q. Deng, G. Zhang, J. Ma, W. Gan, W. Min, F. Mao, and Q. Wang (2003), Active tectonic blocks and strong earthquakes in the continent of China, *Sci. China Ser. Earth Sci.*, *46*(2), 13–24, doi:10.1360/03dz0002.

Zhang, P.-Z., X. Wen, Z.-K. Shen, and J. Chen (2010), Oblique, High-Angle, Listric-Reverse Faulting and Associated Development of Strain: The Wenchuan Earthquake of May 12, 2008, Sichuan, China, *Annu. Rev. Earth Planet. Sci.*, *38*(1), 353–382, doi:10.1146/annurev-earth-040809-152602.

Zhang, Z. M., J. G. Liou, and R. G. Coleman (1984), An outline of the plate tectonics of China, *Geol. Soc. Am. Bull.*, *95*(3), 295–312, doi:10.1130/0016-7606(1984)95<295:AOOTPT>2.0.CO;2.

Zheng, S., X. Sun, X. Song, Y. Yang, and M. H. Ritzwoller (2008), Surface wave tomography of China from ambient seismic noise correlation, *Geochem. Geophys. Geosystems*, *9*(5), n/a–n/a, doi:10.1029/2008GC001981.

Zheng, X.-F., Z.-X. Yao, J.-H. Liang, and J. Zheng (2010), The Role Played and Opportunities Provided by IGP DMC of China National Seismic Network in Wenchuan Earthquake Disaster Relief and Researches, *Bull. Seismol. Soc. Am.*, *100*(5B), 2866–2872, doi:10.1785/0120090257.

Zheng, Y., W. Shen, L. Zhou, Y. Yang, Z. Xie, and M. H. Ritzwoller (2011), Crust and uppermost mantle beneath the North China Craton, northeastern China, and the Sea of Japan from ambient noise tomography, *J. Geophys. Res. Solid Earth*, *116*(B12), B12312, doi:10.1029/2011JB008637.

Zhou, L., J. Xie, W. Shen, Y. Zheng, Y. Yang, H. Shi, and M. H. Ritzwoller (2012), The structure of the crust and uppermost mantle beneath South China from ambient noise and earthquake tomography, *Geophys. J. Int.*, *189*(3), 1565–1583, doi:10.1111/j.1365-246X.2012.05423.x.

Zhou, Y., G. Nolet, F. A. Dahlen, and G. Laske (2006), Global upper-mantle structure from finite-frequency surface-wave tomography, *J. Geophys. Res. Solid Earth*, *111*(B4), B04304, doi:10.1029/2005JB003677.